SAPIENZA
UNIVERSITÀ DI ROMA

DEPARTMENT OF MECHANICAL AND AEROSPACE ENGINEERING
DOCTORATE OF PHILOSOPHY
IN AERONAUTICAL AND SPACE TECHNOLOGY

A New Ultrasonic SHM Procedure for Delamination Detection in Composite Structures: Numerical Analyses and Experimental Tests

PH.D. CANDIDATE:
Michele Pasquali

ADVISOR:
Prof. Walter Lacarbonara

CO-ADVISOR:
Prof. Paolo Gaudenzi

Academic Year 2012-2013

[This page intentionally left blank]

«*The way to solve the conflict between human values and technological needs is not to run away from technology. That's impossible. The way to resolve the conflict is to break down the barriers of dualistic thought that prevent a real understanding of what technology is ... not an exploitation of nature, but a fusion of nature and the human spirit into a new kind of creation that transcends both. When this transcendence occurs in such events as the first airplane flight across the ocean or the first footstep on the moon, a kind of public recognition of the transcendent nature of technology occurs. But this transcendence should also occur at the individual level, on a personal basis, in one's own life, in a less dramatic way..*»

R.M. Pirsig in *Zen and the Art of Motorcycle Maintenance*

[This page intentionally left blank]

Acknowledgements

Thank god I'm done.

[This page intentionally left blank]

Abstract

The objective of this thesis is to develop an innovative Structural Health Monitoring (SHM) technique that exploits piezoelectric-induced ultrasonic waves in composite laminates to detect the presence of delaminations caused by impacts, vibrations and other external disturbances. The ultrasonic SHM technique here proposed is intended to be the initial stage of a broader approach to structural health monitoring aimed at damage detection in composite plate-like structures which resorts to the exploitation of the damage-induced lag in the times of arrival of primary (P) and secondary (S) elastic waves traveling in the plate thickness direction as the fundamental mechanism for enhanced detection capabilities. This approach is envisioned to expand the current performance envelope of ultrasonic SHM techniques since the local character of the proposed technique together with its innovative nature based on the use of P and S elastic waves is expected to combine a high level of reliability with a fast and repeatable SHM routine. The specific tasks in line to achieve the overall objective of the work are organized in four major steps. First, the study of the theoretical problem associated to the development of the SHM procedure is carried out and features the generation (by surface apertures) of appropriate elastodynamic fields in thin-walled structures to identify the lag in the times of arrival of primary and secondary waves as key element in the delamination detection routine. Second, the implementation of two and three-dimensional numerical models is tackled to deliver a better insight into the phenomena associated to the generation of elastodynamic fields in composite laminates undergoing delaminations. Third, efficient differential evolutionary-based numerical codes are implemented with the aim of optimizing the performance of the proposed SHM routine. Finally, the experimental validation of the analyzed SHM procedure is carried out through extensive testing activities, employing different types of setups.

Contents

List of Figures

List of Tables

Chapter 1

Introduction

The impact that the aerospace industry has exerted on various aspects of the technological evolution and the overall world economy over the last sixty years is enormous. Research and development for aerospace applications is at the forefront on engineering achievements and several new technologies have been transferred to other fields in recent years. However, current economic, technical and social demands have resulted in challenges for aircraft designers and operators. New large capacity aircraft are being developed and will be used widely in the future. Many of these structures will make greater use of composite materials. At the same time the current aircraft fleet is ageing continuously. All these developments are a major challenge to inspection and maintenance.

Aerospace structures are currently inspected using traditional Nondestructive Evaluation Techniques (NDE) such as visual inspection, radiography and eddy current [1]. However, today's NDE, usually conducted at regular scheduled intervals during the lifetime of engineered structures and assets, is too unwieldy to achieve automatic damage identification when the structures and assets are in service. That is because the NDE equipment used cannot provide efficient access to appropriate sections of the structures in a real-time manner. Therefore most current NDE approaches provide limited information about structural integrity.

Driven by recent advances and technical breakthroughs in sensor technology, manufacturing, electronic packaging, signal processing, informatics, diagnostics, applied mechanics and material sciences, conventional NDE techniques are now being retrofitted, with the aim of continuous/real-time and automated surveillance of the overall integrity of structures through consideration of working condition updates and structural ageing. This technology is termed online damage identification or Structural Health Monitoring (SHM). SHM is defined as the nondestructive and continuous monitoring characteristics using an array of sensors related to the fitness of an engineered component as it operates, so as to diagnose the onset of anomalous structural behavior. It involves measurements and evaluations of the

state properties so as related them to defined performance parameters [2]. SHM provides comprehensive information concerning (i) operational and environmental loads, (ii) damage caused by loads, (iii) growth of damage, and (iv) performance of the structure as damage accumulates, in aspects such as residual strength and life. Objectives (i)-(iii) are associated with damage diagnosis (qualitative or quantitative identification and assessment of damage), and (iv) falls into the category of damage prognosis (estimate of a system's residual life [3]).

An SHM subsystem typically consists of an onboard network of sensors for data acquisition and some central processors to evaluate the structural health. It may utilize stored knowledge of structural materials, operational parameters, and health criteria. The schemes available for SHM can be broadly classified as active or passive depending on whether or not they involve the use of actuators, respectively. Examples of passive schemes are acoustic emission and strain/load monitoring, which have been demonstrated with some success [4]-[10]. However, these suffer from the drawback of requiring high sensor densities on the structure. They are typically implemented using fiber optic sensors and, for environments that are relatively benign, foil strain gages. Unlike passive methods, active schemes are capable of exciting the structure and, in a prescribed manner, they can examine it for damage within seconds, where and when required. Among active schemes, guided-wave testing has emerged as a very prominent option. It can offer an effective method to estimate the location, severity and type of damage, and it is a well-established practice in the non-destructive evaluation and testing (NDE/NDT) industry. There, guided-waves are excited and received in a structure using handheld transducers for scheduled maintenance. They have also demonstrated suitability for SHM applications, having an onboard, preferably built-in, sensor and actuator network to assess the state of a structure during operation.

1.1 Conventional damage detection procedures

It is well understood that damage can induce changes in the local and global properties of a structure (e.g., local effective stiffness, density, mass, thermal properties, electric/magnetic conductivity, electro-mechanical impedance and strain energy). These changes are included in dynamic response signals propagated through the structure. The challenge in this aspect is to figure out, with the assistance of appropriate mechanisms and tools, what these changes in signals mean physically about the structures. Most NDE approaches have been developed by scrutinizing the structural dynamic response signals captured by various transducers. Then, by referencing baseline signals (collected from a benchmark structure supposed to be healthy), the damage can be pinpointed. That is the premise of these approaches [11].

Theoretically, changes in either global or local properties of a structure under inspection can be associated with damage parameters [12, 13]. However, approaches capitalizing on

changes in global dynamic properties including eigenfrequencies, mode shapes and curvatures, strain energy, and damping properties are less sensitive to damage before it reaches a noticeable extent (e.g., 10% of the characteristic dimension/area of the structure), since damage is a local event which would not significantly change structural global response features. Electro-mechanical impedance and static parameters such as displacement or strain are features that can be used to calibrate local changes in the presence of damage [14], but they are relatively insensitive to damage that is distant from sensors. Acoustic emission is an effective mean to triangulate damage and predict damage growth, but such a passive detection technique is unable to further evaluate damage severity.

One of the most popular category that can be identified among the traditional damage detection procedures is represented by the class of the *model-data-based* approaches [11, 13, 15, 16]. Common features adopted to assess the state of damage of the structure under inspection are its modal parameters as its eigenfrequencies, its mode shapes and their curvatures. These methods are based on the fact that the presence of damage reduces the stiffness of the structure, causes a frequency shift in its eigenfrequencies, and changes its frequency response function and mode shapes. In addition, the analysis of the variation in the strain energy released in the deformation process and due to the presence of a damage is also addressed in this class of damage detection procedures; the study of changes in the flexibility of the structure or in its damping properties is also carried out to detect the presence and location of damage.

Common advantages featured by the NDE methods belonging to the model-data-based class are their simple implementation and their low cost. They have proven to be particularly effective for detecting large damages in large infrastructures or rotating machinery. On the contrary, they are generally insensitive to small damages or to damage growth; moreover, it can be very difficult to excite high frequencies needed to complete these particular NDE approaches. Two major disadvantages characterizing these methods are the need for a large number of measurement points and their hypersensitivity to boundary and environmental changes which can make model-data-based NDE techniques ineffective.

The class of NDE procedures based on the analysis of damage-induced variations in the parameters defining the static behavior of the structure under analysis it often referred to as the *static-parameter-based* class [17]-[20]. The methods which can be grouped into this class rely in general on the observation that the presence of a damage causes changes in displacement and strain distribution in comparison with a pre-defined benchmark. These procedures are locally sensitive to defects, simple and cost-effective; on the other hand, they have shown to be relatively insensitive to undersized damage or to detect the evolution of deterioration of the structure.

Another class of NDE techniques which has gained popularity in recent years is that based on the analysis of changes in the *electromechanical impedance* of the structure [21]-[24]. These damage detection routines rely on the fact that the composition of a system contributes a certain amount to the total amount of electromechanical impedance of the system, with the presence of damage modifying the impedance distributions in a high-frequency range, normally higher than 30 KHz. Based on the use of piezoelectric transducers, these techniques feature a low cost and simple implementation and they have shown particularly good results in detecting defects in planar structures. Due to their local nature, however, they are generally unable to detect damages located at a distant position from the sensors, proving to be accurate only in the identification of large damages or to detect the effects of loosen joints in an assembled structure [25].

Acoustic emissions-based methods, instead, detect the rapid release of strain energy associated with the generation and propagation of damages in a structure [26]-[29]. The release of such elastic energy generates transient damage-emitted acoustic waves, which can be captured (usually adopting piezoelectric sensors) to triangulate the damage position in different modalities including matrix crack, fibre fracture, delamination, microscopic deformation, welding flaw and corrosion. The capability of this NDE class to detect the growth of the damage offering a good coverage of the structure (being surface-mountable) have made these damage detection routines very popular in the SHM community. As every other process to evaluate the state of damage of a structural system, also acoustic emissions-based methods are affected by some important limitations: due to their nature, in fact, they are prone to contamination by environmental noise; the acquisition of complex output signal requires the implementation of a complex and time-demanding post-processing. In addition, due to the high damping ratio affecting the elastic waves emitted by the damage, these NDE methods have proven to be suitable only in detecting damages in small structures.

1.2 Ultrasonic NDE

The earliest exploration of ultrasonic nondestructive evaluation techniques (US-NDE) for the purpose of damage identification can be dated back to the distance measurement (a prototype of the sonar technique) and blemish detection used for ships and submarine hulls in the 19th century. In recent years, researchers have increasingly become interested in taking advantage of elastic waves to develop novel damage identification techniques for various engineered structures and assets, based on mature understanding of elastic waves [30, 31, 32] and awareness of the potential of elastic waves for identifying damage in a cost-effective manner.

The most popular type of elastic waves adopted in thin plate/shell structures to perform

damage detection is represented by Lamb waves (see Appendix A), which have been at the core of intensive efforts since the late 1980s. Lamb waves can propagate over a relatively long distance, even in materials with high attenuation ratios, such as polymer composites, and thus allow a broad area to be covered with only a few transducers. Lamb waves have offered an intriguing avenue to develop novel damage identification and SHM techniques, in recognition of the observations that (i) interaction of Lamb waves with structural damage can significantly influence their propagation properties, accompanying wave scattering and mode conversion. Rich information about damage is encoded in the Lamb waves scattered by that damage; and (ii) different locations and severity of damage cause unique scattering phenomena.

As witnessed over the past two decades, there have been pilot studies for developing damage identification techniques using Lamb waves [33]-[40] highlighted in some review articles in the literature [41]-[45]. Through intensive studies in this area, Lamb waves have identified their superb niche for cost-effective damage identification and SHM. Actually, Lamb waves are now the most widely used acousto-ultrasonic guided waves for damage identification [46]. A popular taxonomy for categorizing these approaches is in terms of the domain where the processing is conducted, i.e., time domain, frequency domain and joint time-frequency domain analyses.

1.2.1 Time-domain methods

In most cases, a Lamb wave signal is presented in the time domain. A time-series signal inherently records the time history of Lamb waves traveling in a structure, thereby providing the most straightforward information about the waves, such as existence of various wave modes, propagation velocity, attenuation and dispersion with distance, scattering from a structural boundary or damage. The characteristics exhibited by a time-series Lamb wave signal, that may be beneficial to damage identification, include the magnitude, the root mean square (RMS) of the signal, the standard deviation, the kurtosis, the characteristic time moment, the trend, the cyclical component, the time-of-flight (ToF), etc. All these characteristics can be modulated to a greater or lesser degree in the presence of structural damage.

The difference in ToFs (difference in ToFs is defined as the time lag between the incident wave that the sensor first captures and the wave scattered by the damage that the same sensor subsequently captures) is one of the most straightforward features of a Lamb wave signal for damage identification. This index suggests the relative positions among the actuator, the sensor and the damage. From the difference in the ToFs between the damage-scattered and incident waves extracted from a certain number of signals, the damage position can

accordingly be triangulated [47]-[50], leading to the determination of a locus which indicates possible locations of the centre of the damage.

Another approach is represented by the use of the *Hilbert transform*: this method is aimed at canvassing a Lamb wave signal in the time domain in terms of its energy distribution [51]-[58]. The Hilbert transform can be fulfilled using a Fast Fourier transform (FFT), capturing the energy envelope of a Lamb wave signal. Composite structures as well as isotropic plates containing delamination have been analyzed in the literature [59]: using the Hilbert transform, the energy distribution of the signal becomes explicit and global or local features such as instantaneous frequency, magnitude and damping characteristics are extracted. Sudden changes in the energy distribution at particular times are used as evidences that a damage may have occurred at those time instants: the degree of the observed changes is often used to quantify the damage severity.

Damaged is a structural state different from the original state that is supposed to be "healthy"; that is to say, the states of "damage" and "health' are defined relatively. Implicit in this definition, a damage event is not meaningful without a comparison between two different states. To facilitate such a comparison and to highlight the difference, a Lamb wave signal captured in a structure under inspection is often evaluated against its counterpart signal in the benchmark structure by using *correlation* in the time domain [60, 61, 62]. An abnormality such as damage in the structure can thus be detected and quantified with respect to the healthy state. In such a correlation processing, the correlation coefficients of two (or more) discrete time-series Lamb wave signals of the same length are estimated. The more the correlation coefficients (calculated comparing the response of undamaged systems and the response of a systems whose state of damage is unknown) differ from unity, the smaller the similarity between two signals, implying the presence of damages in the analyzed structure.

Time reversal is a signal processing approach based on reciprocity of the wave equation, which is mathematically guaranteed by the fact that the wave equation contains only even order derivatives. Reciprocity presumes that if there is a solution to a wave equation, then the time reversal of that solution is also a solution to the wave equation [63]. In other words, for a given process, the solution to the wave equation at time t is the same as that at time -t , even though the waves may be reflected, refracted or scattered by inhomogeneities in the medium in which waves travel. However, this paradox does not hold for macroscopic processes in the real world that are irreversible and dissipative in nature. Some media are not reciprocal (e.g., very lossy or noisy media), but many are approximately so. For example, sound waves in water or air, ultrasonic waves in human bodies, alloys or composites, and electromagnetic waves in free space are all approximately reciprocal examples.

1.2.2 Frequency-domain methods

To reveal singularities induced by structural damages, which may not be clearly ascertained in the time domain, a Lamb wave signal is often transformed in the frequency domain through the Fourier Transform (FT) and Fast Fourier Transform [64]. A Lamb wave signal usually contains a variety of components in a wide frequency range of which only certain bands are of interest for damage identification, such as those bands whose central frequency is the same as that of activation: *digital filters* developed using FT and FFT constitute the main approach used for extracting the components of interest from raw Lamb signals. Digital filter design is actually the process that seeks the most suitable filter coefficients, to cater for certain filtering requirements. Adjusting the filter coefficients, different types of filters can be obtained: (i) low-pass filters, transmitting wave components with frequencies below a threshold and excluding others; (ii) high-pass filters, transmitting wave components with frequencies above a threshold and excluding others; (iii) bandpass filters, which transmit wave components within a particular range of frequencies and excluding others and (iv) band-stop filters, which stop components between a lower and a higher cut-off frequencies. However, when the wave components of interest are in the same frequency band as those not of interest, FT- or FFT-based filtering becomes inefficient to isolate them. It should also be noted that the use of FTs and FFTs to transfer a wave signal from the time to frequency domain comes at the cost of disregarding temporal information of the signal such as its amplitude and ToF.

To separate different wave components or multiple wave modes which share the same frequency range in a Lamb wave signal, *two-dimensional FT* (2D-FT) [65]-[71] is one among a number of diverse applicable methods. Two-dimensional FTs are used to link the magnitudes of different Lamb modes in a wave signal with wavenumber and frequency. More often, a two-dimensional FFT (2D-FFT) algorithm is used because of the improved capacity of calculation of FFTs. This algorithm can present a Lamb wave signal in a two-dimensional contour plot or a three-dimensional plot of magnitude versus wavenumber and frequency: various Lamb modes propagating in the structure can be isolated, allowing clear recognition of multiple wave modes even within the same frequency band [66]. Since 2D-FT/FFT needs Lamb wave signals captured at different locations, a great number of sensors are usually required.

1.2.3 Joint time-frequency domain methods

It is a corollary to combine the analyes in the sole time and sole frequency domains so as to avoid any potential loss of information carried by a Lamb wave signal, leading to the joint time-frequency domain analysis. The joint time-frequency domain analysis is exemplified by the *Short-Time Fourier Transform* (STFT) and the *Wavelet Transform* (WT).

STFT applies the basic FT on a small signal segment about time moment t , by multiplying a time window function (commonly a Hanning or Gaussian window) and neglecting the rest of the signal. This operation is then continued by moving the short time window along the entire time axis, to obtain the energy spectrum of the full signal. With its ability to simultaneously unveil features as to the time and frequency of a signal, STFT has found a great number of applications in Lamb wave signal processing [73, 77]. Upon application of STFT to Lamb wave signals, the energy distribution of various Lamb wave modes in the signals at different time moments and frequencies can be obtained, as shown in [73]. This approach can be thus be used in selecting an optimal excitation frequency at which the activated signal has a high SNR. However, because of the unalterable window size, satisfactory precision cannot be obtained along the time- and frequency-axes synchronously. Therefore STFT may not be the optimal choice for analyzing wave signals whose instantaneous frequency varies rapidly.

As an improvement on direct time-frequency analysis, *WT* is a tool for processing dynamic signals or images. With its rationale established in the 1950s, WT has claimed a wide application domain ranging from geophysics and biomedicine to offshore petroleum exploration and movie , to mention but a few. Since introduced to the analysis of vibration signals in the 1990s [78, 79, 80], this signal processing technique has enjoyed burgeoning popularity in the NDE community [75, 78, 81]. In brief, the wavelet is a waveform with a limited duration or window, whose average amplitude equals zero. During the transformation, a dynamic signal is represented using dual parameters, scale and time, with scale being inversely proportional to frequency. WT is substantially a window technique featuring a window of variable size. A large value of scale stands for a big window, a global view of the signal and accordingly low resolution; a small value of scale represents a small window, a detailed view of the signal and accordingly high resolution. Representation of a dynamic signal over the time-scale domain rather than the direct time-frequency domain is not a degradation or compromise; rather it enhances the resolution of illustration and recognisability of a signal. It allows detailed interpretation of a localized signal fragment so as to canvass hidden characteristics such as singularity or discontinuity in signals. Compared with other time-frequency approaches previously introduced, WT features conservation of energy during the transform, provision of full signal information, localization in both time and frequency domains, and deployment of the signal with multiresolution.

1.3 A local approach for ultrasonic SHM procedures

It can be stated that nowadays damage identification techniques based on ultrasonic waves represent the most frequently adopted approaches in the SHM domain. Such popularity is due to some noteworthy properties the ultrasonic methods feature: among them it is

worth citing (i) the capability of inspecting large portions of the structure in a short time using few transducers in a sparse configuration due to the high traveling velocity of guided-waves and to low wave attenuation (in isotropic media), (it has been demonstrated that the ratio of the planar area of the plate that can be inspected to the area of a circular wave transducer can be about 3000:1 [42]); (ii) the capability of classifying various types of damage using different wave modes; (iii) high sensitivity to damage and therefore high identification precision, due mainly to unique scattering phenomena associated to the presence of a certain type of damage; (iv) the use of piezoelectric transducers as sensors and actuators enabling the implementation of experimental setups at relatively low costs.

The desirable features which characterize the ultrasonic wave-based damage detection techniques can become ineffective when multilayered composite structural systems are analyzed. Due to their mechanical properties, in fact, composite materials have emerged as a preeminent technology in the realization of structural systems in aerospace engineering. The inner complexity of such structures associated to their inhomogeneity, anisotropy and possibly to complex geometrical shapes is reflected into a high complexity of the acquired signal appearance when ultrasonic wave-based techniques are adopted, requiring well-calibrated and time-demanding signal processing and interpretation techniques which are hardly associable to the idea of an on-line identification of the damage which defines the concept of SHM.

These difficulties have caused the need for an SHM routine capable of granting the fastness and reliability required by on-line damage detection procedures maintaining the effectiveness and sensitivity characteristic of ultrasonic methods also when composite multilayer structures are examined. To this end, *localized* or *local* approaches can be taken into account in tackling the SHM problem. The word local is here used to define all those damage detection methods in which the area inspected by a single sensor or by a single actuator-sensor pair has a characteristic dimension which is comparable to the geometric parameters defining the actuators (sensors) size, and which are thus characterized by the implementation of a transducers network. Due to the reduced extension of the main portion of the domain to be investigated by a single unity of the network, the adoption of an ultrasonic wave-based procedure in such a local scheme would feature (i) a lower complexity of the acquired signal (which would lack the effects of multiple wave reflections induced by the boundaries of the system) and, consequently, (ii) an easier extraction of the damage features, and (iii) a higher reliability on SHM procedure results. This, on the other hand, would imply (iv) a lower complexity of the damage identification algorithm to be used in such SHM procedure and thus (v) a faster SHM routine which could be virtually implemented in an on-line detection of the damage in a composite structural system. Moreover, the possibility to isolate simple

SHM unities in the network would reflect in a lower dependence on the system geometry and, thus, in (vi) an easier standardization process for a possible implementation of local SHM methods for real-world applications.

On the other hand, the realization of a network of sensors and actuators requires a higher density of transducers, with a consequent increase of the wiring and thus of the SHM system invasivity. Additional drawbacks are represented by the increase of the weight of the SHM system (a key element in aerospace structures) and, last but not least, higher costs of implementations.

1.4 Objective of the thesis

The objective of this thesis is to develop an innovative Structural Health Monitoring (SHM) technique that exploits piezoelectric-induced ultrasonic waves in composite laminates to detect the presence of delaminations caused by impacts, vibrations and other external disturbances. The ultrasonic SHM technique here proposed is intended to be the initial stage of a broader approach to structural health monitoring aimed at damage detection in composite plate-like structures which resorts to the exploitation of the damage-induced lag in the times of arrival of primary (P) and secondary (S) elastic waves traveling in the plate thickness direction as the fundamental mechanism for enhanced detection capabilities. This approach is envisioned to expand the current performance envelope of ultrasonic SHM techniques since the local character of the proposed technique together with its innovative nature based on the use of P and S elastic waves is expected to combine a high level of reliability with a fast and repeatable SHM routine. The specific tasks in line to achieve the overall objective of the work are organized in four major steps. First, the study of the theoretical problem associated to the development of the SHM procedure is carried out and features the generation (by surface apertures) of appropriate elastodynamic fields in thin-walled structures to identify the lag in the times of arrival of primary and secondary waves as key element in the delamination detection routine. Second the implementation of two and three-dimensional numerical models is tackled to deliver a better insight into the phenomena associated to the generation of elastodynamic fields in composite laminates undergoing delaminations. Third, efficient differential evolutionary-based numerical codes are implemented with the aim of optimizing the performances of the proposed SHM routine. Finally, the experimental validation of the analyzed US-SHM procedure is carried out through extensive testing activities, employing different types of setups.

In the literature, it has been pointed out that advanced SHM techniques should be rooted onto physics-based models other than black-box approaches. This motivates a major undertaking in this work towards formulating a delamination detection procedure in which

the complex phenomena characterizing the generation of elastic waves in plate-like domains and their interactions with the damage are analyzed and therefore used to constitute the basis of the proposed SHM procedure. To this end, the solution of the acoustic problem associated to the presence of point-wise force and strain sources in the three-dimensional domain is discussed to introduce the mathematical framework necessary to achieve a point-source synthesis when the complete elastodynamic problem is considered. In order to obtain the radiation characteristics defining the structure of the elastodynamic field generated by piezoelectric-like sources in the structural system, the analysis of the propagation of elastic ultrasonic waves in half spaces is addressed. As already mentioned, the lag in the times of arrival to the sensor location of primary and secondary waves propagating in the composite laminate thickness direction, generated by a piezoelectric actuator and reflected by the a delamination present between the laminae of the structure is identified as key mechanism in the damage detection procedure. An innovative architecture of the actuating-sensing system is designed to exploit the described phenomena in the proposed SHM routine, and an ad-hoc excitation signal is defined in terms of time-duration, frequency content and amplitude to serve as means of generation of the elastic waves. The governing equations of the composite laminate are then numerically implemented in their strong formulation using the COMSOL Multiphysics® software: the implementation of the constitutive laws of the composite laminate as well as of the equations defining the electromechanical behavior of the piezoelectric transducers allows to use and obtain back input and output signals directly in terms of voltage, granting an accurate description of the physics characterizing the generation of the ultrasonic waves. Two- and three-dimensional numerical simulations are then carried out allowing to achieve a precise definition of the SHM routine which takes into account the observed frequency modulation effects which appear as a consequence of the presence of the delamination. An optimization process aimed at enhancing the performance of the proposed SHM approach is then accomplished, resulting in the realization of a numerical code based on differential evolutionary algorithms and capable of interacting with the mentioned FEM software.

Finally, the proposed SHM procedure is validated through an extensive experimental campaign where both isotropic and anisotropic specimens are tested. In the latter case, in particular, delaminations are induced at different depths in eight-layer carbon fiber composite laminates introducing teflon inserts in the lamination sequence. A good agreement between the theoretical and numerical predictions and the experimental results is obtained, highlighting the effectiveness and validity of the proposed approach.

Chapter 2

Point-Source Synthesis of Acoustic Fields with Green Functions

2.1 Governing equations of acoustics

The Cauchy's equation of motion and the deformation rate equations read:

$$\frac{\partial \boldsymbol{p}(\boldsymbol{r},t)}{\partial t} = \nabla \cdot \boldsymbol{T}(\boldsymbol{r},t) + \boldsymbol{f}(\boldsymbol{r},t), \tag{2.1}$$

$$\frac{\partial \boldsymbol{S}(\boldsymbol{r},t)}{\partial t} = \frac{1}{2}\{\nabla \boldsymbol{v}(\boldsymbol{r},t) + [\nabla \boldsymbol{v}(\boldsymbol{r},t)]\} + \boldsymbol{h}(\boldsymbol{r},t), \tag{2.2}$$

where $\boldsymbol{p}(\boldsymbol{r},t)$ is the linear momentum vector per unit reference volume, $\boldsymbol{v}(\boldsymbol{r},t)$ is the particle velocity, $\boldsymbol{T}(\boldsymbol{r},t)$ is the engineering (symmetric) stress tensor and $\boldsymbol{S}(\boldsymbol{r},t)$ is the symmetric deformation tensor. The terms $\boldsymbol{f}(\boldsymbol{r},t)$ and $\boldsymbol{h}(\boldsymbol{r},t)$ are the force density and the injected deformation rate tensor, respectively. They represent the data of the elastodynamic problem entering the governing equations as inhomogeneities.

Equations (2.1) and (2.2) constitute the governing equations of Elastodynamics and, unlike Maxwell's equations, can be easily derived from the fundamental laws of Mechanics (balance of mass, linear momentum and angular momentum) assuming the Cauchy continuum structure and first-order theory(linearization of the strain tensor and imposition of the balance laws in the reference configuration). To obtain the governing equations of acoustodynamics, we decompose the stress tensor $\boldsymbol{T}$ as follows:

$$\boldsymbol{T} = \sigma \boldsymbol{I} + \left(\boldsymbol{T} - \frac{1}{3}\boldsymbol{I}\,\mathrm{trace}\,[\boldsymbol{T}]\right). \tag{2.3}$$

Neglecting the deviatoric part of the stress tensor $\boldsymbol{T}$, it results

$$\boldsymbol{T} = -p(\boldsymbol{r},t)\boldsymbol{I}, \tag{2.4}$$

where $p(\boldsymbol{r},t)$ is the pressure. The volume dilatation $S(\boldsymbol{r},t)$ and the injection dilatation rate $h(\boldsymbol{r},t)$ can be defined, respectively, as

$$S(\boldsymbol{r},t) = \text{trace}\left[\boldsymbol{S}(\boldsymbol{r},t)\right], \tag{2.5}$$

$$h(\boldsymbol{r},t) = \text{trace}\left[\boldsymbol{h}(\boldsymbol{r},t)\right]. \tag{2.6}$$

Disregarding the deviatoric part of the stress tensor and considering the trace of (2.2), the governing equation of acoustodynamics are obtained as [82, 83]:

$$\frac{\partial \boldsymbol{p}(\boldsymbol{r},t)}{\partial t} = -\nabla p(\boldsymbol{r},t) + \boldsymbol{f}(\boldsymbol{r},t), \tag{2.7}$$

$$\frac{\partial S(\boldsymbol{r},t)}{\partial t} = \nabla \cdot \boldsymbol{v}(\boldsymbol{r},t) + h(\boldsymbol{r},t). \tag{2.8}$$

If the propagation medium is considered linearly elastic, the constitutive equation reads

$$\boldsymbol{S}(\boldsymbol{r},t) = \mathbf{s}(\boldsymbol{r}) : \boldsymbol{T}(\boldsymbol{r},t), \tag{2.9}$$

where $\mathbf{s}(\boldsymbol{r})$ is the complinace matrix. If the deviatoric part of the stress tensor in (2.3) is once more neglected, Eq. (2.9) becomes

$$\boldsymbol{S}(\boldsymbol{r},t) = \mathbf{s}(\boldsymbol{r}) : \frac{1}{3}\boldsymbol{I}\text{trace}\left[\boldsymbol{T}(\boldsymbol{r},t)\right] = -\mathbf{s}(\boldsymbol{r}) : p(\boldsymbol{r},t)\boldsymbol{I} \tag{2.10}$$

and thus

$$S = \text{trace}\left[\boldsymbol{S}(\boldsymbol{r},t)\right] = \boldsymbol{I} : \boldsymbol{S}(\boldsymbol{r},t) = -(\boldsymbol{I} : \mathbf{s}(\boldsymbol{r}) : \boldsymbol{I})p(\boldsymbol{r},t) = -\varrho(\boldsymbol{r})p(\boldsymbol{r},t) \tag{2.11}$$

which is the constitutive law for inhomogeneous non-dissipative acoustic media with adiabatic compressibility equal to $\varrho(\boldsymbol{r})$. The governing equations in (2.7) and (2.8) can be rewritten as follows:

$$\rho(\boldsymbol{r})\frac{\partial \boldsymbol{v}(\boldsymbol{r},t)}{\partial t} = -\nabla p(\boldsymbol{r},t) + \boldsymbol{f}(\boldsymbol{r},t), \tag{2.12}$$

$$-\varrho(\boldsymbol{r})\frac{\partial p(\boldsymbol{r},t)}{\partial t} = \nabla \cdot \boldsymbol{v}(\boldsymbol{r},t) + h(\boldsymbol{r},t). \tag{2.13}$$

The combination of these equations leads to a single higher order differential equation in the pressure field $p(\boldsymbol{r},t)$:

$$\nabla \cdot \left[\frac{1}{\rho(\boldsymbol{r})}\nabla p(\boldsymbol{r},t)\right] - \varrho(\boldsymbol{r})\frac{\partial^2 p(\boldsymbol{r},t)}{\partial t^2} = \nabla \cdot \left[\frac{1}{\rho(\boldsymbol{r})}\boldsymbol{f}(\boldsymbol{r},t)\right] + \frac{\partial h(\boldsymbol{r},t)}{\partial t}. \tag{2.14}$$

Making use of Eq. (2.12), the previous equation can be recast as

$$\Delta p(\boldsymbol{r},t) - \rho(\boldsymbol{r})\varrho(\boldsymbol{r})\frac{\partial^2 p(\boldsymbol{r},t)}{\partial t^2} + \frac{\partial \boldsymbol{v}(\boldsymbol{r},t)}{\partial t} \cdot \nabla\rho(\boldsymbol{r}) = \nabla \cdot \boldsymbol{f}(\boldsymbol{r},t) + \rho(\boldsymbol{r})\frac{\partial h(\boldsymbol{r},t)}{\partial t}. \tag{2.15}$$

In a similar manner, a higher order equation in $\boldsymbol{v}(\boldsymbol{r},t)$ can be obtained as:

$$\nabla\left[\frac{1}{\varrho(\boldsymbol{r})}\nabla \cdot \boldsymbol{v}(\boldsymbol{r},t)\right] - \rho(\boldsymbol{r})\frac{\partial^2 \boldsymbol{v}(\boldsymbol{r},t)}{\partial t^2} = \frac{\partial \boldsymbol{f}(\boldsymbol{r},t}{\partial t} - \nabla\left[\frac{1}{\varrho(\boldsymbol{r})}h(\boldsymbol{r},t)\right]. \tag{2.16}$$

Making use of Eq. (2.13), the previous equation can be recast as

$$\nabla\nabla\cdot\boldsymbol{v}(\boldsymbol{r},t)-\rho(\boldsymbol{r})\varrho(\boldsymbol{r})\frac{\partial^2\boldsymbol{v}(\boldsymbol{r},t)}{\partial t^2}+\frac{\partial p(\boldsymbol{r},t)}{\partial t}\nabla\varrho(\boldsymbol{r})=-\nabla h(\boldsymbol{r},t)-\varrho(\boldsymbol{r})\frac{\partial\boldsymbol{f}(\boldsymbol{r},t)}{\partial t}. \quad (2.17)$$

The differential operator for $p(\boldsymbol{r},t)$ or $\boldsymbol{v}(\boldsymbol{r},t)$ contains additional terms like $\nabla\rho(\boldsymbol{r})$ or $\nabla\varrho(\boldsymbol{r})$ which make the differential equations more difficult to solve. They are, therefore, transferred to the right-hand sides of Eqs. (2.15) and (2.17) as additional inhomogeneities in terms of equivalent sources.

For homogeneous materials, the previous differential equations decouple:

$$\Delta p(\boldsymbol{r},t)-\varrho(\boldsymbol{r})\rho(\boldsymbol{r})\frac{\partial^2 p(\boldsymbol{r},t)}{\partial t^2} = \nabla\cdot\boldsymbol{f}(\boldsymbol{r},t)+\rho(\boldsymbol{r})\frac{\partial h(\boldsymbol{r},t)}{\partial t}, \quad (2.18)$$

$$\nabla\nabla\cdot\boldsymbol{v}(\boldsymbol{r},t)-\varrho(\boldsymbol{r})\rho(\boldsymbol{r})\frac{\partial^2\boldsymbol{v}(\boldsymbol{r},t)}{\partial t^2} = -\nabla h(\boldsymbol{r},t)-\varrho\frac{\partial\boldsymbol{f}(\boldsymbol{r},t)}{\partial t}, \quad (2.19)$$

Given a vector $\boldsymbol{a}(\boldsymbol{r},t)$, the following identity holds:

$$\nabla\nabla\cdot\boldsymbol{a}(\boldsymbol{r},t)-\nabla\cdot\nabla\boldsymbol{a}(\boldsymbol{r},t)=\nabla\times\nabla\times\boldsymbol{a}(\boldsymbol{r},t). \quad (2.20)$$

Equation (2.19) can be rewritten as

$$\Delta\boldsymbol{v}(\boldsymbol{r},t)+\nabla\times\nabla\times\boldsymbol{v}(\boldsymbol{r},t)-\varrho(\boldsymbol{r})\rho(\boldsymbol{r})\frac{\partial^2\boldsymbol{v}(\boldsymbol{r},t)}{\partial t^2}=-\nabla h(\boldsymbol{r},t)-\varrho\frac{\partial\boldsymbol{f}(\boldsymbol{r},t)}{\partial t}. \quad (2.21)$$

An additional modification to this equation can be made if the case of homogeneous medium is considered for Eq. (2.12)

$$\nabla\times\frac{\partial\boldsymbol{v}(\boldsymbol{r},t)}{\partial t}=\frac{1}{\rho(\boldsymbol{r})}\nabla\times\boldsymbol{f}(\boldsymbol{r},t) \quad (2.22)$$

so that Eq. (2.21) becomes

$$\Delta\boldsymbol{v}(\boldsymbol{r},t)-\varrho(\boldsymbol{r})\rho(\boldsymbol{r})\frac{\partial^2\boldsymbol{v}(\boldsymbol{r},t)}{\partial t^2}=-\nabla h(\boldsymbol{r},t)-\varrho(\boldsymbol{r})\frac{\partial\boldsymbol{f}(\boldsymbol{r},t)}{\partial t}-\frac{1}{\rho(\boldsymbol{r})}\nabla\times\int_0^t\boldsymbol{f}(\boldsymbol{r},\tau)d\tau. \quad (2.23)$$

Equations (2.18) and (2.23) form the so-called d'Alembert wave equations:

$$\Delta p(\boldsymbol{r},t)-\varrho(\boldsymbol{r})\rho(\boldsymbol{r})\frac{\partial^2 p(\boldsymbol{r},t)}{\partial t^2} = \nabla\cdot\boldsymbol{f}(\boldsymbol{r},t)+\rho(\boldsymbol{r})\frac{\partial h(\boldsymbol{r},t)}{\partial t}, \quad (2.24)$$

$$\begin{aligned}\Delta\boldsymbol{v}(\boldsymbol{r},t)-\varrho(\boldsymbol{r})\rho(\boldsymbol{r})\frac{\partial^2\boldsymbol{v}(\boldsymbol{r},t)}{\partial t^2} &= -\nabla h(\boldsymbol{r},t)-\varrho(\boldsymbol{r})\frac{\partial\boldsymbol{f}(\boldsymbol{r},t)}{\partial t}\\ &\quad -\frac{1}{\rho(\boldsymbol{r})}\nabla\times\int_0^t\boldsymbol{f}(\boldsymbol{r},\tau)d\tau.\end{aligned} \quad (2.25)$$

Applying Fourier transform to Eqs. (2.24)and (2.25), the Helmholtz equations are obtained:

$$\Delta p(\boldsymbol{r},\omega)+\omega^2\varrho(\boldsymbol{r})\rho(\boldsymbol{r})p(\boldsymbol{r},\omega) = \nabla\cdot\boldsymbol{f}(\boldsymbol{r},\omega)-j\omega\rho(\boldsymbol{r})h(\boldsymbol{r},\omega), \quad (2.26)$$

$$\begin{aligned}\Delta\boldsymbol{v}(\boldsymbol{r},\omega)+\omega^2\varrho(\boldsymbol{r})\rho(\boldsymbol{r})\boldsymbol{v}(\boldsymbol{r},\omega) &= -\nabla h(\boldsymbol{r},\omega)-\frac{1}{j\omega\rho(\boldsymbol{r})}[\omega^2\varrho(\boldsymbol{r})\rho(\boldsymbol{r})\boldsymbol{f}(\boldsymbol{r},\omega)\\ &\quad -\nabla\times\boldsymbol{f}(\boldsymbol{r},\omega)],\end{aligned} \quad (2.27)$$

or, as alternative to Eq. (2.27), the Fourier transform of (2.19) can be considered:

$$\nabla\nabla\cdot\boldsymbol{v}(\boldsymbol{r},\omega)+\omega^2\varrho\rho\boldsymbol{v}(\boldsymbol{r},\omega)=-\nabla h(\boldsymbol{r},\omega)+j\varrho\omega\boldsymbol{f}(\boldsymbol{r},\omega) \quad (2.28)$$

2.2 Point-source synthesis in the frequency domain

2.2.1 The Green function for the three-dimensional frequency-dependent problem

The differential equation

$$\Delta G(\boldsymbol{r},\boldsymbol{r}',\omega)+\kappa^2 G(\boldsymbol{r},\boldsymbol{r}',\omega)=-\delta(\boldsymbol{r}-\boldsymbol{r}') \tag{2.29}$$

yields as solution the three-dimensional scalar Green function $G(\boldsymbol{r},\boldsymbol{r}',\omega)$ with wave number $\kappa=\omega/c$ in a homogeneous infinite space. The δ-function represents the mathematical model of a point source, and the introduced minus sign is just for convenience. The inhomogeneity of (2.29) is a unit point source at $\boldsymbol{r}'$ according to the δ-function property

$$\iiint_V \delta(\boldsymbol{r}-\boldsymbol{r}')d^3\boldsymbol{r}'=\begin{cases}1, & \text{for} \quad \boldsymbol{r}\in V\\ 0, & \text{for} \quad \boldsymbol{r}\notin V\end{cases} \tag{2.30}$$

It is due to these distributional inhomogeneities that (2.29) must be mathematically solved in the sense of distributions [84]. Let

$$\tilde{G}(\boldsymbol{k},\boldsymbol{r}',\omega)=\int_{-\infty}^{+\infty}\int_{-\infty}^{+\infty}\int_{-\infty}^{+\infty} G(\boldsymbol{r},\boldsymbol{r}',\omega)e^{-j\boldsymbol{k}\cdot\boldsymbol{r}}d^3\boldsymbol{r} \tag{2.31}$$

to be the three-dimensional spatial Fourier transform of $G(\boldsymbol{r},\boldsymbol{r}',\omega)$ with respect to $\boldsymbol{r}$; due to the double position vector argument of $G(\boldsymbol{r},\boldsymbol{r}',\omega)$, we denote the three-dimensional Fourier transform with respect to $\boldsymbol{r}$ by a tilde. Hence, the transform of (2.29) yields

$$(j\boldsymbol{k})\cdot(j\boldsymbol{k})\tilde{G}(\boldsymbol{k},\boldsymbol{r}',\omega)+\kappa^2\tilde{G}(\boldsymbol{k},\boldsymbol{r}',\omega)=-e^{-j\boldsymbol{k}\cdot\boldsymbol{r}'} \tag{2.32}$$

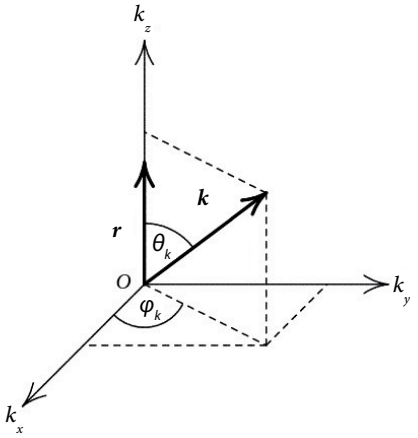

Figure 2.1: $\boldsymbol{k}$-space Cartesian coordinate system (k_x,k_y,k_z) and spherical coordinates k,θ_k,ϕ_k.

due to $\Delta = \nabla \cdot \nabla$. It follows that

$$\tilde{G}(\boldsymbol{k}, \boldsymbol{r}', \omega) = \frac{1}{k^2 - \kappa^2} e^{-j\boldsymbol{k}\cdot\boldsymbol{r}'} \tag{2.33}$$

and

$$G(\boldsymbol{r}, \boldsymbol{r}', \omega) = \frac{1}{(2\pi)^3} \int_{-\infty}^{+\infty} \int_{-\infty}^{+\infty} \int_{-\infty}^{+\infty} \frac{1}{k^2 - \kappa^2} e^{j\boldsymbol{k}\cdot(\boldsymbol{r}-\boldsymbol{r}')} d^3\boldsymbol{k}. \tag{2.34}$$

Clearly, $G(\boldsymbol{r}, \boldsymbol{r}', \omega)$ is only a function of $\boldsymbol{r} - \boldsymbol{r}'$ that is denoted by $G(\boldsymbol{r} - \boldsymbol{r}', \omega)$, where

$$G(\boldsymbol{r}, \omega) = \frac{1}{(2\pi)^3} \int_{-\infty}^{+\infty} \int_{-\infty}^{+\infty} \int_{-\infty}^{+\infty} \frac{1}{k^2 - \kappa^2} e^{j\boldsymbol{k}\cdot\boldsymbol{r}} d^3\boldsymbol{k} \tag{2.35}$$

is now to be calculated. To achieve this, the (k_x, k_y, k_z)-coordinate system is adjusted to the fixed point of observation $\boldsymbol{r}$ (Figure 2.1). With $\boldsymbol{k} \cdot \boldsymbol{r} = kr\cos\theta_k$, we write (2.35) in $\boldsymbol{k}$-space spherical coordinates

$$G(\boldsymbol{r}, \omega) = \frac{1}{(2\pi)^3} \int_0^{2\pi} \int_0^{2\pi} \int_0^{2\pi} \frac{k^2}{k^2 - \kappa^2} e^{jkr\cos\theta_k} \sin\theta_k dk d\theta_k d\phi_k \tag{2.36}$$

where the ϕ_k-integration immediately yields 2π. With the substitution $\cos\theta_k = \eta$, elementary evaluation of the η-integration, and combination of the two resulting integrals, we obtain

$$G(\boldsymbol{r}, \omega) = \frac{1}{jr} \frac{1}{(2\pi)^2} \int_{-\infty}^{+\infty} \frac{k}{k^2 - \kappa^2} e^{jkr} dk. \tag{2.37}$$

To cope with the singularity of the integrand on the so-called Ewald sphere $k = \kappa$, we have the choice between complex-valued functions analysis ([85, 83]) or distributional calculus ([86]). Using complex function analysis, we would like to apply the residue theorem; this requires an appropriate closure of the $(-\infty, +\infty)$-integration path in a complex k-plane, and this is performed in a way such that an outbound traveling spherical wave is obtained. The mathematically possible solution of (2.29) as an inbound traveling spherical wave must be excluded due to this radiation "condition". Therefore, we uniquely obtain

$$G(\boldsymbol{r}, \omega) = G(r, \omega) = \frac{e^{jkr}}{4\pi r} \tag{2.38}$$

or, after reintroducing the source point $\boldsymbol{r}'$

$$G(\boldsymbol{r}, \boldsymbol{r}', \omega) = G(\boldsymbol{r} - \boldsymbol{r}', \omega) = \frac{e^{jk|\boldsymbol{r}-\boldsymbol{r}'|}}{4\pi|\boldsymbol{r} - \boldsymbol{r}'|}. \tag{2.39}$$

Using distributional calculus, the Fourier integrals resulting from a partial fraction decomposition of the $k/(k^2 - \kappa^2)$ integrand are calculated in straightforward fashion. We obtain, however, physically meaningless standing wave $G(r, \omega) = \cos(\kappa r/4\pi r)$. To make it a physically meaningful outbound traveling wave, (2.33) has to be complemented by an appropriate solution of the homogeneous equation (2.29), and a fitting solution is $j\sin(\kappa r/4\pi r)$ again resulting in (2.38).

2.2.2 The Green function for the two-dimensional frequency-dependent problem

For the sake of simplicity, very often simulations and model calculations for ultrasonic non-destructive evaluation are carried out in two spatial dimensions. This requires a completely different scalar Green function again suggesting to present the respective result at first as a time- harmonic cylindrical wave. We postulate two-dimensionality with $\partial/\partial y = 0$ and introduce polar coordinates (r, θ) in the xz-plane (counting θ from the z-axis, then $(\boldsymbol{e}_r, \boldsymbol{e}_\theta, \boldsymbol{e}_y)$ is a right-handed trihedron). Due to the expected rotational symmetry of the Green function $G(\boldsymbol{r}, \omega) = G(r, \omega)$, the two-dimensional pendant to (2.29) reads

$$\frac{1}{r}\frac{\partial}{\partial r}\left[r\frac{\partial G(r,\omega)}{\partial r}\right]\left(= \frac{\partial^2 G(r,\omega)}{\partial r^2} + \frac{1}{r}\frac{\partial G(r,\omega)}{\partial r}\right) + \kappa^2 G(r,\omega) = -\delta(\boldsymbol{r}) \tag{2.40}$$

The homogeneous differential equation (2.40) defines as solution cylindrical functions $J_0(\kappa r)$, $N_0(\kappa r)$, $H_0^{(1)}(\kappa r)$, $H_0^{(2)}(\kappa r)$, known as the Bessel, Neumann and Hankel functions of order zero. A time-harmonic wave propagating in the positive direction has the form

$$G(r,\omega) = U(\omega)\frac{e^{jkr}}{r} \tag{2.41}$$

representing an outbound time-harmonic wave with respect to r. Here, $G(r\omega)e^{jkr}$ would be appropriate; as the amplitude decreases with increasing r, the function $\sqrt{r}$ should be suitable because the phase surfaces e^{jkr} are circles, whose circumferences increase proportional to r accounting for the power density associated with

$$G(r,\omega) \sim \frac{e^{jkr}}{\sqrt{r}} \tag{2.42}$$

as a quadratic quantity to decay in fact equally fast as the "surface" increases yielding a constant total power independent of r. The power radiated by the unit line source is transported to infinity as an outbound radiation. Only $H_0^{(1)}(\kappa r)$ exhibits exactly this behavior for large kr [87]:

$$H_0^{(1)}(\kappa r) \simeq e^{-j\frac{\pi}{4}}\sqrt{\frac{2}{\pi}}\frac{e^{jkr}}{\sqrt{kr}}, \qquad \text{for} \quad \kappa r \gg 1. \tag{2.43}$$

The correct amplitude factor may not be arbitrary because (2.41) should become the solution of the inhomogeneous equation (2.29). Staring from (2.30), we integrate (2.40) over a spherical volume V_k with radius R_0 and surface S_k containing the origin. We can observe that the first term in (2.40) has emerged from $\delta = \nabla \cdot \nabla$ and applying the Gauss' theorem yields:

$$\iint_{S_k} \hat{\boldsymbol{r}} \cdot \nabla G(r,\omega)|_{r=r_0}\left(= \frac{\partial G(r,\omega)}{\partial r}|_{r=r_0}\right) dS + k^2 \iiint_{V_k} G(r,\omega) dV = -1. \tag{2.44}$$

The right-hand side of this equation is r_0-independent; hence, this must also hold for the left-hand side and, therefore, we investigate it for $r_0 \to 0$. In the volume integral, we have $dV = r^2 \sin\theta dr d\theta d\phi$ so that it tends to zero for $r_0 \to 0$ if we insert (2.41). Since $dS = r_0^2 \sin\theta d\theta d\phi$, we finally obtain [85]:

$$G(\boldsymbol{r} - \boldsymbol{r}', \omega) = \frac{j}{4} H_0^{(1)}(\kappa|\boldsymbol{r} - \boldsymbol{r}'|) \tag{2.45}$$

if we again displace the source point from the origin to $\boldsymbol{r}'$.

In connection with the point source synthesis of source and scattered fields, it is useful to know that the integration of the three-dimensional Green function along the independence axis of the two-dimensional problem leads to the two-dimensional Green function; namely, the Hankel function $H^(1)_0(\kappa r)$ has the integral representation [87]

$$\frac{j}{4} H_0^{(1)}(\kappa r) = \int_{-\infty}^{+\infty} \frac{e^{jk\sqrt{r^2+y^2}}}{4\pi\sqrt{r^2+y^2}} dy \tag{2.46}$$

2.3 Point-source synthesis in the time domain

2.3.1 The Green function for the three-dimensional time-dependent problem

The two- and three-dimensional Green functions (2.45) and (2.39) are functions of the circular frequency ω via $\kappa = \omega/c$. Therefore, they may be considered to represent Fourier spectra of time domain Green functions $G(\boldsymbol{r}, \boldsymbol{r}', t)$ and $G(\boldsymbol{r} - \boldsymbol{r}', t)$, respectively:

$$G(\boldsymbol{r} - \boldsymbol{r}', t) = \frac{1}{4\pi|\boldsymbol{r} - \boldsymbol{r}'|} \delta\left(t - \frac{|\boldsymbol{r} - \boldsymbol{r}'|}{c}\right) \tag{2.47}$$

The differential equation defining (2.47) is found via Fourier inversion of (2.29):

$$\Delta G(\boldsymbol{r} - \boldsymbol{r}', t) - \frac{1}{c^2} \frac{\partial^2 G(\boldsymbol{r} - \boldsymbol{r}', t)}{\partial t^2} = -\delta\left(\boldsymbol{r} - \boldsymbol{r}'\right) \delta(t) \tag{2.48}$$

Apparently, the right-hand side of (2.48) is now a pulsed unit point source flashing "briefly" at the source point $\boldsymbol{r}'$ at time $t = 0$. Its field is a pulsed elementary spherical wave according to (2.47), whose time dependence reproduces the source time function. The propagation of elementary waves in three-dimensional space (filled with homogeneous nondissipative material) is thus dispersion-free. A slight generalization of (2.48) and (2.47) introduces a nonzero switch-on time at $t = t'$:

$$\Delta G(\boldsymbol{r} - \boldsymbol{r}', t, t') - \frac{1}{c^2} \frac{\partial^2 G(\boldsymbol{r} - \boldsymbol{r}', t, t')}{\partial t^2} = -\delta\left(\boldsymbol{r} - \boldsymbol{r}'\right) \delta(t - t') \tag{2.49}$$

then the Fourier transform with respect to t leads to

$$\Delta G(\boldsymbol{r} - \boldsymbol{r}', \omega, t') + \kappa^2 G(\boldsymbol{r} - \boldsymbol{r}', \omega, t') = -\delta(\boldsymbol{r} - \boldsymbol{r}') e^{j\omega t'} \tag{2.50}$$

which implies

$$G(\boldsymbol{r}-\boldsymbol{r}',\omega,t') = G(\boldsymbol{r}-\boldsymbol{r}',\omega)e^{j\omega t'}. \tag{2.51}$$

Therefore, the Fourier inversion of (2.51) yields, together with (2.47),

$$G(\boldsymbol{r}-\boldsymbol{r}',t,t') = \frac{1}{4\pi|\boldsymbol{r}-\boldsymbol{r}'|}\delta\left(t-t'-\frac{|\boldsymbol{r}-\boldsymbol{r}'|}{c}\right) = G(\boldsymbol{r}-\boldsymbol{r}',t-t'). \tag{2.52}$$

For Green functions, the δ-pulse time dependence is mandatorily dictated: however this is not the case if a band-limited function (e.g., a Hann-windowed n-tone burst signal) is introduced

$$Tn(t) = h(t)sin(\omega_0 t+\frac{\pi}{2}), \qquad \text{with} \quad -\frac{n\pi}{\omega_0} < t < \frac{n\pi}{\omega_0}, \tag{2.53}$$

where $h(t)$ is the Hann window, and a "band-limited Green function" $\bar{G}(\boldsymbol{r}-\boldsymbol{r}',\omega)$ is defined according to

$$\Delta\bar{G}(\boldsymbol{r}-\boldsymbol{r}',\omega)+\kappa^2\bar{G}(\boldsymbol{r}-\boldsymbol{r}',\omega) = -\delta(\boldsymbol{r}-\boldsymbol{r}')Tn(\omega) \tag{2.54}$$

that may immediately be given comparing (2.54) with (2.29) as

$$\bar{G}(\boldsymbol{r}-\boldsymbol{r}',\omega) = Tn(\omega)\frac{e^{jk|\boldsymbol{r}-\boldsymbol{r}'|}}{4\pi|\boldsymbol{r}-\boldsymbol{r}'|}. \tag{2.55}$$

Fourier inversion yields the function we obtain in the time domain as

$$\bar{G}(\boldsymbol{r}-\boldsymbol{r}',t) = \frac{1}{4\pi|\boldsymbol{r}-\boldsymbol{r}'|}Tn\left(t-\frac{|\boldsymbol{r}-\boldsymbol{r}'|}{c}\right) \tag{2.56}$$

2.3.2 The Green function for the two-dimensional time-dependent problem

To find the two-dimensional Green function in the time domain, we have to apply an inverse Fourier transform. According to the integral representations of the Hankel function [87], we have

$$G(\boldsymbol{r}-\boldsymbol{r}',t) = \frac{c}{2\pi}\frac{1}{\sqrt{c^2t^2-|\boldsymbol{r}-\boldsymbol{r}'|^2}}u(ct-|\boldsymbol{r}-\boldsymbol{r}'|) \tag{2.57}$$

where $u(ct-|\boldsymbol{r}-\boldsymbol{r}'|)$ as unit step-function ensures the causality of $G(\boldsymbol{r}-\boldsymbol{r}',t)$, i.e., $G(\boldsymbol{r}-\boldsymbol{r}',t)\equiv 0$ for $t<|\boldsymbol{r}-\boldsymbol{r}'|/c$. Two considerations can be drawn analyzing Eq. (2.57). Firstly, although the line source radiates a δ-impulse, the time variation of the radiated field *is not* δ-like. In addition to this, it can be seen that the square root singularity $t=|\boldsymbol{r}-\boldsymbol{r}'|/c$ is the same for each distance from the line source; the amplitude decay is hidden in the decreasing

area under the square root function with increasing distance. To make the amplitude decay visible with increasing distance, similar to (2.54) we compute

$$\bar{G}(\boldsymbol{r}-\boldsymbol{r}',\omega) = Tn(\omega)\frac{j}{4}H_0^{(1)}\left(\frac{|\boldsymbol{r}-\boldsymbol{r}'|}{c}\omega\right). \tag{2.58}$$

Consequently, the expression

$$\bar{G}(\boldsymbol{r}-\boldsymbol{r}',t) = Tn(t) * \frac{c}{2\pi}\frac{1}{\sqrt{C^2t^2-|\boldsymbol{r}-\boldsymbol{r}|^2}}u(ct-|\boldsymbol{r}-\boldsymbol{r}'|) \tag{2.59}$$

may be evaluated as a convolution integral. The decreasing area under the square root function then yields the amplitude decay and the dispersion on the $Tn(t)$-pulse. We simply have to insert the asymptotic expression (2.43) of the Hankel function into (2.58) to recognize a $1/\sqrt{\omega}$-multiplication of the $Tn(\omega)$-spectrum:

$$\bar{G}(\boldsymbol{r}-\boldsymbol{r}',\omega) \simeq \frac{1}{4}e^{j\frac{\pi}{4}}\sqrt{\frac{2c}{\pi}}\frac{Tn(\omega)}{\sqrt{\omega}}\frac{e^{jk|\boldsymbol{r}-\boldsymbol{r}'|}}{\sqrt{|\boldsymbol{r}-\boldsymbol{r}'|}} \tag{2.60}$$

where the constraint $kr \ll 1$ must hold for all frequencies contained in the $Tn(\omega)$ spectrum.

These differences in two- and three-dimensional time domain Green functions definitely affect the respective sound field calculations, and restrain the quantitative comparison of two-dimensional simulations with measurements that are always three-dimensional.

2.4 The far-field approximation

A convenient location for only one point source is the origin of the coordinate frame; yet, in general, we have to deal with extended sources necessitating a superimposition of the contribution from several (continuously distributed) point sources. In such a case, the coordinate origin might be conveniently located close to the source volume or even right in it. If, additionally, the observation point distance r is large with regard to the maximum linear dimension of the source volume (and large with regard to the wavelength), the so-called far-field approximation may be introduced simplifying the field calculation considerably.

Figure 2.2 supports the following argument: if $r \gg r'$ (for all $\boldsymbol{r}'$ in the interior of a source volume) holds, then $\boldsymbol{r}-\boldsymbol{r}'$ is somehow parallel to $\boldsymbol{r}$ allowing for the approximation

$$|\boldsymbol{r}-\boldsymbol{r}'| \sim r - \boldsymbol{r}'\cdot\hat{\boldsymbol{r}}. \tag{2.61}$$

Yet, in the Green function (2.39), the expression $|\boldsymbol{r}-\boldsymbol{r}'|$ appears twice; due to the major sensitivity of the phase with respect to approximations, we will use (2.61) in the exponential function $|\boldsymbol{r}-\boldsymbol{r}'|^{-1} \simeq r^{-1}$ for the amplitude. This results in the far-field approximation

$$\hat{G}(\boldsymbol{r},\boldsymbol{r}',\omega) = \frac{e^{jkr}}{4\pi r}e^{-k\boldsymbol{r}'\cdot\hat{\boldsymbol{r}}} \tag{2.62}$$

of the Green function. A precise calculation and estimate reveals [85] that this approximation is practical for $r \ll r'$ and $kr \ll 1$.

The far-field approximate Green function (2.62) exhibits a characteristic structure. It is an elementary spherical wave that emerges from the origin and not from the actual point source $\boldsymbol{r}'$, hence it must be direction-dependent phase corrected through multiplication with the phase directivity characteristic

$$H(\hat{\boldsymbol{r}}, \boldsymbol{r}', \omega) = e^{-jk\boldsymbol{r}'\cdot\hat{\boldsymbol{r}}} \tag{2.63}$$

To present far-field time-version of the Green function, we must consider that (2.62) only holds for $kr \gg 1$; a Fourier inversion is not permitted because $\delta(t)$ contains all frequencies with the same amplitude (the spectrum $F\delta(t)^{-1} = 1$ appears as a factor in (2.39)). In this case we can exploit the band-limited Green function (2.55): for the frequencies contained in $Tn(\omega)$, we globally require $r \gg c/\omega$ resulting in

$$\hat{\tilde{G}}(\boldsymbol{r}, \boldsymbol{r}', t) = \frac{1}{4\pi r} Tn\left(t - \frac{r}{c} + \frac{\boldsymbol{r}'\cdot\hat{\boldsymbol{r}}}{c}\right) \tag{2.64}$$

due to the convolution of the Fourier inversion of (2.62) with $Tn(t)$.

The far-field approximation is particularly useful to give Green functions $\nabla' G(\boldsymbol{r} - \boldsymbol{r}', \omega)$, $\nabla'\nabla' G(\boldsymbol{r} - \boldsymbol{r}', \omega)$ that will be described in Section 2.5 for acoustic source fields, a comparatively simple mathematical structure. The gradient $\nabla' G(\boldsymbol{r} - \boldsymbol{r}', \omega)$ has always the direction of $|\boldsymbol{r} - \boldsymbol{r}'|$, hence it generally has three components in spherical coordinates. We may now either neglect the term with $|\boldsymbol{r} - \boldsymbol{r}'|^{-2}$ as compared to $|\boldsymbol{r} - \boldsymbol{r}'|^{-1}$ to approximate $\nabla|\boldsymbol{r} - \boldsymbol{r}'| \simeq \hat{\boldsymbol{r}}$ or calculate

$$\nabla' \hat{G}(\boldsymbol{r}, \boldsymbol{r}', \omega) = -jk\hat{\boldsymbol{r}} \frac{e^{jkr}}{4\pi r} e^{-jk\boldsymbol{r}\cdot\hat{\boldsymbol{r}}}. \tag{2.65}$$

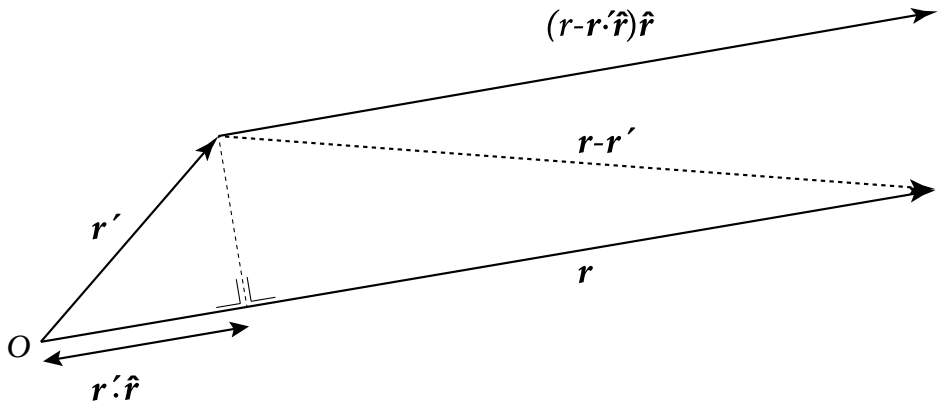

Figure 2.2: Geometry of the far-field approximation

Due to $\nabla G(\boldsymbol{r}-\boldsymbol{r}',\omega) = -\nabla' G(\boldsymbol{r}-\boldsymbol{r}',\omega)$, we have

$$\nabla \hat{G}(\boldsymbol{r},\boldsymbol{r}',\omega) = jk\hat{\boldsymbol{r}}\frac{e^{jkr}}{4\pi r}e^{-jk\boldsymbol{r}'\cdot\hat{\boldsymbol{r}}}. \tag{2.66}$$

We conclude that in the far-field ∇'- and ∇-differential operations on the Green function may be approximated by algebraic $(-jk\hat{\boldsymbol{r}})$- and $(jk\hat{\boldsymbol{r}})$-multiplications, respectively:

$$\nabla' \;\Rightarrow\; -jk\hat{\boldsymbol{r}} \tag{2.67}$$

$$\nabla \;\Rightarrow\; jk\hat{\boldsymbol{r}} \tag{2.68}$$

so that $\nabla'\hat{G}(\boldsymbol{r},\boldsymbol{r}',\omega)$ has only one $\boldsymbol{e}_r$-component in spherical coordinates.

The Δ-operation simultaneously yields a factor ω, giving in the time domain after $Tn(\omega)$-band limitation

$$\Delta'\hat{\tilde{G}}(\boldsymbol{r},\boldsymbol{r}',t) = \frac{1}{c}\frac{\partial\hat{\tilde{G}}(\boldsymbol{r},\boldsymbol{r}',t)}{\partial t}\hat{\boldsymbol{r}}. \tag{2.69}$$

Using (2.67) and (2.68), we may present the far-field approximation of the so-called acoustic dyadic Green function:

$$\begin{aligned}\boldsymbol{G}_v(\boldsymbol{r}-\boldsymbol{r}',\omega) &= -\frac{1}{\kappa^2}\nabla'\nabla' G(\boldsymbol{r}-\boldsymbol{r}',\omega)\\ &= -\frac{1}{\kappa^2}\nabla\nabla G(\boldsymbol{r}-\boldsymbol{r}',\omega)\end{aligned} \tag{2.70}$$

namely

$$\hat{\boldsymbol{G}}_v(\boldsymbol{r},\boldsymbol{r}',\omega) = \frac{e^{jkr}}{4\pi r}e^{-jk\boldsymbol{r}'\cdot\hat{\boldsymbol{r}}}\hat{\boldsymbol{r}}\cdot\hat{\boldsymbol{r}}. \tag{2.71}$$

After band limitation with $Tn(\omega)$

$$\hat{\tilde{\boldsymbol{G}}}_v(\boldsymbol{r},\boldsymbol{r}',t) = \frac{1}{4\pi r}Tn\left(t-\frac{r}{c}+\frac{\boldsymbol{r}'\cdot\hat{\boldsymbol{r}}}{c}\right)\hat{\boldsymbol{r}}\hat{\boldsymbol{r}} \tag{2.72}$$

which turns out to be another $Tn(t)$-pulse. The single components of (2.72) exhibit differently direction-dependent weighted amplitudes.

With (2.43) and the above arguments, we obtain the far-field approximation of the two-dimensional Green function (2.45)

$$\hat{G}(\boldsymbol{r},\boldsymbol{r}',\omega) = \frac{1}{4}e^{j\frac{\pi}{4}}\sqrt{\frac{2}{\pi}}\frac{e^{jkr}}{\sqrt{kr}}e^{-jk\boldsymbol{r}'\cdot\hat{\boldsymbol{r}}}, \qquad \kappa r \gg 1, \quad r \gg r'. \tag{2.73}$$

As before, the transform into the time domain is only meaningful for a band-limited Green function. In consonance with (2.58) and (2.59), we multiply with an $Tn(\omega)$-spectrum and utilize the correspondence [88]

$$\frac{1}{\sqrt{t}}u(t) \circ\!-\!\bullet\, \sqrt{\pi}\frac{1}{\sqrt{|\omega|}}e^{j\frac{\pi}{4}\mathrm{sign}(\omega)} \tag{2.74}$$

as well as the convolution and shifting rules

$$\hat{\tilde{G}}(\boldsymbol{r},\boldsymbol{r}',t) = \frac{c}{2\sqrt{2}\pi}\frac{1}{\sqrt{r}}Tn(t)\cdot\frac{1}{\sqrt{ct-r+\boldsymbol{r}'\cdot\hat{\boldsymbol{r}}}}u(ct-r+\boldsymbol{r}'\cdot\hat{\boldsymbol{r}}). \tag{2.75}$$

In contrast to (2.59), the square root function does not experience an area change while shifted on the t-axis leading to constant dispersion of the $Tn(t)$-pulse (due to the convolution) and to the expected $1/\sqrt{r}$-dependence.

2.5 Point-source synthesis of acoustic source fields in homogeneous materials with Green functions

2.5.1 Green function for pressure sources

With (2.29), the solution of Eq. (2.26) can be written as

$$p(\boldsymbol{r},\omega) = \int_{-\infty}^{+\infty}\int_{-\infty}^{+\infty}\int_{-\infty}^{+\infty}\left[-\nabla'\cdot\boldsymbol{f}(\boldsymbol{r}',\omega)+j\omega\rho h(\boldsymbol{r}',\omega)\right]G(\boldsymbol{r}-\boldsymbol{r}',\omega)d^3\boldsymbol{r}'. \tag{2.76}$$

Since the application of the $(\Delta+\kappa^2)$-operator onto $p(\boldsymbol{r},\omega)$ with respect to $\boldsymbol{r}$ can be pulled under the integral, yet it only applies to the variable $\boldsymbol{r}$ in Green's function, and with (2.29) as well as accounting for the shifting property of δ-distribution, we actually obtain (2.76). The physical interpretation of this mathematical representation of the pressure source field turns out to be a $[-\nabla'\cdot\boldsymbol{f}(\boldsymbol{r}',\omega)+j\omega\rho h(\boldsymbol{r}',\omega)]$-weighted synthesis of $\boldsymbol{r}'$-point sources. From each source point $\boldsymbol{r}'$, a $[-\nabla'\cdot\boldsymbol{f}(\boldsymbol{r}',\omega)+j\omega\rho h(\boldsymbol{r}',\omega)]$-weighted time harmonic elementary spherical wave emerges whose amplitudes and phases are superimposed for each observation point $\boldsymbol{r}$. The travel time $t(\boldsymbol{r},\boldsymbol{r}')=|\boldsymbol{r}-\boldsymbol{r}'|/c$ of the elementary spherical waves from the source point $\boldsymbol{r}'$ to the observation point $\boldsymbol{r}$ only depends on the magnitude of the distance.

In general, the source volume V_Q is finite - the sources are equal to zero outside V_Q - yielding a finite integration volume V in (2.76) that completely contains V_Q in its interior:

$$p(\boldsymbol{r},\omega) = \iiint_{V\supset V_Q}\left[-\nabla'\cdot\boldsymbol{f}(\boldsymbol{r}',\omega)+j\omega\rho h(\boldsymbol{r}',\omega)\right]G(\boldsymbol{r}-\boldsymbol{r}',\omega)d^3\boldsymbol{r}'. \tag{2.77}$$

Using the relationship

$$\nabla'\cdot\left[\boldsymbol{f}(\boldsymbol{r}',\omega)G(\boldsymbol{r}-\boldsymbol{r}',\omega)\right] = \left[\nabla'\cdot\boldsymbol{f}(\boldsymbol{r}',\omega)\right]G(\boldsymbol{r}-\boldsymbol{r}',\omega)+\boldsymbol{f}(\boldsymbol{r}',\omega)\cdot\nabla'G(\boldsymbol{r}-\boldsymbol{r}',\omega), \tag{2.78}$$

we can express $[\nabla'\cdot\boldsymbol{f}]\,G$ as $\boldsymbol{f}\cdot\nabla'G$. The integral over $\nabla'\cdot[\boldsymbol{f}G]$ can be transformed into a surface integral over the surface S of V with Gauss' theorem giving rise to $\boldsymbol{n}'\cdot[\boldsymbol{f}G] = [\boldsymbol{n}'\cdot\boldsymbol{f}]\,G$; according to our assumption, we have $\boldsymbol{f}=0$ on S (also holding for the normal components of $\boldsymbol{f}$), hence this integral vanishes. The remaining volume integral over V can be equally extended over V_Q:

$$p(\boldsymbol{r},\omega) = \iiint_{V_Q}\left[j\omega\rho h(\boldsymbol{r}',\omega)G(\boldsymbol{r}-\boldsymbol{r}',\omega)+\boldsymbol{f}(\boldsymbol{r}',\omega)\cdot\nabla'G(\boldsymbol{r}-\boldsymbol{r}',\omega)\right]d^3\boldsymbol{r}' \tag{2.79}$$

In this integral representation of the pressure field, the sources $h(\boldsymbol{r}', \omega)$ and $\boldsymbol{f}(\boldsymbol{r}', \omega)$ appear explicitly. The inhomogeneities $h(\boldsymbol{r}', \omega)$ of the pressure rate equation (2.13) requires the scalar Green function $G_{ph}(\boldsymbol{r} - \boldsymbol{r}', \omega) = j\omega\rho G(\boldsymbol{r} - \boldsymbol{r}', \omega)$, whereas the inhomogeneity $\boldsymbol{f}(\boldsymbol{r}', \omega)$ of the equation (2.12) requires the vector-valued Green function $\boldsymbol{G}_{pf}(\boldsymbol{r} - \boldsymbol{r}', \omega) = \nabla' G(\boldsymbol{r} - \boldsymbol{r}', \omega) = -\nabla G(\boldsymbol{r} - \boldsymbol{r}', \omega)$ [83]. The point source synthesis defined as such superimposes spherical waves $\nabla' G(\boldsymbol{r} - \boldsymbol{r}', \omega)$ with direction-dependent amplitude and phase, the so-called dipole waves [85]. It is worth underling the fact that the integral representation in Eq. (2.79) holds for all observation points, either in the exterior or in the interior of V_Q: for $\boldsymbol{r} \in V_Q$, a convergent improper integral emerges [89].

2.5.2 Green function for velocity sources

Evidently, a solution with structure (2.76) of the vector Helmholtz equation (2.27) utilizing the scalar Green function $G(\boldsymbol{r}, \boldsymbol{r}', \omega)$ can be written down for each scalar component. Yet, to arrive at a representation equivalent to (2.80), the dyadic Green function (already introduced in Eq.(2.70)) is used

$$\nabla\nabla \cdot \boldsymbol{G}_v(\boldsymbol{r}, \boldsymbol{r}', \omega) + \kappa^2 \boldsymbol{G}_v(\boldsymbol{r}, \boldsymbol{r}, \omega) = -\boldsymbol{I}\delta(\boldsymbol{r} - \boldsymbol{r}'). \tag{2.80}$$

In the resulting source representation

$$\begin{aligned} \boldsymbol{v}(\boldsymbol{r}, \omega) &= \iiint_{V \supset V_Q} \boldsymbol{G}_v(\boldsymbol{r} - \boldsymbol{r}', \omega) \cdot \left[\nabla' h(\boldsymbol{r}', \omega) - j\omega\varrho \boldsymbol{f}(\boldsymbol{r}', \omega)\right] d^3\boldsymbol{r}' \\ &= \iiint_{V \supset V_Q} \left[\nabla' h(\boldsymbol{r}', \omega) - j\omega\varrho \boldsymbol{f}(\boldsymbol{r}', \omega)\right] \cdot \boldsymbol{G}_v(\boldsymbol{r} - \boldsymbol{r}', \omega) d^3\boldsymbol{r}' \end{aligned} \tag{2.81}$$

of the particle velocity, we can basically choose source points exterior and interior of the finite source volume. To transform (2.81) into a structure comparable to (2.79), we advantageously utilize the three-dimensional Fourier transform:

$$\begin{aligned} \tilde{\boldsymbol{v}}(\boldsymbol{k}, \omega) &= j\boldsymbol{k}\tilde{h}(\boldsymbol{k}, \omega) \cdot \tilde{\boldsymbol{G}}_v(\boldsymbol{k}, \omega) - j\omega\varrho \boldsymbol{f}(\boldsymbol{k}, \omega) \cdot \tilde{\boldsymbol{G}}_v(\boldsymbol{k}, \omega) \\ &= \tilde{h}(\boldsymbol{k}, \omega) \frac{j\boldsymbol{k}}{k^2 - \kappa^2} \end{aligned} \tag{2.82}$$

It follows:

$$\boldsymbol{v}(\boldsymbol{r}, \omega) = \iiint_{V_Q} \left[-j\omega\varrho \boldsymbol{f}(\boldsymbol{r}', \omega) \cdot \boldsymbol{G}_v(\boldsymbol{r} - \boldsymbol{r}', \omega) - h(\boldsymbol{r}', \omega) \nabla' G(\boldsymbol{r} - \boldsymbol{r}', \omega)\right] d^3\boldsymbol{r}' \tag{2.83}$$

This integral representation of the particle velocity field again explicitly exhibits the sources $\boldsymbol{f}(\boldsymbol{r}', \omega)$ and $h(\boldsymbol{r}', \omega)$. Equivalently to what has been done for the case of pressure sources, it can be stated that the inhomogeneity $\boldsymbol{f}(\boldsymbol{r}', \omega)$ of the equation of motion (2.12) requires the dyadic Green function $\boldsymbol{G}_{vf}(\boldsymbol{r} - \boldsymbol{r}', \omega) = -j\omega\varrho \boldsymbol{G}_v(\boldsymbol{r} - \boldsymbol{r}', \omega)$ and the inhomogeneity $h(\boldsymbol{r}', \omega)$ of the pressure equation (2.13) requires the vector-valued Green function $\boldsymbol{G}_{vh}(\boldsymbol{r} - \boldsymbol{r}', \omega) = -\nabla' G(\boldsymbol{r} - \boldsymbol{r}', \omega) = -\boldsymbol{G}_{pf}(\boldsymbol{r} - \boldsymbol{r}', \omega)$.

Chapter 3

Elastodynamic Source Fields

3.1 Homogeneous isotropic infinite space Green tensor of elastodynamics

3.1.1 Governing equations of elastodynamics

In acoustics, the differential equations (2.18) and (2.19) for the field quantities $p(\boldsymbol{r},t)$ and $\boldsymbol{v}(\boldsymbol{r},t)$ result from the acoustic governing equations for a homogeneous infinite (non-dissipative) space, where only the spherical part of the stress and deformation tensors was taken into account. The governing equations of elastodynamics can be obtained from Equations (2.1) and (2.2) making use of linearly elastic constitutive laws; due to the fact that only homogeneous isotropic materials allow for explicit mathematical expressions for Green functions (tensors), we assume

$$\boldsymbol{c} = \lambda \boldsymbol{I}^{tr} + 2\mu \boldsymbol{I}^{s}, \tag{3.1}$$

where $\boldsymbol{I}^{tr}$ and $\boldsymbol{I}^{s}$ are four rank tensors such that

$$\boldsymbol{I}^{tr} : \boldsymbol{A} = \boldsymbol{A} : \boldsymbol{I}^{tr} = \boldsymbol{I}\,\mathrm{trace}\,[\boldsymbol{A}]\,, \tag{3.2}$$

$$\boldsymbol{I}^{s} : \boldsymbol{A} = \boldsymbol{A} : \boldsymbol{I}^{s} = \frac{1}{2}\left(\boldsymbol{A} + \boldsymbol{A}^{\intercal}\right) = \boldsymbol{A}^{sym}. \tag{3.3}$$

The basis to calculate elastodynamic source fields are the governing Equations (2.1) and (2.2) in the field quantities $\boldsymbol{T}(\boldsymbol{r},t)$ and $\boldsymbol{v}(\boldsymbol{r},t)$:

$$\boldsymbol{I}^{s} : \nabla\left[\nabla \cdot \boldsymbol{T}(\boldsymbol{r},t)\right] - \rho \mathbf{s} : \frac{\partial^2 \boldsymbol{T}(\boldsymbol{r},t)}{\partial t^2} = -\boldsymbol{I}^{s} : \nabla \boldsymbol{f}(\boldsymbol{r},t) - \rho \frac{\partial \boldsymbol{h}(\boldsymbol{r},t)}{\partial t} \tag{3.4}$$

$$\mu \Delta \boldsymbol{v}(\boldsymbol{r},t) + (\lambda+\mu)\nabla\nabla \cdot \boldsymbol{v}(\boldsymbol{r},t) - \rho \frac{\partial^2 \boldsymbol{v}(\boldsymbol{r},t)}{\partial t^2} = -\frac{\partial \boldsymbol{f}(\boldsymbol{r},t)}{\partial t} - \nabla \cdot \boldsymbol{c} : \boldsymbol{h}(\boldsymbol{r},t) \tag{3.5}$$

where $\mathbf{s} = \boldsymbol{c}^{-1}$. Equation (3.5) is essentially different from the associated acoustic Equation (2.19) by the additional $\Delta \boldsymbol{v}(\boldsymbol{r},t)$-term. It is expected that this term is due to shear waves

and that the respective Green function for equation (3.5) will account for pressure and shear elementary waves.

3.1.2 Second-rank Green tensor

After the Fourier transform of (3.5) with respect to t according to

$$(\mu\Delta + \rho\omega^2)\boldsymbol{v}(\boldsymbol{r},\omega) + (\lambda,\mu)\nabla\nabla\cdot\boldsymbol{v}(\boldsymbol{r},\omega) = \boldsymbol{Q}(\boldsymbol{r},\omega) \tag{3.6}$$

where

$$\boldsymbol{Q}(\boldsymbol{r},\omega) = -j\omega\boldsymbol{f}(\boldsymbol{r},\omega) + \nabla\cdot\boldsymbol{c}:\boldsymbol{h}(\boldsymbol{r},\omega) \tag{3.7}$$

we define a time harmonic (second rank) Green tensor $\boldsymbol{G}(\boldsymbol{r},\boldsymbol{r}',\omega)$ through

$$\left[\left(\mu\Delta + \rho\omega^2\right)\boldsymbol{I} + (\lambda+\mu)\,\nabla\nabla\right]\cdot\boldsymbol{G}(\boldsymbol{r},\boldsymbol{r}',\omega) = -\delta(\boldsymbol{r}-\boldsymbol{r}')\boldsymbol{I}. \tag{3.8}$$

To calculate $\boldsymbol{G}(\boldsymbol{r},\boldsymbol{r}',\omega)$, the dyadic differential operator $(\mu\Delta + \rho\omega^2)\boldsymbol{I} + (\lambda+\mu)$ must be inverted as a dyadic operator, and as a differential operator. We formally apply a three-dimensional Fourier transform with respect to $\boldsymbol{r}$ (compare (2.31)):

$$\tilde{\boldsymbol{G}}(\boldsymbol{k},\boldsymbol{r}',\omega) = \int_{-\infty}^{+\infty}\int_{-\infty}^{+\infty}\int_{-\infty}^{+\infty}\boldsymbol{G}(\boldsymbol{r},\boldsymbol{r}',\omega)e^{-j\boldsymbol{k}\cdot\boldsymbol{r}}d^3\boldsymbol{r}' \tag{3.9}$$

This way the differential equation (3.8) turns into the following algebraic equations

$$\tilde{\boldsymbol{W}}(\boldsymbol{k})\cdot\tilde{\boldsymbol{G}}(\boldsymbol{k},\boldsymbol{r}',\omega) = \frac{1}{\lambda+\mu}e^{-j\boldsymbol{r}'\cdot\boldsymbol{k}}\boldsymbol{I} \tag{3.10}$$

where

$$\tilde{\boldsymbol{W}}(\boldsymbol{k}) = \left(\frac{\mu k^2 - \rho\omega^2}{\lambda+\mu}\boldsymbol{I} + \boldsymbol{k}\boldsymbol{k}\right) \tag{3.11}$$

is the so-called wave tensor [84]. To solve (3.10) the inversion of the wave tensor $\tilde{\boldsymbol{W}}(\boldsymbol{k})$ is required. using algebraic methods yields

$$\tilde{\boldsymbol{W}}^{-1}(\boldsymbol{k}) = \frac{\mathrm{adj}\tilde{\boldsymbol{W}}(\boldsymbol{k})}{\mathrm{det}\tilde{\boldsymbol{W}}(\boldsymbol{k})} \tag{3.12}$$

where

$$\mathrm{det}\tilde{\boldsymbol{W}}(\boldsymbol{k}) \neq 0 \tag{3.13}$$

must be ensured. It can be demonstrated [84] that if $\boldsymbol{k} \to \omega\hat{\boldsymbol{k}}/c$, i.e. for the case of homogeneous plane waves, $\mathrm{det}\tilde{\boldsymbol{W}}(\boldsymbol{k}) \neq 0$ for $k \neq \omega/c_p = \kappa_p$ and $k \neq \omega/c_s = \kappa_s$, where

$$c_p = \sqrt{\frac{\lambda+2\mu}{\rho}} \tag{3.14}$$

$$c_s = \sqrt{\frac{\lambda}{\rho}} \tag{3.15}$$

are the primary and secondary waves phase velocities, respectively. Consequently, we obtain for the inverse

$$\begin{aligned}\tilde{\boldsymbol{W}}^{-1}(\boldsymbol{k}) &= \frac{\lambda+\mu}{\mu k^2-\rho\omega^2}\left[\boldsymbol{I}-\frac{\lambda+\mu}{(\lambda+2\mu)k^2-\rho\omega^2}\boldsymbol{k}\boldsymbol{k}\right] \\ &= \frac{\lambda+\mu}{\mu}\left[\frac{1}{k^2-\kappa_s^2}\boldsymbol{I}-\frac{\lambda+\mu}{\lambda+2\mu}\frac{1}{(k^2-\kappa_s^2)(k-\kappa_p^2)}\boldsymbol{k}\boldsymbol{k}\right].\end{aligned} \tag{3.16}$$

As expected $\tilde{\boldsymbol{W}}^{-1}(\boldsymbol{k})$, and hence $\tilde{\boldsymbol{G}}(\boldsymbol{k},\boldsymbol{r}',\omega)$, is singular on the two so-called Ewald spheres $k=\kappa_p$ and $k=\kappa_s$ in $\boldsymbol{k}$-space. Using Equations (3.10), (3.12) and considering the inverse Fourier transform on $\tilde{\boldsymbol{G}}(\boldsymbol{k},\boldsymbol{r}',\omega)$, yields:

$$\begin{aligned}\boldsymbol{G}(\boldsymbol{r}-\boldsymbol{r}',\omega) &= \frac{1}{\mu}\left[\left(\boldsymbol{I}+\frac{1}{\kappa_s^2}\nabla'\nabla'\right)\frac{e^{j\kappa_s|\boldsymbol{r}-\boldsymbol{r}'|}}{4\pi|\boldsymbol{r}-\boldsymbol{r}'|}-\frac{1}{\kappa_s^2}\nabla'\nabla'\frac{e^{j\kappa_p|\boldsymbol{r}-\boldsymbol{r}'|}}{4\pi|\boldsymbol{r}-\boldsymbol{r}'|}\right] \\ &= \frac{1}{\mu}\left[\left(\boldsymbol{I}+\frac{1}{\kappa_s^2}\nabla\nabla\right)\frac{e^{j\kappa_s|\boldsymbol{r}-\boldsymbol{r}'|}}{4\pi|\boldsymbol{r}-\boldsymbol{r}'|}-\frac{1}{\kappa_s^2}\nabla\nabla\frac{e^{j\kappa_p|\boldsymbol{r}-\boldsymbol{r}'|}}{4\pi|\boldsymbol{r}-\boldsymbol{r}'|}\right] \\ &= \frac{1}{\mu}\left[\left(\boldsymbol{I}+\frac{1}{\kappa_s^2}\nabla\nabla\right)G_S(\boldsymbol{r}-\boldsymbol{r}',\omega)-\frac{1}{\kappa_s^2}\nabla\nabla G_P(\boldsymbol{r}-\boldsymbol{r}',\omega)\right] \\ &= \frac{1}{\mu}\{\boldsymbol{I}G_S(\boldsymbol{r}-\boldsymbol{r}',\omega)+\frac{1}{\kappa_s^2}\nabla\nabla\left[G_S(\boldsymbol{r}-\boldsymbol{r}',\omega)-G_P(\boldsymbol{r}-\boldsymbol{r}',\omega)\right]\}\end{aligned} \tag{3.17}$$

where

$$G_{P,S}(\boldsymbol{r}-\boldsymbol{r}',\omega)=\frac{e^{jk_{p,s}|\boldsymbol{r}-\boldsymbol{r}'|}}{4\pi|\boldsymbol{r}-\boldsymbol{r}'|}. \tag{3.18}$$

From a physical point of view, the two terms

$$\boldsymbol{G}_P(\boldsymbol{r},\omega)=-\frac{1}{\kappa_p^2}\nabla\nabla\frac{e^{j\kappa_s r}}{4\pi r}, \tag{3.19}$$

$$\boldsymbol{G}_S(\boldsymbol{r},\omega)=\left(\boldsymbol{I}+\frac{1}{k_s^2}\nabla\nabla\right)\frac{e^{j\kappa_s r}}{4\pi r}, \tag{3.20}$$

composing $\boldsymbol{G}(\boldsymbol{r},\omega)$ according to

$$\boldsymbol{G}(\boldsymbol{r},\omega)=\frac{1}{\lambda+2\mu}\boldsymbol{G}_P(\boldsymbol{r},\omega)+\frac{1}{\mu}\boldsymbol{G}_S(\boldsymbol{r},\omega) \tag{3.21}$$

exactly satisfy our expectation: $\boldsymbol{G}_P(\boldsymbol{r},\omega)$ represents primary and $\boldsymbol{G}_S(\boldsymbol{r},\omega)$ secondary waves. We immediately show that for $\boldsymbol{r}\neq 0$, we have

$$\nabla\times\boldsymbol{G}_P(\boldsymbol{r},\omega) = 0 \tag{3.22}$$

$$\nabla\cdot\boldsymbol{G}_S(\boldsymbol{r},\omega) = 0 \tag{3.23}$$

i.e., $\boldsymbol{G}_P(\boldsymbol{r},\omega)$ equally stands for pressure and $\boldsymbol{G}_S(\boldsymbol{r},\omega)$ for shear waves.

For $\boldsymbol{r} \neq 0$, the evaluation of the $\nabla\nabla$-differentiation in the separately appearing terms (3.19) and (3.20) does not cause any problems:

$$\boldsymbol{G}_P(\boldsymbol{r},\omega) = \left[\hat{\boldsymbol{r}}\hat{\boldsymbol{r}} - \frac{j}{\kappa_p r}(\boldsymbol{I} - 3\hat{\boldsymbol{r}}\hat{\boldsymbol{r}}) + \frac{1}{\kappa_p^2 r^2}(\boldsymbol{I} - 3\hat{\boldsymbol{r}}\hat{\boldsymbol{r}})\right]\frac{e^{ej\kappa_p r}}{4\pi r}, \tag{3.24}$$

$$\boldsymbol{G}_P(\boldsymbol{r},\omega) = \left[\boldsymbol{I} - \hat{\boldsymbol{r}}\hat{\boldsymbol{r}} + \frac{j}{\kappa_s r}(\boldsymbol{I} - 3\hat{\boldsymbol{r}}\hat{\boldsymbol{r}}) + \frac{1}{\kappa_s^2 r^2}(\boldsymbol{I} - 3\hat{\boldsymbol{r}}\hat{\boldsymbol{r}})\right]\frac{e^{ej\kappa_s r}}{4\pi r}. \tag{3.25}$$

The following considerations are pointed out:

- Even if the source point is located in the coordinate origin, the elementary elastodynamic pressure and shear waves possess direction-dependent amplitudes that are functions of r and $\hat{\boldsymbol{r}}$.

- The amplitudes of elementary elastodynamic pressure and shear waves each contain terms with characteristic r-dependencies: $1/r$, $1/r^2$, and $1/r^3$. Clearly, we have

$$\boldsymbol{G}_P^{far}(\boldsymbol{r},\omega) = \frac{e^{j\kappa_p r}}{4\pi r}\hat{\boldsymbol{r}}\hat{\boldsymbol{r}} \tag{3.26}$$

$$\boldsymbol{G}_S^{far}(\boldsymbol{r},\omega) = \frac{e^{j\kappa_s r}}{4\pi r}(\boldsymbol{I} - \hat{\boldsymbol{r}}\hat{\boldsymbol{r}}) \tag{3.27}$$

  Accordingly, the $1/r^3$-terms represent the near-field and the $1/r^2$-terms a transition field.

- Near-field, transition field, and far-field are different in terms of frequency dependence; only in the far-field, the $\delta(t)$-impulse of the source in the time domain version of (3.8) appears as $\delta(t) - \boldsymbol{G}_{P,S}$-elementary wavefront.

- With respect to a sphere (in the far-field),

$$\boldsymbol{G}_P^{far}(\boldsymbol{r},\omega) = \frac{e^{j\kappa_p r}}{4\pi r}\boldsymbol{e}_r\boldsymbol{e}_r \tag{3.28}$$

  has only a radial (tensor) component and

$$\boldsymbol{G}_S^{far}(\boldsymbol{r},\omega) = \frac{e^{j\kappa_s r}}{4\pi r}(\boldsymbol{e}_\theta\boldsymbol{e}_\theta + \boldsymbol{e}_\phi\boldsymbol{e}_\phi) \tag{3.29}$$

  only tangential (tensor) components, because we have $\boldsymbol{I} = \boldsymbol{e}_r\boldsymbol{e}_r + \boldsymbol{e}_\theta\boldsymbol{e}_\theta + \boldsymbol{e}_\phi\boldsymbol{e}_\phi$ in spherical coordinates.

The tensor components of $\boldsymbol{G}_P(\boldsymbol{r},\omega)$ and $\boldsymbol{G}_S(\boldsymbol{r},\omega)$ in spherical coordinates read:

$$\boldsymbol{G}_P(\boldsymbol{r},\omega):\boldsymbol{e}_r\boldsymbol{e}_r = \left(1+j\frac{2}{\kappa_p r}-\frac{2}{\kappa_p^2 r^2}\right)\frac{e^{j\kappa_p r}}{4\pi r} \tag{3.30}$$

$$\boldsymbol{G}_P(\boldsymbol{r},\omega):\boldsymbol{e}_\theta\boldsymbol{e}_\theta = \left(-j\frac{1}{\kappa_p r}+\frac{1}{\kappa_p^2 r^2}\right)\frac{e^{j\kappa_p r}}{4\pi r} \tag{3.31}$$

$$\boldsymbol{G}_P(\boldsymbol{r},\omega):\boldsymbol{e}_\phi\boldsymbol{e}_\phi = \left(-j\frac{1}{\kappa_p r}+\frac{1}{\kappa_p^2 r^2}\right)\frac{e^{j\kappa_p r}}{4\pi r} \tag{3.32}$$

$$\boldsymbol{G}_S(\boldsymbol{r},\omega):\boldsymbol{e}_r\boldsymbol{e}_r = \left(-j\frac{2}{\kappa_s r}+\frac{2}{\kappa_s^2 r^2}\right)\frac{e^{j\kappa_s r}}{4\pi r} \tag{3.33}$$

$$\boldsymbol{G}_S(\boldsymbol{r},\omega):\boldsymbol{e}_\theta\boldsymbol{e}_\theta = \left(1+j\frac{1}{\kappa_s r}-\frac{1}{\kappa_s^2 r^2}\right)\frac{e^{j\kappa_s r}}{4\pi r} \tag{3.34}$$

$$\boldsymbol{G}_S(\boldsymbol{r},\omega):\boldsymbol{e}_\phi\boldsymbol{e}_\phi = \left(1+j\frac{1}{\kappa_s r}-\frac{1}{\kappa_s^2 r^2}\right)\frac{e^{j\kappa_s r}}{4\pi r} \tag{3.35}$$

In spherical coordinates $\boldsymbol{G}(\boldsymbol{r},\omega)$ is diagonal, and apparently the far-field approximation (3.28) and (3.29) is found to be related to the 1-terms in the brackets of (3.30), (3.34) and (3.35).

3.1.3 Third-rank Green tensor

Due to the definition of $\boldsymbol{G}(\boldsymbol{r}-\boldsymbol{r}',\omega)$ as solution of the point-source elastodynamic problem, it can be proved that

$$\boldsymbol{v}(\boldsymbol{r},\omega)=\iiint_{V_Q}\boldsymbol{G}(\boldsymbol{r}-\boldsymbol{r}',\omega)\cdot\boldsymbol{Q}(\boldsymbol{r}',\omega)d^3\boldsymbol{r}' \tag{3.36}$$

is a solution of the differential equation (3.6) if $\boldsymbol{G}(\boldsymbol{r}-\boldsymbol{r}',\omega)$ satisfies (3.8).Utilizing (3.7) gives

$$\boldsymbol{v}(\boldsymbol{r},\omega)=\iiint_{V_Q}\boldsymbol{G}(\boldsymbol{r}-\boldsymbol{r}',\omega)\cdot\left[-j\omega\boldsymbol{f}(\boldsymbol{r}',\omega)+\nabla'\cdot\boldsymbol{c}:\boldsymbol{h}(\boldsymbol{r}',\omega)\right]d^3\boldsymbol{r}' \tag{3.37}$$

Similar to the transition from (2.77) to (2.79), we want to shift the operation $\nabla'\cdot\boldsymbol{c}:$ on $\boldsymbol{h}(\boldsymbol{r}',\omega)$ to $\boldsymbol{G}(\boldsymbol{r}-\boldsymbol{r}',\omega)$. For this purpose, we can use the equality [85]:

$$\begin{aligned}\nabla\cdot(\boldsymbol{B}\cdot\boldsymbol{A}) &= (\nabla\cdot\boldsymbol{B})\cdot\boldsymbol{A}+\boldsymbol{B}^\intercal:\nabla\boldsymbol{B}\\ &= \boldsymbol{A}^\intercal\cdot(\nabla\cdot\boldsymbol{B})+\boldsymbol{B}^\intercal:\nabla\boldsymbol{A}\end{aligned} \tag{3.38}$$

If we identify $\boldsymbol{A}^\intercal$ with $\boldsymbol{G}$ and $\boldsymbol{D}$ with $\boldsymbol{c}:\boldsymbol{h}$ we have a suitable formula at hand:

$$\begin{aligned}\nabla'\cdot\left[\boldsymbol{c}:\boldsymbol{h}(\boldsymbol{r}',\omega)\cdot\boldsymbol{G}^\intercal(\boldsymbol{r}-\boldsymbol{r}',\omega)\right] &= \boldsymbol{G}(\boldsymbol{r}-\boldsymbol{r}',\omega)\cdot\nabla'\cdot\left[\boldsymbol{c}:\boldsymbol{h}(\boldsymbol{r}',\omega)\right]\\ &\quad+\left[\boldsymbol{c}:\boldsymbol{h}(\boldsymbol{r}',\omega)\right]^\intercal:\nabla'\boldsymbol{G}^\intercal(\boldsymbol{r}-\boldsymbol{r}',\omega)\end{aligned} \tag{3.39}$$

Due to symmetries of $\boldsymbol{c}$ and $\boldsymbol{h}$, we can write $(\boldsymbol{c} : \boldsymbol{h})^{\intercal} = \boldsymbol{h} : \boldsymbol{c}$. Moreover, because of the symmetry of $\boldsymbol{G}(\boldsymbol{r} - \boldsymbol{r}', \omega)$, we can write the expression

$$-\boldsymbol{c} : \nabla' \boldsymbol{G}^{\intercal}(\boldsymbol{r} - \boldsymbol{r}', \omega) = \boldsymbol{\Sigma}(\boldsymbol{r} - \boldsymbol{r}', \omega) \tag{3.40}$$

which defines a third-rank tensor that plays the role of a ("right-sided") third rank Green tensor for the injected deformation rate

$$\boldsymbol{v}(\boldsymbol{r}, \omega) = \iiint_{V_Q} \left[-j\omega \boldsymbol{f}(\boldsymbol{r}', \omega) \cdot \boldsymbol{G}(\boldsymbol{r} - \boldsymbol{r}', \omega) + \boldsymbol{h}(\boldsymbol{r}', \omega) : \boldsymbol{\Sigma}(\boldsymbol{r} - \boldsymbol{r}', \omega) \right] d^3\boldsymbol{r}' \tag{3.41}$$

Due to the separation (3.21), $\boldsymbol{\Sigma}$ is also composed of a primary pressure and a secondary shear elementary wave term:

$$\boldsymbol{\Sigma}(\boldsymbol{r}, \omega) = \frac{1}{\lambda + 2\mu} \boldsymbol{\Sigma}_P(\boldsymbol{r}, \omega) + \frac{1}{\mu} \boldsymbol{\Sigma}_S(\boldsymbol{r}, \omega) \tag{3.42}$$

where for $\boldsymbol{r} \neq 0$

$$\boldsymbol{\Sigma}_P(\boldsymbol{r}, \omega) = \lambda \boldsymbol{I} \nabla \cdot \boldsymbol{G}_P(\boldsymbol{r}, \omega) + \mu \{ \nabla \boldsymbol{G}_P(\boldsymbol{r}, \omega) + [\nabla \boldsymbol{G}_P(\boldsymbol{r}, \omega)]^{\intercal} \}, \tag{3.43}$$

$$\boldsymbol{\Sigma}_S(\boldsymbol{r}, \omega) = \mu \{ \nabla \boldsymbol{G}_S(\boldsymbol{r}, \omega) + [\nabla \boldsymbol{G}_S(\boldsymbol{r}, \omega)]^{\intercal} \}. \tag{3.44}$$

The far-field approximations $\boldsymbol{\Sigma}_P(\boldsymbol{r}, \omega)^{far}$ and $\boldsymbol{\Sigma}_S(\boldsymbol{r}, \omega)^{far}$ can be easily obtained substituting the expressions of $\boldsymbol{G}_{P,S}(\boldsymbol{r}, \omega)^{far}$ in the above equations.

3.1.4 Fourth-rank Green tensor: stress tensor of a point source deformation rate

The source field representation of $\boldsymbol{v}$ requires $\boldsymbol{G}$ and $\boldsymbol{\Sigma}$, calculating the stress tensor from $\boldsymbol{v}$ via "Hooke's differentiation" $\boldsymbol{c} : \nabla$ a fourth-rank Green tensor $\boldsymbol{\Pi}$ comes out from $\boldsymbol{\Sigma}$ that afterwards relates the given deformation rates and the resulting stresses through a double contraction with $\boldsymbol{h}$. From a physical point of view, $\boldsymbol{\Pi}$ represents the (Huygens) stress elementary waves emanating from $\boldsymbol{h}$.

With the stress tensor $\boldsymbol{T}(\boldsymbol{r}, \omega) = \boldsymbol{c} : \nabla \boldsymbol{u}(\boldsymbol{r}, \omega)$ and considering that $j\omega \boldsymbol{u}(\boldsymbol{r}, \omega) = \boldsymbol{v}(\boldsymbol{r}, \omega)$, we immediately compute:

$$\boldsymbol{T}(\boldsymbol{r}, \omega) = \iiint_{V_Q} \left[\boldsymbol{c} : \nabla \boldsymbol{G}(\boldsymbol{r} - \boldsymbol{r}', \omega) \cdot \boldsymbol{f}(\boldsymbol{r}', \omega) - \frac{1}{j\omega} \times \boldsymbol{c} : \nabla \boldsymbol{\Sigma}(\boldsymbol{r} - \boldsymbol{r}', \omega) : \boldsymbol{h}(\boldsymbol{r}', \omega) \right] d^3\boldsymbol{r}' \tag{3.45}$$

with

$$\boldsymbol{c} : \nabla \boldsymbol{G}(\boldsymbol{r} - \boldsymbol{r}', \omega) \cdot \boldsymbol{f}(\boldsymbol{r}', \omega) = \boldsymbol{\Sigma}(\boldsymbol{r} - \boldsymbol{r}', \omega) \cdot \boldsymbol{f}(\boldsymbol{r}', \omega) \tag{3.46}$$

and

$$\boldsymbol{c} : \nabla \boldsymbol{\Sigma}(\boldsymbol{r} - \boldsymbol{r}', \omega) : \boldsymbol{h}(\boldsymbol{r}', \omega) \doteq \boldsymbol{\Pi}(\boldsymbol{r} - \boldsymbol{r}', \omega) : \boldsymbol{h}(\boldsymbol{r}', \omega) \tag{3.47}$$

so that

$$\boldsymbol{T}(\boldsymbol{r},\omega) = \iiint_{V_Q} \left[\boldsymbol{\Sigma}(\boldsymbol{r}-\boldsymbol{r}',\omega) \cdot \boldsymbol{f}(\boldsymbol{r}',\omega) - \frac{1}{j\omega} \boldsymbol{\Pi}(\boldsymbol{r}-\boldsymbol{r}',\omega) : \boldsymbol{h}(\boldsymbol{r}',\omega) \right] d^3\boldsymbol{r}'. \tag{3.48}$$

With the Green tensors $\boldsymbol{\Sigma}$ and $\boldsymbol{\Pi}$, we are now able to express the stress elementary waves emanating from point-like $\hat{\boldsymbol{f}}$- and $\hat{\boldsymbol{h}}$-sources:

$$\boldsymbol{T}^{PS_{f,h}}(\boldsymbol{r},\omega) = \hat{\boldsymbol{f}} \cdot \boldsymbol{\Sigma}(\boldsymbol{r},\omega) + \hat{\boldsymbol{h}} : \boldsymbol{\Pi}(\boldsymbol{r},\omega). \tag{3.49}$$

Assuming a homogeneous isotropic material, and due to (3.42), this also leads to the separation

$$\boldsymbol{\Pi}(\boldsymbol{r},\omega) = \frac{1}{\lambda+2\mu} \boldsymbol{\Pi}_P + \frac{1}{\mu} \boldsymbol{\Pi}_S(\boldsymbol{r},\omega). \tag{3.50}$$

The substitution of the expressions of $\boldsymbol{\Sigma}_{P,S}(\boldsymbol{r},\omega)^{far}$ in Eq. (3.47) leads to the definitions of $\boldsymbol{\Pi}_{P,S}(\boldsymbol{r},\omega)^{far}$.

3.2 Two- and Three-Dimensional Elastodynamic Source Fields

3.2.1 Elastodynamic point source synthesis

With the integral representation (3.41) and (3.45), we formulate the point source synthesis for elastodynamic source fields in homogeneous isotropic materials as:

$$\boldsymbol{v}(\boldsymbol{r},\omega) = \iiint_{V_Q} \left[-j\omega \boldsymbol{f}(\boldsymbol{r}',\omega) \cdot \boldsymbol{G}(\boldsymbol{r}-\boldsymbol{r}',\omega) + \boldsymbol{h}(\boldsymbol{r}',\omega) : \boldsymbol{\Sigma}(\boldsymbol{r}-\boldsymbol{r}',\omega) \right] d^3\boldsymbol{r}', \tag{3.51}$$

$$\boldsymbol{T}(\boldsymbol{r},\omega) = \iiint_{V_Q} \left[\boldsymbol{f}(\boldsymbol{r}',\omega) \cdot \boldsymbol{\Sigma}^{312}(\boldsymbol{r}',\omega) - \frac{1}{j\omega} \boldsymbol{h}(\boldsymbol{r}',\omega) : \boldsymbol{\Pi}(\boldsymbol{r}-\boldsymbol{r}',\omega) \right] d^3\boldsymbol{r}'. \tag{3.52}$$

The amplitude and phase distributions of force density sources $\boldsymbol{f}(\boldsymbol{r}',\omega)$ and deformation rate sources $\boldsymbol{h}(\boldsymbol{r}',\omega)$ in the interior of a source volume V_Q tune the elastodynamic elementary waves emanating from each source point $\boldsymbol{r}'$ as given mathematically by the Green tensors $\boldsymbol{G}(\boldsymbol{r}-\boldsymbol{r}',\omega)$, $\boldsymbol{\Sigma}(\boldsymbol{r}-\boldsymbol{r}',\omega)$ and $\boldsymbol{\Pi}(\boldsymbol{r}-\boldsymbol{r}',\omega)$.

Let a be the maximum linear dimension of V_Q; then we obtain the far-field approximations of the source fields for $r \gg a$ and $\kappa_{p,s} r \gg 1$ with Equation (3.21) and the far-field approximations (3.26) and (3.27), with Equation (3.42) and Equation (3.50) and the associated far-field approximations; these may be separated into primary and secondary terms. At first, we discuss the primary terms

$$\begin{aligned} \boldsymbol{v}_P^{far} &= -j\omega \frac{1}{\lambda+2\mu} \iiint_{V_Q} \boldsymbol{f}(\boldsymbol{r}',\omega) \cdot \boldsymbol{G}_P^{far}(\boldsymbol{r},\boldsymbol{r}',\omega) d^3\boldsymbol{r}' \\ &= \frac{1}{\lambda+2\mu} \iiint_{V_Q} \boldsymbol{h}(\boldsymbol{r}',\omega) : \boldsymbol{\Sigma}_P^{far}(\boldsymbol{r},\boldsymbol{r}',\omega) d^3\boldsymbol{r}' \end{aligned} \tag{3.53}$$

$$\begin{aligned}\boldsymbol{T}_P^{far}(\boldsymbol{r},\omega) &= \frac{1}{\lambda+2\mu}\iiint_{V_Q}\boldsymbol{f}(\boldsymbol{r}',\omega)\cdot\boldsymbol{\Sigma}_P^{far}(\boldsymbol{r},\boldsymbol{r}',\omega)d^3\boldsymbol{r}' \\ &= -j\omega\frac{1}{\lambda+2\mu}\iiint_{V_Q}\boldsymbol{h}(\boldsymbol{r}',\omega):\boldsymbol{\Pi}_P^{far}(\boldsymbol{r},\boldsymbol{r}',\omega)d^3\boldsymbol{r}'\end{aligned} \tag{3.54}$$

and write (3.53) in the particle displacement as

$$\begin{aligned}\boldsymbol{u}_P^{far}(\boldsymbol{r},\omega) &= \frac{e^{j\kappa_p r}}{r}\left[\boldsymbol{H}_P^f(\hat{\boldsymbol{r}},\omega)+\boldsymbol{H}_P^h(\hat{\boldsymbol{r}},\omega)\right] \\ &= \frac{e^{j\kappa_p r}}{r}\left[H_P^f(\hat{\boldsymbol{r}},\omega)+H_P^h(\hat{\boldsymbol{r}},\omega)\right]\hat{\boldsymbol{r}}\end{aligned} \tag{3.55}$$

with the short-hand notations

$$\boldsymbol{H}_P^f = \frac{1}{4\pi c_P Z_P}\iiint_{V_Q}\boldsymbol{f}(\boldsymbol{r}',\omega)\cdot\hat{\boldsymbol{r}}e^{-j\kappa_p\hat{\boldsymbol{r}}\cdot\boldsymbol{r}'}d^3\boldsymbol{r}', \hat{\boldsymbol{r}} = H_P^f(\hat{\boldsymbol{r}},\omega)\hat{\boldsymbol{r}}, \tag{3.56}$$

$$\boldsymbol{H}_P^h = -\frac{1}{4\pi c_P^2 Z_P}\iiint_{V_Q}\boldsymbol{h}(\boldsymbol{r}',\omega):(\lambda\boldsymbol{I}+2\mu\hat{\boldsymbol{r}}\hat{\boldsymbol{r}})\,e^{-j\kappa_p\hat{\boldsymbol{r}}\cdot\boldsymbol{r}'}d^3\boldsymbol{r}', \hat{\boldsymbol{r}} = H_P^h(\hat{\boldsymbol{r}},\omega)\hat{\boldsymbol{r}}. \tag{3.57}$$

The functions $H_P^f(\hat{r},\omega)$ and $H_P^h(\hat{\boldsymbol{r}},\omega)$ are scalar radiation characteristics of the source distributions that completely describe the particle velocity field of the primary wave [90](not only in the far-field). With

$$\boldsymbol{H}_P^{f,h}(\hat{\boldsymbol{r}},\omega)\cdot(\boldsymbol{I}-\hat{\boldsymbol{r}}\hat{\boldsymbol{r}}) = 0 \tag{3.58}$$

the primary wave identifies itself as a longitudinal pressure wave. It is worth emphasizing that the primary displacement source field is longitudinally polarized only in the far field.

For the stress tensor (3.54), we obtain the explicit representation

$$\boldsymbol{T}^{far}(\boldsymbol{r},\omega) = j\kappa_p\left[H_P^f(\hat{\boldsymbol{r}},\omega)+H_P^f(\hat{\boldsymbol{r}},\omega)\right]\frac{e^{j\kappa_p r}}{r}(\lambda\boldsymbol{I}+2\mu\hat{\boldsymbol{r}}\hat{\boldsymbol{r}}). \tag{3.59}$$

The comparison of (3.55) and (3.59) with the case of plane waves [84] reveals a local plane wave behavior of the primary far-field approximation of elastodynamic source fields.

We now turn to the S-term of the source field; the counterparts to (3.53) and (3.54) read

$$\begin{aligned}\boldsymbol{v}_S^{far}(\boldsymbol{r},\omega) = &-j\omega\frac{1}{\mu}\iiint_{V_Q}\boldsymbol{f}(\boldsymbol{r}',\omega)\cdot\boldsymbol{G}_S^{far}(\boldsymbol{r},\boldsymbol{r}',\omega)d^3\boldsymbol{r}' \\ &\frac{1}{\mu}\iiint_{V_Q}\boldsymbol{h}(\boldsymbol{r}',\omega):\boldsymbol{\Sigma}_S^{far}(\boldsymbol{r},\boldsymbol{r}',\omega)d^3\boldsymbol{r}',\end{aligned} \tag{3.60}$$

$$\begin{aligned}\boldsymbol{T}_S^{far}(\boldsymbol{r},\omega) = &\frac{1}{\mu}\iiint_{V_Q}\boldsymbol{f}(\boldsymbol{r}',\omega)\cdot\boldsymbol{\Sigma}_S^{far}(\boldsymbol{r},\boldsymbol{r}',\omega)d^3\boldsymbol{r}' \\ &-\frac{1}{j\omega}\frac{1}{\mu}\iiint_{V_Q}\boldsymbol{h}(\boldsymbol{r}',\omega):\boldsymbol{\Pi}_S^{far}(\boldsymbol{r},\boldsymbol{r}',\omega)d^3\boldsymbol{r}'.\end{aligned} \tag{3.61}$$

With (3.27) and (3.60), we obtain for the particle velocity an expression similar to (3.55):

$$\begin{aligned}
\boldsymbol{u}_S^{far}(\boldsymbol{r},\omega) &= \frac{e^{j\kappa_s r}}{r}\left[\boldsymbol{H}_S^f(\hat{\boldsymbol{r}},\omega)+\boldsymbol{H}_S^h(\hat{\boldsymbol{r}},\omega)\right] \\
&= \frac{e^{j\kappa_s r}}{r}\left[H_{S\theta}^f(\hat{\boldsymbol{r}},\omega)+H_{S\theta}^h(\hat{\boldsymbol{r}},\omega)\right]\boldsymbol{e}_\theta + \frac{e^{j\kappa_s r}}{r}\left[H_{S\phi}^f(\hat{\boldsymbol{r}},\omega)+H_{S\phi}^h(\hat{\boldsymbol{r}},\omega)\right]\boldsymbol{e}_\phi \\
&= u_{S\theta}^{far}(\boldsymbol{r},\omega)\boldsymbol{e}_\theta + u_{S\phi}^{far}(\boldsymbol{r},\omega)\boldsymbol{e}_\phi
\end{aligned} \tag{3.62}$$

with the short-hand notations

$$\begin{aligned}
\boldsymbol{H}_S^f(\hat{\boldsymbol{r}},\omega) &= \frac{1}{4\pi c_S Z_S}\iiint_{V_Q}\boldsymbol{f}(\boldsymbol{r}',\omega)e^{-\kappa_s\hat{\boldsymbol{r}}\cdot\boldsymbol{r}'}d^3\boldsymbol{r}'\cdot(\boldsymbol{I}-\hat{\boldsymbol{r}}\hat{\boldsymbol{r}}) \\
&= \frac{1}{4\pi c_S Z_S}\iiint_{V_Q}\boldsymbol{f}(\boldsymbol{r}',\omega)e^{-\kappa_s\hat{\boldsymbol{r}}\cdot\boldsymbol{r}'}d^3\boldsymbol{r}'\cdot(\boldsymbol{e}_\theta\boldsymbol{e}_\theta+\boldsymbol{e}_\phi\boldsymbol{e}_\phi) \\
&= \frac{1}{4\pi c_S Z_S}\iiint_{V_Q}\boldsymbol{f}(\boldsymbol{r}',\omega)\boldsymbol{e}_\theta e^{-\kappa_s\hat{\boldsymbol{r}}\cdot\boldsymbol{r}'}d^3\boldsymbol{r}'\boldsymbol{e}_\theta \\
&+ \frac{1}{4\pi c_S Z_S}\iiint_{V_Q}\boldsymbol{f}(\boldsymbol{r}',\omega)\boldsymbol{e}_\phi e^{-\kappa_s\hat{\boldsymbol{r}}\cdot\boldsymbol{r}'}d^3\boldsymbol{r}'\boldsymbol{e}_\phi \\
&= H_{S\theta}^f(\hat{\boldsymbol{r}},\omega)\boldsymbol{e}_\theta + H_{S\phi}^f(\hat{\boldsymbol{r}},\omega)\boldsymbol{e}_\phi,
\end{aligned} \tag{3.63}$$

$$\begin{aligned}
\boldsymbol{H}_S^h(\hat{\boldsymbol{r}},\omega) &= \frac{1}{2\pi c_S}\iiint_{V_Q}\boldsymbol{h}(\boldsymbol{r}',\omega)\cdot\hat{\boldsymbol{r}}e^{-\kappa_s\hat{\boldsymbol{r}}\cdot\boldsymbol{r}'}d^3\boldsymbol{r}'\cdot(\boldsymbol{I}-\hat{\boldsymbol{r}}\hat{\boldsymbol{r}}) \\
&= -\frac{1}{2\pi c_S}\iiint_{V_Q}\boldsymbol{h}(\boldsymbol{r}',\omega):\hat{\boldsymbol{r}}\boldsymbol{e}_\theta e^{-\kappa_s\hat{\boldsymbol{r}}\cdot\boldsymbol{r}'}d^3\boldsymbol{r}'\boldsymbol{e}_\theta \\
&- -\frac{1}{2\pi c_S}\iiint_{V_Q}\boldsymbol{h}(\boldsymbol{r}',\omega):\hat{\boldsymbol{r}}\boldsymbol{e}_\phi e^{-\kappa_s\hat{\boldsymbol{r}}\cdot\boldsymbol{r}'}d^3\boldsymbol{r}'\boldsymbol{e}_\phi \\
&= H_{S\theta}^h(\hat{\boldsymbol{r}},\omega)\boldsymbol{e}_\theta + H_{S\phi}^h(\hat{\boldsymbol{r}},\omega)\boldsymbol{e}_\phi.
\end{aligned} \tag{3.64}$$

Based on these results, we immediately realize that

$$\boldsymbol{H}_S^{f,h}\cdot\hat{\boldsymbol{r}}=0 \tag{3.65}$$

holds: in the far-field. shear waves from arbitrary $\boldsymbol{f}-$ and/or $\boldsymbol{h}-$sources are transversely polarized, with regard to $\hat{\boldsymbol{r}}$. This confirms that they behave locally like plane waves. This is also true for the corresponding stress tensor:

$$\boldsymbol{T}^{far}(\boldsymbol{r},\omega)=j\kappa_s\mu\frac{e^{j\kappa_s r}}{r}\{\hat{\boldsymbol{r}}\left[\boldsymbol{H}_S^f(\hat{\boldsymbol{r}},\omega)+\boldsymbol{H}_S^h(\hat{\boldsymbol{r}},\omega)\right]+\left[\boldsymbol{H}_S^f(\hat{\boldsymbol{r}},\omega)+\boldsymbol{H}_S^h(\hat{\boldsymbol{r}},\omega)\right]\hat{\boldsymbol{r}}\} \tag{3.66}$$

In order to improve the understanding of the mathematical and physical properties of elastodynamic fields characterized by the presence of point sources, the cases of a point-wise force density source and point-wise deformation rate source acting separately are presented in the next Sections.

3.2.2 Particle displacement of a point source force density, point radiation characteristic

The equation

$$\boldsymbol{u}^{PS_f}(\boldsymbol{r},\omega) = \iiint_{V_Q} \boldsymbol{G}(\boldsymbol{r}-\boldsymbol{r}',\omega)\cdot\boldsymbol{f}(\boldsymbol{r}',\omega)d^3\boldsymbol{r}' \tag{3.67}$$

with $\boldsymbol{f}(\boldsymbol{r},\omega) = \delta(\boldsymbol{r})\hat{\boldsymbol{f}}$ represents the displacement field due to a point source force density which by exploiting the properties of the $\delta(\boldsymbol{r})$-function, can be rewritten as

$$\begin{aligned} \boldsymbol{u}^{PS_f}(\boldsymbol{r},\omega) &= \boldsymbol{G}(\boldsymbol{r},\omega)\cdot\hat{\boldsymbol{f}} && (3.68)\\ &= \hat{\boldsymbol{f}}\cdot\boldsymbol{G}(\boldsymbol{r},\omega). && (3.69)\end{aligned}$$

This helps to understand the tensor character of the elementary waves: the vector force density $\hat{\boldsymbol{f}}$ is rotated into the vector particle displacement, so that they do not have the same direction. The vector (3.68) may be separated into its spherical coordinate components:

$$\begin{aligned} u^{PS_f}_{r,\theta,\phi}(\boldsymbol{r},\omega) &= \boldsymbol{u}^{PS_f}(\boldsymbol{r},\omega)\cdot\boldsymbol{e}_{r,\theta,\phi}\\ &= \boldsymbol{G}(\boldsymbol{r},\omega):\hat{\boldsymbol{f}}\boldsymbol{e}_{r,\theta,\phi} && (3.70)\end{aligned}$$

with (3.30) through (3.35), we find

$$u_r^{PS_f}(\boldsymbol{r},\omega) = \left[\frac{1}{\lambda+2\mu}\left(1+j\frac{2}{\kappa_p r}-\frac{2}{\kappa_p^2 r^2}\right)\frac{e^{j\kappa_p r}}{4\pi r}+\frac{1}{\mu}\left(-j\frac{2}{\kappa_s r}+\frac{2}{\kappa_s^2 r^2}\right)\frac{e^{j\kappa_s r}}{4\pi r}\right]\hat{\boldsymbol{f}}\cdot\boldsymbol{e}_r, \tag{3.71}$$

$$u_\theta^{PS_f}(\boldsymbol{r},\omega) = \left[\frac{1}{\lambda+2\mu}\left(-j\frac{1}{\kappa_p r}+\frac{1}{\kappa_p^2 r^2}\right)\frac{e^{j\kappa_p r}}{4\pi r}+\frac{1}{\mu}\left(1+j\frac{1}{\kappa_s r}-\frac{1}{\kappa_s^2 r^2}\right)\frac{e^{j\kappa_s r}}{4\pi r}\right]\hat{\boldsymbol{f}}\cdot\boldsymbol{e}_\theta, \tag{3.72}$$

$$u_\theta^{PS_f}(\boldsymbol{r},\omega) = \left[\frac{1}{\lambda+2\mu}\left(-j\frac{1}{\kappa_p r}+\frac{1}{\kappa_p^2 r^2}\right)\frac{e^{j\kappa_p r}}{4\pi r}+\frac{1}{\mu}\left(1+j\frac{1}{\kappa_s r}-\frac{1}{\kappa_s^2 r^2}\right)\frac{e^{j\kappa_s r}}{4\pi r}\right]\hat{\boldsymbol{f}}\cdot\boldsymbol{e}_\phi. \tag{3.73}$$

We now confirm what was already stated in the previous Section: each elastodynamic (in this case a force density) point source radiates pressure and shear waves. Moreover, the primary pressure wave is generally not longitudinal, and the secondary shear wave is not transverse since both waves appear in each component. The terminology "longitudinal and shear waves" is in fact strictly valid only for plane waves; pressure as shear elementary waves have both longitudinal $\boldsymbol{e}_r$-as well as transverse $\boldsymbol{e}_\theta$, $\boldsymbol{e}_\phi$-particle displacement components. Only in the far-field approximation

$$\begin{aligned} u_r^{PS_f}(\boldsymbol{r},\omega) &= \frac{1}{\lambda+2\mu}\frac{e^{j\kappa_p r}}{4\pi r}\hat{\boldsymbol{f}}\cdot\boldsymbol{e}_r, && (3.74)\\ u_\theta^{PS_f}(\boldsymbol{r},\omega) &= \frac{1}{\mu}\frac{e^{j\kappa_s r}}{4\pi r}\hat{\boldsymbol{f}}\cdot\boldsymbol{e}_\theta, && (3.75)\\ u_\phi^{PS_f}(\boldsymbol{r},\omega) &= \frac{1}{\mu}\frac{e^{j\kappa_s r}}{4\pi r}\hat{\boldsymbol{f}}\cdot\boldsymbol{e}_\phi, && (3.76)\end{aligned}$$

the familiar terminology holds: primary far-field pressure waves are longitudinally polarized, secondary far-field shear waves are transversely polarized. In the far-field, primary waves only appear in the r-component and shear waves only in the θ, ϕ-components of the particle velocity. Specially choosing $\hat{\boldsymbol{f}} = \hat{\boldsymbol{f}}(\hat{\boldsymbol{r}}) = \boldsymbol{e}_r$ (so-called breathing sphere), tangential components basically do not appear in the particle displacement radiation field, and the far-field of this special source only consist of a pressure wave. With (3.68) and (3.21) as well as with (3.26) and (3.27), we may write the far-field approximation (3.74) through (3.76) in a coordinate-free way:

$$\boldsymbol{u}_P^{PS_f,far}(\boldsymbol{r},\omega) = u_P(\hat{\boldsymbol{f}},\hat{\boldsymbol{r}})\frac{e^{j\kappa_p r}}{r}\hat{\boldsymbol{u}}_P(\hat{\boldsymbol{f}},\hat{\boldsymbol{r}}) \tag{3.77}$$

with

$$\hat{\boldsymbol{u}}_P(\hat{\boldsymbol{f}},\hat{\boldsymbol{r}}) = \hat{\boldsymbol{r}} \tag{3.78}$$

$$u_P(\hat{\boldsymbol{f}},\hat{\boldsymbol{r}}) = \frac{1}{4\pi(\lambda+2\mu)}\hat{\boldsymbol{r}}\cdot\hat{\boldsymbol{f}} \tag{3.79}$$

as well as

$$\boldsymbol{u}_S^{PS_f,far}(\boldsymbol{r},\omega) = u_S(\hat{\boldsymbol{f}},\hat{\boldsymbol{r}})\frac{e^{j\kappa_s r}}{r}\hat{\boldsymbol{u}}_S(\hat{\boldsymbol{f}},\hat{\boldsymbol{r}}) \tag{3.80}$$

with

$$\hat{\boldsymbol{u}}_S(\hat{\boldsymbol{f}},\hat{\boldsymbol{r}}) = \frac{(\boldsymbol{I}-\hat{\boldsymbol{r}}\hat{\boldsymbol{r}})\cdot\hat{\boldsymbol{f}}}{|(\boldsymbol{I}-\hat{\boldsymbol{r}}\hat{\boldsymbol{r}})\cdot\hat{\boldsymbol{f}}|} \tag{3.81}$$

$$u_S(\hat{\boldsymbol{f}},\hat{\boldsymbol{r}}) = \frac{1}{4\pi\mu}|(\boldsymbol{I}-\hat{\boldsymbol{r}}\hat{\boldsymbol{r}})| \tag{3.82}$$

where the amplitude (unit) vectors $\hat{\boldsymbol{u}}_P(\hat{\boldsymbol{f}},\hat{\boldsymbol{r}})$ and $\hat{\boldsymbol{u}}_S(\hat{\boldsymbol{f}},\hat{\boldsymbol{r}})$ according to

$$(\boldsymbol{I}-\hat{\boldsymbol{r}}\hat{\boldsymbol{r}})\cdot\hat{\boldsymbol{u}}_P(\hat{\boldsymbol{f}},\hat{\boldsymbol{r}}) = 0 \tag{3.83}$$

$$\hat{\boldsymbol{r}}\cdot\hat{\boldsymbol{u}}_S(\hat{\boldsymbol{f}},\hat{\boldsymbol{r}}) = 0 \tag{3.84}$$

are longitudinally, respectively transversely, oriented with regard to the propagation direction $\hat{\boldsymbol{r}}$. The comparison of this notation with the case of plane waves [84] reveals that the particle displacement far-field of a point source behaves locally as a plane wave. One essential difference: a potential $F(\omega)$-band limitation of the point source according to $\boldsymbol{f}(\boldsymbol{r},\omega) = F(\omega)\delta(\boldsymbol{r})\hat{\boldsymbol{f}}$ appears as a factor in both amplitudes $u_{P,S}(\hat{\boldsymbol{f}},\hat{\boldsymbol{r}}) \Rightarrow u_{P,S}(\hat{\boldsymbol{f}},\hat{\boldsymbol{r}},\omega) = F(\omega)u_{P,S}(\hat{\boldsymbol{f}},\hat{\boldsymbol{r}})$. For plane waves in infinite space, instead, we could independently prescribe the time (frequency) dependence of the pressure and shear waves; for elementary waves from point sources, the time (frequency) dependence of the shear wave is coupled to the time dependence of the pressure wave via the time (frequency) dependence of the source.

3.2.3 Particle displacement of a point source deformation rate, point radiation characteristic

According to (3.41), the second-rank tensor for the particle velocity is related to a force density source and the third-rank Green tensor for the particle velocity to a deformation rate source. Accordingly, we investigate the case $\boldsymbol{f} = 0$ and $\boldsymbol{h} \neq 0$ in some more detail:

$$\boldsymbol{v}(\boldsymbol{r},\omega) = \iiint_{V_Q} \boldsymbol{h}(\boldsymbol{r}',\omega) : \boldsymbol{\Sigma}(\boldsymbol{r}-\boldsymbol{r}',\omega) d^3\boldsymbol{r}'. \tag{3.85}$$

With

$$\hat{\boldsymbol{h}} = \frac{\boldsymbol{h}}{\sqrt{\boldsymbol{h} : \boldsymbol{h}^H}} \tag{3.86}$$

(where $\boldsymbol{h}^H$ denotes the Hermitian of $\boldsymbol{h}$) and

$$\boldsymbol{h}(\boldsymbol{r},\omega) = \delta(\boldsymbol{r})\hat{\boldsymbol{h}} \tag{3.87}$$

we postulate a point-like deformation rate unit source in the origin and find

$$\boldsymbol{v}^{PS_h}(\boldsymbol{r},\omega) = \hat{\boldsymbol{h}} : \boldsymbol{\Sigma}(\boldsymbol{r},\omega) \tag{3.88}$$

as the counterpart to (3.68). In the far-field, similarly to (3.77) and (3.80), we have:

$$\begin{aligned} \boldsymbol{v}^{PS_h,far}(\boldsymbol{r},\omega) &= \hat{\boldsymbol{h}} : \left[\frac{1}{\lambda} 2\mu \boldsymbol{\Sigma}_P^{far}(\boldsymbol{r},\omega) + \frac{1}{\mu}\boldsymbol{\Sigma}_S^{far}(\boldsymbol{r},\omega)\right] \\ &= \boldsymbol{v}_P^{PS_h,far}(\boldsymbol{r},\omega) + \boldsymbol{v}_S^{PS_h,far}(\boldsymbol{r},\omega) \end{aligned} \tag{3.89}$$

where

$$\begin{aligned} \boldsymbol{v}_P^{PS_h,far}(\boldsymbol{r},\omega) &= j\frac{\kappa_p}{\lambda+2\mu}\frac{e^{j\kappa_p r}}{4\pi r}\hat{\boldsymbol{h}} : (\lambda \boldsymbol{I} + 2\mu\hat{\boldsymbol{r}}\hat{\boldsymbol{r}})\hat{\boldsymbol{r}} \\ &= \boldsymbol{v}_P(\hat{\boldsymbol{h}},\hat{\boldsymbol{r}})\frac{e^{j\kappa_p r}}{4\pi r} \end{aligned} \tag{3.90}$$

with

$$\begin{aligned} \boldsymbol{v}(\hat{\boldsymbol{h}},\hat{\boldsymbol{r}}) &= v_p(\hat{\boldsymbol{h}},\hat{\boldsymbol{r}})\hat{(\boldsymbol{r}}) \\ &= j\frac{\kappa_p}{4\pi(\lambda+2\mu)}\hat{\boldsymbol{h}} : (\lambda\boldsymbol{I} + 2\mu\hat{\boldsymbol{r}}\hat{\boldsymbol{r}})\hat{\boldsymbol{r}} \end{aligned} \tag{3.91}$$

as well as

$$\begin{aligned} \boldsymbol{v}_S^{PS_h,far}(\boldsymbol{r},\omega) &= 2j\kappa_s\frac{e^{j\kappa_s r}}{4\pi r}\hat{\boldsymbol{h}} : (\boldsymbol{I} - \hat{\boldsymbol{r}}\hat{\boldsymbol{r}}) \\ &= \boldsymbol{v}_S(\hat{\boldsymbol{h}},\hat{\boldsymbol{r}})\frac{e^{j\kappa_s r}}{4\pi r} \end{aligned} \tag{3.92}$$

with

$$\begin{aligned} \boldsymbol{v}_S(\hat{\boldsymbol{h}},\hat{\boldsymbol{r}}) &= v_S(\hat{\boldsymbol{h}},\hat{\boldsymbol{r}})\hat{\boldsymbol{v}}_S(\hat{\boldsymbol{h}},\hat{\boldsymbol{r}}) \\ &= j\frac{\kappa_s}{2\pi}\hat{\boldsymbol{h}} : \hat{\boldsymbol{r}}(\boldsymbol{I} - \hat{\boldsymbol{r}}\hat{\boldsymbol{r}}) \end{aligned} \tag{3.93}$$

With

$$\begin{aligned}\boldsymbol{u}_P^{PS_h,far}(\boldsymbol{r},\omega) &= -\frac{1}{4\pi c_P(\lambda+2\mu)}\frac{e^{j\kappa_p r}}{4\pi r}\hat{\boldsymbol{h}} : (\lambda\boldsymbol{I}+2\mu\hat{\boldsymbol{r}}\hat{\boldsymbol{r}}) \\ &= u_P(\hat{\boldsymbol{h}},\hat{\boldsymbol{r}})\frac{e^{j\kappa_p r}}{4\pi r}\hat{\boldsymbol{u}_P}(\hat{\boldsymbol{h}},\hat{\boldsymbol{r}}) \end{aligned} \tag{3.94}$$

$$\begin{aligned}\boldsymbol{u}_S^{PS_h,far}(\boldsymbol{r},\omega) &= -\frac{1}{2\pi c_S}\frac{e^{j\kappa_s r}}{r}\hat{\boldsymbol{h}} : \hat{\boldsymbol{r}}(\boldsymbol{I}-\hat{\boldsymbol{r}}\hat{\boldsymbol{r}}) \\ &= u_S(\hat{\boldsymbol{h}},\hat{\boldsymbol{r}})\frac{e^{j\kappa_s r}}{r}\boldsymbol{u}_S(\hat{\boldsymbol{h}},\hat{\boldsymbol{r}}) \end{aligned} \tag{3.95}$$

where

$$\hat{\boldsymbol{u}}_P(\hat{\boldsymbol{h}},\hat{\boldsymbol{r}}) = \hat{\boldsymbol{r}} \tag{3.96}$$

$$u_P(\hat{\boldsymbol{h}},\hat{\boldsymbol{r}}) = -\frac{\hat{\boldsymbol{h}} : \hat{\boldsymbol{r}}(\lambda\boldsymbol{I}+2\mu\hat{\boldsymbol{r}}\hat{\boldsymbol{r}})}{4\pi c_P(\lambda+2\mu)} \tag{3.97}$$

$$\hat{\boldsymbol{u}}_S(\hat{\boldsymbol{h}},\hat{\boldsymbol{r}}) = \frac{\hat{\boldsymbol{h}} : \hat{\boldsymbol{r}}(\boldsymbol{I}-\hat{\boldsymbol{r}}\hat{\boldsymbol{r}})}{|\hat{\boldsymbol{h}} : \hat{\boldsymbol{r}}(\boldsymbol{I}-\hat{\boldsymbol{r}}\hat{\boldsymbol{r}})|} \tag{3.98}$$

$$u_S(\hat{\boldsymbol{h}},\hat{\boldsymbol{r}}) = -\frac{|\hat{\boldsymbol{h}} : \hat{\boldsymbol{r}}(\boldsymbol{I}-\hat{\boldsymbol{r}}\hat{\boldsymbol{r}})|}{2\pi c_S} \tag{3.99}$$

we switch to the particle displacement. The polarization equations (3.83) and (3.84) also hold for the $\hat{\boldsymbol{h}}$-source; even the particle displacement far-field of a point-like deformation rate source behaves locally as a plane wave. It was stated that the special choice $\hat{\boldsymbol{f}}(\hat{\boldsymbol{r}}) = \hat{\boldsymbol{r}}$ of the force density cuts off the pertinent shear wave in the far-field (equations (3.74) to (3.76)); with the special choice $\hat{\boldsymbol{h}} = \boldsymbol{I}/\sqrt{3}$ of a deformation rate unit source, we may completely cut off the pertinent shear wave, i.e., in the near- and far-fields because we have $\boldsymbol{I} : \boldsymbol{\Sigma}_S = 0$ with (3.44). Deceptions of that kind become useful the physical interpretation of side echoes.

Chapter 4

Radiatiation Fields in Homogeneous Isotropic Half Spaces

In the previous chapter the radiation characteristics of point-wise force density and dilatation rate sources located in full-space have been derived. In so doing, the second-rank Green tensor $\boldsymbol{G}(\boldsymbol{r}, \boldsymbol{r}', \omega)$ has been defined, allowing for the definition of the generation and propagation of primary and secondary elementary spherical waves in homogeneous isotropic spaces. Due to the linearity of the analyzed elastodynamic problem, the superimposition principle has been used to represent the solution of elastodynamic fields, characterized by the presence of finite-sized sources, thought as distributed point-sources, in terms of the velocity vector and of the Cauchy stress tensor:

$$\boldsymbol{v}(\boldsymbol{r}, \omega) = \iiint_{V_Q} \left[-j\omega \boldsymbol{f}(\boldsymbol{r}', \omega) \cdot \boldsymbol{G}(\boldsymbol{r} - \boldsymbol{r}', \omega) + \boldsymbol{h}(\boldsymbol{r}', \omega) : \boldsymbol{\Sigma}(\boldsymbol{r} - \boldsymbol{r}', \omega) \right] d^3\boldsymbol{r}' \tag{4.1}$$

$$\boldsymbol{T}(\boldsymbol{r}, \omega) = \iiint_{V_Q} \left[\boldsymbol{f}(\boldsymbol{r}', \omega) \cdot \boldsymbol{\Sigma}(\boldsymbol{r}', \omega) - \frac{1}{j\omega} \boldsymbol{h}(\boldsymbol{r}', \omega) : \boldsymbol{\Pi}(\boldsymbol{r} - \boldsymbol{r}', \omega) \right] d^3\boldsymbol{r}' \tag{4.2}$$

where $\boldsymbol{\Sigma}(\boldsymbol{r}, \boldsymbol{r}', \omega)$ and $\boldsymbol{\Pi}(\boldsymbol{r}, \boldsymbol{r}', \omega)$ are the third-rank and fourth-rank Green tensor, respectively. These theoretical results constitute the basis from which to develop the study of the actual radiation fields generated in solid media by some physical source located in an infinite full space. In general, however, ultrasonic nondestructive evaluation techniques have to cope with finite-sized parts that contain sources either in the interior or on the surface within an aperture S_A (Fig4.1). Usually, the rest of the surface S_M surrounding the given system of volume V_M is a measurement surface for ultrasonic signal, assuming vacuum in the exterior. The simplest as well as the most common scenario, in this case, is represented by a point-wise or finite-sized source placed at the boundary of an isotropic and homogeneous half space, generating an acoustic or an elastodynamic field.

A crucial remark has to be done at this point. On one hand, in fact, the solution of

acoustic and elastodynamic fields generated by force density or dilatation rate point sources located in full space do not present relevant differences from a theoretical point of view, the treatment of elastodynamic field being characterized just by a higher rank of the mathematical objects which have to be handled to describe the analyzed field (i.e. the Green scalar function vs. the Green tensors mentioned above). When the case of half-spaces is taken into account, instead, substantial differences arise, as it will be shown in the next sections.

4.1 The acoustic case

4.1.1 Rayleigh-Sommerfeld integral representation

The acoustic problem can be solved as an inhomogeneous boundary-value problem with the definition of half space scalar Green functions $G^{N,D}(\boldsymbol{r},\boldsymbol{r},\omega)$ satisfying the Helmholtz equation

$$\Delta' G^{D,N}(\boldsymbol{r},\boldsymbol{r}',\omega) + k^2 G^{D,N}(\boldsymbol{r},\boldsymbol{r}',\omega) = -\delta(\boldsymbol{r}-\boldsymbol{r}'), \qquad \boldsymbol{r},\boldsymbol{r}' \in V_M \tag{4.3}$$

and the Dirichlet boundary conditions

$$G^{D}(\boldsymbol{r},\boldsymbol{r}',\omega) = 0, \qquad \boldsymbol{r}' \in S_M \tag{4.4}$$

or the Neumann boundary conditions,

$$\nabla' G^{N}(\boldsymbol{r},\boldsymbol{r}',\omega)\cdot \boldsymbol{n}'_M = 0, \qquad \boldsymbol{r}' \in S_M \tag{4.5}$$

respectively. The half-space scalar Green functions $G^{N,D}(\boldsymbol{r},\boldsymbol{r},\omega)$ can be analytically derived for a planar boundary surface imaging the unit point source located at $\boldsymbol{r}$ at the boundary (method of images). The solution can thus be found as

$$P^{N,D}(\boldsymbol{r},\omega) = \iiint_{V_Q} j\omega h(\boldsymbol{r}',\omega) G^{D,N}(\boldsymbol{r},\boldsymbol{r}',\omega) d^3\boldsymbol{r}' \tag{4.6}$$

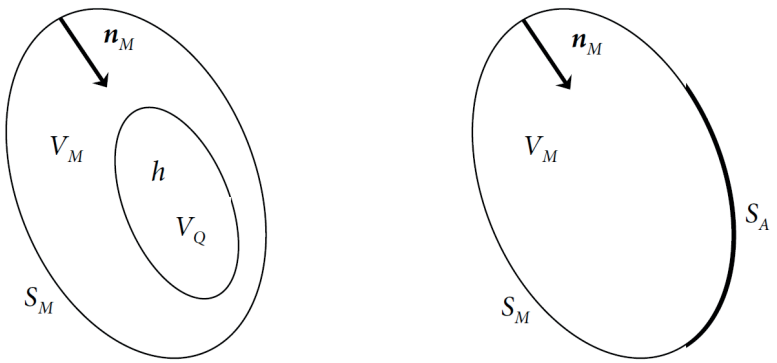

Figure 4.1: The propagation domain in presence of volume and surface sources.

where $P^{N,D}(\boldsymbol{r},\omega)$ is, obviously, the sum of the incident and the scattered pressure field. If the dilatation rate source is represented by a surface source

$$h(\boldsymbol{r}',\omega) = g(x',y',\omega)\delta(z') \tag{4.7}$$

we have

$$\begin{aligned} p^D(\boldsymbol{r},\omega) &= 0, \qquad \boldsymbol{r} \in V_M & (4.8)\\ p^N(\boldsymbol{r},\omega) &= 2\iint_{S_M} j\omega g(x',y',\omega)G(x-x',y-y',z,\omega)dx'dy', \boldsymbol{r} \in V_M & (4.9) \end{aligned}$$

in which we assumed that

$$\begin{aligned} \boldsymbol{r} &= x\boldsymbol{e}_x + y\boldsymbol{e}_y + z\boldsymbol{e}_z & (4.10)\\ \boldsymbol{r}' &= x'\boldsymbol{e}_x + y'\boldsymbol{e}_y + z'\boldsymbol{e}_z & (4.11) \end{aligned}$$

and where $G(x-x',y-y',z-z',\omega)$ is the already described full-space scalar Green function. In an analogous way we can find the solution to the case of a surface (normal) force density source as

$$\begin{aligned} p^N(\boldsymbol{r},\omega) &= 0, \qquad \boldsymbol{r} \in V_M; & (4.12)\\ p^D(\boldsymbol{r},\omega) &= 2\iint_{S_M} f_z(x',y',\omega)\boldsymbol{n}'_M \cdot \nabla G(x-x',y-y',z-z',\omega)|_{z'=0}dx'dy', \\ &\qquad\qquad \boldsymbol{r} \in V_M. & (4.13) \end{aligned}$$

The integral solution in equations (4.8), (4.9) and (4.12), (4.13) is called integral representation of the Rayleigh-Sommerfeld type.

The complementary elastodynamic problem cannot be solved resorting to this kind of approach: the half-space Green tensors satisfying the Dirichlet or the Neumann boundary conditions, in fact, are not known explicitly. A line or point force density in front of a stress-free surface (for instance) creates pressure and shear waves with different speeds whose respective mode conversion at the surface cannot be represented making use of images of the source as in the acoustic case.

For these reasons, an alternative approach has to be adopted to determine elastodynamic field in isotropic and homogeneous half-spaces. This method relies on a spectral plane (or cylindrical) wave spatial decomposition of the elastodynamic field. Being valid also for the acoustic counterpart, it will be firstly introduced for the simpler case of the scalar Green function in full space and then applied to the elastodynamic problem in the half space.

4.1.2 Weyl integral representation

We write the differential equation in (4.3) for the three-dimensional scalar Green function $G(\boldsymbol{r}-\boldsymbol{r}',\omega)$ in Cartesian coordinates:

$$\begin{aligned}&\frac{\partial^2}{\partial x^2}G(x-x',y-y',z-z',\omega)+\frac{\partial^2}{\partial y^2}G(x-x',y-y',z-z',\omega)+\\&+\frac{\partial^2}{\partial z^2}G(x-x',y-y',z-z',\omega)+\kappa G(x-x',y-y',z-z',\omega)=\\&=-\delta(x-x')\delta(y-y')\delta(z-z').\end{aligned}\tag{4.14}$$

We introduce a two-dimensional Fourier transform with respect to x and y:

$$\tilde{G}(k_x,k_y,z,\omega)=\int_{-\infty}^{+\infty}\int_{-\infty}^{+\infty}G(x,y,z,\omega)e^{-jk_xx-jk_yy}dxdy\tag{4.15}$$

where k_x, k_y denote the conjugate Fourier variables referring to x and y. Equations (4.14) thus turns into the ordinary differential equation

$$-k_x^2\tilde{G}(k_x,k_y,z-z',\omega)-k_y^2\tilde{G}(k_x,k_y,z-z',\omega)+\frac{\partial^2}{\partial z^2}\tilde{G}(k_x,k_y,z-z',\omega)=-\delta(z-z').\tag{4.16}$$

Imposing $k_z\doteq\kappa^2-k_x^2-k_y^2$ we have

$$\frac{\partial^2}{\partial z^2}\tilde{G}(k_x,k_y,z-z',\omega)+k_z^2\tilde{G}(k_x,k_y,z-z',\omega)=-\delta(z-z')\tag{4.17}$$

which defines he one-dimensional Green function $\tilde{G}(k_x,k_y,z-z',\omega)$ with respect to the coordinate z. Linearly independent solutions of this equation are represented by one-dimensional plane waves with wave number k_z propagating away from the source point z':

$$\tilde{G}(k_x,k_y,z-z',\omega)=\tilde{G}_o(k_x,k_y,\omega)e^{k_z|z-z'|}.\tag{4.18}$$

As for the three-dimensional case, the amplitude factor $\tilde{G}_o(k_x,k_y,\omega)$ must be evaluated inserting (4.18) into (4.17) which gives

$$\tilde{G}_o(k_x,k_y,\omega)=\frac{j}{2k_z}.\tag{4.19}$$

The three-dimensional scalar Green function with source point $x'=y'=z'=0$ results as Weyl's integral representation in terms of the inverse Fourier transform

$$\begin{aligned}G(x,y,z,\omega)&=\frac{e^{j\kappa\sqrt{x^2+y^2+z^2}}}{4\pi\sqrt{x^2+y^2+z^2}}\\&=\frac{1}{(2\pi)^2}\int_{-\infty}^{+\infty}\int_{-\infty}^{+\infty}\frac{j}{2k_z}e^{j|z|k_z}e^{jk_xx+jk_yy}dk_xdk_y.\end{aligned}\tag{4.20}$$

For $z>0$ we can write

$$G(x,y,z,\omega)=\frac{1}{(2\pi)^2}\int_{-\infty}^{+\infty}\int_{-\infty}^{+\infty}\frac{1}{k_z}e^{j\boldsymbol{k}\cdot\boldsymbol{r}}dk_xdk_y\tag{4.21}$$

where it is apparent that the three-dimensional Green function can be thought as composed of elementary plane waves; the above definition equally holds for $z < 0$. The definition of the two-dimensional Green function in terms of the Hankel function of zero order allows for an immediate spectral plane wave decomposition of the solution of the two-dimensional version of the analyzed problem:

$$\begin{aligned} G(x,z,\omega) &= \frac{j}{4} H_o^{(1)}\left(\kappa\sqrt{x^2+z^2}\right) \\ &= \frac{1}{2\pi}\frac{j}{2}\int_{-\infty}^{+\infty} \frac{e^{j|z|\sqrt{\kappa^2-k_x^2}}}{\sqrt{\kappa^2-k_x^2}} e^{jk_x x} dk_x \end{aligned} \tag{4.22}$$

4.1.3 Sommerfeld integral representation

The formal transition to polar coordinates

$$\begin{aligned} x &= r\cos\phi \\ y &= r\sin\phi \end{aligned} \tag{4.23}$$

in the xy-plane and polar coordinates

$$\begin{aligned} k_x &= k_r\cos\phi_k \\ y &= k_r\sin\phi_k \end{aligned} \tag{4.24}$$

in the $k_x k_y$-plane turns (4.20) into

$$G(x,y,z,\omega) = \frac{1}{(2\pi)^2}\frac{j}{2}\int_0^{+\infty}\int_0^{2\pi} \frac{e^{j|z|\sqrt{\kappa^2-k_r^2}}}{\sqrt{\kappa^2-k_r^2}} e^{jk_r r\cos(\phi-\phi_k)} k_r d\phi_k dk_r \tag{4.25}$$

The rotational symmetry with respect to ϕ and the integral representation of the Bessel function

$$J_0(\zeta) = \frac{1}{2\pi}\int_0^{2\pi} e^{\pm j\zeta\cos\alpha} d\alpha \tag{4.26}$$

reveal (4.25) to be the spectral decomposition of the three-dimensional Green function into cylindrical waves:

$$\begin{aligned} G(x,y,z,\omega) &= \frac{e^{j\kappa\sqrt{r^2+z^2}}}{4\pi\sqrt{r^2+z^2}} \\ &= \frac{j}{(4\pi)}\int_0^{2\pi} \frac{e^{j|z|\sqrt{\kappa^2-k_r^2}}}{\sqrt{\kappa^2-k_r^2}} k_r J_0(k_r r) dk_r \end{aligned} \tag{4.27}$$

where must have the positive sign for $k_r\kappa$. Equation (4.27) is known as the Sommerfeld integral decomposition of the Green function.

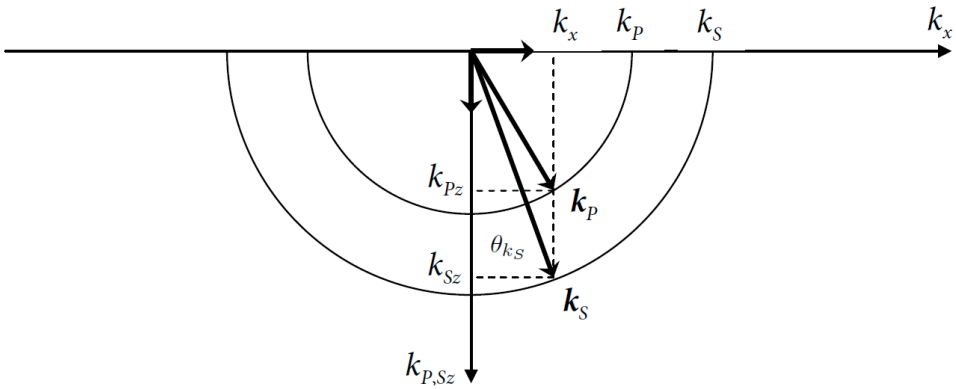

Figure 4.2: Propagating spectral components of plane P- and S-waves.

4.2 The elastodynamic case

4.2.1 Strip-like normal force density distribution

We consider a homogeneous isotropic half space V_M $(z > 0)$ with a stress-free boundary surface S_M (the xy-plane) characterized by the presence of a strip-like aperture, where a constant synchronous surface force density independent of y acts, yielding:

$$\boldsymbol{t}(x,\omega) = F(\omega)q_a(x)\boldsymbol{e}_z \tag{4.28}$$

The two-dimensional inhomogeneous elastodynamic boundary-value problem can be formulated in terms of the differential equation

$$\mu\Delta_{\boldsymbol{r}}\boldsymbol{u}(x,z,\omega) + (\lambda+\mu)\nabla_{\boldsymbol{r}}\nabla_{\boldsymbol{r}}\cdot\boldsymbol{u}(x,z,\omega) + \omega^2\rho\boldsymbol{u}(x,z,\omega) = 0 \tag{4.29}$$

for $z > 0$ under the condition

$$\boldsymbol{T}(x,z=0,\omega)\cdot\boldsymbol{e}_z = -\boldsymbol{t}(x,z), \quad \forall x \in S_M. \tag{4.30}$$

It can be demonstrated that the source in (4.28) radiates only pressure (P) and shear-vertical(SV) waves [32, 91], i.e., plane elastic waves propagating in the xy-plane with polarization direction orthogonal and tangent to the propagation direction, respectively (Fig.4.2). P and SV waves constitute the building blocks to represent the elastodynamic source field in a spatial spectrum of elastic plane waves:

$$\boldsymbol{u}_{PSV}(x,z,\omega) = \frac{1}{2\pi}\int_{-\infty}^{+\infty}\left[\tilde{u}_P(k_x,\omega)e^{j\boldsymbol{k}_P\cdot\boldsymbol{r}}\hat{\boldsymbol{k}}_P + \tilde{u}_{SV}(k_x,\omega)e^{j\boldsymbol{k}_S\cdot\boldsymbol{r}}\boldsymbol{e}_{\theta_{k_S}}\right]dk_x \tag{4.31}$$

where

$$\begin{aligned}\boldsymbol{k}_P &= k_P\hat{\boldsymbol{k}}_P \\ &= k_x\boldsymbol{e}_x + \sqrt{k_P^2 - k_x^2}\boldsymbol{e}_z = k_x\boldsymbol{e}_x + k_{P_z}\boldsymbol{e}_z\end{aligned} \tag{4.32}$$

$$\begin{aligned}\boldsymbol{k}_S &= k_S\hat{\boldsymbol{k}}_S \\ &= k_x\boldsymbol{e}_x + \sqrt{k_S^2 - k_x^2}\boldsymbol{e}_z = k_x\boldsymbol{e}_x + k_{S_z}\boldsymbol{e}_z \end{aligned} \tag{4.33}$$

As a result, the spectral P contribution is polarized in the direction $\tilde{\boldsymbol{k}}_P$ and the spectral SV-contribution in the direction $\boldsymbol{e}_{\theta_{k_S}}$, with $\boldsymbol{e}_{\theta_{k_S}} \cdot \boldsymbol{e}_{\theta_{k_S}} = 0$ and where

$$\boldsymbol{e}_{\theta_{k_S}} = \cos\theta_{k_S}\boldsymbol{e}_x - \sin\theta_{k_S}\boldsymbol{e}_z \tag{4.34}$$

The radiation field in (4.31) must fulfill the inhomogeneous boundary condition (4.30). Its Fourier transform reads

$$\mathfrak{F}_x\{\boldsymbol{T}(x, z=0, \omega)\} \cdot \boldsymbol{e}_z = -F(\omega)\frac{2\sin ak_x}{k_x}\boldsymbol{e}_z \tag{4.35}$$

The spectral decomposition of the stress tensor in terms of plane waves, using (4.31), can be written as

$$\begin{aligned}\boldsymbol{T}(x, z, \omega) =& \frac{1}{2\pi}\int_{-\infty}^{+\infty}\left[jk_P\tilde{u}_P(k_x, \omega)e^{j\boldsymbol{k}_P\cdot\boldsymbol{r}}(\lambda\boldsymbol{I} + 2\mu\hat{\boldsymbol{k}}_P\hat{\boldsymbol{k}}_P)\right] + \\ &+ \left[jk_s\mu\tilde{u}_{SV}(k_x, \omega)e^{j\boldsymbol{k}_S\cdot\boldsymbol{r}}(\hat{\boldsymbol{k}}_s\boldsymbol{e}_{\theta_{k_S}} + \boldsymbol{e}_{\theta_{k_S}}\hat{\boldsymbol{k}}_s)\right]dk_x\end{aligned} \tag{4.36}$$

so that the requirement for the boundary conditions becomes

$$\boldsymbol{T}(x, z=0, \omega)\cdot\boldsymbol{e}_z = -\frac{F(\omega)}{2\pi}\int_{-\infty}^{+\infty}\frac{2\sin ak_x}{k_x}e^{jk_xx}dk_x\boldsymbol{e}_z \tag{4.37}$$

and hence

$$\begin{aligned}&jk_P\tilde{u}_P(k_x, \omega)\left(\lambda\boldsymbol{I} + \frac{2\mu}{k_P^2}\boldsymbol{k}_P\boldsymbol{k}_P\right)\cdot\boldsymbol{e}_z + \\ &+ jk_S\mu\tilde{u}_{SV}(k_x, \omega)\left(\frac{\boldsymbol{k}_S}{k_S}\boldsymbol{e}_{\theta_{k_S}} + \boldsymbol{e}_{\theta_{k_S}}\frac{\boldsymbol{k}_S}{k_S}\right)\cdot\boldsymbol{e}_z = \\ &= -F(\omega)\frac{2\sin ak_x}{k_x}\boldsymbol{e}_z.\end{aligned} \tag{4.38}$$

This vector equation can be written in terms of its x- and z- components as

$$\frac{2}{k_P}k_xk_{Pz}\tilde{u}_P(k_x, \omega) + \left(k_x\boldsymbol{e}_{\theta_{k_S}}\cdot\boldsymbol{e}_z + \boldsymbol{e}_{\theta_{k_S}}\cdot\boldsymbol{e}_xk_{Sz}\right)\tilde{u}_{SV}(k_x, \omega) = 0 \tag{4.39}$$

$$\frac{1}{k_P}(k_S^2 - 2k_x^2)\tilde{u}_P(k_x, \omega) + 2k_{Sz}\boldsymbol{e}_{\theta_{k_S}}\cdot\boldsymbol{e}_z\tilde{u}_{SV}(k_x, \omega) = j\frac{F(\omega)}{\mu}\frac{2\sin ak_x}{k_x} \tag{4.40}$$

which constitutes an inhomogeneous system of equations for the two unknowns $\tilde{u}_P(k_x, \omega)$ and $\tilde{u}_{SV}(k_x, \omega)$. It results

$$\tilde{u}_P(k_x, \omega) = jk_P\frac{F(\omega)}{\mu}\frac{2\sin ak_x}{\mu}\frac{k_s\left(k_x\boldsymbol{e}_{\theta_{k_S}}\cdot\boldsymbol{e}_z + k_{Sz}\boldsymbol{e}_{\theta_{k_S}}\cdot\boldsymbol{e}_x\right)}{R(k_x)}, \tag{4.41}$$

$$\tilde{u}_{SV}(k_x, \omega) = -j\frac{F(\omega)}{\mu}\frac{2\sin ak_x}{\mu}\frac{2k_Sk_xk_{Pz}}{R(k_x)}. \tag{4.42}$$

If we consider

$$k_x = k_S \sin\theta_{k_S} \tag{4.43}$$

$$k_{Sz} = k_S \cos\theta_{k_S} \tag{4.44}$$

and (4.34), we have

$$\boldsymbol{e}_{\theta_{k_S}} \cdot \boldsymbol{e}_x = \frac{k_{Sz}}{k_S} \tag{4.45}$$

$$\boldsymbol{e}_{\theta_{k_S}} \cdot \boldsymbol{e}_z = -\frac{k_x}{k_S} \tag{4.46}$$

so that we can write

$$R(k_x) = (k_S^2 - 2k_x^2)^2 + 4k_x^2\sqrt{k_S^2 - k_x^2}\sqrt{k_P^2 - k_x^2} \tag{4.47}$$

which is the well-known Rayleigh function [32]. Noting that

$$\hat{\boldsymbol{k}}_P \cdot \boldsymbol{e}_x = \frac{k_x}{k_P} \tag{4.48}$$

$$\hat{\boldsymbol{k}}_P \cdot \boldsymbol{e}_z = \frac{k_{Pz}}{k_P} \tag{4.49}$$

we obtain explicit representation of the Cartesian components of the two-dimensional particle velocity field of a strip-like force density aperture with constant amplitude located on the elsewhere stress-free surface of an elastic half space in terms of a spectral plane wave decomposition [32, 92, 93]:

$$\begin{aligned}\tilde{u}^{f_z}_{PSV_x}(x,z,\omega) = j\frac{F(\omega)}{2\pi\mu}\int_{-\infty}^{+\infty}\frac{2\sin ak_x}{k_x}\frac{k_x}{R(k_x)}\times \\ \times\left[(k_S^2 - 2k_x^2)e^{j\boldsymbol{k}_P\cdot\boldsymbol{r}} - 2\sqrt{k_S^2 - k_x^2}\sqrt{k_P^2 - k_x^2}e^{j\boldsymbol{k}_S\cdot\boldsymbol{r}}\right]dk_x,\end{aligned} \tag{4.50}$$

$$\begin{aligned}\tilde{u}^{f_z}_{PSV_z}(x,z,\omega) = j\frac{F(\omega)}{2\pi\mu}\int_{-\infty}^{+\infty}\frac{2\sin ak_x}{k_x}\frac{\sqrt{k_P^2 - k_x^2}}{R(k_x)}\times \\ \times\left[(k_S^2 - 2k_x^2)e^{j\boldsymbol{k}_P\cdot\boldsymbol{r}} + 2k_x^2 e^{j\boldsymbol{k}_S\cdot\boldsymbol{r}}\right]dk_x.\end{aligned} \tag{4.51}$$

For $k_x > k_P$, respectively $k_x > k_S$, the two vectors $\boldsymbol{k}_P$, respectively $\boldsymbol{k}_S$, become complex vectors (and, hence, also $\boldsymbol{e}_{\theta_{k_S}}$); the sign choice

$$\Im\boldsymbol{k}P, S = \sqrt{k_{P,S}^2 - k_x^2}\boldsymbol{e}_z \tag{4.52}$$

ensures the convergence of the integrals in (4.50) and (4.51), for $z > 0$.

4.2.2 Strip-like tangential force density distribution

For the tangential force density source

$$\boldsymbol{t}(x,\omega) = F(\omega)q_a(x)\boldsymbol{e}_x \tag{4.53}$$

the radiation field is obtained after a brief calculation:

$$\begin{aligned}\tilde{u}^{f_x}_{PSV_x}(x,z,\omega) = j\frac{F(\omega)}{2\pi\mu}\int_{-\infty}^{+\infty}\frac{2\sin ak_x}{k_x}\frac{\sqrt{k_S^2-k_x^2}}{R(k_x)}\times \\ \times\left[2k_x^2 e^{j\boldsymbol{k}_P\cdot\boldsymbol{r}} + (k_S^2-2k_x^2)e^{j\boldsymbol{k}_S\cdot\boldsymbol{r}}\right]dk_x,\end{aligned} \tag{4.54}$$

$$\begin{aligned}\tilde{u}^{f_x}_{PSV_z}(x,z,\omega) = j\frac{F(\omega)}{2\pi\mu}\int_{-\infty}^{+\infty}\frac{2\sin ak_x}{k_x}\frac{k_x}{R(k_x)}\times \\ \times\left[2\sqrt{k_S^2-k_x^2}\sqrt{k_P^2-k_x^2}e^{j\boldsymbol{k}_P\cdot\boldsymbol{r}} - (k_S^2-2k_x^2)e^{j\boldsymbol{k}_S\cdot\boldsymbol{r}}\right]dk_x.\end{aligned} \tag{4.55}$$

4.2.3 Spectral plane wave decomposition of the second-rank Green tensor in half-space

Once we have obtained the radiation fields for a strip-like aperture with a normal (tangential) force density source, we can proceed with the definition of the components of the second-rank Green tensor $\boldsymbol{G}^{HS}_{PSV}(\boldsymbol{r},\omega)$ according to the equation

$$\boldsymbol{u}^{LS_t}_{PSV}(\boldsymbol{r},\omega) = \boldsymbol{G}^{HS}_{PSV}(\boldsymbol{r},\omega)\cdot\hat{\boldsymbol{t}} \tag{4.56}$$

where we switched from the strip-like to the line source and we assumed $F(\omega)=1$ in (4.28)

$$\boldsymbol{t}(x,\omega) = \delta(x)\hat{\boldsymbol{t}} \tag{4.57}$$

$$\mathfrak{F}\{\boldsymbol{t}(x,\omega)\} = \hat{\boldsymbol{t}} \tag{4.58}$$

If the case $\hat{\boldsymbol{t}} = \boldsymbol{e}_x$ is considered, the following Cartesian components of $\boldsymbol{G}^{HS}_{PSV}(\boldsymbol{r},\omega)$ can be derived from (4.56):

$$\begin{aligned}\boldsymbol{G}^{HS}_{PSV}(\boldsymbol{r},\omega):\boldsymbol{e}_x\boldsymbol{e}_x &\doteq \boldsymbol{u}^{LS_{t_x}}_{PSV}(\boldsymbol{r},\omega)\cdot\boldsymbol{e}_x \\ &= u^{LS_{t_x}}_{PSV_x}(\boldsymbol{r},\omega),\end{aligned} \tag{4.59}$$

$$\begin{aligned}\boldsymbol{G}^{HS}_{PSV}(\boldsymbol{r},\omega):\boldsymbol{e}_x\boldsymbol{e}_z &\doteq \boldsymbol{u}^{LS_{t_x}}_{PSV}(\boldsymbol{r},\omega)\cdot\boldsymbol{e}_z \\ &= u^{LS_{t_x}}_{PSV_z}(\boldsymbol{r},\omega).\end{aligned} \tag{4.60}$$

In a similar way, for $\hat{\boldsymbol{t}} = \boldsymbol{e}_z$ the following holds:

$$\begin{aligned}\boldsymbol{G}^{HS}_{PSV}(\boldsymbol{r},\omega):\boldsymbol{e}_z\boldsymbol{e}_x &\doteq \boldsymbol{u}^{LS_{t_z}}_{PSV}(\boldsymbol{r},\omega)\cdot\boldsymbol{e}_x \\ &= u^{LS_{t_z}}_{PSV_x}(\boldsymbol{r},\omega),\end{aligned} \tag{4.61}$$

$$\begin{aligned}\boldsymbol{G}^{HS}_{PSV}(\boldsymbol{r},\omega):\boldsymbol{e}_z\boldsymbol{e}_z &\doteq \boldsymbol{u}^{LS_{t_z}}_{PSV}(\boldsymbol{r},\omega)\cdot\boldsymbol{e}_z \\ &= u^{LS_{t_z}}_{PSV_z}(\boldsymbol{r},\omega).\end{aligned} \tag{4.62}$$

Using the results obtained in (4.50), (4.51), (4.54), (4.55)yields

$$\boldsymbol{G}^{HS}_{PSV}(\boldsymbol{r},\omega):\boldsymbol{e}_x\boldsymbol{e}_x = \frac{j}{2\pi\mu}\int_{-\infty}^{+\infty}\frac{\sqrt{k_S^2-k_x^2}}{R(k_x)}\times \\ \times\left[2k_x^2 e^{j\boldsymbol{k}_P\cdot\boldsymbol{r}} + (k_S^2-2k_x^2)e^{j\boldsymbol{k}_S\cdot\boldsymbol{r}}\right]dk_x, \tag{4.63}$$

$$\boldsymbol{G}^{HS}_{PSV}(\boldsymbol{r},\omega):\boldsymbol{e}_x\boldsymbol{e}_z = \frac{j}{2\pi\mu}\int_{-\infty}^{+\infty}\frac{k_x}{R(k_x)}\times \\ \times\left[2\sqrt{k_S^2-k_x^2}\sqrt{k_P^2-k_x^2}e^{j\boldsymbol{k}_P\cdot\boldsymbol{r}} - (k_S^2-2k_x^2)e^{j\boldsymbol{k}_S\cdot\boldsymbol{r}}\right]dk_x, \tag{4.64}$$

$$\boldsymbol{G}^{HS}_{PSV}(\boldsymbol{r},\omega):\boldsymbol{e}_z\boldsymbol{e}_x = \frac{j}{2\pi\mu}\int_{-\infty}^{+\infty}\frac{k_x}{R(k_x)}\times \\ \times\left[(k_S^2-2k_x^2)e^{j\boldsymbol{k}_P\cdot\boldsymbol{r}} - 2\sqrt{k_S^2-k_x^2}\sqrt{k_P^2-k_x^2}e^{j\boldsymbol{k}_S\cdot\boldsymbol{r}}\right]dk_x, \tag{4.65}$$

$$\boldsymbol{G}^{HS}_{PSV}(\boldsymbol{r},\omega):\boldsymbol{e}_z\boldsymbol{e}_z = \frac{j}{2\pi\mu}\int_{-\infty}^{+\infty}\frac{\sqrt{k_P^2-k_x^2}}{R(k_x)}\times \\ \times\left[(k_S^2-2k_x^2)e^{j\boldsymbol{k}_P\cdot\boldsymbol{r}} + 2k_x^2 e^{j\boldsymbol{k}_S\cdot\boldsymbol{r}}\right]dk_x. \tag{4.66}$$

4.2.4 Rayleigh-Sommerfeld integral representation of elastodynamic source fields in half-spaces

The derivation of the half-space Green tensor $\boldsymbol{G}^{HS}_{PSV}(\boldsymbol{r},\omega)$ by its components shown in the previous section constitutes the starting point to obtain an integral representation of the Rayleigh-Sommerfeld type of the source field generated by a finite-sized aperture in half-spaces also for the elastodynamic case. We consider, for instance, the normal force surface source

$$\boldsymbol{t}(x,y,t) = A(x,y,t)\Gamma_A(x,y)\boldsymbol{e}_z \tag{4.67}$$

where $A(x,y,\omega) = F(\omega)q_a(x)$: the restriction to S_A is ensured be the characteristic function $\Gamma_A(x,y)$ of S_A. We can define a half-space second-rank Green tensor $\boldsymbol{G}^N(x,y,z,x',y',z',t)$ and a half-space third-rank Green tensor $\Sigma^N(x,y,z,x',y',z',t)$ such that

$$\left[\left(\mu\Delta'+\rho\omega^2\right)\boldsymbol{I} + (\lambda+\mu)\nabla'\nabla'\right]\cdot\boldsymbol{G}^N(x,y,z,x',y',z',t) = -\delta(x-x')\delta(y-y')\delta(z-z')\boldsymbol{I} \tag{4.68}$$

$$\Sigma^N(x,y,z,x',y',z',t) = \boldsymbol{c}:\nabla'\boldsymbol{G}^N(x,y,z,x',y',z',t) \tag{4.69}$$

and

$$\boldsymbol{e}_z\cdot\Sigma^N(x,y,z,x',y',z',t) = 0, \qquad \text{for} \quad x',y'\in S_M \tag{4.70}$$

where $\boldsymbol{c}$ is the stiffness tensor. Using the results in (4.63), (4.64),(4.65) and (4.66) we can obtain $\boldsymbol{G}^N$ as

$$\boldsymbol{G}^{HS}_{PSV}(x,y,\omega)\cdot\boldsymbol{e}_z = \frac{1}{2\pi}\int_{-\infty}^{+\infty}\boldsymbol{G}^N(k_x,k_y,z,z',\omega)\cdot\boldsymbol{e}_z e^{jk_x x}dk_x \tag{4.71}$$

with $k_y = 0$ and $z' = 0$. This allows to write the equation

$$\boldsymbol{v}(x,y,z,\omega) = -j\omega\iint_{S_A}A(x',y',\omega)\boldsymbol{e}_z\cdot\boldsymbol{G}^N(x-x',y-y',z'=0,z,\omega)dx'dy' \tag{4.72}$$

which constitutes the elastodynamic version of the Rayleigh-Sommerfeld integral representation of the solution.

4.3 Radiation field of a PZT-like force density source in homogenous isotropic half spaces

The ultimate goal of the theoretical study which has been carried out in the previous pages lays in the reconstruction of the sound field generated by a piezoelectric transducer in the underlying structure. To this end, the derivation of the radiation fields for a strip-like force density source in half spaces performed in the previous sections constitutes a stepping stone: the two-dimensional strip-like aperture can be seen, in fact, as the simplest model of a circular surface-mounted PZT transducer. The rotational symmetry of the source with regard to ϕ in the polar representation $\boldsymbol{r}' = r'\cos\phi'\boldsymbol{e}_x + r'\sin\phi\boldsymbol{e}_y + z'\boldsymbol{e}_z$ leads to the rotational symmetry of the radiation characteristics: therefore, we can assume $\phi' = 0$ so that $x' = r'$, limiting the analysis of the elastodynamic field to the xz-plane as in Sections 4.2.1 and 4.2.2.

4.3.1 Far-field radiation characteristics of normal and tangential line force density sources

We apply the method of stationary phase [84] to the formulas in (4.50), (4.50) and (4.54), (4.55) to obtain the far-field generated by normal and tangential force-density sources in homogeneous-isotropic half spaces. In so doing, we choose

$$u_r = \sin\theta u_x + \cos\theta u_z \tag{4.73}$$

$$u_\theta = \cos\theta u_x - \sin\theta u_z \tag{4.74}$$

and finally obtain [92]

$$\begin{aligned} u_P^{LS_{t_z},far}(r,\theta,\omega) &= \frac{e^{jk_P r}}{\sqrt{r}}H_P^{LS_{t_z}}(\theta,\omega) \\ H_P^{LS_{t_z}}(\theta,\omega) &= \frac{e^{j\frac{\pi}{4}}\cos\theta}{2\gamma^2\mu\sqrt{2\pi k_P}}M_P^{t_z}(\theta) \\ M_P^{t_z}(\theta) &= \frac{2\gamma^2(\gamma^2-2\sin^2\theta)}{(\gamma^2-2\sin^2\theta)^2+2\sin\sin 2\theta\sqrt{\gamma^2-\sin^2\theta}} \end{aligned} \tag{4.75}$$

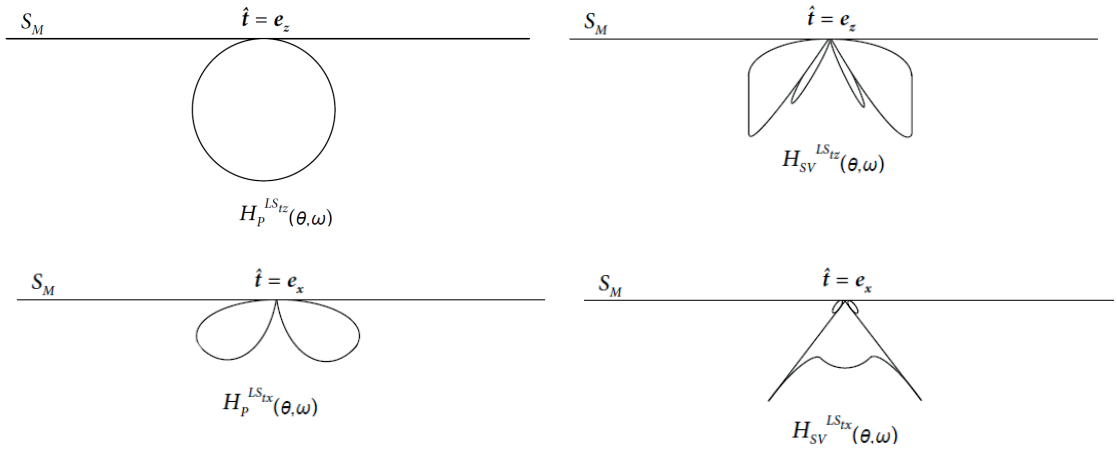

Figure 4.3: P and SV waves patterns for the particle displacement a normal or tangential (first and second raw, respectively) line force density source on the surface on an elastic half space.

$$\begin{aligned} u_{SV}^{LS_{t_z},far}(r,\theta,\omega) &= \frac{e^{jk_S r}}{\sqrt{r}} H_{SV}^{LS_{t_z}}(\theta,\omega) \\ H_{SV}^{LS_{t_z}}(\theta,\omega) &= \frac{e^{-j\frac{3\pi}{4}}\sin\theta}{2\mu\sqrt{2\pi k_S}} M_S^{t_z}(\theta) \\ M_S^{t_z}(\theta) &= \frac{4\cos\theta\sqrt{1-\gamma^2\sin^2\theta}}{\gamma(1-2\sin^2\theta)^2 + 2\sin\sin 2\theta\sqrt{1-\gamma^2\sin^2\theta}} \end{aligned} \tag{4.76}$$

$$\begin{aligned} u_{P}^{LS_{t_x},far}(r,\theta,\omega) &= \frac{e^{jk_P r}}{\sqrt{r}} H_{P}^{LS_{t_x}}(\theta,\omega) \\ H_{P}^{LS_{t_x}}(\theta,\omega) &= \frac{e^{j\frac{\pi}{4}}\sin\theta}{2\mu\sqrt{2\pi k_P}} M_P^{t_x}(\theta) \\ M_P^{t_x}(\theta) &= \frac{4\cos\theta\sqrt{\gamma^2-\sin^2\theta}}{(\gamma^2-2\sin^2\theta)^2 + 2\sin\sin 2\theta\sqrt{\gamma^2-\sin^2\theta}} \end{aligned} \tag{4.77}$$

$$\begin{aligned} u_{SV}^{LS_{t_x},far}(r,\theta,\omega) &= \frac{e^{jk_S r}}{\sqrt{r}} H_{SV}^{LS_{t_x}}(\theta,\omega) \\ H_{SV}^{LS_{t_x}}(\theta,\omega) &= \frac{e^{j\frac{\pi}{4}}\cos\theta}{\gamma\mu\sqrt{2\pi k_S}} M_S^{t_x}(\theta) \\ M_S^{t_x}(\theta) &= \frac{\gamma^2(1-\sin^2\theta)}{\gamma(1-2\sin^2\theta)^2 + 2\sin\sin 2\theta\sqrt{1-\gamma^2\sin^2\theta}} \end{aligned} \tag{4.78}$$

where $\gamma = \frac{k_S}{k_P}$ and $M_{P,S}^{t_{z,x}}$ are the Miller-Pursey factors [92]. The far-field radiation characteristics $H_{P,S}^{t_{x,z}}$ in (4.75)-(4.78) are shown in Fig. 4.3 [84]. Note that while the radiation pattern of P waves has a maximum for $\theta = 0$ (at least for $\hat{\boldsymbol{t}} = \boldsymbol{e}_z$), $H_{SV}^{t_{x,z}}$ have their maximum at approximately an angle value of $\theta \simeq 45^o$, while they assume a much lower value in the direction normal to the surface. This has a large influence on the features of the elastodynamic

field that radiates from a piezoelectric transducers. One final remark: being $H_{P,S}^{t_{x,z}}$ far-field representations of the elastodynamic field features, they do not account for near-field effects, as mode conversion phenomena, that occur at the boundary. These effects, nonetheless, play an important role in the definition of the radiation field, as it will bee seen in the following.

4.3.2 Description of the elastodynamic field generated by a PZT transducer in a homogeneous isotropic half space

A two-dimensional numerical representation of the elastodynamic field generated by a normal force density aperture with $Tn(t)$ time-dependence in a homogeneous isotropic half space characterized by a stress-free surface is shown in Fig. 4.4 [84]: the EFIT (Elastodynamic Finite Integration Technique) was used to reproduce the radiation field in terms of particle velocity magnitude [94]. As already stated, this source model can be considered as the simplest model of a piezoelectric transducer acting on a structure.

Semi-circular pressure as well as shear wavefronts can be recognized in the figure. As anticipated in the previous section, while pressure waves superimpose to form a planar common wavefront underneath the normal force aperture, shear waves do not give rise to such a structure, due to the zero of their radiation characteristics in the normal direction (Fig. 4.3): only the shear pulses from the aperture edges prevail. In addition to the described wave structures, two more phenomena can be observed in the figure: the shear and pressure plane waves which rise where the semi-circular pressure and shear waves meet the boundary, respectively. The pressure and shear waves cannot fulfill, in fact, the stress-free condition at the surface, originating new plane pressure and shear waves with appropriate incidence angles, in accordance with the phenomenon of mode conversion [82, 32, 91]. The reflection-

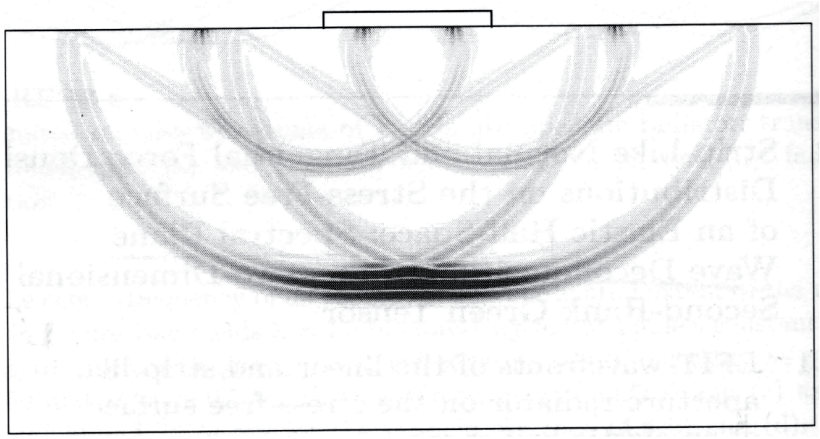

Figure 4.4: EIFT-wavefronts of the line source and the strip-like aperture radiator on the stress-free surface on an elastic half space (the magnitude of the particle velocity is shown)[94].

refraction laws for plane pressure waves at a stress-free boundary read:

$$\sin\theta_{r_P} = \sin\theta_{i_P} \tag{4.79}$$

$$k_S \sin\theta_{c_S} = k_P \sin\theta_{i_P} \tag{4.80}$$

where $\theta_{i,r,c_{P,S}}$ denote the incident, reflected and mode-converted pressure and shear waves, respectively. This means that for a pressure wave with an incidence angle of 90^o, reflection and incident direction coalesce; moreover, a shear plane wave with mode conversion angle of about 40^o (depending on the acoustic impedance of the analyzed material) is generated. These waves are visible in Fig. 4.4 and are usually known as "head waves". The reflection-refraction laws for plane shear waves at a stress-free boundary read:

$$\sin\theta_{r_S} = \sin\theta_{i_S} \tag{4.81}$$

$$k_P \sin\theta_{c_P} = k_S \sin\theta_{i_S}. \tag{4.82}$$

At a first observation, a behavior similar to the one described for the reflection of pressure waves holds also for shear waves: in fact this is not entirely true. The incident shear wave give rise to a pressure wave to fulfill the stress-free condition at the boundary, in a way that constitutes the dual boundary problem of the one previously seen for pressure waves. A closer observation of Equation (4.82) reveals, however, that θ_{c_P} needs to be complex to have the said equation satisfied, being $\theta_{i_S} = 90^o$ and $k_S > k_P$. The plane primary wave that is generated by the reflection of the semicircular shear wavefront at the boundary is thus an inhomogeneous wave with negative imaginary part that attenuates itself as it propagates: in fact, it almost instantaneously disappears after being generated at the boundary, as it is shown in Fig 4.4.

The generation and propagation of pressure and shear waves does not complete the description of the elastodynamic field radiated by a PZT-like aperture: the presence of the force-density source located on a stress-free surface allows the generation and propagation of Rayleigh-surface waves. These waves can be thought of as the result of a superimposition of partial inhomogeneous longitudinally and transversely-polarized pressure and shear waves, with a characteristic elliptical resultant polarization in the xz-plane. More details on Rayleigh waves can be found in Appendix B.

Chapter 5

The Damage Detection Procedure

In the previous chapters the generation and propagation of waves in homogeneous and isotropic half spaces has been discussed. Particular attention has been dedicated to presenting the theoretical aspects which characterize the solution of the elastodynamic problem in this type of domain, underlying differences and similarities with the case of the wave propagation in full space. A plane wave spectral decomposition of the radiation field generated by force density sources has been performed to obtain the second-rank Green tensor for half spaces. Finally, the radiation patterns for the case of strip-like normal force density aperture have been introduced, allowing to elaborate a detailed description of the elastodynamic field generated by a piezoelectric transducer acting on a structure.

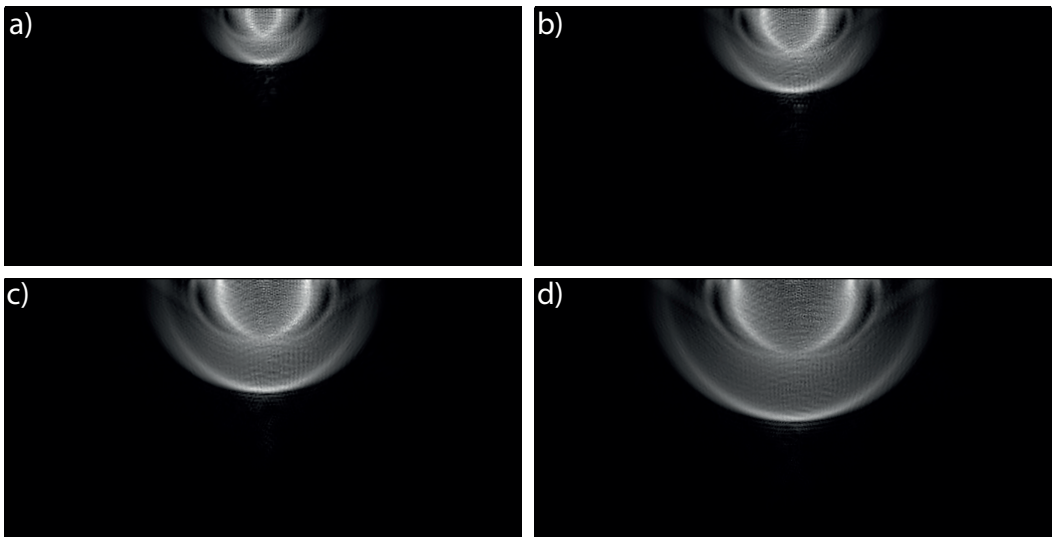

Figure 5.1: Numerical simulation of the elastodynamic field generated by a strip-like normal force density distribution in an aluminum half space domain. Here the amplitude of the velocity vector is shown.

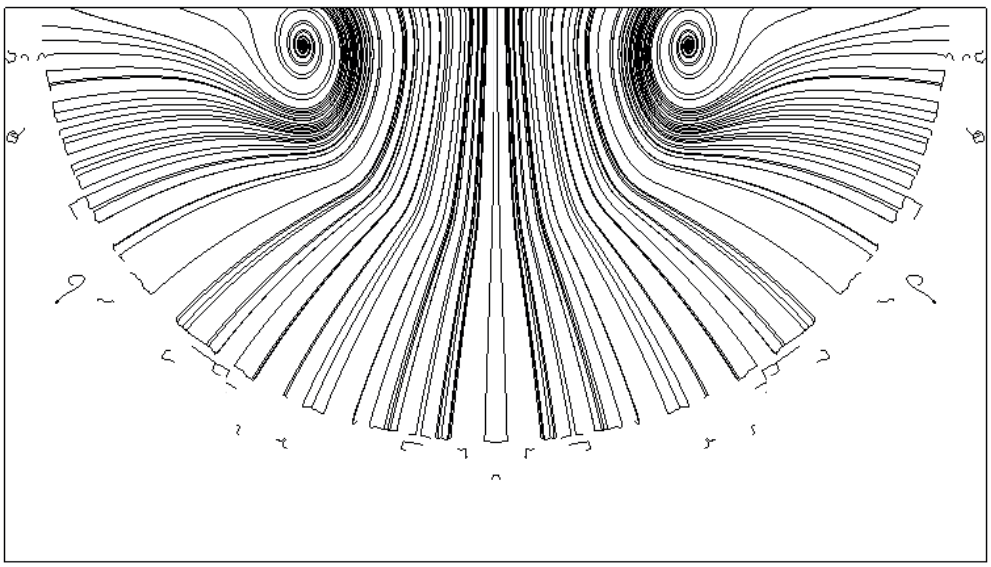

Figure 5.2: Lines tangent to the displacement vector in the elastodynamic field generated by a strip-like normal force density source in an aluminum half space: the typical elliptical polarization of the displacement field generated by Rayleigh waves is observable.

The results numerical estimation of the particle velocity of the mentioned radiation field for the case of aluminum has been obtained using COMSOL Multiphysics® are shown in Fig. 5.1: pressure and shear semicircular wavefronts as well as the mode-converted waves are clearly observable. Rayleigh waves, instead, are more difficult to notice as they are confined to the region of the domain close to the surface and they posses a propagation velocity which is similar to that which characterizes shear waves, implying a superimposition effect which makes them hardly identifiable. A clearer representation of Rayleigh waves is possible if the streamlines (i.e. lines everywhere tangent to the displacement vector) are analyzed as in Fig. 5.2: the typical elliptical polarization of the displacement field which characterizes these waves [95] is evident.

The analysis of the physical phenomena that are involved in the generation of the elastodynamic field radiating from a PZT-like force source constitutes the basis of the ultrasonic nondestructive evaluation of composite structures that is poposed in this work. An exhaustive description of the physics of the problem at hand is always a mandatory requirement in every engineering application: this is particularly true in the field of damage identification, where the possibility to adopt more reliable and efficient detection mechanisms is critical in the process of designing innovative SHM systems.

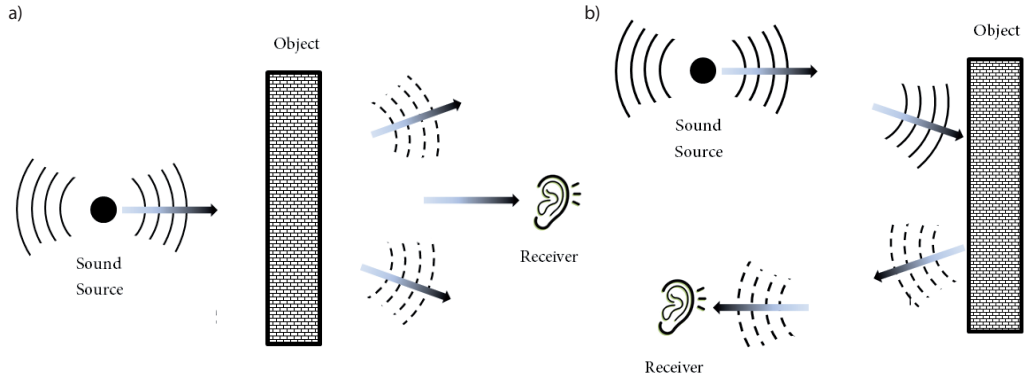

Figure 5.3: Schematic showing the principles governing the two main configurations of the actuating/sensing architecture: the pitch-catch (a) and the pulse-echo (b) approach.

5.1 Time-of-flight (ToF) as damage index

As anticipated in the Introduction, the most dangerous as well as the most subtle damage scenario that can apply to composite structures is without doubt represented by a delamination propagating into the system [98]. The reason of this consideration can be easily explained: a delamination can critically affect the stiffness and the rigidity of a composite structure and, at the same time, it can be virtually invisible to many damage detection procedures, first of all to a visual inspection of the structure. Together with other issues, this can be considered as one of the main problems affecting the use of composite materials that still prevents the use of this class of materials in many engineering applications [98].

The structural health monitoring methodology here proposed aims at detecting the presence of a delamination in a plate-like composite structure exploiting the radiation field generated by a piezoelectric transducer mounted on the surface of the structure adopting a "pulse-echo" configuration. This architecture of the damage detection procedure constitutes, together with the "pitch-catch" option, one of the basic configurations that are usually used in elastic-wave-based damage identification, in a manner similar to the human procedure of locating an object in terms of acoustic waves [99] (Fig.5.3).

In a pitch-catch configuration, elastic waves activated by a source travel across an object and are then captured by a sensor at the other end of the wave path. In the pulse-echo configuration, instead, both source and sensor are located at the same side of the object, and the sensor receives the echoed wave signals from the object. In the problem at hand, in particular, both the actuator and the sensor are thought to be mounted on the same surface of the plate.

The choice of the pulse-echo configuration as fundamental architecture of the proposed ultrasonic nondestructive evaluation technique ensues from to different considerations. On

one hand, in fact, this particular configuration offers the advantage of requiring only one point of access to the structure, i.e., the actuator and the sensor are both placed on the same side of the system with respect to the damage, implying that access has to be granted only to one side of the structure (here, the upper surface of the plate). This aspect becomes crucial if, as in the present case, the considered SHM routine is envisioned to imply the realization of a transducers network.

Another main reason for the choice of adopting the pulse-echo configuration is related to the nature of the detection mechanism here proposed: the key element of the designed approach consists, in fact, in the estimation of the time-of-flight (ToF) of the primary and secondary wavefronts in their back and forth propagation through the thickness of the structure (Fig. 5.4). This detection methodology implies a capability to acquire an information that returns from the damage that only a pulse-echo configuration of the actuating/sensing system can ensure.

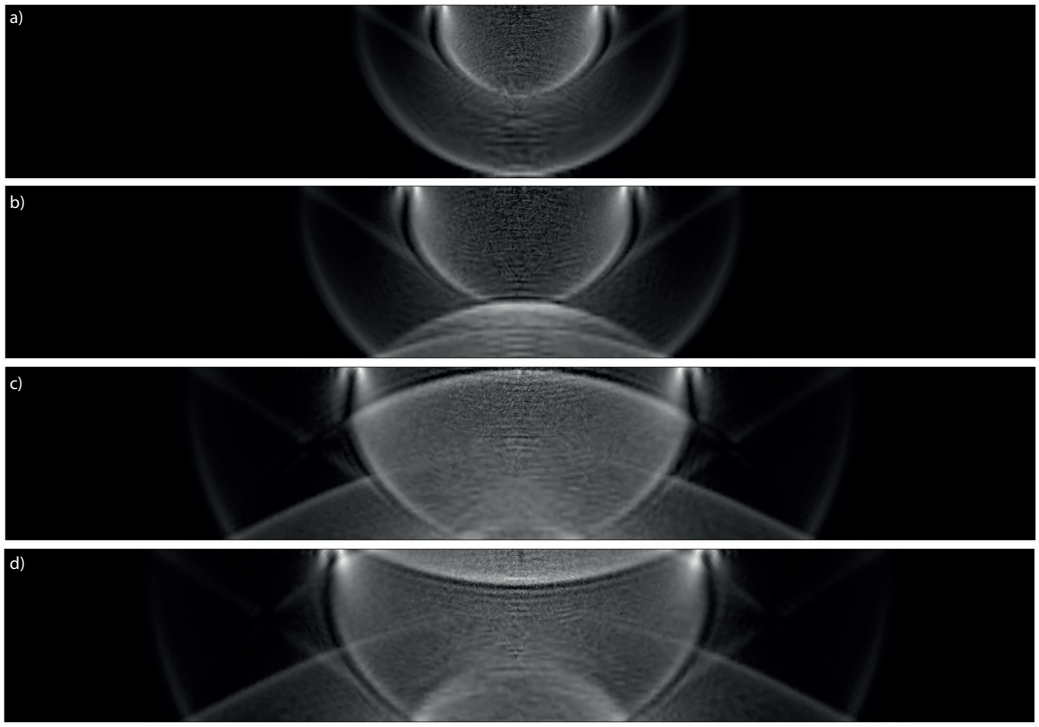

Figure 5.4: Numerical simulation showing the different phases of the variation of the elastodynamic field generated by a strip-like normal force density distribution in an aluminum layer in which the amplitude of the velocity vector is shown. P and S waves are clearly noticeable, as well as head and inhomogeneous waves resulting from the fulfillment of the stress free condition at the boundaries.

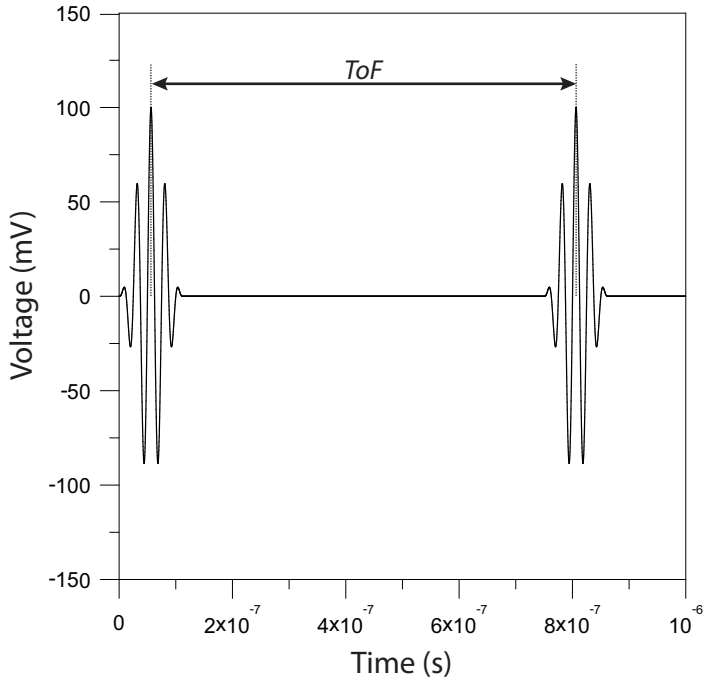

Figure 5.5: Time-of-flight (ToF) is usually referred to as the time lag between the acquisition of the incident wave and the acquisition of the wave scattered by the damage.

5.1.1 ToF in traditional waves-based SHM

The estimation of the ToF represents one of the most popular approaches in the time domain signal processing regarding usual Lamb waves-based ultrasonic evaluation techniques [47]. In general ToFs can be defined as the time lag between the incident wave that the sensor first captures and the wave scattered by damage that the same sensor subsequently captures. It suggests the relative positions of actuator, sensor and damage. From the estimation of the ToFs between the damage-scattered and incident waves extracted from a certain number of signals, damage can accordingly be triangulated [48, 49, 50, 100]. In a one-dimensional case (e.g., a structural beam or rod), the actuator, sensor and damage are in a straight line the sensor captures the incident wave from the actuator first and then the wave scattered back from the damage. The damage can thus be located with regard to the position of the sensor in terms of the difference in the times of arrival of the damage-scattered and incident waves, Δt,

$$d = \frac{c_g \Delta t}{2} \tag{5.1}$$

where d is the distance between the damage and the sensor; c_g is the group velocity of the diagnostic Lamb wave [32]. Expanding the above discussion to a two-dimensional plate with

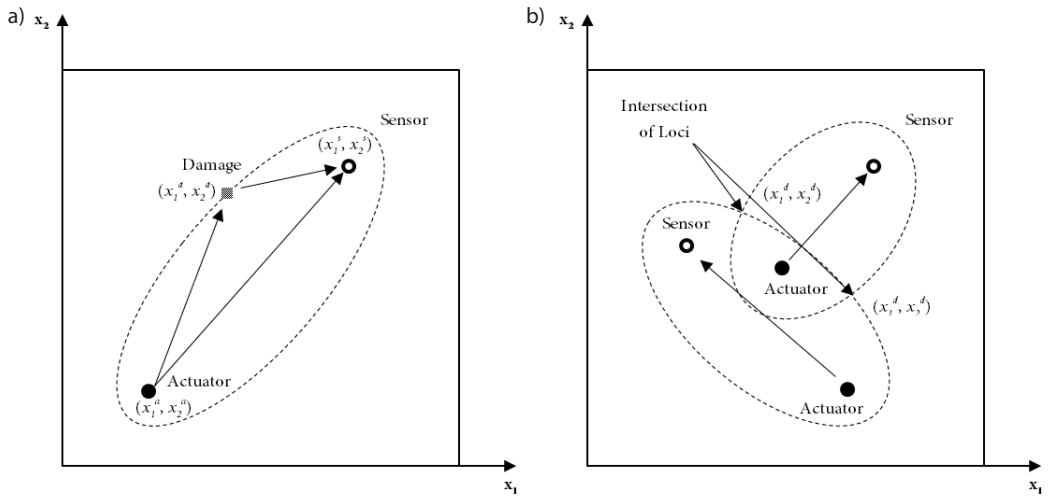

Figure 5.6: Different ToF-based architectures of the actuating/sensing system.

an actuator-sensor pair (a sensing path, see Fig. 5.6). Equation (5.1) is then extended to

$$t^{ads} - t^{as} = \left(\frac{d^{ad}}{c_{g_1}} + \frac{d^{ds}}{c_{g_2}}\right) - \frac{d^{as}}{c_{g_1}} = \text{ToF} \tag{5.2}$$

where

$$\begin{aligned} d^{ad} &= \sqrt{(x_1^d - x_1^a)^2 + (x_2^d - x_2^a)^2} \\ d^{ds} &= \sqrt{(x_1^d - x_1^s)^2 + (x_2^d - x_2^s)^2} \\ d^{as} &= \sqrt{(x_1^s - x_1^a)^2 + (x_2^s - x_2^a)^2} \end{aligned} \tag{5.3}$$

In the above equation, t^{ads} is the time the incident wave needs to propagate from the actuator to the damage and then to the sensor, and t^{as} is the time the incident wave consumes propagating directly from the actuator to the sensor. ToF is thus the difference between the above two quantities, which can be extracted from the captured Lamb wave signal. d^{ad} is the distance between the actuator located at (x_1^a, x_2^a) and the damage centre, assumed at (x_1^d, x_2^d) and to be determined; d^{ds} is the distance between the damage centre and the sensor located at (x_1^s, x_2^s); d^{as} is the distance between the actuator and sensor (see Fig. 5.6(a) for the coordinate system). c_{g_1} and c_{g_2} are the group velocities of the incident Lamb wave activated by the actuator and the wave scattered by the damage (c_{g_1} and c_{g_1} need not be the same, provided that mode conversion occurs upon interaction of the incident wave with the damage).

From a mathematical point of view, the solutions to Equation (5.2) give rise to a locus, a dotted line in Fig. 5.6(a), indicating possible locations of the centre of the damage. With ToF extracted from another actuator-sensor pair (sensing path), an equation similar

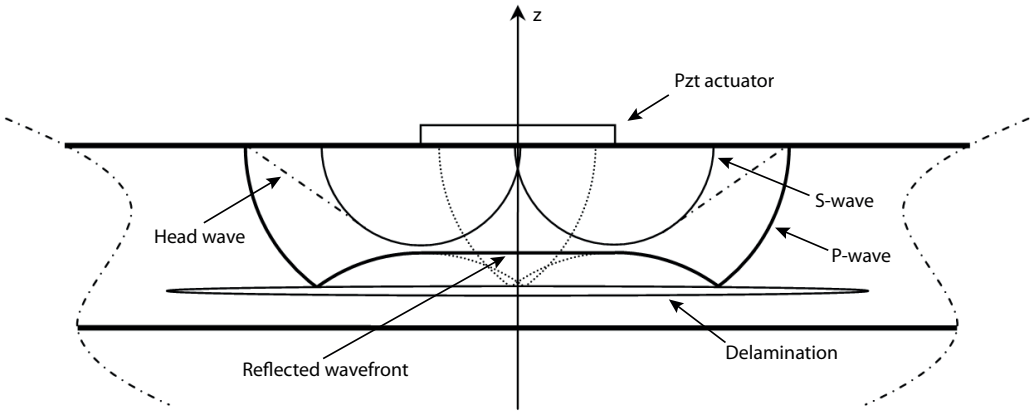

Figure 5.7: Schematic of the damage detection mechanism.

to Eq. (5.2) can be obtained, and a nonlinear equation group, containing two equations contributed by two actuator-sensor pairs and involving the position of the damage centre (x_1^d, x_2^d) (two unknown variables), is available. Two loci established by the two equations lead to intersection(s), i.e., the solution(s) to the equation group, sketched in Fig. 5.6(b), which is the location of the damage centre (x_1^d, x_2^d).

5.1.2 ToF of primary and secondary wave

In the problem under examination, no in-plane propagation of waves is considered: the study of the properties of the so-called class of *guided-waves*, which comprehend the popular Rayleigh-Lamb waves, is not addressed here. As a matter of fact, analyzing the generation and the propagation of primary and secondary wavefronts in the plate thickness direction, we are concerned with phenomena which precede the propagation of Rayleigh-Lamb waves.

The present study is focused on the analysis of the propagation of P and S wavefronts in the plate thickness direction. Making a comparison with Fig. 5.4, actuator and sensor are located on the same side of the structure with respect to the damage, namely, on the plate upper surface; the reflecting surface can be represented, in the healthy case, by the bottom surface of the model or, in the case a damage is present, by the delamination itself. A schematic of the problem is shown in Fig. 5.7.

A delamination can be ideally thought of as a physical discontinuity in the domain virtually separating it into two different regions [98]. It is apparent that in the considered model, any possibility for a disturbance to propagate from one of the two regions to the other one is prevented. This simple and effective phenomenon constitutes the key element of the detection mechanism at the base of the SHM routine proposed in this work.

When a delamination is located along the propagation path of primary and secondary waves in the through-the-thickness direction, it prevents the excitation signal to access the

portion of the structure that lays beyond the damage itself. The immediate consequence of this effect is that P and S waves are reflected by the delamination boundaries and not by the bottom surface of the plate-like structure, shortening the propagation path of the waves. The time of arrival of the primary and secondary wavefronts to the upper surface of the structure is then affected by the presence of the delamination: a strong correlation between the presence and the location of the damage in the normal direction and the ToF of the generated elastodynamic signal is then to be expected.

Denoting with t_P and t_S the time of arrival of P and S waves at the sensor location, respectively, the ToF can be defined as ToF $= t_S - t_P$ or, introducing the wavelength $\lambda_{w_{P,S}}$, the wave frequency $f_{w_{P,S}}$ and the traveled distance d

$$ToF = \frac{d}{\lambda_{w_{P,S}} f_{w_{P,S}}} = d\frac{(\lambda_{w_P} f_{w_P}) - (\lambda_{w_S} f_{w_S})}{\lambda_{w_P}\lambda_{w_S} f_{w_P} f_{w_S}} \tag{5.4}$$

This shows that, as expected, a variation of the traveled distance d due to the presence of damage results into a change of the ToF.

The system that constitutes the object of our analyses consists in a composite laminated plate onto which piezoelectric transducers are mounted to generate or to sense the elastodynamic field described in the previous sections. The plate is an eight-layer symmetric laminate with epoxy matrix and carbon fibers oriented according to the stacking sequence $(0/45/90/135)_s$. The description of the piezoelectric transducers and of the composite laminate models are addressed in the next sections.

5.2 The damage model

The development of the model of a structural damage is a crucial step for the development of a damage identification procedure. This topic has attracted intensive research efforts over a long period, associated with the development of fracture, fatigue and damage mechanics for life prediction and integrity analysis of engineering materials and structures [101]. Delamination, appearing as debonding between adjoining plies in composite laminates, is the most common but hazardous damage in fibre-reinforced composite structures under out-of-plane stresses or subjected to transverse impact and vibrations.

From an experimental point of view two major approaches have been extensively adopted in the literature to study the effect of delaminations in composite structures: the realization of impacts to induce delaminations in a predefined region of the system [102, 103, 104, 105] and the use of inserts of soft materials in between the composite layers [111, 112, 113, 114].

The most important advantage of using impacts to study delaminations is that no simulation of the damage but an effective introduction of the delamination in the system is

performed. The main disadvantages associated with this technique are represented by the difficulty to predict the extent and in general the features of the damage induced. In spite of the fact that a great deal of effort has been directed towards the experimental characterization of impact damage, an efficient and accurate method for the prediction of impact damage is still lacking. The slow development of an adequate model is a consequence of the three-dimensional nature of impact damage and the complexity of the geometry of delamination [101].

On the other side, the use of inserts (mainly made of teflon) placed in between the composites layers during the manufacturing process can ensure an optimal control of the damage properties in terms of size and location [115, 116]. It is apparent, however, that the adoption of inserts constitutes only a way to simulate the presence of the damage in the system, with all the limitations and drawbacks of such an approach. While a consistent local reduction of the structural stiffness can be achieved (naturally describable as damage effect), a contemporary augmentation of the mass of the system difficult to associate to the presence of a damage is also obtained.

In FEM models, delaminations are frequently represented moving apart the nodes at the

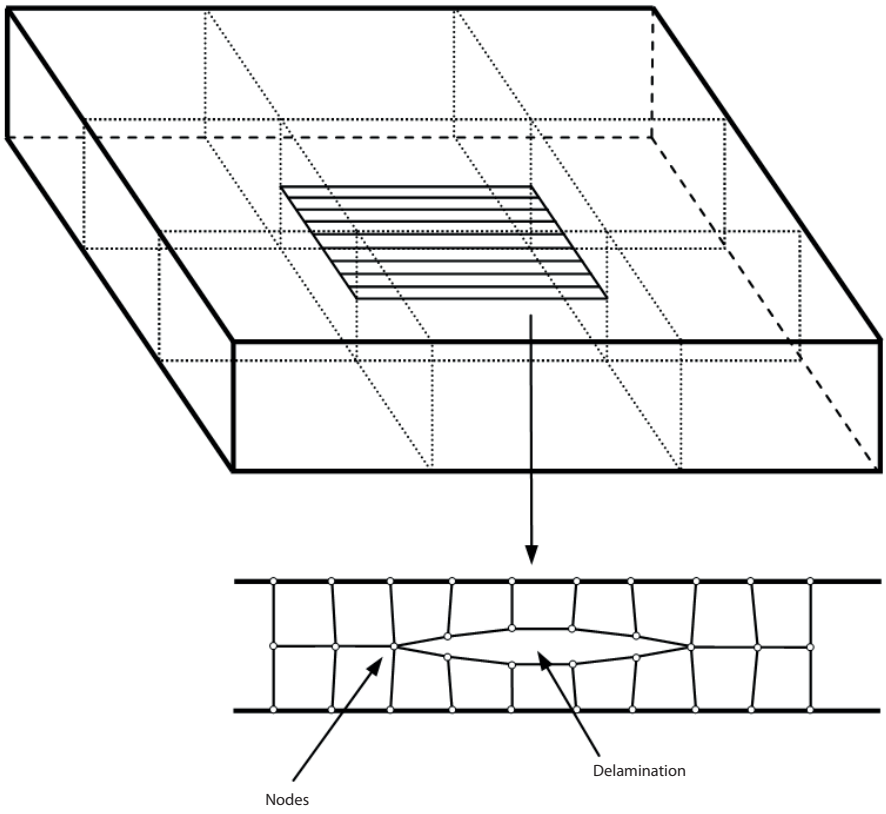

Figure 5.8: Classical representation of delaminations in numerical codes.

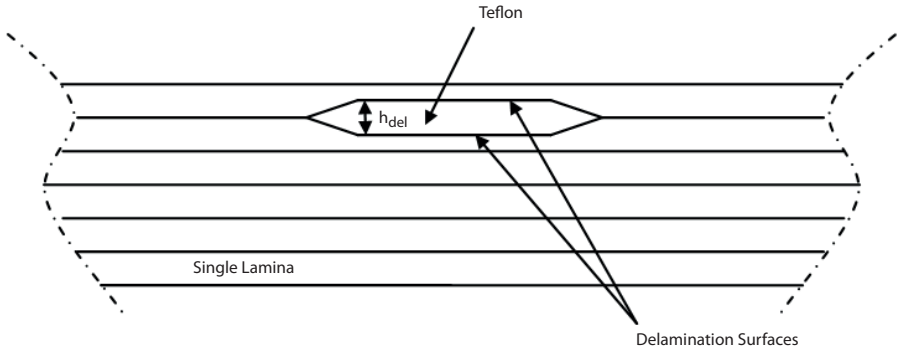

Figure 5.9: Schematic layout of teflon inserts in experimental tests to simulate the presence of a delamination.

interface between layers where the damage is located by a small distance, so as to form the delamination itself [98, 99](see Fig. 5.8). In addition to pure numerical approaches, hybrid modeling techniques which combine analytical tools with FEM simulation have also been developed, so as to improve damage characterization and to achieve better insight into the physics of the phenomena [118]-[122].

In this work the delamination has been represented as a teflon insert located between the layers of the composite laminate (Fig. 5.9). The reasons for this choice are multifaceted. The implementation of this technique to model the delamination in the numerical simulations has been guided by the possibility of performing a comparison with the results achieved in the subsequent experimental phase of the study, where the use of teflon inserts can guarantee control and careful reproduction of the damage features, both of them representing fundamental requirements for the analysis of the problem. In addition, modeling the delamination as a local yet significant reduction of the system mechanical properties (e.g., 120-150 GPa for Young's modulus of a typical carbon fiber composite laminate estimated in the fibers direction with respect to 0.5 GPa for a teflon insert) and not as a pure discontinuity of the wave propagation domain, represents a conservative approach in simulating the presence of the damage in terms of its reflectivity properties. If a complete void region were taken into account to model de damage, in fact, the incident wave would be entirely reflected and no refraction would take place, enhancing the detection of the reflected wave arrival at the plate upper surface. The teflon inserts, instead, allow the presence of refraction phenomena (weakening the intensity of the reflected wave) which can be associated to the presence of a not fully developed delamination, where a complete debonding between the layers has not taken place yet, representing a conservative model of the damage. An exhaustive validation of this theoretical consideration in carried out in the experimental campaign.

5.3 The actuating/sensing system

5.3.1 Main features of the PZT transducers

The most commonly used transducers in SHM applications are embedded or surface-bonded piezoelectric wafer transducers. Piezoelectric transducers are inexpensive and are available in very fine thicknesses (0.1 mm for ceramics and 9 μm for polymer films), making them very unobtrusive and conducive for integration into structures. They operate according to the piezoelectric and inverse piezoelectric principles that couple the electrical and mechanical behavior of the material. An electric charge is collected on the surface of the piezoelectric material when it is strained. The converse effect also happens, that is, the generation of mechanical strain in response to an applied electric field. Hence, they can be used as both actuators and sensors. The most commonly available materials are lead zirconium titanate ceramics (known as PZT) and polyvinylidene fluoride (PVDF), which is a polymer film. Both of these are usually poled through the thickness (normally designated the 3-direction), which is the direction in which the voltage is applied or sensed. Uniformly poled PZTs are typically used in the *1-3 coupling configuration*, where the sensing/actuation effect is along the thickness or 3-direction while the actuation/sensing effect is in the plane of the PZT, normal to the poling axis.

5.3.2 The piezoelectric constitutive law

The linear constitutive laws for a piezoelectric material are [96]

$$\boldsymbol{D} = \boldsymbol{p}\boldsymbol{E} + \boldsymbol{d}\boldsymbol{T} \tag{5.5}$$

$$\boldsymbol{S} = \boldsymbol{d}^{\intercal}\boldsymbol{E} + \boldsymbol{c}^{-1}\boldsymbol{T} \tag{5.6}$$

where $\boldsymbol{D}$ and $\boldsymbol{E}$ are the electric displacement and the electric field vectors while $\boldsymbol{p}$ and $\boldsymbol{d}$ are the dielectric permittivity and the electromechanical coupling tensors, respectively. $\boldsymbol{S}$, $\boldsymbol{T}$ and $\boldsymbol{c}$ denote the deformation and stress tensors and the elasticity matrix, respectively. The most frequent representation for $\boldsymbol{p}$ and $\boldsymbol{d}$, which is here adopted, reads [96, 97]

$$\boldsymbol{p} = \begin{bmatrix} p_1 & 0 & 0 \\ 0 & p_1 & 0 \\ 0 & 0 & p_3 \end{bmatrix}, \tag{5.7}$$

$$\boldsymbol{d} = \begin{bmatrix} 0 & 0 & 0 & 0 & d_{15} & 0 \\ 0 & 0 & 0 & d_{15} & 0 & 0 \\ d_{31} & d_{31} & d_{33} & 0 & 0 & 0 \end{bmatrix}. \tag{5.8}$$

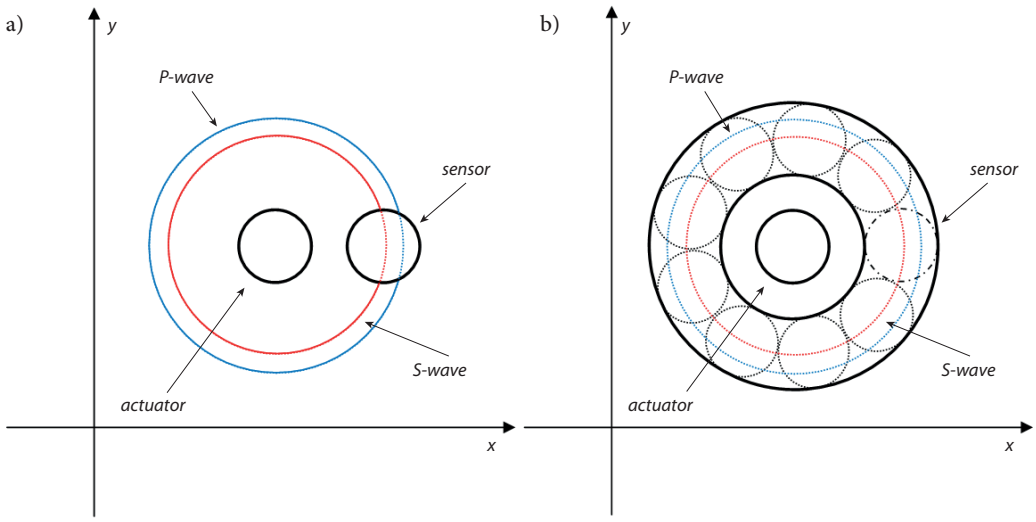

Figure 5.10: No in-plane directivity is required for the actuator: a cylindrical shape is thus adopted (a). A ring-shaped geometry is considered for the sensor in order to be able to acquire most of the generated P and S waves (b).

It is usually preferred to write equations (5.5) and (5.6) in terms of the electric field vector $\boldsymbol{E}$ and the deformation tensor $\boldsymbol{S}$ as

$$\boldsymbol{D} = (\boldsymbol{p} - \boldsymbol{d}\boldsymbol{c}\boldsymbol{d}^{\mathsf{T}})\,\boldsymbol{E} + \boldsymbol{d}\boldsymbol{c}\boldsymbol{S}, \tag{5.9}$$

$$\boldsymbol{T} = -\boldsymbol{c}\boldsymbol{d}^{\mathsf{T}}\boldsymbol{E} + \boldsymbol{c}\boldsymbol{S}. \tag{5.10}$$

5.3.3 Design of the transducers shape

As previously observed, if the case of a homogeneous isotropic material is taken into account for an in-plane analysis of the generated elastodynamic radiation field, a circular PZT element can generate P and S waves propagating normal to the actuator circumference, while those of non-circular shapes such as a rectangle can exhibit strong directivity of the generated waves. Here attention is drawn to the propagation of primary and secondary waves through the plate thickness: it is therefore apparent that no preferential in-plane propagation direction is required. This makes the cylindrical symmetry a desirable feature for the design of the actuator geometry, reducing the options for the actuator shape to two: a cylindrical and a ring-like geometry. For the damage detection mechanism here proposed, based on the generation, propagation and reflection of primary and secondary waves, the option represented by the cylinder can offer the important advantage of a simpler radiation field in terms of number of generated waves and relative reflections on the domain boundary, leading to an acquired output signal which is much clearer and easier to interpret. The design of the sensor geometry can be informed by the same principles. If, for instance, a

cylindrical shape is chosen for the sensor too, this would imply to neglect the greatest part of the elastodynamic field radiating for the actuator, as shown in Fig. 5.10(a), with a low signal-to-noise ratio as main consequence. A wiser choice is to adopt a ring-like geometry for the sensor, which can be eventually seen as the envelope of different cylinders surrounding the actuator (Fig. 5.10(b)). The resultant geometry of the designed actuator-sensor pair is shown in Fig. 5.11: the characteristic parameters of this configuration consist in the actuator and sensor thickness t_a and t_s, the actuator radius r_a, and the sensor width w_s and mid-radius r_s. Once the detection mechanism is established (i.e., the estimation of the boundary/damage-reflected primary and secondary waves ToF), an optimization process of these parameters aimed at enhancing the performance of the actuating/sensing system evaluated by an appropriate functional can be carried out.

5.4 The sensor optimization process

Optimal sensor/actuator design strategies aim to maximize the ability to detect and discriminate relevant data features given limited resources [123]. In the case at hand the aim of the optimization process is meant to improve the ability of the actuating/sensing system to detect the presence of a delamination in the structure when different possible damage scenarios are considered. To this end, the values of the geometric parameters defining the actuator-sensor pair are used as entries for the optimization routine, adopted within the class of Genetic Algorithms (GAs). In particular, a differential Evolutionary Algorithm-based approach (EAs) is implemented.

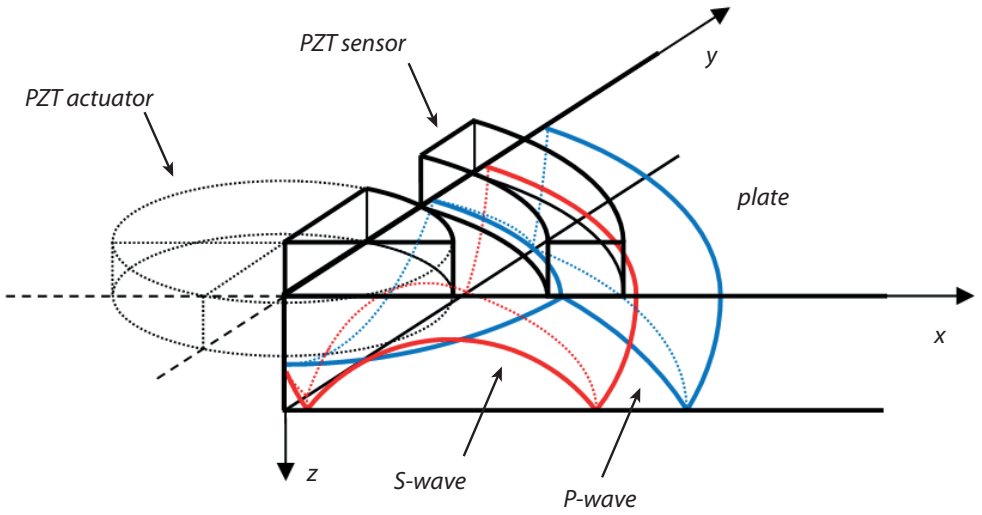

Figure 5.11: 3D schematic of the designed geometry for the piezoelectric actuator and sensor.

5.4.1 Differential evolutionary algorithms

Differential evolutionary algorithms are part of the widely used genetic optimization method: a biology-inspired approach, which uses the concept of natural selection to iteratively optimize an objective function over successive generations of candidates [124, 125]. The differences with respect to the conventional GAs are mostly in the way the mechanisms of mutation and crossover are performed using real floating point numbers instead of long strings of zeros and ones [1].

The great advantage of this optimization method is that there is no need to evaluate derivatives, since the optimization is performed evaluating the solution for many iteratively found populations of candidates and choosing among them the ones which give the best solution in terms of the objective function (OF) [128, 129].

A representation of EAs key algorithmic steps is shown in Fig. 5.12. An initial pool of N vectors to be tested, each one containing M parameters (usually referred to as *genes*), is taken into account as starting point: it represents the so-called *first generation* (or population). Moreover the ranges of the different genes constituting the vectors are given as input to the algorithm. The following steps are thus performed:

- Initialization

  At the first iteration, vector i is selected among the N possible candidates as *target vector*. Three more vectors among the remaining $N-1$ M-vectors of the first generation are randomly selected. These vectors are usually addressed to as vector A, vector B, and vector C.

- Mutation

  This process allows to expand the search space: vector A and vector B are subtracted, their result is multiplied by a *crossover probability* K and subsequently added to vector C: this leads to the definition of a new *mutated vector* (called vector D).

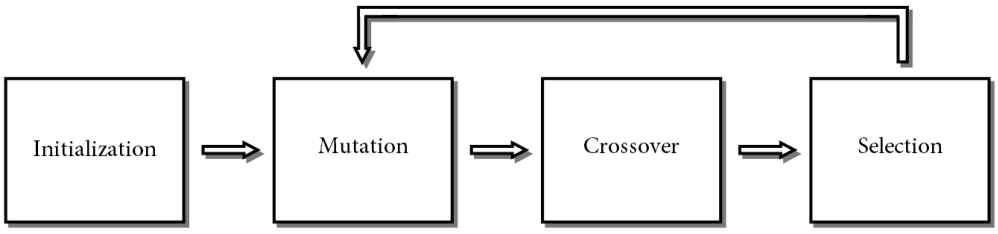

Figure 5.12: The different phases of the optimization process based on the use of differential evolutionary algorithms (EAs).

- Crossover

  This step of the EA algorithm is aimed at defining a *trial vector*, through which successful solutions from the previous generation are incorporated. A random number n between zero and one is randomly chosen: if n is smaller than a previously defined *crossover ratio* CR (also comprised between 0 and 1) the first gene of the trial vector is defined selecting it from vector D; otherwise, if a is bigger or equal to the crossover ratio, the first gene of the trial vector is selected from the target vector. The same is done for the second gene, extracting another number.

- Selection

  This phase reproduces natural selection: the problem (here, the damage detection) is solved for both the target vector and the trial vector. Subsequently the OF is estimated for both cases: the vector which can guarantee the best performance in terms of objective function is selected to replace the initial i-vector and to form the next generation.

When these steps are repeated for all the N vectors constituting the first generation, a new generation is created. This process is carried out until the desired number of generations is reached or until a stop criterion is satisfied. A more detailed schematic description of the algorithm can be found in Fig. 5.13. All of the random variables are selected using a uniform probability density, which ensures that the space in which the selection is done, is equally spanned. An important aspect is that after the mutation, the genes vector D can possibly exceed the limit values of the search space: a controller which eventually brings back in the right range the parameters have thus to be implemented. One more controller is also positioned after the crossover is carried out: if the trial vector's genes are both equal to those defining the target vector, the mutation and the crossover are repeated until two

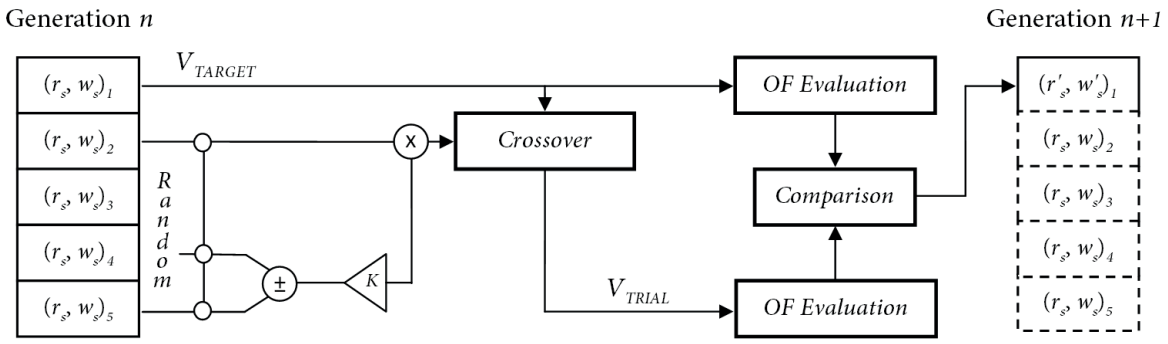

Figure 5.13: Schematic flow chart showing the numerical implementation of the optimization process based on differential evolutionary algorithms.

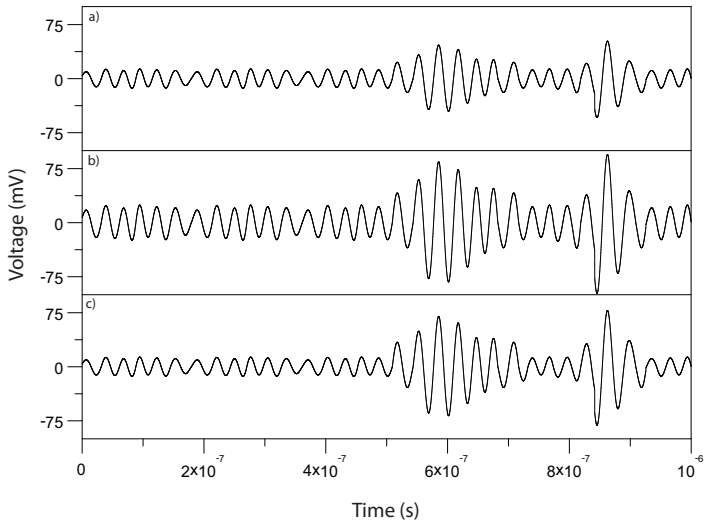

Figure 5.14: Different time histories showing the effects of the sensing system optimization process on the acquired output of the system shown in Fig. 5.4: while the peak of the second wave group noticeable in the plots increases (defined as the object of the trial optimization), the rest of the signal remains almost unaltered in terms of amplitude (from (a) to (c)).

different vectors can pass to the selection step. Usual values found in the literature for the crossover probability K and the crossover ratio CR are 0.7 and 0.5, respectively [126]: these values are adopted hereafter.

5.4.2 The objective function (OF)

The described optimization algorithm is based on definition of a suitable objective function. The ToF-based damage detection discussed in section 5.1 relies on the identification of the peaks that primary and secondary waves approaching the upper surface of the plate appearing int the output signal delivered by a PZT sensor: it thus becomes crucial to be able to clearly distinguish these peaks in the sensor response. To this end, the objective function should be designed in such a way to rank output signals in terms of the P and S waves observability.

Denoting by V_i^P, V_i^S and V_i^{RMS} the peak values in the voltage output of the PZT sensor and its root mean square (RMS), respectively, the objective function for the differential evolutionary optimization algorithm above described can be defined as

$$OF = \sum_{i=1}^{I+1} \frac{a_i^P (V_i^P - V_i^{RMS}) + a_i^S (V_i^S - V_i^{RMS})}{V_i^{RMS}} \tag{5.11}$$

where $I + 1$ represents the number of different damage scenarios evaluated considering the same actuator/sensor configuration in terms of the characteristic geometric parameters plus the undamaged case. The parameters a_i^P and a_i^S are the weights of the sum which take into

account the wavefront attenuation with the traveled distance affecting P and S waves: the farther is the damage location with respect to the actuator sensor pair, the higher is the value of the related weight $a_i^{P,S}$. With some trivial passages Eq. (5.11) can be rearranged as

$$OF = \sum_{i=1}^{I+1} \left[a_i^P \left(\frac{V_i^P}{V_i^{RMS}} - 1 \right) + a_i^S \left(\frac{V_i^S}{V_i^{RMS}} - 1 \right) \right]. \tag{5.12}$$

A relative value of the voltage peaks in the sensor response is taken into account in the expression of the OF in Eq. (5.12): the RMS value of the output signal V_i^{RMS} is introduced as reference for the value of the voltage peaks V_i^P and V_i^S. This means that a mere increase of the peak values in the sensor response due to a particular configuration of the PZTs does not automatically imply an improvement of the calculated OF value. When a comparable increase of the RMS of the output signal is also registered (due, for instance, to a higher value of the voltage used to generate the waves), so that no improvement of the effective observability of the peaks V_i^P and V_i^S is achieved, the obtained values of the OF do not experience significant changes (Fig. 5.14).

5.5 Design of the excitation signal

It is widely accepted that in the class of the active sensing methods, which represents an important part of SHM procedures [98, 130], the choice of an appropriate excitation signal is a fundamental step towards the damage identification in the structural systems [131]. As a simple example, consider a beam or column with a crack that is nominally closed due to a pre-load. If the provided excitation is not sufficient to open and close the crack, the detectability of the crack in the measured output will be severely limited [132]. A survey of the SHM literature, however, reveals that a great deal of attention has been paid to the data interrogation portion of the SHM process, while no equal attention has been paid to the excitation design [127]. This disparity is quite reasonable in many applications where only ambient excitation is available, such as most civil engineering applications. However, there are many applications where the excitation can be prescribed (e.g., most wave propagation approaches to SHM), for which a proper selection is essential.

As a general approach to the design of optimal excitation signals for SHM purposes, four different steps can be identified in the process of input signal definition: i) the selection of the signal shape, ii) the choice of its frequency content, iii) the definition of the signal time-length and of iv) its amplitude.

5.5.1 Shape

A first step in the definition of the shape of the input signal is the choice between sinusoidal and non-sinusoidal signals: tone-burst, sweep and chirp signals can be identified as belonging to the first group, to name but a few [127, 133]. Among the second group, impulses and white noise constitute a frequently adopted option in SHM [127, 134]. In the case at hand, where, as discussed in Section 5.1, the generation of primary and secondary waves is the core of the proposed damage detection methodology, the choice of sinusoidal signals is preferred as it allows to select an appropriate operating frequency (see Fig. 4.4in Section 4.3.2): this feature is of paramount importance to guarantee the effectiveness of the present damage detection procedure. As a result, a sine with a limited number of cycles (namely, a tone-burst) is therefore chosen as input signal.

In order to reduce the *spectral leakage* phenomenon, a time-windowing of the input signal is also addressed. In signal processing, a window function is a mathematical function that is zero-valued outside of some chosen interval [136]. For instance, a function that is constant inside the interval and zero elsewhere is called a rectangular window. When another function or waveform/data-sequence is multiplied by a window function, the product is also zero-valued outside the interval: all that is left is the part where they overlap. A more general definition of window functions does not require them to be identically zero outside an interval, as long as the product of the window multiplied by its argument is square integrable, so that the function sufficiently rapidly des out [136].

As already anticipated, the scope of time-windowing is to reduce the appearance of frequency components different from the desired ones. The Fourier transform of a general signal $f(t)$, with $f(t) = 0$ for $t < 0$ (i.e. causality is invoked), reads:

$$\tilde{f}(\omega) = \int_0^{+\infty} f(t) e^{-j\omega t} dt. \tag{5.13}$$

It is then assumed that $f(t)$ is a signal of infinite time length; this is of course not the case for real signals, which always have a finite time duration. The effect of this discrepancy on a waveform like $\sin(\Omega t)$ is that its Fourier transform develops non-zero values (commonly called spectral leakage) at frequencies other than Ω. The leakage tends to be worst (highest) near Ω and least at frequencies farthest from Ω (Fig. 5.15). The effect of applying a time-window on a signal which is finite in time, e.g. which has a time length T, is to make it quasi-periodic in the said interval, decreasing the number of harmonics needed for its spectral representation and moderating the effects due to its finite time length. If the considered waveform comprises two sinusoids of different frequencies, leakage can interfere with the ability to distinguish them spectrally. If their frequencies are dissimilar and one component is weaker, then leakage from the larger component can obscure the presence of the

weaker ones. But if the frequencies are similar, leakage can render them unresolvable even when the sinusoids are of equal strength. The rectangular window has excellent resolution characteristics for sinusoids of comparable strength, but it is a poor choice for sinusoids of disparate amplitudes. This characteristic is sometimes described as low-dynamic-range. At the other extreme of dynamic range are the windows with the poorest resolution: the ability to find weak sinusoids amidst the noise is diminished by a high-dynamic-range window. High-dynamic-range windows are probably most often justified in wide-band applications, where the spectrum being analyzed is expected to contain many different components of various amplitudes.

In between the extremes there are moderate windows, such as the Hann (or Hanning) windowing, which is here adopted. It is defined as

$$h(n) = 0.5\left[1 - \cos\left(\frac{2\pi n}{N-1}\right)\right], \qquad \text{for} n = 0, .., N-1. \tag{5.14}$$

A representation of the Hann window is shown in Fig. 5.16.

5.5.2 Frequency content

The selection of the frequency of the input represents a fundamental step towards the definition of an appropriate excitation signal for SHM purposes. This is particularly true in this

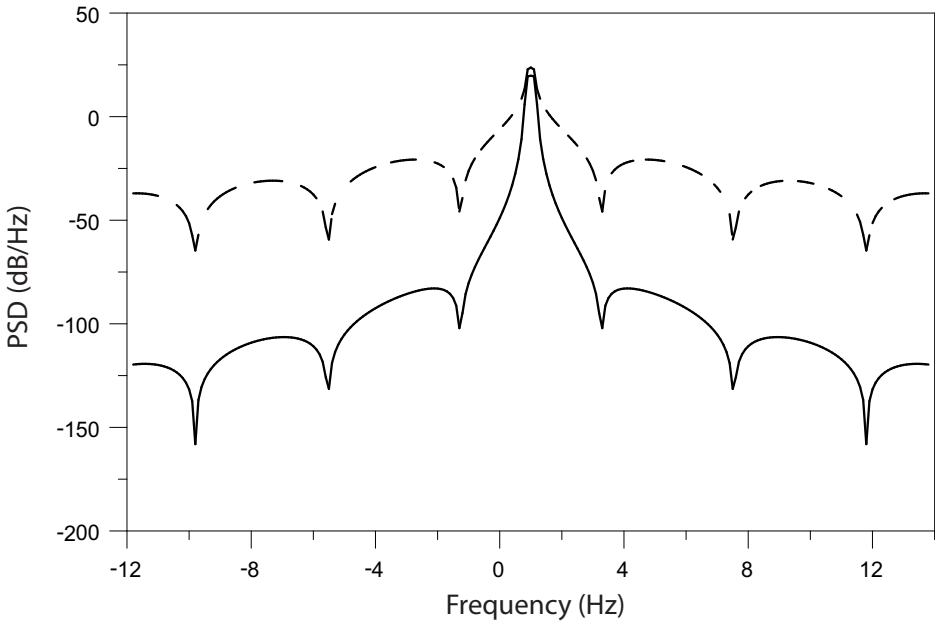

Figure 5.15: The effects of the Hann time-windowing on a 4.5 cycles tone-burst with a characteristic frequency of 1Hz: the frequency content of the signal is gathered about the main frequency when the windowing technique is used (solid line).

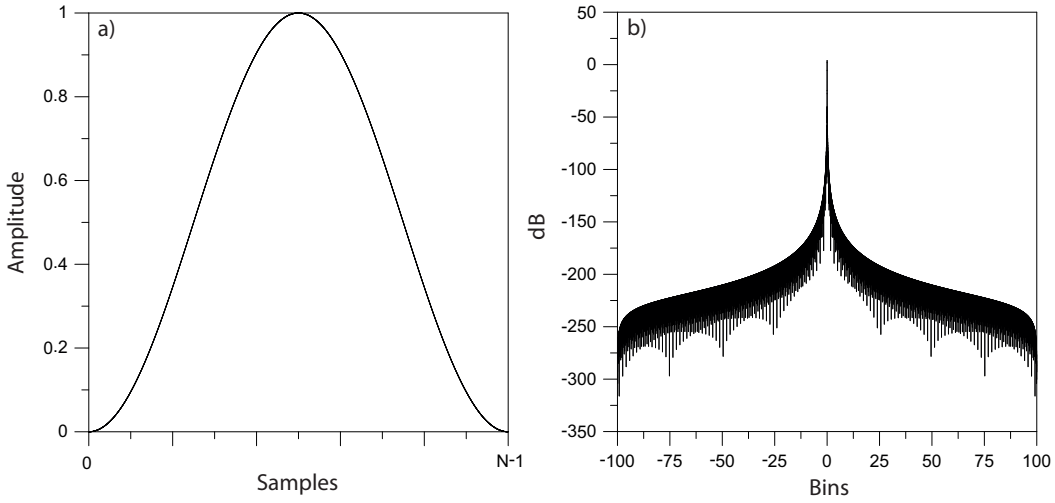

Figure 5.16: The Hann-window in the time (a) and frequency (b) domains.

case, where a nonconventional damage-detection strategy is designed so as to make necessary the consideration of a frequency region for the design of the input signal which does not coincides with that usually considered in traditional Us-SHM approaches. While, in fact, the usual frequency content of an excitation signal aimed at activating Rayleigh-Lamb propagation modes in waveguides belongs to the kiloHertz range (from tens to hundreds of KHz), in this work the band of megaHertz is considered. The minimum requirement for an input signal frequency thought to be sensitive to a damage whose characteristic dimension (in the wave propagation direction) is of the order of the thickness of one of the composite single layer h_{layer} is:

$$f_{min} = \frac{c_P^{(3)}}{2h_{layer}} \tag{5.15}$$

where $c_P^{(3)}$ is primary wave propagation velocity in the normal direction and estimated as

$$c_P^{(3)} = \sqrt{\frac{\lambda^{(3)} + 2\mu^{(3)}}{\rho}} \tag{5.16}$$

with $\lambda^{(3)}$ and $\mu^{(3)}$ representing the Lame' constants in the through-the-thickness direction of a transversely isotropic medium as a composite multilayer plate. If common values for $\lambda^{(3)}$ and $\mu^{(3)}$ are taken into account, a f_{min} of about 3 MHz is finally obtained.

Moreover, one additional important aspect of the input signal frequency design has to be addressed. The use of PZT transducers as actuators, in fact, paves the way to exploit resonance effects if the appropriate resonant frequency of the actuator is adopted for the excitation signal, resulting in a significant enhancement of the actuator performances in terms of the generated strain field (given that the input signal amplitude is kept constant).

The optimal resonance condition can be identified if the variation of the electromechanical impedance $Z(\omega)$ of the PZT transducer with the frequency is obtained (Fig. 5.17): from an experimental point of view this can be achieved using an impedance analyzer. The resonance condition with the eigenmode that results as being dominantly excited by the imposition of the input signal voltage can be identified as a minimum in the absolute value of the impedance, and, as said, it constitutes the optimal excitation condition in terms of the actuating capabilities of the PZT transducer. Assumed that this frequency satisfies the f_{min} condition (i.e. $f_{resonance} > f_{min}$), it represents the optimal choice for the input signal frequency design.

5.5.3 Time length

The definition of the length in time (and thus in space) of a excitation signal can result from different considerations. If, on one hand, a "long" signal implies major effects related to interference and multiple reflection phenomena (interaction of the input signal with waves reflected by the structure boundaries, refracted by inhomogeneities or scattered by the damage itself) resulting, among the other issues, in a higher complexity of the acquired output signal, on the other hand, a "short" excitation signal can miss to deliver the desired information (mainly in terms of frequency content, with the rise of non-trivial side lobes in its

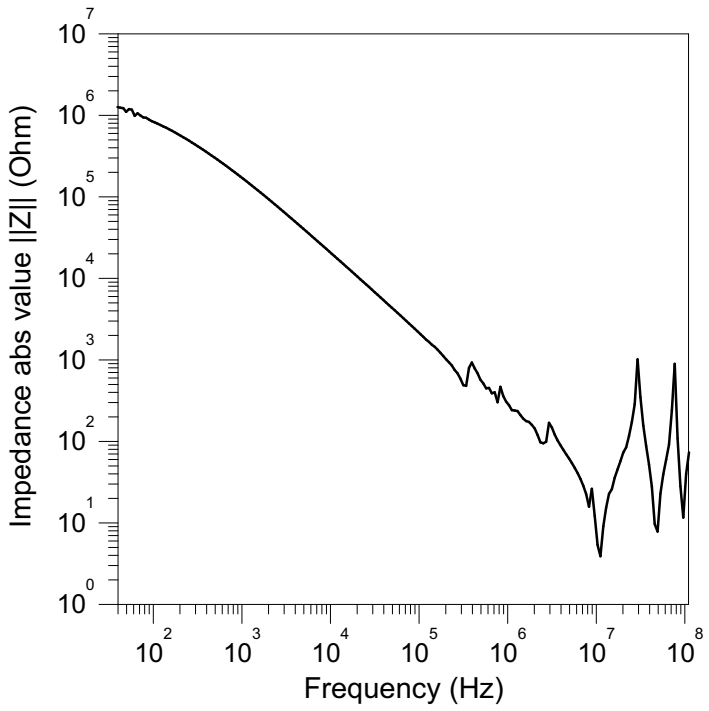

Figure 5.17: Impedance modulus measured on a PZT disk with a 1.5 mm radius and 0.5 mm thick using an impedance analyzer.

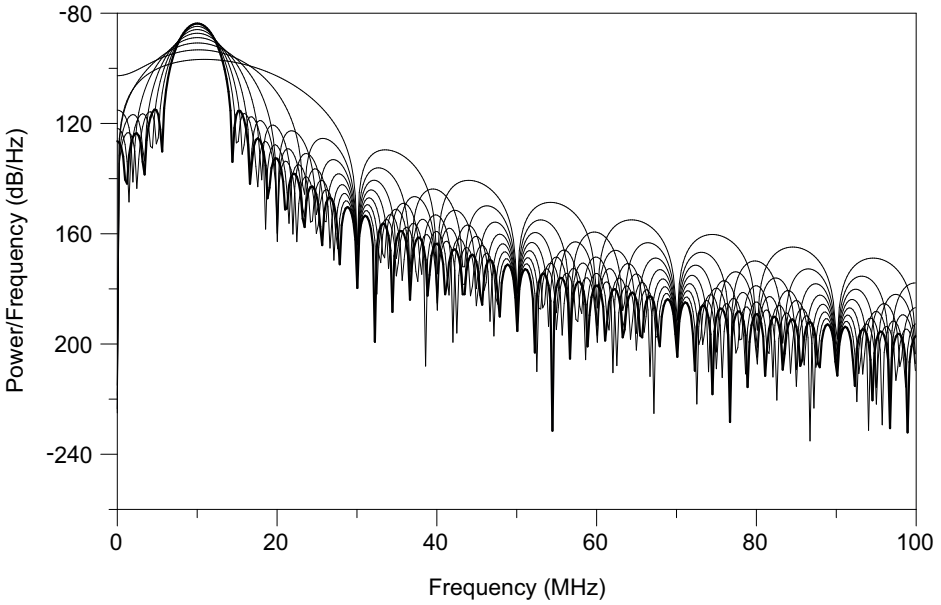

Figure 5.18: Power spectral density of the input signal with a varying number of cycles: the power content of the signal gathers about its main frequency as the number of the cycles increases.

frequency spectrum).

A possible approach in designing the excitation signal time length consists in adopting the minimum signal duration that allows the desired features of the input to be achieved. This can be done if an analysis of the variation of the input signal power content in a pre-definite bandwidth about its main frequency with respect to the number of cycles which constitute it is performed. Figure 5.18 gives a qualitative indication about how the frequency content of the input signal shrinks about its main frequency as long as the number of cycles is increased. A more quantitative information is provided by Fig. 5.19, where the power content of the excitation signal in a -3dB bandwidth about a main frequency of 8 MHz with respect to the number of cycles is shown: when a number of 4.5 cycles is selected, more than 95% of the entire signal power content is concentrated in the mentioned -3dB bandwidth. As no significant increases in this percent power content is observed when a higher number of cycles is considered, a 4.5 cycles tone-burst is finally selected as excitation signal for the proposed SHM procedure.

5.5.4 Amplitude

The amplitude of a signal is one of the key feature that defines the excitation in a SHM strategy. Given the linearity of the problem, two major limitations are present in the definition of the maximum value of the input signal amplitude: the PZT failure and the PZT-structure bonding breakdown.

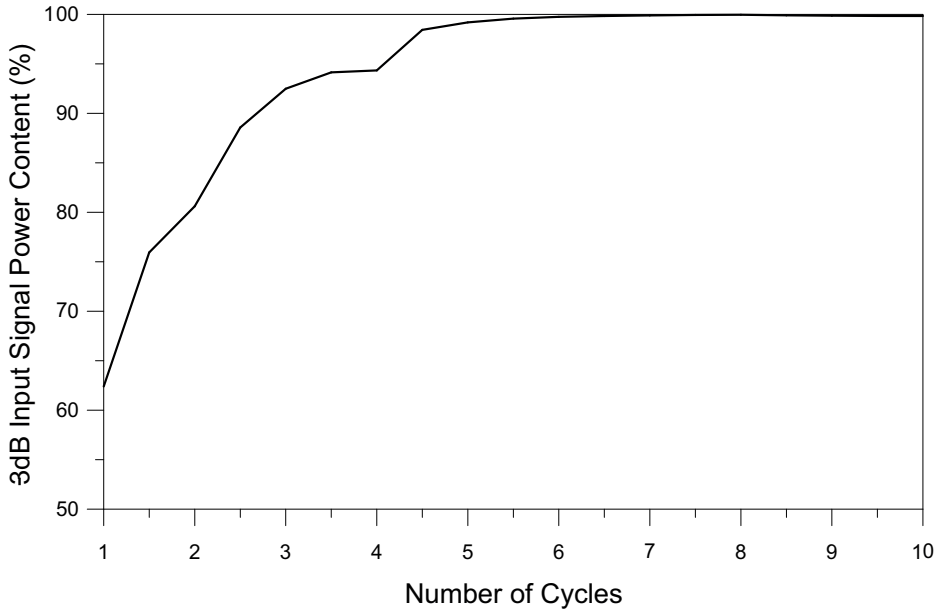

Figure 5.19: Percent of the power content of the input signal contained in a -3dB bandwidth about its main frequency: a 95% value is reached when 4.5 cycles are adopted to form the input signal.

For the materials used in standard piezoelectric actuators, d_{33} is of the order of 250 to 550 pm/V, d_{31} is of the order of -180 to -210 pm/V [137]. The highest values are attainable with shear actuators in d_{15} mode. Consequently, the maximum allowable field strength in piezoelectric actuators ranges between 1 and 2 kV/mm in the polarization direction. In the reverse direction (semi-bipolar operation), at most 300 V/mm is allowable; as expected the maximum voltage depends on the ceramic and insulation materials. Exceeding the maximum voltage may cause dielectric breakdown and irreversible damage to the piezoelectric actuator: if a 0.1 mm thick PZT transducer is considered (a common value for PZTs used in damage detection applications), the estimated maximum value of the voltage that can be exerted is about 200 Volts. As a matter of fact, these voltages are not reached in common SHM studies: the reason is that another limitations occurs before the breakdown of the PZT actuator, i.e., the failure of the bonding between the piezoelectric transducer and the support.

If a cylindrical PZT actuator with a thickness of $t = 0.1mm$ and a radius of $r = 2mm$ is considered, its capacitance can be written as [138]:

$$C = \frac{4r^2 e_{33}}{t} = 2.12 \cdot 10^{-9} F \tag{5.17}$$

where a common value for the relative dielectric permittivity of $e_{33}^r = 1500$, resulting in an overall permittivity of $e_{33} = 1.33 \cdot 10^{-8} F/m$, has been considered. The following formula holds [138]

$$\varepsilon_{max} = \frac{V_{max} C}{4r^2 E_{pzt} d_{31}} \tag{5.18}$$

where E_{pzt} is the Young's modulus of the PZT actuator. A general value for the characteristic shear lap of adhesives commonly used to bond the piezoelectric transducers to the structure can be assumed to be $\tau_{max} = 20MPa$. Equation (5.19) can thus be used to estimate the maximum value of the voltage that can be applied to the actuator:

$$V_{max} = \frac{4r^2 d_{31} \tau_{max}}{C} \sim 31V \tag{5.19}$$

where a d_{31} of $180 \cdot 1o^{-12}$ C/N is considered (absolute value). From this result, it is apparent that the major limitation in the definition of the maximum amplitude in terms of voltage of the excitation signal is represented by the breakdown of the PZT-structure bonding.

5.6 The propagation domain: constitutive law for the laminate

As already mentioned in previous pages, the propagation medium for P and S waves in the present ultrasonic wave-based damage detection procedure is represented by a composite laminated plate. The constitutive equation for such domain in a 3D theory can be easily derived if a global basis $(\boldsymbol{e}_1, \boldsymbol{e}_2, \boldsymbol{e}_3)$ and a local basis $(\boldsymbol{b}_1, \boldsymbol{b}_2, \boldsymbol{b}_3)$, sharing the same orientation of the composite fibers, are taken into account: denoting with $\phi^{(k)}$ the angle formed by the fibers orientation and the $\boldsymbol{e}_1$ unit vector, we can write

$$\boldsymbol{e}_i = \boldsymbol{R}^{(k)} \boldsymbol{e}_i \tag{5.20}$$

where $\boldsymbol{R}^{(k)}$ represents the matrix associated to a rotation of $\phi^{(k)}$ about the $\boldsymbol{e}_3$-defined axis (see Fig. 5.20). We have

$$\boldsymbol{R}^{(k)} = \begin{bmatrix} \cos\phi^{(k)} & -\sin\phi^{(k)} & 0 \\ \sin\phi^{(k)} & \cos\phi^{(k)} & 0 \\ 0 & 0 & 1 \end{bmatrix}. \tag{5.21}$$

Making use of the dyadic product and adopting the Einstein notation, we can write the Cauchy stress tensor $\boldsymbol{T}$ in the k-th lamina of the plate as

$$\boldsymbol{T} = \tilde{T}_{ij} \boldsymbol{b}_i \boldsymbol{b}_j = \tilde{T}_{ij} (\boldsymbol{R}^{(k)} \boldsymbol{e}_i)(\boldsymbol{R}^{(k)} \boldsymbol{e}_j) = T_{ij} \boldsymbol{e}_i \boldsymbol{e}_j \qquad \text{for} \quad i,j = 1,2,3 \tag{5.22}$$

where the $\tilde{\cdot}$ indicates the stress tensor components expressed in the local basis. We thus have that

$$T_{ij} = \tilde{T}_{mn} R^{ij(k)}_{mn} \qquad \text{for} \quad m,n = 1,2,3 \tag{5.23}$$

where $R^{ij(k)}_{mn}$ denotes the ij-element of the dyad $\boldsymbol{R}^{(k)}_m \boldsymbol{R}^{(k)}_n$, being $\boldsymbol{R}^{(k)}_m$ and $\boldsymbol{R}^{(k)}_n$ the m-th and n-th column of the matrix $\boldsymbol{R}^{(k)}$, respectively. If Voigt's notation is used to denote the

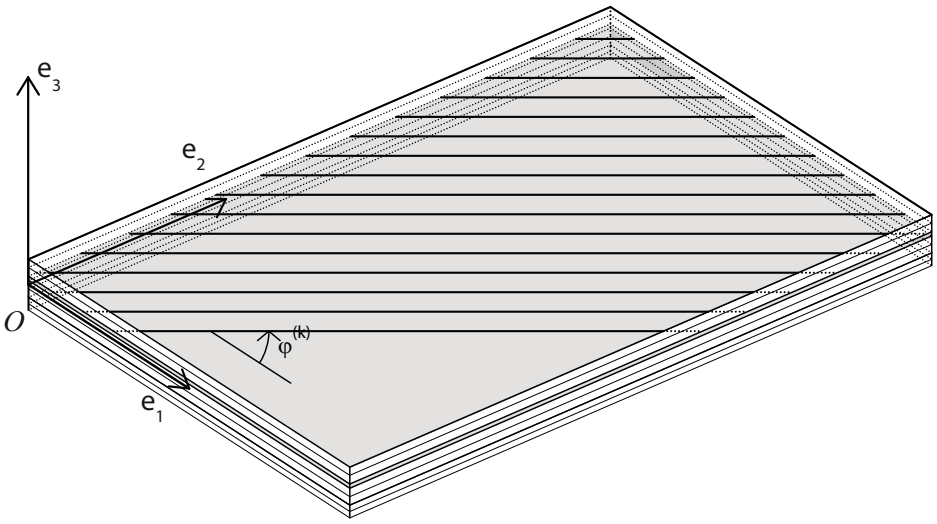

Figure 5.20: Schematic of the composite single lamina showing the orientation of the fiber $\phi^{(k)}$.

components of the Cauchy stress tensor in the global ($\boldsymbol{\sigma}$) and local ($\tilde{\boldsymbol{\sigma}}$) basis, Eq. (5.23) can be rewritten as

$$\boldsymbol{\sigma} = \boldsymbol{\Xi}_{\sigma}^{(k)} \tilde{\boldsymbol{\sigma}} \tag{5.24}$$

with

$$\boldsymbol{\Xi}_{\sigma}^{(k)} = \begin{bmatrix} \cos^2\phi^{(k)} & \sin^2\phi^{(k)} & 0 & 0 & 0 & 2\cos\phi^{(k)}\sin\phi^{(k)} \\ \sin^2\phi^{(k)} & \cos^2\phi^{(k)} & 0 & 0 & 0 & -2\cos\phi^{(k)}\sin\phi^{(k)} \\ 0 & 0 & 1 & 0 & 0 & 0 \\ 0 & 0 & 0 & \cos\phi^{(k)} & -\sin\phi^{(k)} & 0 \\ 0 & 0 & 0 & \sin\phi^{(k)} & \cos\phi^{(k)} & 0 \\ -\cos\phi^{(k)}\sin\phi^{(k)} & \cos\phi^{(k)}\sin\phi^{(k)} & 0 & 0 & 0 & \cos^2\phi^{(k)} - \sin^2\phi^{(k)} \end{bmatrix}. \tag{5.25}$$

In the same way, the relationship between global ($\boldsymbol{\varepsilon}$) and local ($\tilde{\boldsymbol{\varepsilon}}$) components of the infinitesimal strain tensor $\boldsymbol{S}$ can be found:

$$\boldsymbol{\varepsilon} = \boldsymbol{\Xi}_{\sigma}^{(k)} \tilde{\boldsymbol{\varepsilon}} \tag{5.26}$$

If shear strains $\gamma_{ij} = 2\epsilon_{ij}$ for $i \neq j$ are introduced, we can write

$$\boldsymbol{\gamma} = \boldsymbol{\Gamma}^{-1} \boldsymbol{\Xi}_{\sigma}^{(k)} \tilde{\boldsymbol{\varepsilon}} = \boldsymbol{\Xi}_{\gamma}^{(k)} \tilde{\boldsymbol{\varepsilon}} \tag{5.27}$$

where $\boldsymbol{\varepsilon} = \boldsymbol{\Gamma}\boldsymbol{\gamma}$. The constitutive law for the k-th lamina of the composite reads

$$\boldsymbol{T} = \boldsymbol{c}^{(k)} \boldsymbol{S} \tag{5.28}$$

where $\boldsymbol{c}^{(k)}$ denotes the fourth-order stiffness matrix. Using Voigt's notation we have

$$\tilde{\boldsymbol{\sigma}} = \tilde{\boldsymbol{C}}^{(k)}\tilde{\boldsymbol{\varepsilon}} \tag{5.29}$$

where $\boldsymbol{C}^{(k)}$ is a 6×6 stiffness matrix. Making use of Eqs. (5.24) and (5.27) we obtain the constitutive law of the composite plate for the k-th lamina in the fixed basis as

$$\boldsymbol{\sigma} = \Xi_{\sigma}^{-1}\tilde{\boldsymbol{C}}^{(k)}\Xi_{\gamma}\boldsymbol{\gamma} = \boldsymbol{C}^{(k)}\boldsymbol{\gamma} \tag{5.30}$$

with

$$\boldsymbol{C}^{(k)} = \Xi_{\sigma}^{-1}\tilde{\boldsymbol{C}}^{(k)}\Xi_{\gamma}. \tag{5.31}$$

5.7 The governing equations of the problem

The governing equations of the problem can be finally presented so as to set up the numerical computations. It is an usual practice to put these equation in nondimensional form due to the simultaneous presence of different space-time scales which regulate the different phenomena exhibited in the problem. A nondimensionalization of the variables and parameters makes possible an easier understanding of the relative importance of the different terms which appear in the equations. In addition, another important reason makes the nondimensionalization of the governing equations a fundamental step in the analysis of the phenomena being investigated, namely, their implementation in a numerical code. Given that the frequency range involved in the problem is of the order of $10^6 \div 10^7$ Hz, the order of magnitude of the time step of a numerical simulation can be of $10^{-8} \div 10^{-9}$ seconds. Such small time steps can easily result in nontrivial truncation errors and, consequently, in time convergence problems.

The characteristic length l_c and time t_c used to carry out the nondimensionalization of the equations are represented by the delamination width b and the input frequency ω_c (see

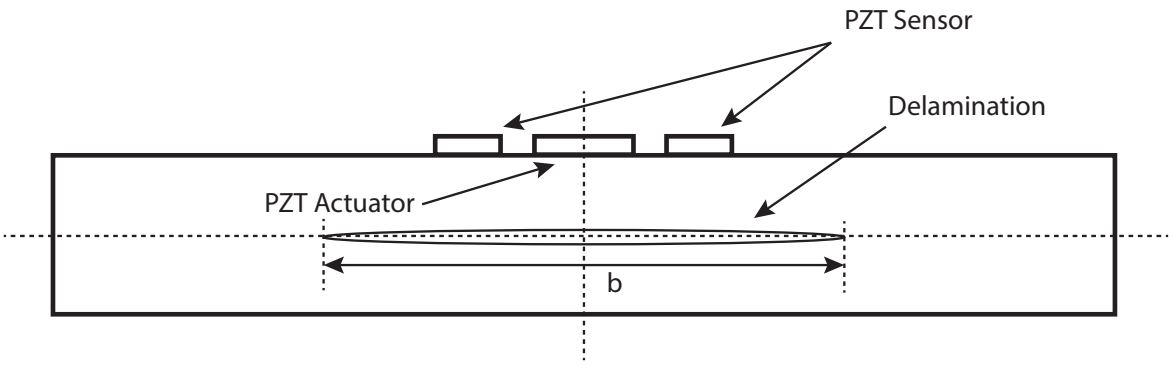

Figure 5.21: Schematic representation of the delaminated composite laminate.

Fig. 5.21), so that

$$\begin{aligned} l_c &= b, \\ t_c &= \frac{1}{\omega_c}. \end{aligned} \tag{5.32}$$

The following nondimensional quantities are introduced: $x^* = \frac{x}{l_c}$, $y^* = \frac{y}{l_c}$, $z^* = \frac{z}{l_c}$, $t^* = \frac{t}{t_c}$. The constitutive equations for a non-piezoelectric medium (i.e. the composite plate and the teflon insert representing the delamination) read (see Eqs. (5.5), (5.6) and (5.28)):

$$\begin{aligned} \boldsymbol{D} &= \boldsymbol{pE} \\ \boldsymbol{T} &= \boldsymbol{cS} \end{aligned} \tag{5.33}$$

where no electromechanical coupling is present. To proceed with the nondimensionalization of the equations of motion for the non-piezoelectric part of system, the following quantities are defined:

$$\begin{aligned} E_c &= \frac{V_0}{l_c} \\ p_c &= \frac{1}{3}\text{Trace}(\boldsymbol{p}) \\ K_c &= \frac{1}{3}\text{Trace}(\boldsymbol{c}) \\ D_c &= p_c E_c \end{aligned} \tag{5.34}$$

where V_0 is a reference value for the voltage field set for convenience equal to 1. For the non-piezoelectric constituents of the domain the mechanical and electrical equilibrium read

$$\nabla \cdot \boldsymbol{T} + 2\zeta_n \omega_n \rho \boldsymbol{I} \boldsymbol{u}_t = \rho \boldsymbol{u}_{tt} \tag{5.35}$$

together with

$$\nabla \cdot \boldsymbol{D} = 0. \tag{5.36}$$

We can write

$$\frac{K_c}{l_c}\nabla^* \cdot \boldsymbol{T}^* + 2\zeta_n \omega_n \omega_c l_c \boldsymbol{I} \boldsymbol{u}_t^* = \rho l_c \omega_c^2 \boldsymbol{u}_{tt}^* \tag{5.37}$$

$$\frac{D_c}{l_c}\bar{\nabla} \cdot \bar{\boldsymbol{D}} = 0 \tag{5.38}$$

where the $(\cdot^*)$ sign represents non-dimensional quantities. Setting $K_c^* = \frac{K_c}{l_c^2 \rho \omega_c^2}$ and $\omega_n^* = \frac{\omega_n}{\omega_c}$ yields

$$K_c^* \nabla^* \cdot \boldsymbol{T}^* + 2\zeta_n \omega_n^* \boldsymbol{I} \boldsymbol{u}_t^* = \boldsymbol{u}_{tt}^*. \tag{5.39}$$

This equation can be specialized for the laminate and for the teflon insert introducing the quantities

$$\begin{aligned} K_c^{lam^*} &= \frac{K_c^{lam}}{l_c^2 \rho^{lam} \omega_c^2} \\ K_c^{tef^*} &= \frac{K_c^{tef}}{l_c^2 \rho^{tef} \omega_c^2} \\ \omega_n^{lam^*} &= \frac{\omega_n^{lam}}{\omega_c} \\ \omega_n^{tef^*} &= \frac{\omega_n^{tef}}{\omega_c} \end{aligned} \tag{5.40}$$

so that

$$\begin{aligned} K_c^{lam^*} \nabla^* \cdot \boldsymbol{T}^{lam^*} + 2\zeta_n^{lam} \omega_n^{lam^*} \boldsymbol{I} \boldsymbol{u}_t^* &= \boldsymbol{u}_{tt}^* \\ \nabla^* \cdot \boldsymbol{D}^{lam^*} &= 0 \end{aligned} \tag{5.41}$$

and

$$\begin{aligned} K_c^{tef^*} \nabla^* \cdot \boldsymbol{T}^{tef^*} + 2\zeta_n^{tef} \omega_n^{tef^*} \boldsymbol{I} \boldsymbol{u}_t^* &= \boldsymbol{u}_{tt}^* \\ \nabla^* \cdot \boldsymbol{D}^{tef^*} &= 0. \end{aligned} \tag{5.42}$$

The constitutive law for the piezoelectric actuator and sensor read (Eqs. (5.11) and (5.12)):

$$\boldsymbol{D} = (\boldsymbol{p} - \boldsymbol{d}\boldsymbol{c}\boldsymbol{d}^\intercal)\,\boldsymbol{E} + \boldsymbol{d}\boldsymbol{c}\boldsymbol{S}, \tag{5.43}$$

$$\boldsymbol{T} = -\boldsymbol{c}\boldsymbol{d}^\intercal \boldsymbol{E} + \boldsymbol{c}\boldsymbol{S}. \tag{5.44}$$

Introducing the matrices $\boldsymbol{h}$ and $\boldsymbol{g}$ as

$$\boldsymbol{h} = \boldsymbol{p} - \boldsymbol{d}\boldsymbol{c}\boldsymbol{d}^\intercal \tag{5.45}$$

$$\boldsymbol{g} = \boldsymbol{d}\boldsymbol{c} \tag{5.46}$$

the above equations become

$$\boldsymbol{D} = \boldsymbol{h}\boldsymbol{E} + \boldsymbol{g}\boldsymbol{S} \tag{5.47}$$

$$\boldsymbol{T} = -\boldsymbol{g}^\intercal \boldsymbol{E} + \boldsymbol{c}\boldsymbol{S} \tag{5.48}$$

together with their nondimensional form

$$D_c \boldsymbol{D}^* = \boldsymbol{h} E_c \boldsymbol{E}^* + \boldsymbol{g}\boldsymbol{S} \tag{5.49}$$

$$K_c \boldsymbol{T}^* = -\boldsymbol{g}^\intercal E_c \boldsymbol{E}^* + \boldsymbol{c}\boldsymbol{S}. \tag{5.50}$$

Defining $\boldsymbol{h}^* = \frac{E_c \boldsymbol{h}}{D_c}$ and $\boldsymbol{g}^* = \frac{\boldsymbol{g}}{D_c}$ yields

$$\boldsymbol{D}^* = \boldsymbol{h}^* \boldsymbol{E}^* + \boldsymbol{g}^* \boldsymbol{S} \tag{5.51}$$

$$\boldsymbol{T}^* = -\frac{D_c}{K_c} \boldsymbol{g}^{\intercal^*} \boldsymbol{E} + \frac{D_c}{K_c} \boldsymbol{c}\boldsymbol{S}. \tag{5.52}$$

The equilibrium equations can thus be written as

$$\begin{aligned} \nabla \cdot \boldsymbol{T}^{pzt} &= \rho^{pzt} \boldsymbol{u}_{tt} \\ \nabla \cdot \boldsymbol{D}^{pzt} &= 0. \end{aligned} \tag{5.53}$$

In a way similar to the procedure followed for the non-piezoelectric part of the domain, we introduce the quantity $K_c^{pzt^*} = \frac{K_c^{pzt}}{l_c \rho^{pzt} \omega_c^2}$ to obtain

$$\begin{aligned} K_c^{pzt^*} \nabla^* \cdot \boldsymbol{T}^{pzt^*} &= \boldsymbol{u}_{tt}^* \\ \nabla^* \cdot \boldsymbol{D}^{pzt^*} &= 0. \end{aligned} \tag{5.54}$$

Chapter 6

Numerical Analysis and Formulation of the ultrasonic SHM Procedure.

A theoretical approach towards understanding the physics involved in the phenomena related to the identification of some form of damage in a structural system is a necessary step towards the subsequent design of an effective SHM strategy. Due to its inner complexity, this becomes particularly true when the use of ultrasonic waves constitutes the key element of a damage detection procedure. To this end a detailed analysis of the generation and propagation of elastodynamic waves in solids is carried out in Chapters 1,2 and 3.

In the present work, in the context of the proposed SHM procedure, we aim at a design phase. Therefore, numerical simulations play a crucial role in the ultimate definition of the damage detection approach. The use of numerical codes indeed allows to implement and consequently to analyze physical models characterized by a higher degree of complexity with respect to the purely theoretical models, where a certain level of abstraction in tackling the problem is required, resulting in a loss of the predictive capabilities of finer details. Enabling a detailed analysis of the phenomena of interest, numerical simulations can thus be used to optimize the performance of the SHM methodology under study in terms of both its effectiveness and invasivity for the hosting structure.

In this chapter, two- and three-dimensional numerical analyses of the elastodynamic field generated by a piezoelectric disk and sensed by a ring-shaped PZT in presence of a delamination (represented by a teflon insert) are carried out. The obtained results are then discussed and commented, paving the way to a detailed SHM routine. A differential evolutionary algorithm-based optimization process is also implemented to improve the performances of the proposed damage detection procedure.

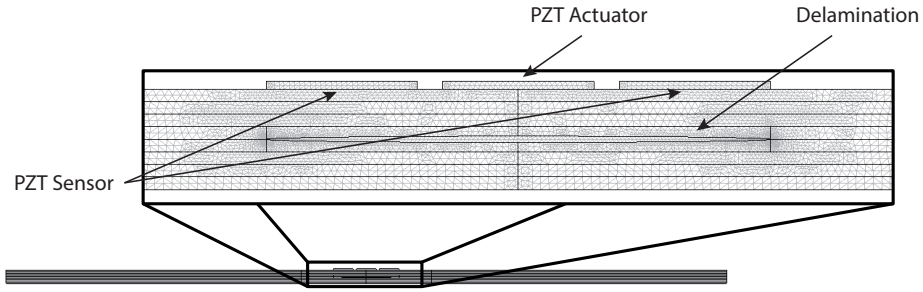

Figure 6.1: The 2D numerical model: the teflon-made delamination and the piezoelectric transducers are shown in greater details in the zoomed-in region.

6.1 The 2D model

Numerical simulations are implemented using the software COMSOL Multiphysics®: the choice of this particular numerical code to perform the numerical tests is due, among other considerations, to the possibility offered to directly implement in the software the governing equations of the problem in its strong form (see Section 5.7). This allows to obtain a full description of the physics of the problem, as both the dynamics of the composite laminate and the electromechanical coupling characterizing the piezoelectric transducers are implemented in detail, resulting in an accurate and realistic representation of the problem at hand. As stated above, numerical simulations are firstly implemented in a two-dimensional domain, as this results in a lower complexity of the model geometry and, consequently, in minor requirements in terms of computational costs and simulation times.

6.1.1 Model description

A representation of the two-dimensional numerical model is shown in Fig. 6.1: it consists of a cross-section of the composite laminate considered where the piezoelectric transducers are located. The PZT actuator, in particular, is represented by a rectangular domain positioned

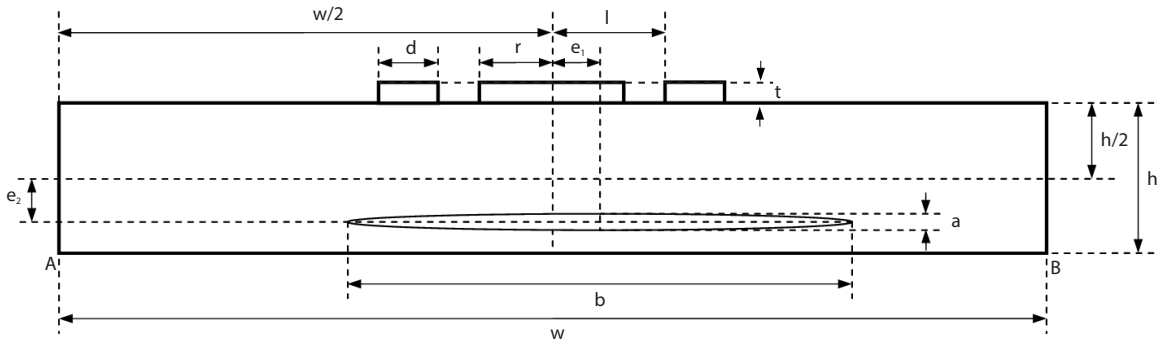

Figure 6.2: Schematic of the 2D numerical model.

Ceramic Type	PIC 255	PIC 151
Span ($2 \times r$)	$3{\cdot}10^{-3}$ m	$3{\cdot}10^{-3}$ m
Thickness	$1.5{\cdot}10^{-4}$ m	$1.5{\cdot}10^{-4}$ m
Density	7800 kg/m^3	7800 kg/m^3
d_{33}	$400{\cdot}10^{-12}$ C/N	$500{\cdot}10^{-12}$ C/N
d_{31}	$-180{\cdot}10^{-12}$ C/N	$-210{\cdot}10^{-12}$ C/N
d_{15}	$550{\cdot}10^{-12}$ C/N	$400{\cdot}10^{-12}$ C/N
$\varepsilon_{33}/\varepsilon_0$	1750	2400

Table 6.1: Geometrical and electromechanical properties of the PZT actuator and sensor shown in second and third column, respectively.

on the top surface of the composite plate, as clearly visible in the picture. At its sides, the cross-section of the ring-shaped PZT sensor (represented by two rectangular sub-domains) can be noticed. With respect to the quantities r, l, d and t reported in Fig. 6.2, the values of 1.5 mm, 2 mm, 3 mm and 0.15 mm are assumed, respectively. All geometric and electromechanical parameters characterizing the piezoelectric transducers are reported in Table 6.1.

Underneath the piezoelectric transducer, the laminated plate cross-section is modeled. it consists of an 8-layer Graphil 34-600/NTC301 composite laminate realized with carbon fibers and epoxy matrix and with a symmetric stacking sequence of $[0°/45°/90°/135°]_s$. As for its geometric parameters, a thickness $h = 25.4$ mm is considered, while the span $w = 0.11$ m is taken into account (i.e, ten times the delamination diameter $b = 0.01$ m (plus its own length). It is assumed that the delamination span is about three times the PZT

Composite plate	Graphil 34-600/NTC301
Span	$1.408{\cdot}10^{-1}$ m
Thickness	$2.54 \cdot 10^{-3}$ m
Lamination sequence	$[0°/45°/90°/135°]_s$
Young's modulus E_1	137.137 GPa
Young's modulus E_3	9.308 GPa
Poisson's ratio ν_{13}	0.304
Poisson's ratio ν_{31}	0.017
Density	1568 kg/m^3

Table 6.2: Geometrical and mechanical properties of the Graphil 34-600/NTC301 composite laminate.

actuator diameter ($\frac{b}{2r} = 3.33$). A value of $a = 0.625$ mm is assumed for the delamination thickness (i.e., half of the thickness of a single lamina of the plate). The complete mechanical properties of the composite plate are reported in Table 6.2.

The equations that define the problem are those described in Sections 5.3.2, 5.6 and 5.7: appropriate boundary conditions have to be defined to achieve a closed mathematical representation of the problem. A stress-free condition is imposed on all boundaries, with the exception of the common boundaries where the continuity of the displacement is numerically enforced. A null value of the voltage is prescribed at all the four boundaries of the plate (including those parts which are in common with the PZTs), while zero electrical displacement is imposed at the vertical sides of all PZTs and at the sensor upper boundary. The values assumed by the excitation signal are prescribed at the top surface of the actuator. Both horizontal and vertical displacements denoted by u_1 and u_3, are constrained at A in Fig. 6.2, while only the vertical displacement u_3 is prevented in B.

As final remark it is important to emphasize that, in consonance with Section 5.7, the governing equations of the problem are implemented in the numerical model in non-dimensional form as this prevents issues concerning the numerical stability of the model itself, positively affecting its convergence in the time and space domain. As natural consequence of this considerations, the space dimensions of the model are made non-dimensional with respect to the delamination diameter b, while the period T of the excitation signal is considered as nondimensional parameter for the simulation time. The value $V_o = 1$ Volt is considered to

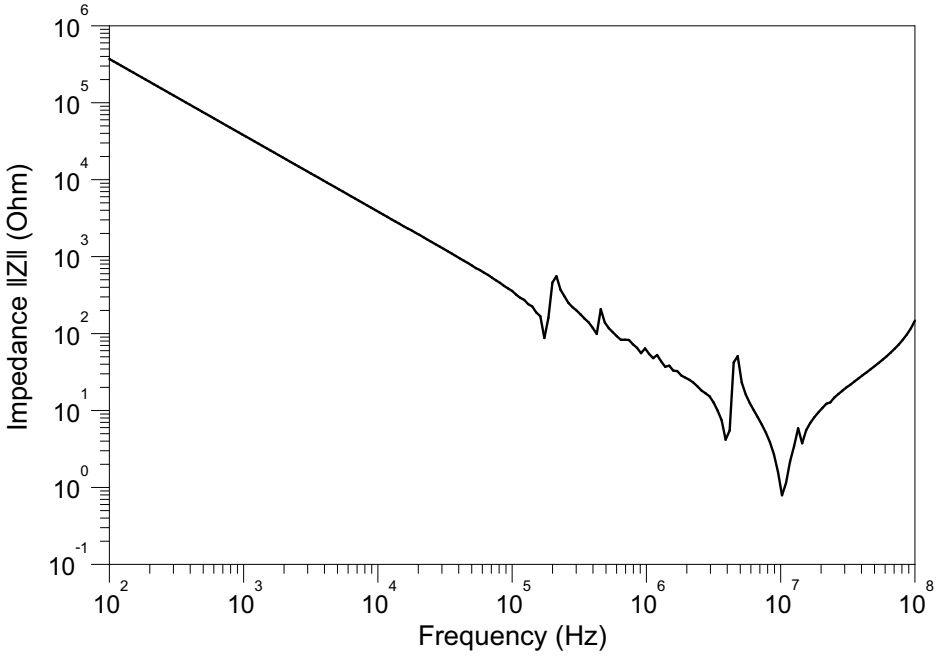

Figure 6.3: Experimentally estimated impedance of the PZT actuator.

estimate the nondimensional voltage V^*.

6.1.2 Optimal excitation signal - Modal analysis

Before proceeding with the study of the space and time convergence of the numerical model, a few more words need to be spent about the design of the excitation signal adopted in the present SHM procedure: in particular, some more physical insight is to be achieved about the definition of its frequency content.

In Section 5.5 a minimum frequency characterizing the input signal was defined as

$$f_{min} = \frac{c_P^{(3)}}{2h_{layer}} \tag{6.1}$$

Substituting the values of Table 6.2 in (6.1) yields $f_{min} = 3.34$ MHz. In addition, it was stated that with a PZT actuator, a resonance effect may be used to improve its performance. To do so, the frequency content of the excitation signal has to be set equal to the eigenfrequency of that eigenmode which results to be more excited during the actuating process (i.e., by the imposition of a certain voltage on the upper free surface of the actuator). From the point of view of the electrical characterization of the piezoelectric transducer, this resonance condition results in a minimum in the absolute value of the actuator impedance. This information can be obtained experimentally using an impedance analyzer: the variation of the absolute value of the impedance $\parallel Z_a \parallel$ with the frequency of the excitation signal is shown in Fig. 6.3, where a PZT disk characterized by the geometric and electromechanical parameters reported in Table 6.1 and attached on the top of the composite laminate is considered. A global minimum in the absolute value of the impedance is located at the frequency $f_{res} = 8.00$ MHz. To gain a better understanding of this phenomenon, a modal analysis of the piezoelectric actuator is numerically carried out. The actuator is modeled with its lower surface attached to an elastic foundation of given stiffness acting both in the in-plane and in out-of-plane directions, which prevents any rigid displacement of the PZT. A fictitious value of the stiffness is assumed (namely, a staring value of $K_{soil} = 10^4$ N is considered, successively increased to $K_{soil} = 10^7$ N to analyze the dependence of the obtained results on the foundation stiffness, see Fig. 6.4) so that the convergence of the numerical model is granted.

Results of the modal analysis are shown in Fig. 6.5: the lowest nine mode shapes are shown. The lowest four are associated to the effects of the elastic foundation and their corresponding eigenfrequencies belong to the KiloHertz range. The fifth to the ninth mode shapes describe the actual dynamics of the actuator. Particular attention is drawn on the sixth mode shape characterized by a frequency of 7.96 MHz, which turns out to be very close to the one indicating a minimum in the impedance in Fig. 6.3, minimum located at a

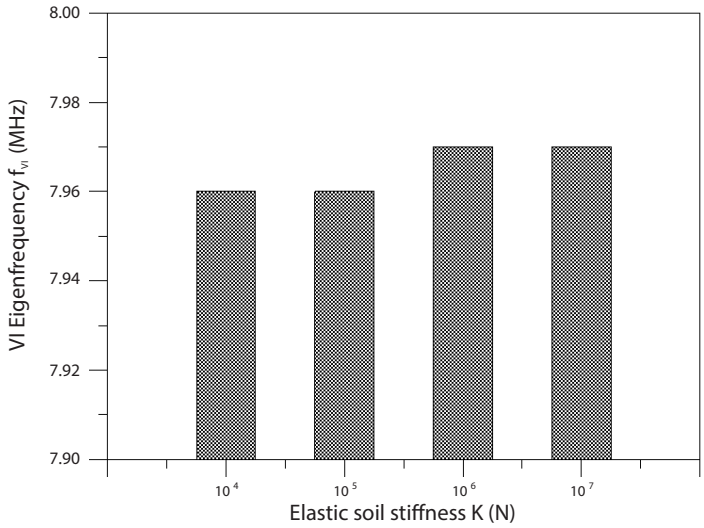

Figure 6.4: Variations of the sixth eigenfrequency f_{VI} with the elastic soil stiffness value K: no significant dependence of f_{VI} on K is noticeable.

frequency of 8.00 MHz. An additional proof indicating that the sixth eigenmode represents the minimum in the impedance value can be obtained observing Fig. 6.6. Here, the vertical displacement field u_3 generated by the quasi-static imposition of a voltage at the upper surface of the actuator is shown: the deformed shape is similar to that exhibited by the sixth eigenmode. The analysis is completed by considering a 4.5 cycles toneburst with a frequency of $f = 8.00$ MHz as excitation signal for the SHM procedure at hand. The other feature of the input signal to be defined is the amplitude. To this end, Eq. (5.19) is used to define the maximum value of the Voltage which can be withstanded by the PZT-laminate interface. With the values reported in Table 6.1, we obtained

$$V_{max} = \frac{4r^2 d_{31} \tau_{max}}{C} = 19.2\text{V} \tag{6.2}$$

where $\tau_{max} = 10$ MPa. A conservative value of 15 Volts is chosen as maximum amplitude of the excitation signal.

6.1.3 Space and time convergence

The subsequent step in the implementation of a numerical model consists in carrying out a convergence analysis. Here, space and time convergence of the proposed model are investigated. To do so, the value of the speed of sound in the horizontal and in the vertical

direction are estimated using the Newton-Laplace equation:

$$\begin{aligned} c_1 &= \sqrt{\frac{E_1}{\rho}} \\ c_3 &= \sqrt{\frac{E_1}{\rho}} \end{aligned} \tag{6.3}$$

where E_1 and E_3 represent the Young's moduli of the single lamina of the plate respectively along the fibers direction and in the orthogonal direction; ρ is the laminate density. The sound speeds c_1 and c_3 can be made nondimensional according to

$$\begin{aligned} c_1^* &= \frac{c_1}{b/T} \\ c_3^* &= \frac{c_3}{b/T} \end{aligned} \tag{6.4}$$

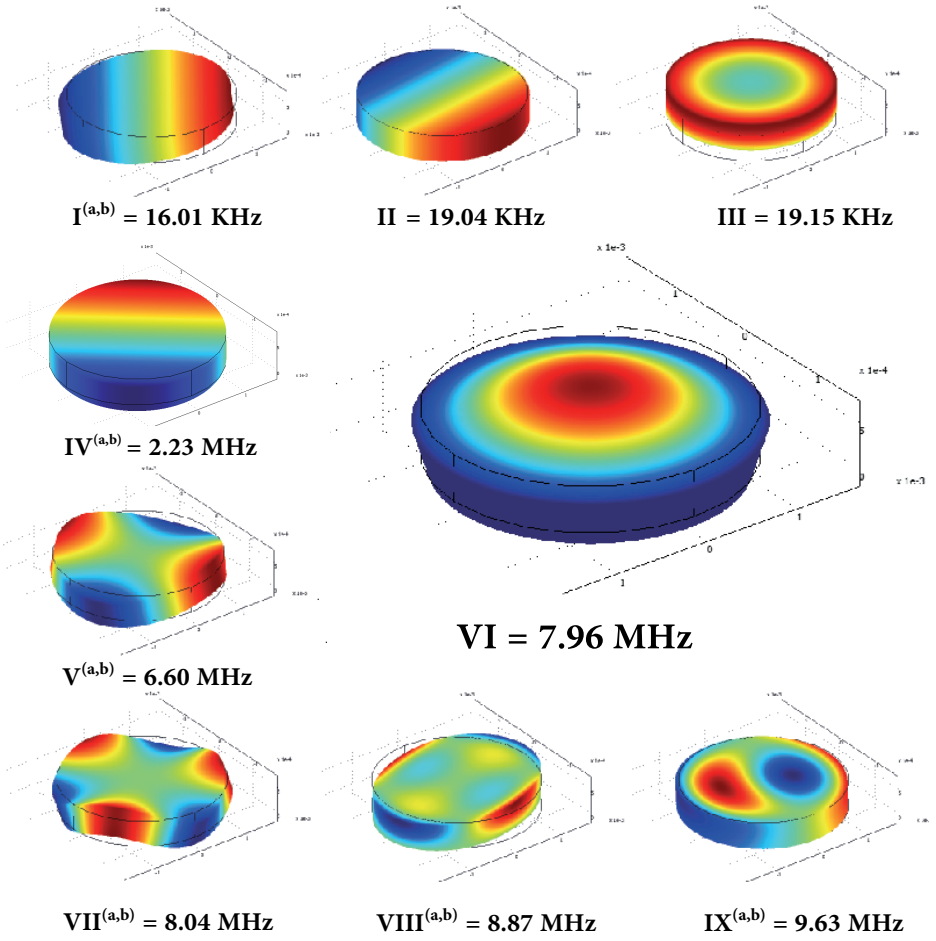

Figure 6.5: The vertical displacement field u_3 of the lowest nine eigenmodes of the piezoelectric actuator: eigenmodes from one to four describe the elastic foundation dynamics (whose eigenfrequencies are confined to the KHz range) while the higher eigenmodes are characteristic of the PZT actuator dynamics.

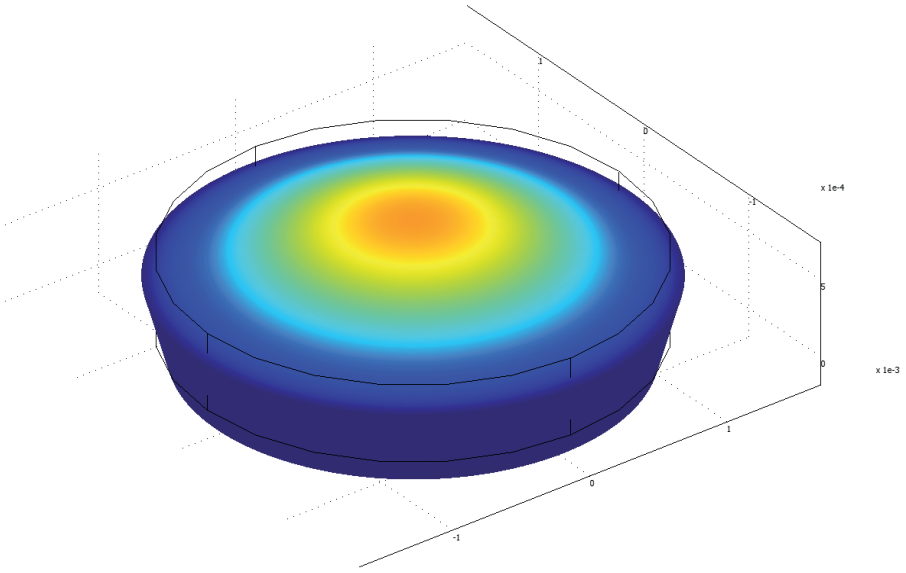

Figure 6.6: The vertical displacement field u_3 generated by the quasi-static imposition of a voltage on the upper surface of the PZT actuator.

where b is the delamination diameter and T is the period of the excitation signal. Two characteristic wavelength can thus be introduced as $\lambda_1 = \frac{c_1}{f}$ and $\lambda_3 = \frac{c_3}{f}$, with $f = \frac{1}{T}$. In nondimensional form the wavelengths become:

$$\begin{aligned} \lambda_1^* &= \frac{\lambda_1}{b} = \frac{c_1}{b/T} = c_1^* \\ \lambda_3^* &= \frac{\lambda_3}{b} = \frac{c_3}{b/T} = c_3^* \end{aligned} \tag{6.5}$$

Given that $E_1 > E_3$ (see Table 6.1), it follows that $\lambda_3 < \lambda_1$ which leads us to assume

$$\Delta x_{max}^* = \frac{\lambda_3^*}{2} = \frac{c_3^*}{2} \tag{6.6}$$

as the maximum value for the nondimensional space-step Δx^*. As for the time convergence of the numerical model, the Courant-Friedrichs-Lewy (CFL) condition reads

$$CFL = \frac{\Delta x}{c_3} \tag{6.7}$$

and in the nondimensional form for the maximum value of the space-step

$$CFL_{max}^* = \frac{\Delta x_{max}^*}{\bar{c}_3} \tag{6.8}$$

The maximum value for the non-dimensional time-step Δt^* is thus assumed to be

$$\Delta t_{max}^* = \frac{CFL_{max}^*}{2}. \tag{6.9}$$

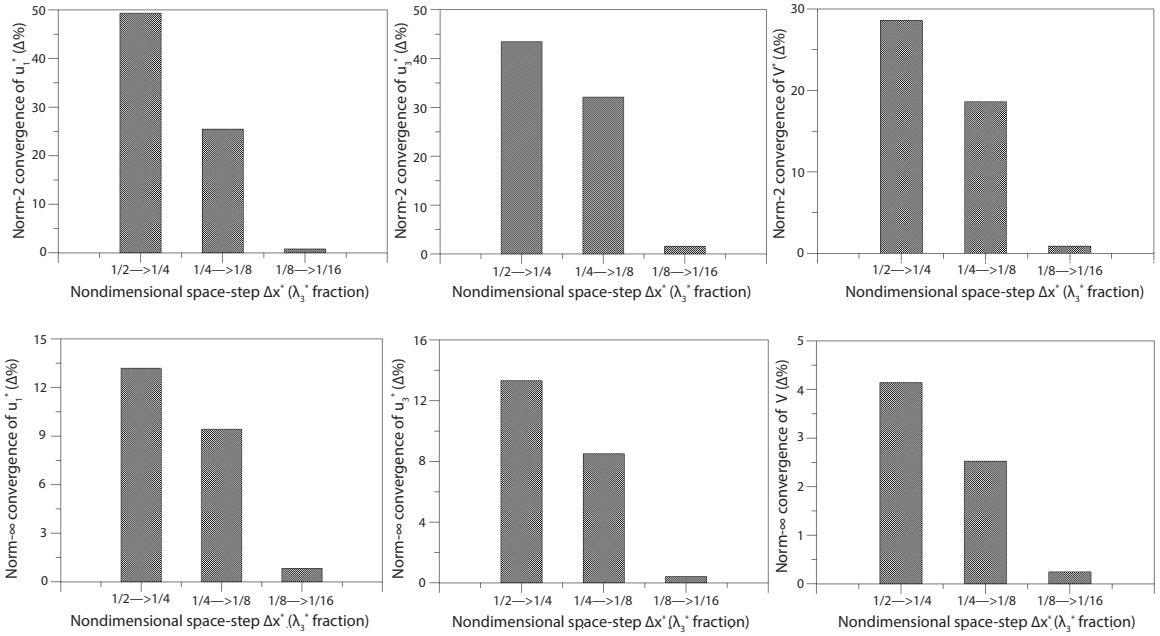

Figure 6.7: Space convergence of the numerical model: in the first row, the percent variation of the norm-2 difference of two consecutive solutions obtained decreasing by a factor of two the space-step is shown for the horizontal and vertical displacement fields u_1^* and u_3^* (acquired at points A and B in Fig. 6.9) and for the non-dimensional voltage V^* (acquired at point C). The point-wise convergence in the space domain of the numerical model (expressed as the percent variation of the maximum point-wise difference of two consecutive solutions) for the same quantities is reported in the second row.

As for the overall duration of the simulations, this is assumed to be equal to the time needed for a wave propagating with speed c_3 to travel back and forth through the plate thickness for three times:

$$T^*_{overall} = 3\frac{h}{c_3^* b}. \tag{6.10}$$

The convergence analysis, both in the time and space domains, is performed estimating the point-wise and global convergence of a given quantity by decreasing by a factor of two the time the space steps. It is important to emphasize that a linear variation of the space mesh size in the horizontal direction with a characteristic ratio of 1/10 is implemented, starting from the Δx^* value adopted at the plate center and increasing towards the model boundaries. For this analysis, the values of $e_1 = e_2 = 0$ are considered, i.e, the delamination is located in the plate midplane, exactly underneath the pair of piezoelectric transducers. Results can be observed in Fig. 6.7: in the first row, the point-wise convergence of the nondimensional horizontal and vertical displacement fields u_1^* and u_3^* (acquired at points A and B in Fig. 6.9) and of the nondimensional voltage V^* (acquired at point C) with respect to the space

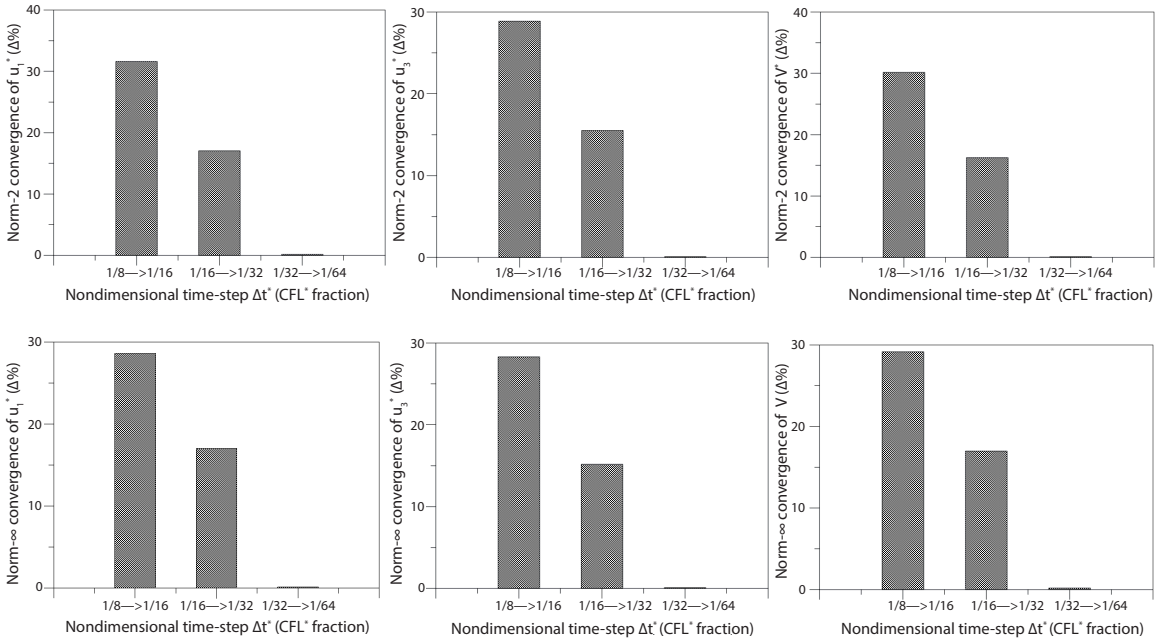

Figure 6.8: Time convergence of the numerical model: in the first row, the percent variation of the norm-2 difference of two consecutive solutions obtained decreasing by a factor of two the time-step is shown for the horizontal and vertical displacement fields u_1^* and u_3^* (acquired at points A and B in Fig. 6.9) and for the non-dimensional voltage V^* (acquired at point C). The point-wise convergence in the time domain of the numerical model (expressed as the percent variation of the maximum point-wise difference of two consecutive solutions) for the same quantities is reported in the second row.

step dimension is shown, while the global convergence in the space domain of the numerical model in terms of the same quantities is reported in the second row. It can be observed that no appreciable variation of the solutions is obtained when the nondimensional space step Δx^* is decreased from 1/8 to 1/16 of the nondimensional wavelength λ_3^*, meaning that convergence is achieved. Similar results for the time convergence are shown in Fig. 6.8: here no appreciable variation of the non-dimensional horizontal and vertical displacement fields u_1^* and u_3^* and of the non-dimensional voltage V^* (acquired at points A, B and C,

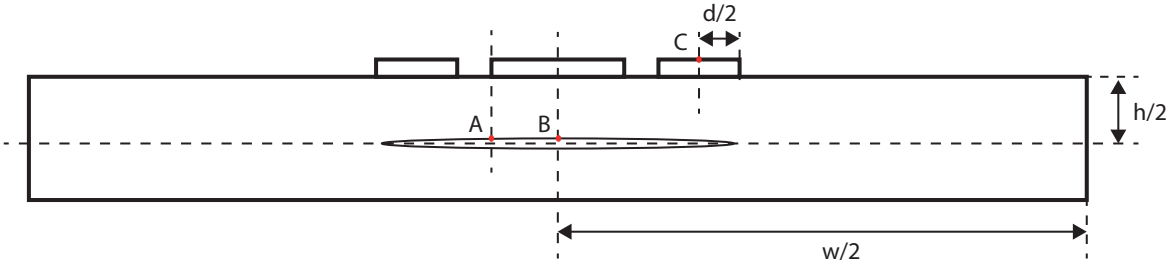

Figure 6.9: The 2D numerical model tested for the convergence analysis: the acquisition points A, B and C for the displacement fields u_1^* and u_3^* and the voltage V^* are marked in red.

respectively) is obtained when the non-dimensional time-step Δt^* is decreased from 1/32 to 1/64 of the non-dimensional CFL* condition, thus implying that convergence is reached in the time domain. It can be finally concluded that for the following space and time steps

$$\begin{aligned} \Delta x^* &= \frac{\lambda_3^*}{8} \\ \Delta t^* &= \frac{CFL^*}{32} \end{aligned} \tag{6.11}$$

numerical convergence is achieved for the implemented model.

6.1.4 Preliminary numerical tests

Numerical simulations are carried out for the seven different damage scenarios summarized in Table 6.3: each one of them is characterized by a different depth of the delamination (from case I, with the delamination located between the first and the second layer of the laminate, to case VII, where the damage is located between the seventh and the eighth layers), while all other geometric parameters defining the plate and the actuating/sensing system are left unchanged.

Results are shown in Fig. 6.10. The time histories of the voltage acquired by the PZT sensor for the damage cases I to VII are shown in Figures (a) to (g), respectively: the undamaged system response is shown in (g). All the time histories are characterized by the presence of a wave appearing at about 3 s*, whether a damage is present or not. This implies that the mentioned wave is not particularly affected by the delamination presence and location under the laminate surface, making it possible to consider it a surface wave, namely, the Rayleigh wave generated by the PZT-like force density source in a half-space domain analyzed in Chapter 4. A proof confirming this conjecture is given by the comparison of the theoretical value of the Rayleigh wave speed with the value estimated from the time histories obtained with the numerical simulations. From a theoretical point of view, we have

Damage Case	Damage Position
Case I	between layers 1 and 2
Case II	between layers 2 and 3
Case III	between layers 3 and 4
Case IV	between layers 4 and 5
Case V	between layers 5 and 6
Case VI	between layers 6 and 7
Case VII	between layers 7 and 8

Table 6.3: The damage locations in the composite plate.

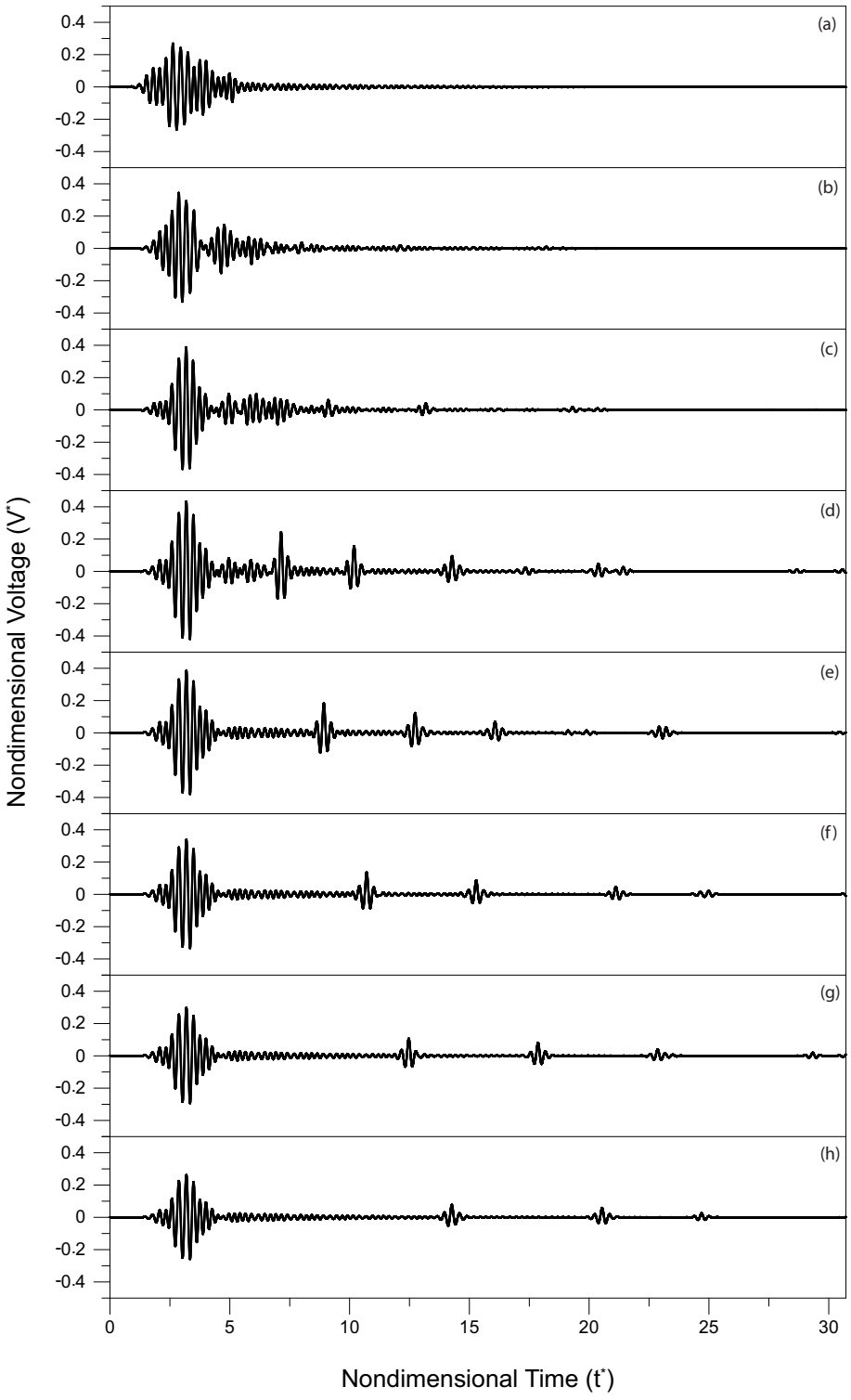

Figure 6.10: The time histories of the voltage acquired by the sensor for different damage scenarios: the delamination is located in position 1 through 7 (parts (a) through (g)). The non-damaged case is also shown in part (h).

[32]:

$$c_{R_1} = \frac{0.862 + 1.14\nu_{13}}{1 + \nu_{13}} c_{S_1} = 5367.12 \quad \text{m/s} \tag{6.12}$$

where the 1 subscript means that the value of the Young's modulus estimated in the fibers direction is used in the computation of the Rayleigh (c_R) and S waves (c_S) speeds (it is worth recollecting here that the first layer of the laminate has 0^o-oriented fibers, so that in the 2D model at hand, the value of the stiffness modulus in the first layer in the horizontal direction is exactly E_1). The estimation of c_{R_1} from the numerical results can be easily obtained dividing the traveling distance s = l-r+d/2 (i.e., the difference between the sensor middle radius) and the actuator radius, and the time corresponding to the appearance of the mentioned peaks in Fig 6.10. Results are shown in Fig 6.11: the numerically estimated speed of the analyzed waves appears to be very close to that theoretically obtained in Eq. (6.12), with an average value of c_R = 5266.07 m/s and a percent difference of 1.8%. This proves that the considered wave is a Rayleigh wave.

The most interesting feature shown in Fig. 6.10 consists, however, in the appearance of different peaks in the time histories of the voltage delivered by the sensor: in particular, a progressive time shift in their rise in the output signal is observable as the considered delamination is located in a deeper position through the plate thickness. It is important to notice, however, that no such peaks can be observed in the time histories associated with the damage cases I and II (Fig. 6.10 (a) and (b)), while some structure similar to the analyzed ones can be observed in Fig. 6.10 (c) (damage case III).

The analysis of the propagation speeds of the first and second peak appearing in Fig. 6.10 (d)-(g) similar to that carried out for Rayleigh waves, together with the theoretical considerations made in Chapter 4, leads to the identification of those waves as the P and S waves which return to the upper surface of the plate once they are reflected by the delamination /

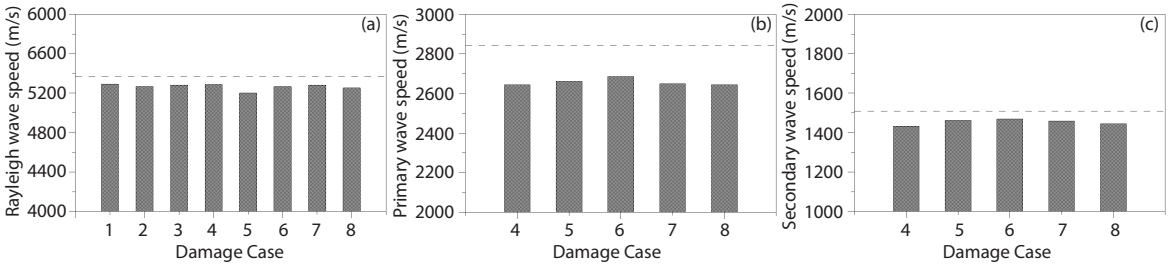

Figure 6.11: The theoretically (dot line) and numerically (columns) estimated values for the Rayleigh c_{R_1} (a), Primary c_{P_3} (b) and Secondary c_{S_3} (c) wave speeds for different damage scenarios.

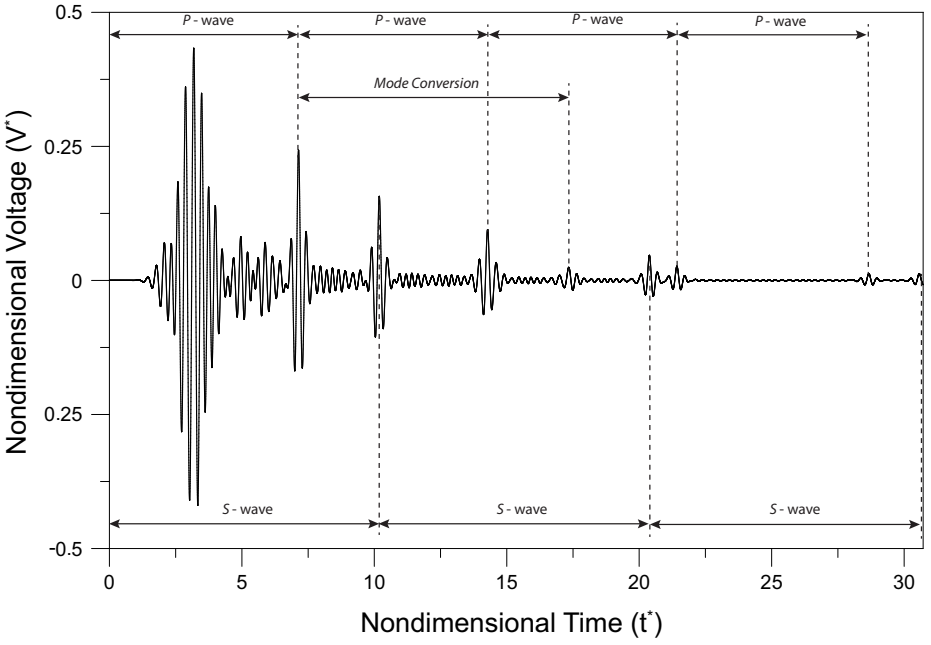

Figure 6.12: The time history of the voltage acquired by the PZT sensor is shown for the damage case VI: precise time intervals separate the different peaks, namely those driven by the same propagation speeds of P- and S-waves. Mode conversion can also be observed.

the lower surface of the laminate (see Fig. 5.4). We have that

$$\begin{aligned} c_{P_3} &= \sqrt{\frac{2\boldsymbol{\lambda}_3 + \boldsymbol{\mu}_3}{\rho}} = 2843.01 \quad \text{m/s} \\ c_{S_3} &= \sqrt{\frac{\boldsymbol{\mu}_3}{\rho}} = 1508.69 \quad \text{m/s} \end{aligned} \tag{6.13}$$

while the numerically estimated (average) values for the same quantities are $c_{P_3} = 2657.15$ m/s and $c_{S_3} = 1453.18$ m/s respectively, with a difference of -6.54% and -3.65% with respect to the values in Eq. (6.13) (Fig. 6.11(b) and (c)). It is important to stress that the Lamè constants in the through-the-thickness direction $\boldsymbol{\lambda}_3$ and $\boldsymbol{\mu}_3$ are considered in the theoretical calculations, since P and S waves propagate essentially in the normal direction.

An additional evidence that leads to conclude that the considered waves are P and S waves is given by the study of the time intervals between the main peaks appearing in Fig. 6.10 and the subsequent peaks which appear afterwards. In Fig. 6.12 the time history of the voltage acquired by the PZT sensor is shown for the damage case VI. Here it is made clear that precise time intervals separate the different peaks, namely those driven by the same propagation speeds for P and S waves. Finally, mode conversion phenomena can also be observed in Fig. 6.12. The progressive increase in time for the P wave and the S wave to arrive at the upper surface of the plate and thus to be acquired by the sensor as the considered

delamination is located deeper in the laminate leads to define the time lag between the times of arrival of the two waves as an index of state of damage of the structure, at least for the cases ranging from IV to VII. The other damage scenarios will be discussed subsequently. An index similar to that already introduced in Section 5.1 can be here adopted:

$$\mathrm{ToF}_n = 100 \cdot \frac{\mathrm{T}_{P_n} - \mathrm{T}_{S_n}}{\mathrm{T}_{P_h} - \mathrm{T}_{S_h}} \tag{6.14}$$

where T_P and T_S represent the time of arrival of P and S waves, respectively: the n and the h subscripts denote the damage case number and the healthy configuration of the system.

Results are shown in Fig 6.13: a regular increment in the values of the ToF can be noticed. In order to ascertain the role of the delamination position in determining the observed variations in the times of arrival of P and S waves, some theoretical considerations can be made. If the varying propagation path traveled by the waves is assumed to be represented as the diagonal of a rectangle having one side of constant length (the actuator-sensor distance x_1^*) and the other side which is linearly incremented (the plate top surface-delamination distance $x_{3_n}^*$), a theoretical variation of the type

$$\mathrm{T}_{P,S_n} = \frac{\sqrt{(x_1^*)^2 + (x_{3_n}^*)^2}}{c_{P,S_3}} \tag{6.15}$$

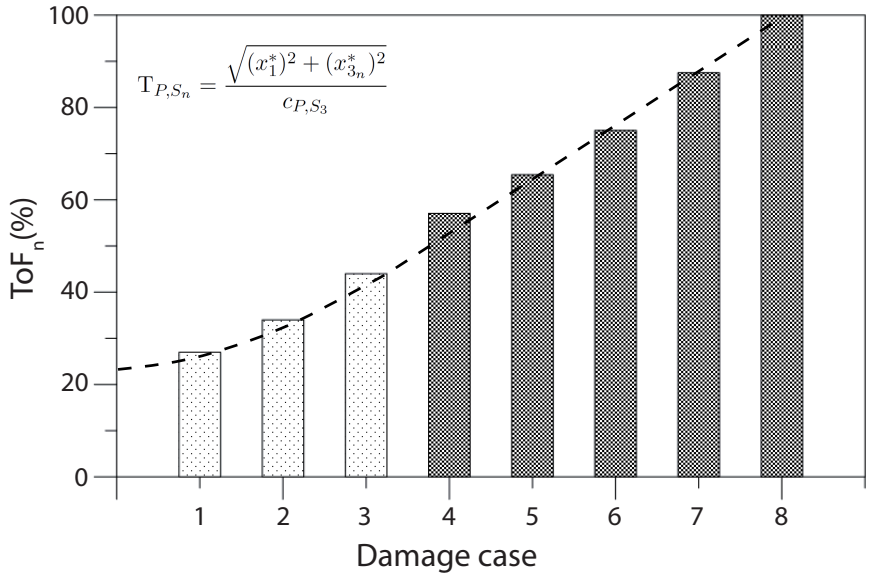

Figure 6.13: The ToF_n estimated for the different damage scenarios: column 8 represents the undamaged case. Bars from 1 to 3 indicate the simulated response of the system for cases I, II, and III. The dotted line shows the variations of the ToF_n associated with the theoretically estimated values of the times arrival $\mathrm{T}_{P,S}$ of P and S waves reported in the figure.

for the times of arrival of primary and secondary waves is obtained. Such variation is shown in Fig. 6.13 as a dotted black line: the good agreement observed with the obtained numerical results is an evidence that it is the delamination location ($x^*_{3_n}$ in (6.14)) that regulates the time of arrival of P- and S-waves at the plate upper surface and acquired by the sensor.

In Fig. 6.13 the simulated results for the damage cases I, II, and III when a phenomenology similar to the other cases was obtained are also shown. As already stated, differently from the other case studies, no primary or secondary waves appear in the associated time histories of the voltage: the study of this particular behavior is addressed in the next Section.

6.1.5 The transverse resonance effect - Definition of the SHM routine

An analysis of the time histories of the acquired voltage for the different damage cases in Fig. 6.10 shows that two main phenomenologies can be detected in the system response: for cases IV to VII, voltage peaks corresponding to the arrival of primary and secondary waves (as well as of reflected and mode-converted waves) are clearly visible, together with the appearance of wave structure corresponding to a generated Rayleigh wave which seems not to be affected by the presence of the delamination. For cases I and II, instead, no peaks corresponding to P and S waves are detectable: Rayleigh waves are still present but they appear to be superimposed to a more complex wave structure. In damage case III small peaks are visible but they do not seem to correspond to the appearance of P-waves or S-waves both in terms of propagation speed and delamination location, thus representing a transition between the two main observed behaviors.

The study in the frequency domain of the different time histories provides us with some means of interpretation of the obtained results. The power spectral density (PSD) of the acquired output signals and of the excitation signal is shown in Fig. 6.14: here, a qualitative analysis of the data reveals that the PSD associated to damage scenarios characterized by surface delaminations feature a remodulation of the frequency content of the signal, with the appearance of peaks at frequencies different from the main one (namely, 8 MHz). In particular, it is apparent that the deeper the delamination is located in the laminate, the closer the acquired voltage becomes in terms of frequency content to the input signal, with most of the power gathered about the excitation frequency.

A more quantitative analysis of this phenomenon can be achieved if the power content of the different output signals in the -3dB bandwidth about the main frequency of 8 MHz is calculated and then compared to the same quantity estimated for the input signal, as shown in Fig. 6.15. Here an additional evidence of the observed dual behavior of the system can be seen: while about 40% of the input signal power content remains confined in the -3dB bandwidth about 8 MHz for the output signals associated to damage cases IV to VII (on

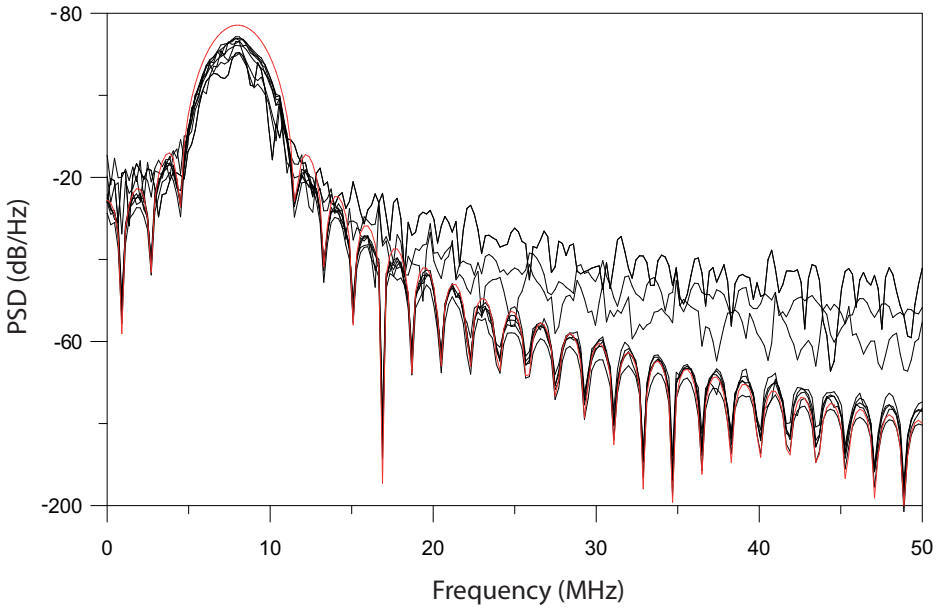

Figure 6.14: The power spectral density (PSD) of the acquired voltage for the different damage cases considered (black lines) and of the excitation signal (red line).

average), less that 10% of the described quantity stays in the mentioned bandwidth for cases I and II, implying that a strong remodulation of the power content in the frequency domain has taken place. Again, a transition behavior is observed for case III.

An interpretation of the described phenomena can be achieved if the effects of wave interference in the plate thickness are considered. As already seen in Chapter 4, the semi-circular P- and S-waves emanating from the piezoelectric actuator can be thought of as the

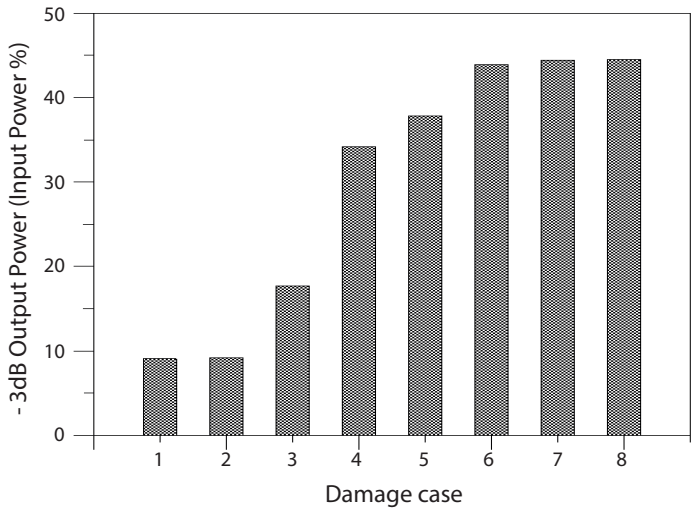

Figure 6.15: The percent power content of the output voltage in the -3 dB bandwidth about 8 MHz with respect to the same quantity estimated for the excitation signal.

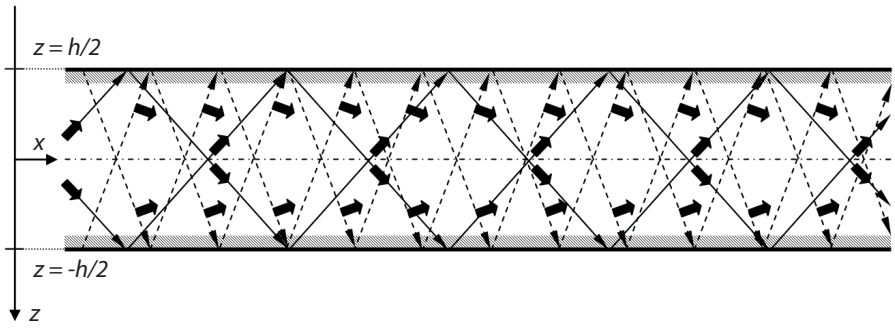

Figure 6.16: The transverse resonance effect in the plate: the plane waves in which the semicircular primary and secondary waves (in solid and dotted line, respectively) can be decomposed are reflected at the boundaries and are superimposed to the arriving waves, giving rise to a constructive and destructive interference which can modulate the power content of the original signal in the frequency domain.

envelope generated by a series of elastic plane waves propagating in different directions from the upper limit of the domain. When these waves meet the lower boundary, they are reflected (generating a wave of the other type, P or S, to fulfil the stress free condition) and start propagating in the opposite direction. In so doing, they get superimposed to the portion of the signal which is still propagating downward, giving rise to an interference effect [82, 91]. It can be demonstrated, through the use of simple trigonometric formulas [32], that only those waves that can replicate themselves being reflected at the boundary are able to survive and thus get propagated further in the in-plane direction of the plate, while a destructive interference tends to erase the rest of the waves. This phenomenon, which is driven by the incident angle of the plane waves in which the P and S waves can be decomposed, leads to the selection of certain plain waves over the others, which eventually contribute to generate standing waves in the thickness direction, and propagating in the in-plane directions. These standing waves constitute the propagation modes of the Rayleigh-Lamb waves: the described phenomenon is know as *transverse resonance* [82, 84, 32, 91, 93] (see Fig. 6.16). A consequence of the transverse resonance is that the power content of the initial wave is redistributed among the different modes that are activated by the excitation signal [135], as it is shown by Fig. 6.17 [139].

The considerations made above allow to consistently interpret the obtained results. When the delamination is located close to the plate upper surface, the thickness of the portion of the domain through which the waves can propagate becomes small enough with respect to the actuator-sensor distance (cases I and II), so that the number of reflections at the boundaries for P and S waves that can take palace before the sensor is reached is high enough to cause an effective modulation of the power content of the signals. On the contrary, when

the delamination is located in a position across the plate thickness so that the traveling distance for P- and S-waves in the laminate thickness becomes large enough with respect to the actuator-sensor distance (cases IV to VII) so that the effects associated to the transverse resonance are negligible, the power content of the signal does not suffer any evident modulation in the frequency domain with respect to the PSD of the excitation signal.

The obtained results furnish additional fundamental elements in the description of the onset and propagation of the PZT-generated elastodynamic field, paving the way to a refinement of the SHM strategy described in Chapter 5. Two different phases are well now defined in the proposed routine: (i) a first phase in which the PSD of the signal is extracted and its -3dBp power content is estimated, enabling the practitioner to state whether a surface delamination is present (cases I, II and III); (ii) a second phase in which the ToFs of P- and S- waves appearing in the signal are estimated to ascertain the presence and location of the delamination.

6.1.6 Optimization of the sensing system

An optimization procedure based on the use of differential evolutionary algorithms (EAs) was described in Section 5.4. The aim of this process is the enhancement of the damage detection capabilities of the designed SHM routine. Here the key element for identifying the presence of a delamination in the laminate thickness consists in the acquisition of the voltage

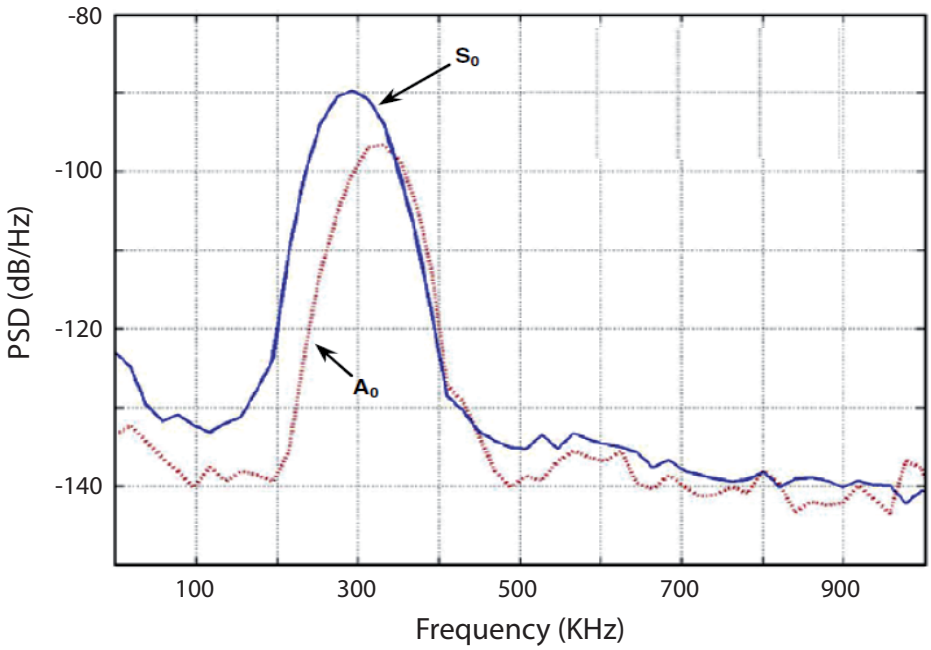

Figure 6.17: The power spectral density (PSD) of the A_0 and S_0 modes after propagating a certain distance (original excitation frequency = 300 KHz) [139].

peaks associated with the arrival of the damage/lower plate boundary-reflected primary and secondary waves. In this sense, an improvement in the detectability of the mentioned peaks in the voltage time histories acquired by the piezoelectric sensor would imply an higher sensitivity of the sensing system with respect to the presence of damage.

Denoting by V_i^P, V_i^S and V_i^{RMS} the peak values in the voltage output of the PZT sensor and its root mean square (RMS) value, respectively, the objective function for the differential evolutionary optimization algorithm above described was already defined as

$$OF = \sum_{i=1}^{I+1} \left[a_i^P \left(\frac{V_i^P}{V_i^{RMS}} - 1 \right) + a_i^S \left(\frac{V_i^S}{V_i^{RMS}} - 1 \right) \right] \tag{6.16}$$

where $I+1$ represents the number of different damage scenarios evaluated considering the same actuator/sensor configuration in terms of the defining geometric parameters plus the undamaged case: for the case at hand we have $I+1=8$. The parameters a_i^P and a_i^S were defined as the weights in the sum which take into account the wavefront attenuation with the traveled distance affecting P and S-waves: the farther is the damage location with respect to the actuator sensor pair, the higher is the value of the related weight $a_i^{P,S}$. The expressions for the displacements fields associated with P- and S-waves in Equations (4.75) and (4.76) were characterized by a $\sqrt{r^{-1}}$ dependence on the propagation distance: for this reason, the

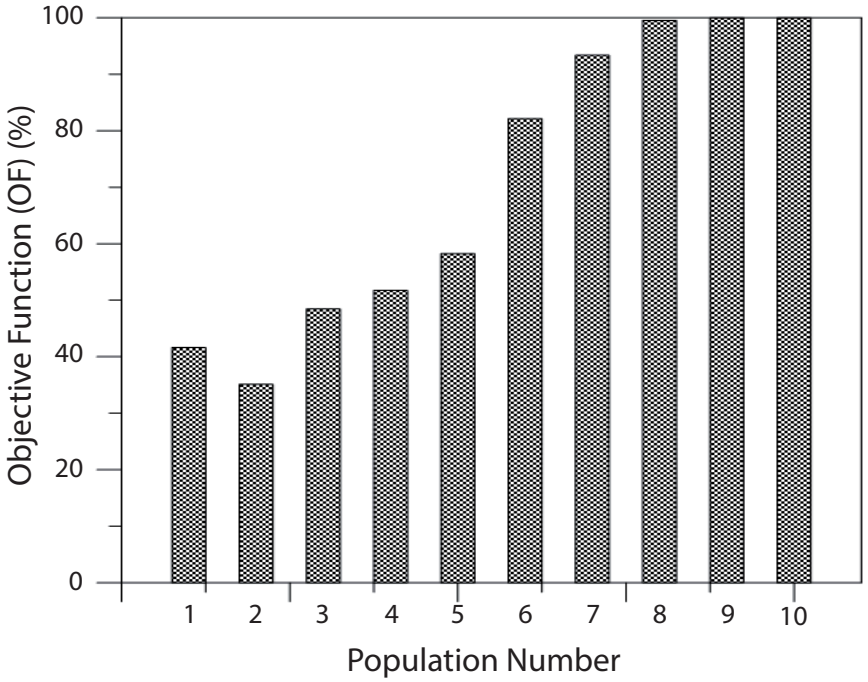

Figure 6.18: The variations of the OF (averaged over five different genes contained in each population) with respect to its value at the 10th iteration.

weights a_i^P and a_i^S are defined as

$$a_i^P = a_i^S = \sqrt{i \cdot h_{\text{layer}}} \tag{6.17}$$

where h_{layer} represents the thickness of the single lamina of the plate.

The geometric parameters chosen to be optimized are the sensor span d and its middle radius $r_s = l + d/2$: ten different populations of five elements each are generated implementing the optimization algorithm described in Section 5.4 using MATLAB® (Table 6.4). Upper and lower bounds are set for d and r_s values, to prevent the sensor from overlapping with the actuator and from being excessively large: we have that $r_s - d/2 - r - r_{tol} = r_{min}$ and $r_s + d/2 = r_{max}$ (see Fig. 6.2, where r_{tol} represents the minimum acceptable distance between the sensor and the actuator. We let $r_{tol} = 0.5$ mm, $r_{min} = 2$ mm, and $r_{max} = 10$ mm . Results are shown in Fig. 6.18: here the variations of the OF (averaged over the five different genes contained in each population) with respect to its value at the 10th iteration indicate that an optimal configuration of the sensor is reached at the 8th iteration and it is then maintained in the following generated populations. Moreover, a 20% increase with respect to the initial OF value is noticeable. The increase in the voltage values of the P- and S-waves peaks in the acquired response of the system is shown in Fig. 6.19, where no significant increase of the other portions of the system can be observed, implying an enhanced

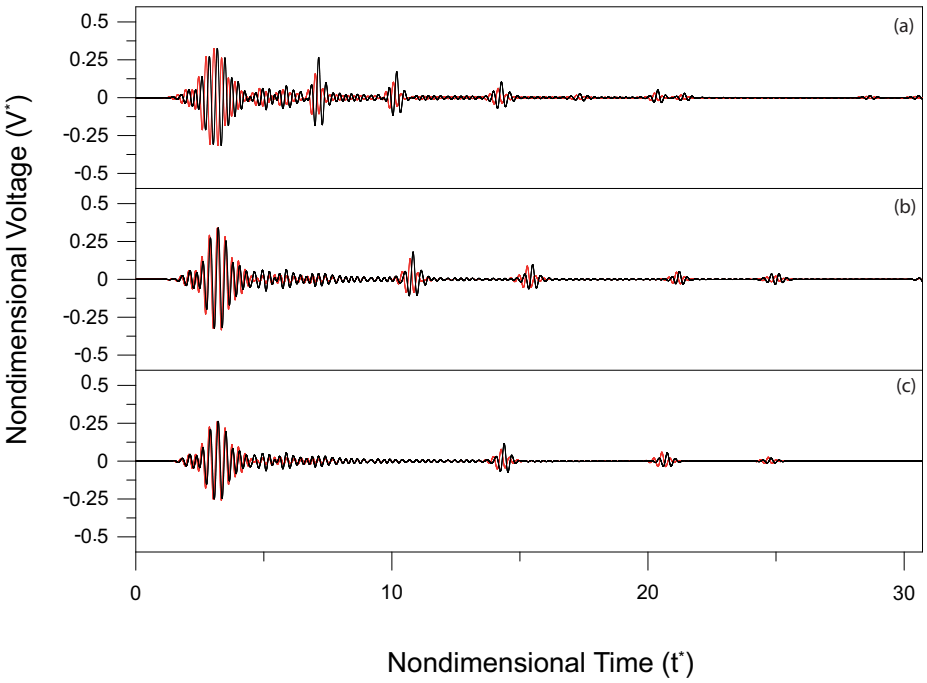

Figure 6.19: The time histories of the acquired voltage for the basic (red line) and for the optimized (black line) model: the resposnse of the system for the damage cases IV (a) and VI (b) and for the undamaged structure (c) are shown.

Population	0
d	r_s
0.1000	0.3000
0.2000	0.4000
0.3000	0.5000
0.4000	0.6000
0.5000	0.7000

Population	10
d	r_s
0.2136	0.2881
0.2136	0.2881
0.2136	0.2881
0.2136	0.2881
0.2136	0.2881

Table 6.4: The trial population (left) and the obtained population after ten iterations (right): all the elements of the 10th population are the same, indicating that the convergence of the algorithm convergence is achieved.

detectability of the delamination.

Finally, it is important to stress that the phenomena observed for the basic configuration of the sensor are maintained also in optimized case: the modulation of the power content of the output signals in the frequency domain allow to identify the presence of a surface delamination in the plate, as shown in Fig. 6.20. The presence and position of the delamination is detected when deeper damages are considered through the estimation of the ToF$_n$, as shown in Fig. 6.21.

6.1.7 Delamination extent and off-axis distance

In the damage detection procedure described in the previous sections several damage scenarios are investigated, considering a delamination located at different depths across the composite laminate thickness. All the damage cases are characterized by a value of the ratio between the delamination and the actuator diameters of about 3. Moreover, all the studied

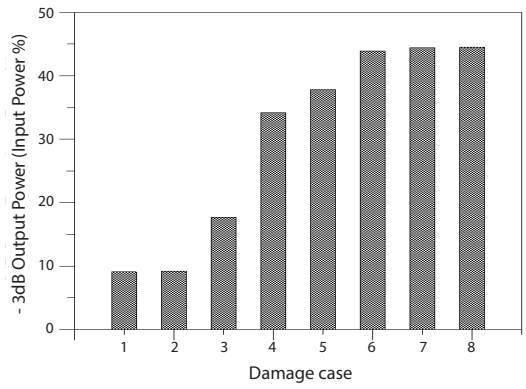

Figure 6.20: The PSD fraction of the output signals in the -3dB bandwidth.

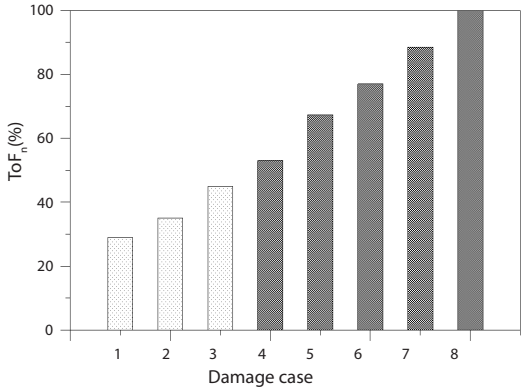

Figure 6.21: The estimated ToF$_n$ for the different damage cases of the plate.

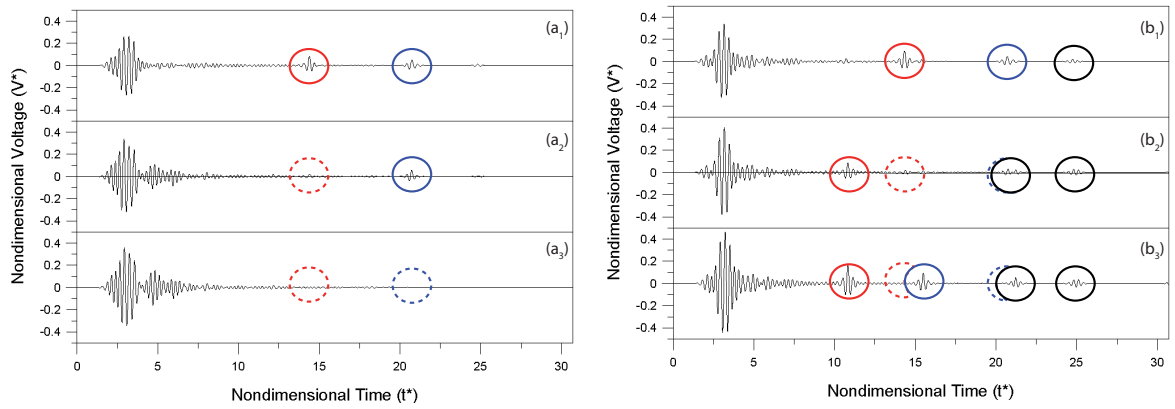

Figure 6.22: The time histories of the acquired voltage for the damage cases II (a) and VI (b) and the delamination dimensions A, C and F in Table 6.5 are shown: P-waves and S-waves are circled in blue and red, respectively (rising waves = solid line, disappearing waves = dotted line). Multiple reflections are circled in black.

delaminations are centred with the actuator, being positioned exactly underneath the pair of piezoelectric transducers attached on the plate surface.

In this Section, the effects of a variation of the damage extent and of an off-axis distance of the delamination position on the voltage acquired by the sensor are investigated. Firstly the delamination diameter is varied assuming the values reported in Table 6.5, ranging from one quarter to four times the sensor diameter. The effects of such variations are shown in Fig. 6.22 for the damage cases II (a) and VI (b), respectively. When the delamination diameter is progressively increased in II, a gradual disappearance of weak voltage peaks associated, in terms of their time location, to the arrival of P- and S-waves at the plate upper surface can be observed: in particular it is apparent that P-waves are the first to vanish as a result of the increase of the delamination dimensions, while S-waves are still present in the voltage time histories. This can be due to the different nature of the displacement fields associated to the

Test Case	$2r/b$
A	0.25
B	0.5
C	1
D	2
E	3
F	4

Test Case	$2r/e$
G	0.5
H	1
I	2
L	3

Table 6.5: The different analyzed test cases for studying the effects of the delamination extent (left) and the off-axis distance (right) on the SHM procedure.

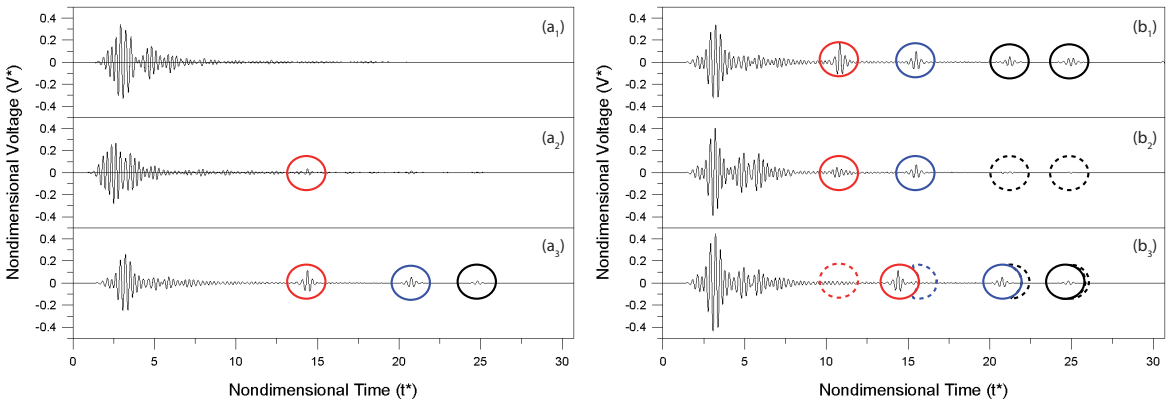

Figure 6.23: The time histories of the acquired voltage for the damage cases II (a) and VI (b) and the off-axis distance G, I and L in Table 6.5 are shown: P-waves and S-waves are circled in blue and red, respectively (rising waves = solid line, disappearing waves = dotted line). Multiple reflections are circled in black.

propagation of primary and secondary waves: P-waves space,in fact, feature the generation of a wavefront located at the center of the aperture, while S-waves appear to propagate from the sensor edges (see Chapter 4). When the delamination diameter becomes twice as large as the sensor diameter, the behavior previously analyzed is obtained. A similar phenomenology is observable when the damage case VI is analyzed (Fig. 6.22 (b)): here, as the delamination diameter is increased, a progressive transition of the acquired voltage in terms of appearance and locations in time of peaks associated to the arrival of P- and S-waves, from the undamaged case to the damage case VI is noticed.

The obtained results for all cases reported in Table 6.5 lead to conclude that a delamination extent equal to twice the actuator diameter constitutes the smallest damage (regardless of its position in the plate thickness direction) that can be detected by the proposed SHM procedure. When smaller delaminations are considered (as in (a_1)), the system response cannot be distinguished from the one obtained in the undamaged case for arbitrary positions of the damage (from I to VII), making the delamination not detectable.

In the analysis of the effects of the presence of an eccentricity between the delamination and the actuator centers, the four cases (G to L) shown in Table 6.5 are taken into account. Results can be observed in Fig. 6.23, for the damage cases II (a) and VI (b), respectively. When the off-axis distance is progressively increased in II, a gradual appearance of weak voltage peaks associated, in terms of their time location, to the arrival of P- and S-waves at the plate upper surface can be noticed. Differently from what is observed when the effects of the damage extent is considered, here P-waves are the first to appear in the voltage time histories (Fig. 6.23(a_2)) as a result of the shifting of the delamination location, while S-waves arrive only afterwards (Fig. 6.23(a_3)). As before, this behavior is be due to the different

nature of the displacement fields associated to the propagation of primary and secondary waves. When the off-axis distance becomes large enough so that the delamination is no more included in the portion of the domain which lays underneath the actuator-sensor pair, the response of the system is no longer properly distinguishable from that obtained in the undamaged case. A similar behavior is observable when the damage case VI is analyzed (Fig. 6.23 (b)): here a progressive transition of the acquired voltage in terms of appearance and locations in time of peaks associated to the arrival of P- and S-waves, from the undamaged case to the damage case VI, as the delamination diameter is increased, is noticed.

The obtained results for all cases reported in Table 6.5 lead to the conclusion that when an off-axis distance is three times the actuator diameter between the delamination center and the actuator center, the system response cannot be distinguished from that obtained in the undamaged case for arbitrary positions of the damage (from I to VII): in this case the delamination can no longer be detected.

6.2 The 3D model

The implementation of a 2D physics-based numerical model allowed to gain a better understanding of the phenomena related to the generation and propagation of elastodynamic fields in an eight-layer laminated composite plate, and to analyze in depth the interaction of primary and secondary waves with a delamination located in the laminate at different depths. In particular, the study of the changes in the system response due to variations of the delamination position and the rise of effects associated to the interference of P- and S-waves in the plate thickness led to the formulation of a two-phase SHM strategy, in which the presence of surface or deep delaminations is ascertained through the analysis of the frequency content and the ToFs of the acquired output signals.

It must be highlighted, however, that the mere implementation of a 2D numerical model is not only possible, but also sufficient to complete the analysis of a given problem (from the numerical point of view) only if three-dimensional effects can be considered negligible. The steep increase of computational costs in terms of time and numerical resources associated to the implementation of complex 3D models makes this possibility very appealing, leading to the realization of reduced-order models. In the present problem, the anisotropy of the model associated to the presence of differently oriented carbon fibers in the laminae, represents a principal source of effects connected to the three-dimensional nature of the problem. One main consequence of such anisotropy of the propagation medium is a fiber orientation dependence of the wave propagation velocity, with particular reference to Rayleigh waves, which are less subject to the averaging effect of the lamination sequence since they travel in the plate surface. By traveling mainly in the plate thickness direction, no strong orientation

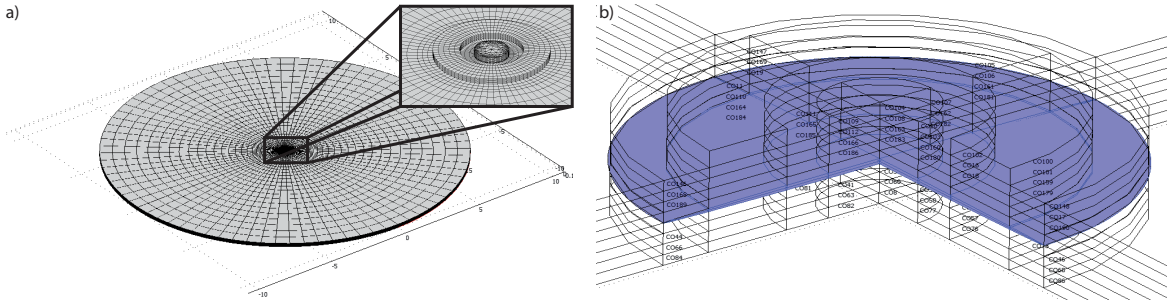

Figure 6.24: The geometry of the 3D model of the laminate with the piezoelectric actuator-sensor pair is visible on the right (a) and the teflon insert simulating the presence of a delamination in blue (b).

dependence of the propagation velocity of P- and S-waves is expected.

It is apparent, however, that the 2D model doesn't take account for such effects as they are neglected by the invoked cylindrical symmetry constituting the theoretical basis of the model itself. For this reason, the implementation of a 3D numerical model becomes necessary step of a more thorough study of the considered phenomena.

6.2.1 Model description

The geometry of the 3D model of the composite laminate is shown in Fig. 6.24 (a): it can be thought of as the assembly obtained by a revolution of the 2D model discussed in the previous sections about an axis normal to the plate midplane and passing through its center. A cross section of the 3D model containing the axis of revolution is thus characterized by the same geometric parameters defined for the 2D model reported in Tables 6.1 and 6.2, both for the laminate and the piezoelectric transducers. The PZT sensor, in particular, is defined by the optimal values obtained in Section 6.1.6 for its span and middle radius d and r_s, respectively. Also the electromechanical properties of the model coincide with those selected for the two-dimensional numerical analyses. Boundary conditions similar to those adopted for the 2D model are implemented, with the exception of the constrains on the displacements at the model edges, which are assumed to be clamped. Finally, the delamination presence is simulated inserting a teflon-made domain between the laminate layers, as shown in Fig. 6.24 (b).

The mesh for the 3D model is obtained as the revolution of that adopted in the two-dimensional case (for which a convergence analysis in the time and space domains is performed, see Section 6.1.3) about the direction defined by the unit vector normal to the plate midplane and passing through its center. Due to its demanding features in terms of required computational resources, a limited convergence analysis in the time and space domains is

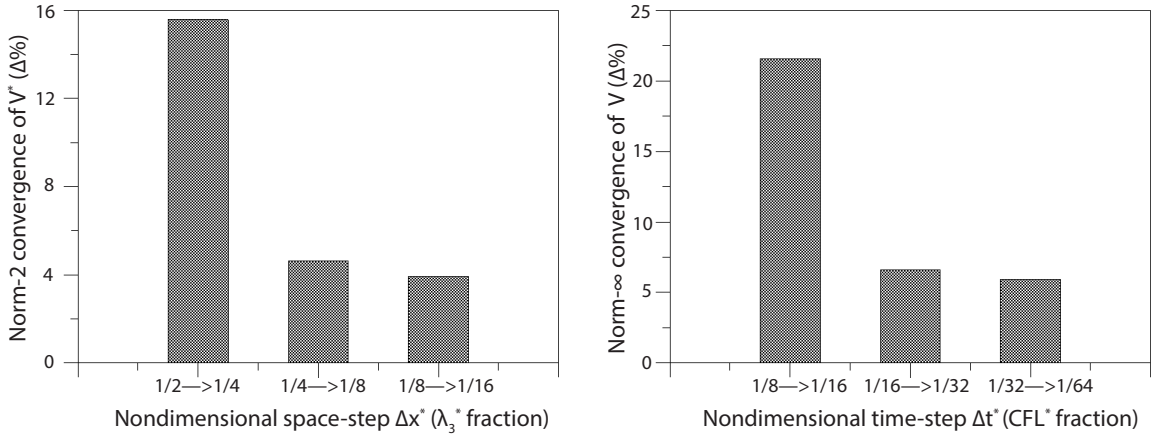

Figure 6.25: The global (left) and point-wise (right) convergence of the voltage output of the 3D numerical model: the analysis is arrested before convergence is confirmed.

performed for the 3D model. The value of the space step obtained as result of the convergence analysis for the 2D model, in fact, represents the frontier of the feasibility for the 3D numerical anlyses, since a further refinement of the model would imply too large computational times. Due to these facts, the convergence study for the three-dimensional model is arrested before numerical convergence is achieved, as shown in Fig 6.25. The accordance of the obtained numerical predictions with the results of the 2D simulations, however, is indeed

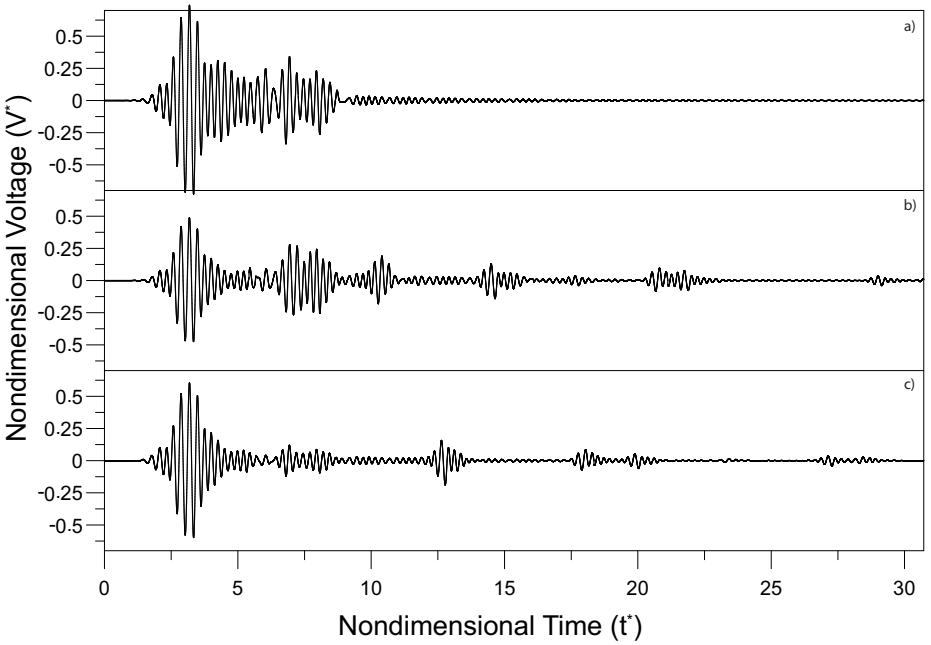

Figure 6.26: The voltage time histories of the 3D numerical model for damage locations I (a), III (b) and VI (c).

a good indication of the validity of the performed analyses.

6.2.2 Results and discussion

Results of the three-dimensional numerical simulations are shown in Fig. 6.26: here, in particular, the time histories of the voltage (acquired in the direction defined by the carbon fibers of the first layer, as in the 2D problem) for damage scenarios I (a), III (b) and VI (c) are reported. One major observation is that a behavior similar that obtained in the two-dimensional analyses can be identified: as in the previous numerical simulations, a two-regime phenomenology of the system response is present. Damage cases I and II deliver a time history of the output voltage characterized by the presence of a waves group in which a peak associated to the propagation of Rayleigh waves can be identified, together with a more complex wave structure which can be related to the effects of the interference of P- and S-waves. Moreover, a simultaneous absence of the peaks associated to the arrival to the plate upper surface of reflected primary and secondary waves is noticed. When damage cases ranging from IV to VII are taken into account, the appearance of primary and secondary waves in the voltage output signal is noticeable: again, a transition between the two regimes is observed in damage scenario III (b).

These qualitative considerations are confirmed by Fig. 6.27, where the percent of PSD in the -3dB bandwidth about the 8 MHz frequency in comparison with the same quantity estimated for the input signal is shown. As for the 2D problem, a strong modulation of the power content of the output signal is observed when surface delaminations are analyzed (damage scenarios I and II); if the delamination is located deeper in the plate, instead, a

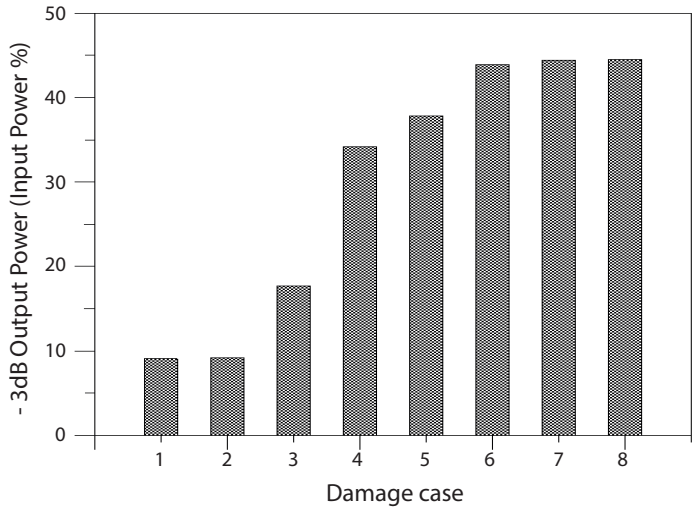

Figure 6.27: The ratio between the power content of the output and input signals in the -3dB bandwidth about 8MHz (%).

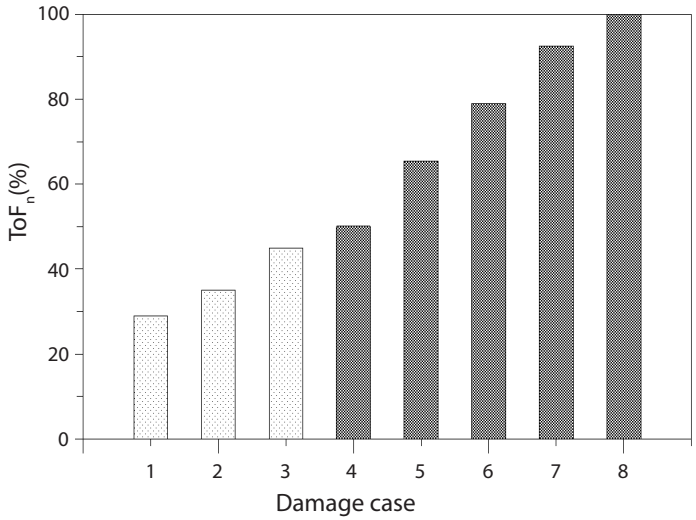

Figure 6.28: The ToF_n estimated for the different damage scenarios: column 8 represents the undamaged case. Bars from 1 to 3 indicate the simulated response of the system for cases I, II, and III.

distribution of the power among the different frequencies closer to the one estimated for the excitation signal is present. If the designed SHM routine is implemented to its second phase, estimating the time lag between the arrival of P- and S-waves at the sensor location, a behavior similar to that observed for the 2D cases is obtained, as shown in Fig. 6.28. Here, in fact, a strong dependence of the ToF on the delamination position is again found, enabling the identification of the damage location in the plate thickness when deep delaminations are analyzed. As already stated, no such analysis can be performed for surface damages, whose presence but not their exact location in the structure thickness can be detected.

Differently from the two-dimensional case, however, the peaks in the voltage signal acquired by the piezoelectric sensor associated to P- and S-waves appear to be longer in time and less definite, as the 4.5 cycles structure of the input signal is hardly recognizable in them. This particular feature is associated to slightly different time of arrival of primary and secondary waves at the sensor location due to the anisotropy of the propagation medium.

A more quantitative analysis of the dependence of the wave propagation velocity is carried out through a comparison of theoretical and numerical analysis: in particular, for Rayleigh waves, extending Eq. (6.12) on the fiber orientation (see Section 6.1.4) yields:

$$c_{R_\alpha} = \frac{0.862 + 1.14\nu_{13}}{1 + \nu_{13}} c_{S_\alpha} \tag{6.18}$$

where c_{R_α} and c_{S_α} are the propagation velocities of Rayleigh and S-waves estimated in the direction making and angle α with the carbon fibers orientation of the first layer. We can

thus write that

$$c_{S_\alpha} = \sqrt{\frac{\boldsymbol{\mu}_\alpha}{\rho}} = \sqrt{\frac{E_\alpha}{2(1+\nu_{13})\rho}} \tag{6.19}$$

The value of E_α obtained is the laminate theory described in Section 5.6 is given by

$$E_\alpha = \frac{(E_1 E_3)}{(E_3 \cos^4(\alpha) + E_1 \sin^4(\alpha) + ((4+2\nu 13)E_3)\sin^2(\alpha)\cos^2(\alpha))} \tag{6.20}$$

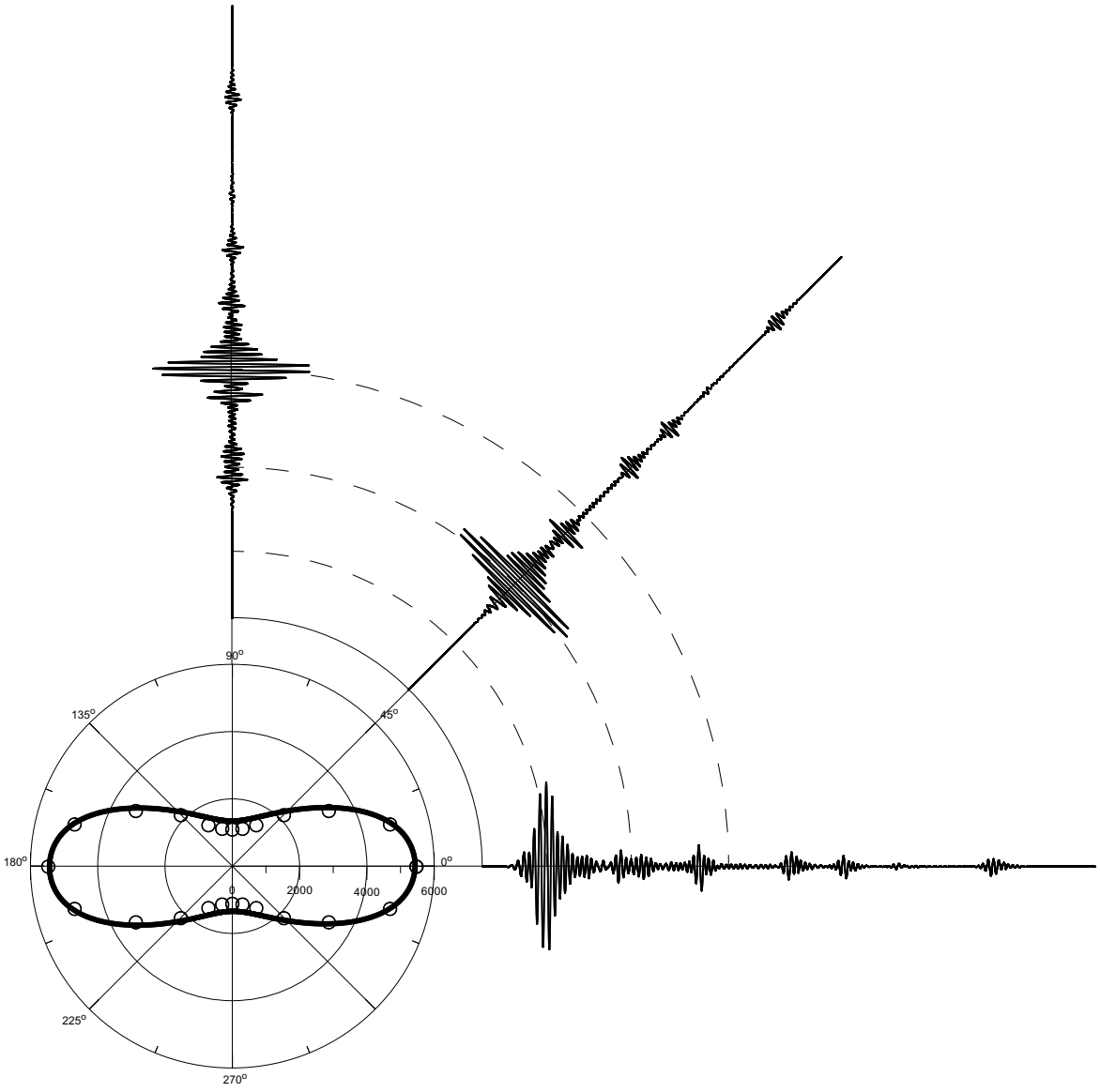

Figure 6.29: The theoretical (solid line) and numerical (circles) estimations for the Rayleigh wave speed at different orientation with respect to the direction defined by the carbon fibers constituting the first layer of the laminate. The time histories of the voltage acquired at 0, 45 and 90 degrees are also shown.

where the values of E_1 and E_3 are obtained for $\alpha = 0$ and $\alpha = 90^o$, respectively. The variations of c_{R_α} with the considered propagation direction are shown in Fig. 6.29 with a solid black line: here numerical estimations of the Rayleigh velocity (obtained associating the peaks appearing in the voltage with the propagation distance, as done in the 2D case) at angular intervals of 15^o are denoted by white circles. The obtained good agreement between theoretical and numerical results, besides giving evidence of the validity of the proposed model, shows that, as expected, strong dependence of Rayleigh surface wave propagation characterizes the 3D model. The main consequences of such dependence is shown in the voltage time histories collected at $\alpha = 0, 45^0$ and 90^o, respectively, and reported in Fig. 6.29. A careful observation of these signals reveals that while almost no change due to the different considered orientation affecting the location in time of P- and S-waves (and of the associated reflection/mode conversion phenomena) is noticeable, an apparent large variation of the Rayleigh wave location in the mentioned time histories takes place. Such change is dramatic when a 90^o orientation is considered, as the Rayleigh wave arriving at the sensor location is superimposed to primary and secondary waves, making it impossible to identify them in the signal, and thus preventing the estimation of the associated ToF.

A result of paramount importance in the design of the SHM routine is thus achieved through the analysis of the three-dimensional effects associated to the anisotropy of the propagation medium: the proposed damage detection strategy is strongly influenced by the effects induced by the carbon fiber orientation on the propagation of the surface component of the generated elastodynamic field. In this sense, the choice of an appropriate direction with respect to the stacking sequence of the analyzed composite laminate for the acquisition of the voltage output is important to guarantee the effectiveness of the proposed SHM approach.

Chapter 7

Experimental validation of the SHM routine

The numerical investigations carried out in the previous chapter allowed to gain a better understanding of the phenomena associated to the generation and propagation of elasto-dynamic fields radiating from a piezoelectric actuator. In particular, a transition between a guided-wave like response of the system and a behavior characterizing the propagation of primary and secondary waves in elastic half spaces is observed, with the delamination position regulating such transition between the two different phenomenologies through the enhancement or the attenuation of the effects associated to ultrasonic interference.

The study of such dual phenomenology in the system behavior allowed the definition of a two-stage SHM routine, in which a first analysis of the power content of the signals acquired by the PZT sensor is performed to ascertain the presence of surface delaminations, while a subsequent estimation of the time lag between the arrival of P-waves and S-waves at the sensor location allows to detect possible delaminations located in deeper regions of the structure.

The analysis of the effects associated to delamination extent and to the presence of an eccentricity between the actuator-sensor pair and the damage location revealed important limitations of the proposed SHM approach. It was found that delaminations smaller than twice the actuator diameter are not detectable by the described procedure, while no possibility of identification the damage is granted if the delamination is not located in the portion of the domain which lays beneath the transducers pair. Besides results, three-dimensional effects caused by the inner anisotropy of the propagation medium were analyzed, unfolding an important dependence of the obtained results on the orientation of the carbon fiber constituting the surface portion of the laminate, and thus on the point of acquisition of the voltage from the piezoelectric sensor.

Figure 7.1: The experimental setup for the tests preformed to validate the proposed SHM routine.

The main goal of this chapter is to describe the validation of the numerical results from an experimental point of view. To this end, an extensive experimental campaign was performed: several different specimen were tested and a large amount of data is collected following a precise test protocol, so as to achieve a good statistical consistency for the obtained results. Due to the complexity of the experimental tests, no perfect quantitative match with the numerical predictions is searched here; instead, confirmation of on the physic phenomena theoretically and numerically analyzed is demonstrated

7.1 Preliminary experimental tests

The conducted experimental campaign consists of two different phases: first, validation of the setup (including the characterization of the piezoelectric transducers) and the SHM routine in the isotropic case (i.e, aluminum plates) is performed; then, composite laminates with teflon inserts simulating the presence of the delaminations are investigated. The choice to analyze the behavior of the PZT transducers (in particular of the piezoelectric actuator) is important in view of the design of the optimal frequency of the excitation signal to be used for the damage detection procedure (see Sections 5.5.2 and 6.1.2). The study of the generation and propagation of elastodynamic fields in aluminum plates is carried out, instead, to test the feasibility and the effectiveness of the proposed SHM routine in a less complex

case represented by an isotropic domain of propagation for the ultrasonic waves, where delaminations are introduced using a special resin, as shown in the following sections.

7.1.1 Description of the experimental setup

To perform the experimental tests, different pieces of equipment are used: a Rigol DG-1000 arbitrary waveform generator with a frequency bandwidth of 100 Hz - 200 MHz and a sampling rate of 1 MSa/s is adopted to generate the 8 MHz 4.5 cycles tone-burst described in Section 6.1.2 (Fig. 7.1). Once generated, the excitation signal is not fed as input to a RF power amplifier, as the small entity of the voltage amplitude to be given to the PZTs (15 Volts) and the small size of the transducers (the actuator diameter is 3 mm) together with the associated electric impedance do not make necessary the use of a power amplifier. Once generated by the sensor, the output signals are acquired using a Rigol DS-1000E digital oscilloscope, characterized by a frequency bandwidth of 100 MHz and a sampling rate of 1 GSa/s, high enough to be able to detect the fast dynamics which take place in the analyzed signals.

7.1.2 Characterization of the piezoelectric actuator

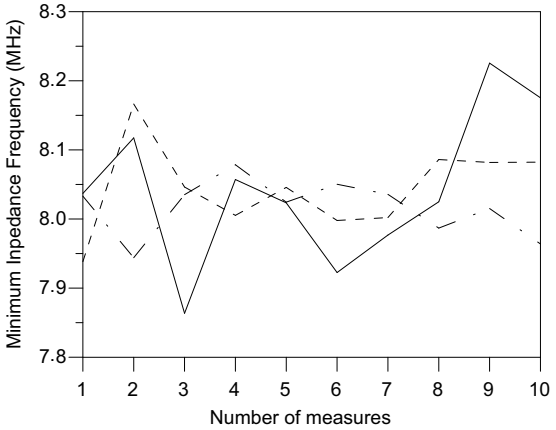

Figure 7.2: The measured values of the frequency for which a minimum in the impedance absolute value is obtained for the piezoelectric actuator: three different sets of measures are shown (solid, dashed and dotted line, respectively).

Specimen	E[f_{res}] (MHz)	σ[f_{res}] (KHz)
1	8.004	62.016
2	8.008	52.023
3	8.001	47.399
Final	E[f_{res}] (MHz)	σ[f_{res}] (KHz)
×	8.005	62.016

Table 7.1: Average values and standard deviations of the resonance frequency for the three sets of measures: the final adopted value of f_{res} (obtained averaging the values associated to the three sets of measures) and its deviations σ (the largest among the three previous values) are reported on the bottom row.

The characterization of the piezoelectric actuator is driven by the need to identify the resonance condition for which the electromechanical impedance assumes the lowest possible value, so that the actuating capabilities of the transducer are enhanced if a input voltage at

that particular frequency is fed to the actuator. The identification of such optimal excitation condition can be carried out by making use of an impedance analyzer: here, an Agilent 4294A with an operational bandwidth of 40 Hz - 110 MHz is adopted.

The tests are performed giving to the actuator a logarithmic sweep signal ranging from 100 Hz to 100 MHz in 10 seconds, with a voltage amplitude of 15 Volts and a (nominal) value of the output impedance of 25 Ohm. Ten measures for each of the three PZT actuators used for the tests are acquired: the values of the frequency for which a minimum in the absolute value of the measured impedance $\|Z\|$ is obtained are shown in Fig. 7.2 and summarized in Table 7.1. Here a final average value of $f_{res} = 8.005$ MHz with a standard deviation of $\sigma = 62.016$ KHz is obtained: the frequency f_{res} is thus selected for the excitation signal.

7.1.3 The isotropic case: aluminum plates

After the behavior of the piezoelectric actuator is investigated in terms of its electromechanical properties, the SHM approach described in the previous chapters is tested on aluminum plates. Analyzing the effectiveness of the proposed SHM routine on aluminum specimens is part of a step by step validation process: the use of an isotropic propagation medium allows to focus on the potential drawbacks associated to the practical implementation of the hardware constituting the SHM system, overcoming the complex effects of anisotropy characterizing composite laminates. In addition, the use of aluminum plates allows to adopt a controllable and effective method of simulating the presence of the delamination in the system. A schematic of the setup used for the tests is shown in Fig. 7.4: each of the two analyzed specimens is composed of two aluminum laminae (see Table 7.2) bonded together using a bi-component epoxy adhesive whose properties are reported in Table 7.3. The pres-

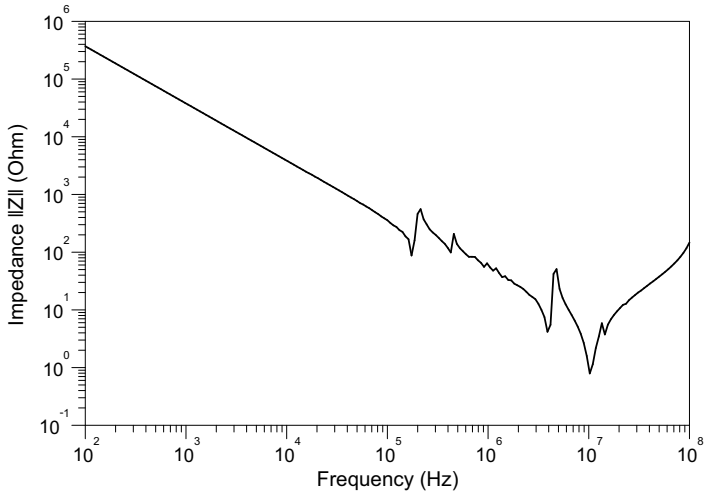

Figure 7.3: The measured impedance absolute value $\|Z\|$ of the piezoelectric sensor.

Aluminum alloy	6061
Width (w)	$1.40 \cdot 10^{-1}$ m
Span (s)	$1.85 \cdot 10^{-1}$ m
Thickness (h)	$(2.00 \pm 0.02) \cdot 10^{-3}$ m
Young's modulus E	72.10 GPa
Poisson's ratio ν	0.301
Density	2700 kg/m^3

Table 7.2: The geometrical and mechanical parameters of the aluminum specimens.

ence of a delamination is simulated removing the adhesive from a 1" × 1" (2.54 cm × 2.54 cm) portion of the bonding surface of the plates before inserting them in a mechanical press where they are subject to a pressure of 0.1 bar for 15 hours (the resin drying time). In this way, the fully-developed debonding effect associated to delaminations is reproduced. Two of the actuator-sensor pairs described in the previous chapter are attached on the upper and lower surfaces of the obtained specimen at the center of the no-bonding region, as shown in Fig. 7.4. Two more PZT pairs are then mounted on the upper and lower surfaces of the aluminum specimen in correspondence of the center of one of the two halves in which the plate surfaces can be ideally divided (see Fig. 7.4), for a total of 8 PZT transducers used for the two specimens realized for the tests. The choice of mounting the actuator-sensor pair on both surfaces of the specimens (implementing a pulse-echo configuration, see Section 5.1) is due to the fact that this way the number of available measures is doubled for a given number of specimens.

To attach the piezoelectric sensor on the plates surface a silver-based bi-component epoxy resin is used (see Table 7.3).A conductive adhesive is chosen because the piezoelectric transducers used for the tests have the electrodes placed on both upper and lower surfaces, implying that a non-conductive bonding over the plate surface would result in the loss of the

Conductive resin	CW2400
Volume resistivity	0.1 Ohm/m
Operative range	-91^{o}C to 100^{o}C
Shear lap σ	22.10 MPa
Shore hardness	> 70
Density	2850 kg/m^3

Epoxy adhesive	ITW Plastic Steel
Drying time	15 h
Operative range	-72^{o}C to 156^{o}C
Young's modulus E	2.46 GPa
Poisson's ratio ν	0.400
Density	2170 kg/m^3

Table 7.3: The physical properties of the conductive resin and the epoxy adhesives used in the realization of the aluminum specimens.

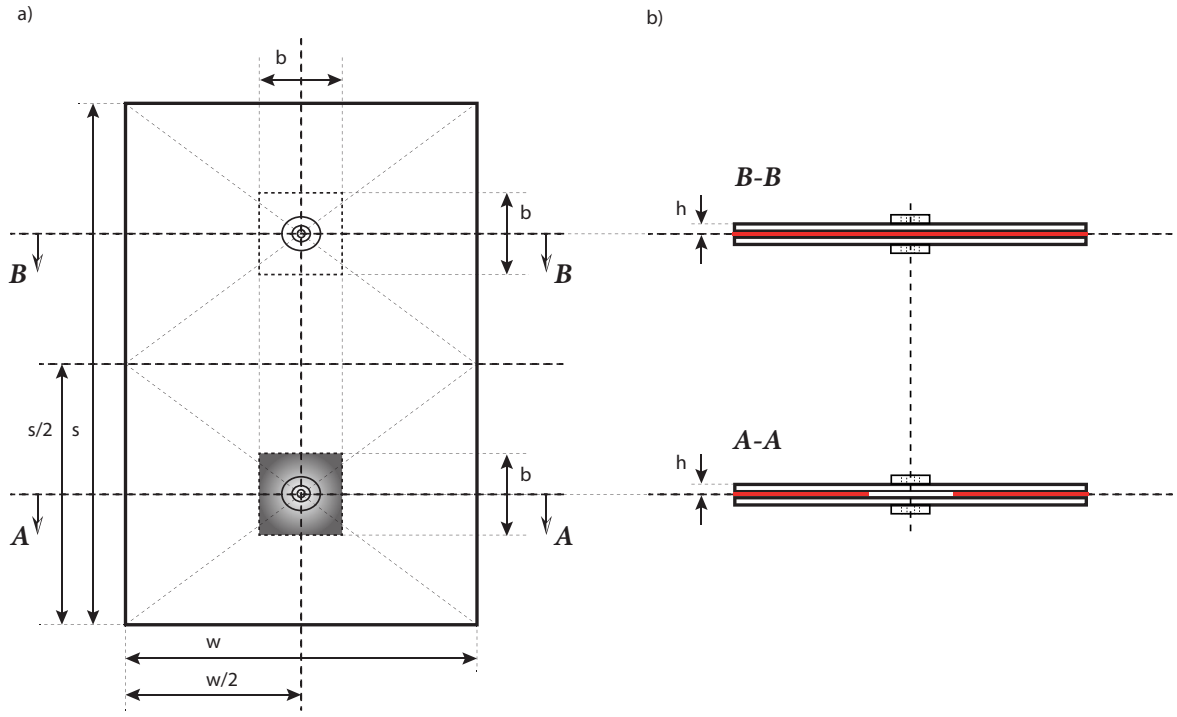

Figure 7.4: A schematic of aluminum specimens: the epoxy resin used to bond the two plates is represented in red. The 1"×1" no-bonding zone is represented by the faded square in (a) and as a white strip-like region in (b).

electric access to one of the electrodes of the transducers. Moreover, being the actuator and the sensor both mounted on a conductive substrate represented by the aluminum plates, the electrodes in contact with the laminae are used as ground, as shown in Fig. 7.5.

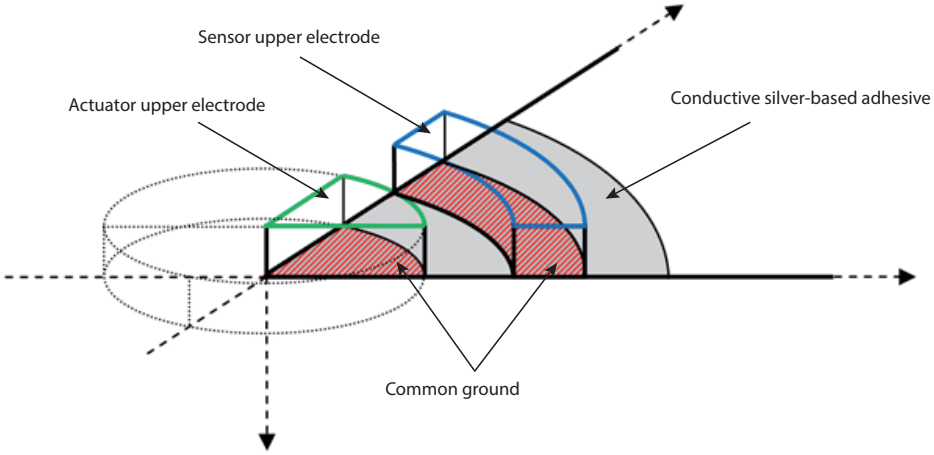

Figure 7.5: A schematic of the electrical configuration of the PZT actuator-sensor pair.

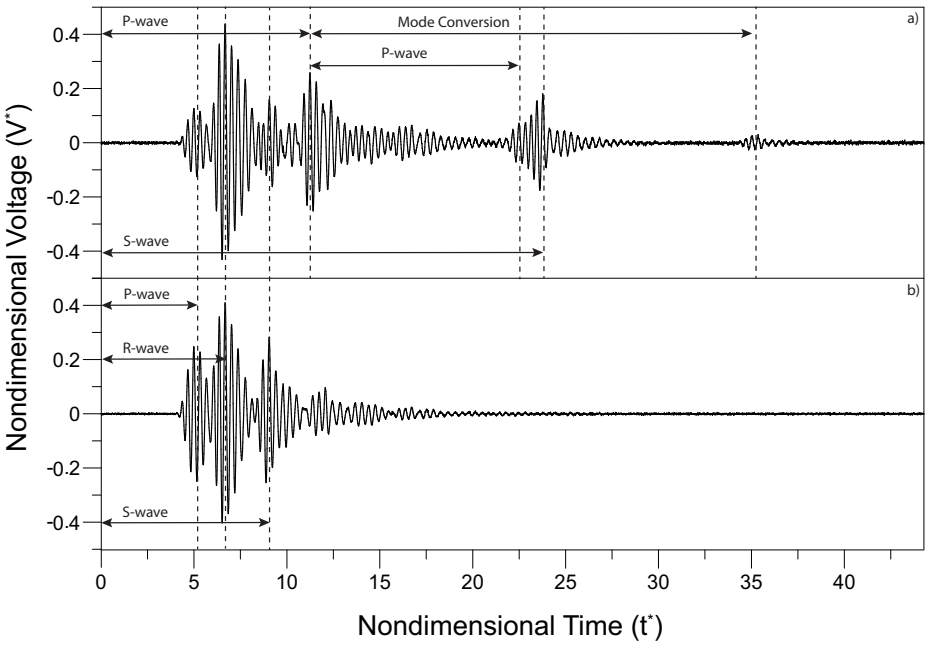

Figure 7.6: The time histories of the voltage acquired for the aluminum specimen: the healthy (a) and the damaged case (b) are shown, respectively.

7.1.4 Results

Results are shown in Fig 7.6: the time histories of the acquired voltage for the healthy (a) and the damaged structure (b) are reported, respectively. The analysis of the propagation speed associated to the different peaks appearing in Fig 7.6 and reported in Table 7.4 as well as the estimation of the time intervals between the different waves groups allow to identify the several wave structures that compose the output signals.

Due to the inhomogeneity of the specimen, the estimation of the propagation velocity for P- and S-waves is carried out as follows: first the theoretical values for P and S waves are calculated as [32]

$$c_{P_a} = \sqrt{\frac{2\boldsymbol{\lambda}_a + \boldsymbol{\mu}_a}{\rho_a}} = 6408.4 \quad \text{m/s} \tag{7.1}$$

$$c_{S_a} = \sqrt{\frac{\boldsymbol{\mu}_a}{\rho_a}} = 3204.2 \quad \text{m/s}$$

$$c_{P_r} = \sqrt{\frac{2\boldsymbol{\lambda}_r + \boldsymbol{\mu}_r}{\rho_a}} = 1918.5 \quad \text{m/s} \tag{7.2}$$

$$c_{S_r} = \sqrt{\frac{\boldsymbol{\mu}_r}{\rho_r}} = 636.1 \quad \text{m/s}$$

where the a and r subscripts identify the aluminum plates and the epoxy resin, respectively.

The time of arrival of primary and secondary and Rayleigh waves are estimated as

$$\begin{aligned} T_P &= \frac{4h_a}{c_{P_a}} + \frac{2h_r}{c_{P_r}} \\ T_S &= \frac{4h_a}{c_{S_a}} + \frac{2h_r}{c_{S_r}} \end{aligned} \tag{7.3}$$

where, as already seen, d indicates the actuator-sensor distance. The final values of the propagation speed for primary and secondary waves can be obtained as

$$\begin{aligned} c_P &= \frac{T_p}{4h_a + 2h_r} = 2697.2 \quad \text{m/s} \\ c_S &= \frac{T_p}{4h_a + 2h_r} = 5911.1 \quad \text{m/s} \end{aligned} \tag{7.4}$$

while the Rayleigh wave speed turns out to be [32]

$$c_{R_a} = \frac{0.862 + 1.14\nu_{13}}{1 + \nu_{13}} c_{S_a} = 598.9 \quad \text{m/s} \tag{7.5}$$

Results are summarized in Table 7.4: here, the different wave speeds are estimated considering the values of the aluminum plates and resin layer thicknesses measured with a caliber and reported in the same Table. The thickness of the resin layer, in particular, is obtained measuring the thickness of the single aluminum laminae composing one specimen first, and subtracting that value to the thickness of the overall specimen measured after it is removed from the press. A good agreement between experimental results and theoretical predictions is noticeable.

The estimation of the wave propagation speeds allow to identify a Rayleigh wave in the system response, given by the voltage time histories in Fig 7.6, as obtained in the numerical

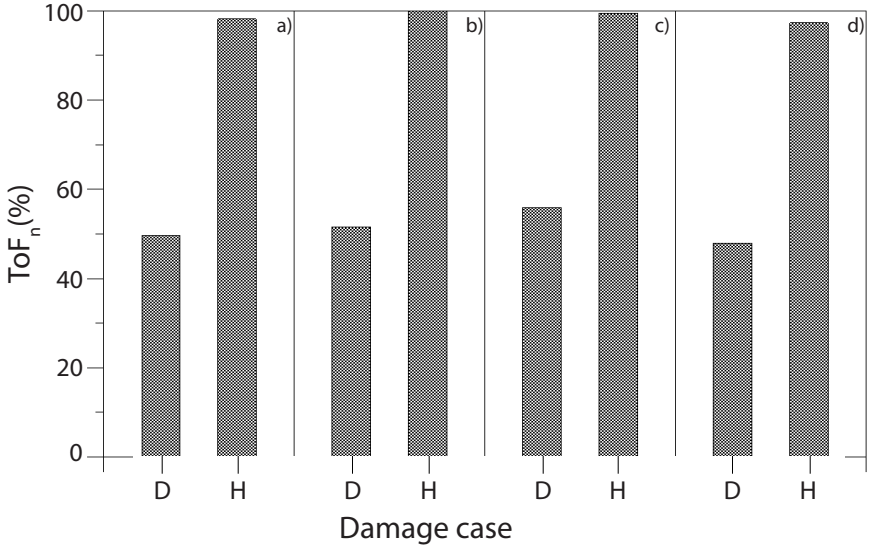

Figure 7.7: The estimated ToF for the aluminum specimens: the analysis is conducted using the PZT transducers mounted on the upper (a,c) and lower (b,d) surfaces.

Test Number	c_R	c_P	c_S
Theory	2697(m/s)	5911(m/s)	2796(m/s)
1	2657 (m/s)	5843 (m/s)	2812 (m/s)
2	2659 (m/s)	5846 (m/s)	2816 (m/s)
3	2663 (m/s)	5842 (m/s)	2821 (m/s)
4	2632 (m/s)	5853 (m/s)	2825 (m/s)
5	2663 (m/s)	5851 (m/s)	2819 (m/s)
6	2671 (m/s)	5839 (m/s)	2823 (m/s)
6	2661 (m/s)	5837 (m/s)	2823 (m/s)
8	2659 (m/s)	5843 (m/s)	2823 (m/s)

Aluminum plate	
Nominal value	Tolerance
2.000 mm	0.200 mm
h_{a_1}	2.003 mm
h_{a_2}	2.009 mm
h_{a_3}	2.011 mm
h_{a_4}	1.995 mm
Resin layer	
h_{r_1}	0.151 mm
h_{r_2}	0.137 mm

Table 7.4: The physical properties of the conductive resin and the epoxy adhesives used in the realization of the aluminum specimens.

tests. Moreover, also in this case and due to the surface nature of this wave type, the Rayleigh waves appear not to be affected by the presence of the delamination, both in amplitude and in terms of their appearance in time. Differently to what was observed in the numerical tests, however, here the appearance of P-waves in the healthy case precedes the arrival of Rayleigh waves, in accordance to the different geometrical and propagation properties of the analyzed specimens. Moreover, both the P-waves and the S-waves associated to the undamaged case are still observable in the voltage time history of the case where the presence of the delamination is simulated: these peaks however are sensitively smaller if compared to the counterpart appearing as a consequence of the presence of the no-bonding zone in the specimens. Once again, the time positioning of primary and secondary waves appears to be an excellent indicator of the presence and position of a delamination in the structure, as shown in Fig. 7.7. Moreover, the presence of multiple reflections and mode conversion phenomena can be noticed also in this case, as shown in Fig 7.6 (a).

7.2 Tests on composite laminates

The geometrical and mechanical properties of the two T600s/G91 carbon fiber composite laminates used as specimens in the subsequent phase of the experimental campaign are shown in Table 7.5: as done for the numerical analyses, a $[0^o/45^o/90^o/135^o]_s$ configuration is here considered. A schematic of the specimens is shown in Fig. 7.8: each one of the plate is ideally divided into four quadrants at the center of which a 1"×1" teflon ply is inserted at different depths in the structure, in between the composite layers to simulate the presence of a delamination and to replicate the damage cases I to VII already analyzed in the previous chapter

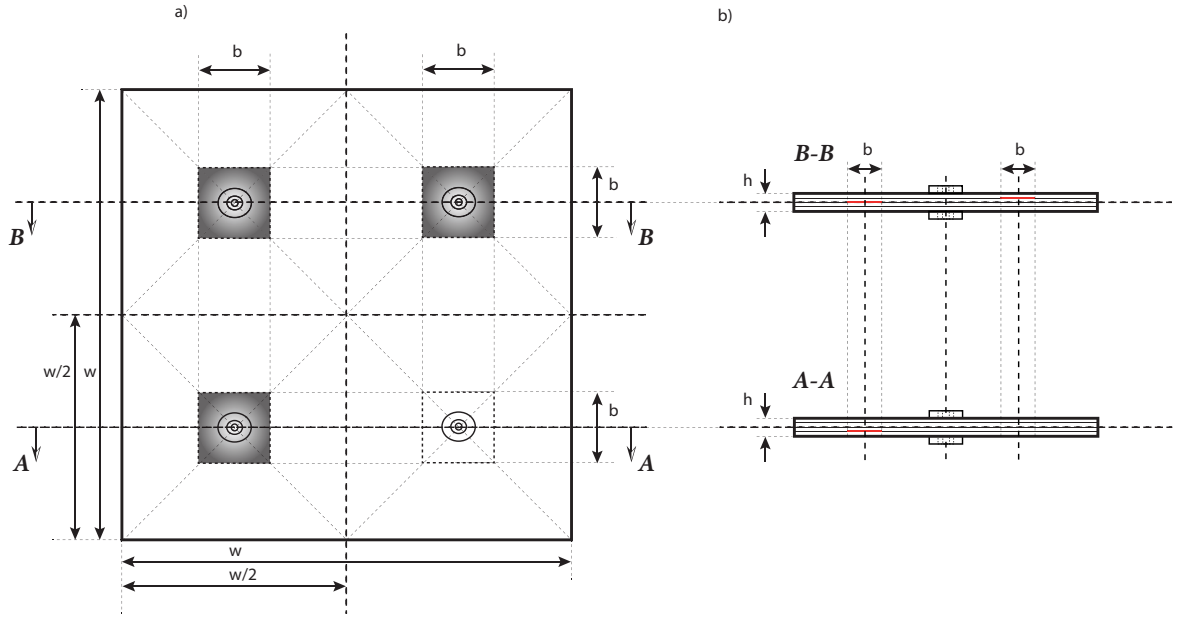

Figure 7.8: A schematic of composite specimens: the teflon inserts used to simulate the presence of a delamination are represented in red. The 1"×1" delaminated zones are represented by the faded squares in (a) and as red strip-like regions in (b).

(plus one undamaged case). As done for the aluminum specimens, two actuator-sensor pairs are mounted in a pulse-echo configuration at the center of each delamination, one on the upper and one on the lower surface of the plates, for a total of 32 PZT transducers mounted on the two specimens. In this way, two sets of 8 PZT pairs constituting two actuating-sensing systems disposed in a pulse-echo architecture can be defined depending on which surface of the specimens they are mounted on: here and henceforth, the are referred to as the Top and the Bottom configurations, respectively. Finally, as done for the aluminum specimen,

Composite plate	T600s/G91
Span (w)	$3.048{\cdot}10^{-1}$ m
Thickness (h)	$2.54 \cdot 10^{-3}$ m
Lamination sequence	$[0°/45°/90°/135°]_s$
Young's modulus E_1	134.44 GPa
Young's modulus E_3	8.201 GPa
Poisson's ratio ν_{13}	0.301
Poisson's ratio ν_{31}	0.015
Density	1501 kg/m^3

Table 7.5: Geometrical and mechanical properties of T600s/G91 composite laminates.

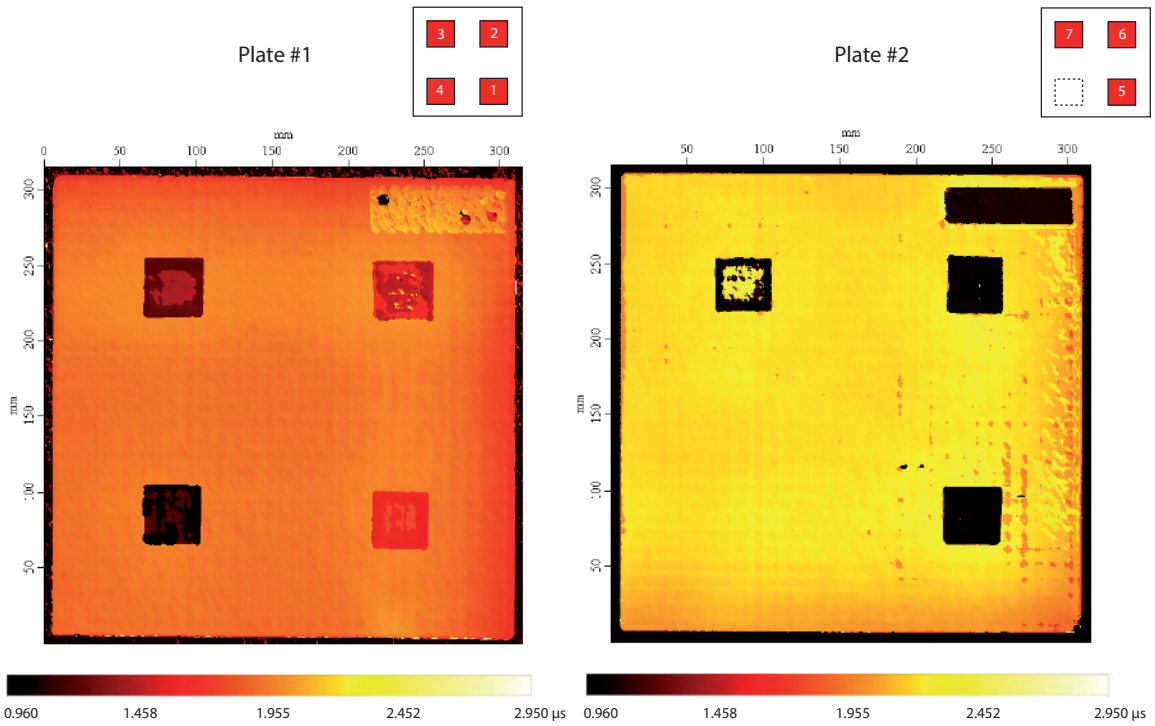

Figure 7.9: ToF images of the two composite specimen: darker regions indicate the presence of teflon inserts.

the PZT transducers are attached to the composite plates using the silver-based conductive epoxy resin, connecting two electrodes to create a common ground made accessible thanks to the use of the conductive resin, while the other two electrodes of the PZT pair constitute the autonomous poles of the actuating-sensing system. The acquisition points on the PZT ring-like sensors are located along the direction collinear with the orientation of the carbon fibers in the first/last layer of the plate, so as to meet the same test conditions adopted in the 2D numerical simulation and to avoid the onset of three-dimensional effects that can make more difficult the detection of the damage, as shown in the previous chapter.

7.2.1 Validation of the composite specimens - ToF and MA analyses

Before proceeding with the tests, the composite laminates are subject to an ultrasonic scan to ascertain the validity of the method adopted to simulate the presence of a delamination in the structure, namely, inserting a teflon ply in between the composite laminae. To this end, an AET-6 large-axis immersion scanner is used to perform a traditional ToF analyses together with a maximum amplitude (MA) analysis of the specimen. ToF images are maps of the time required for sound to travel to and back from the strongest reflector in the gate of the scanner. Longer times indicate greater distance from the surface. MA images, instead,

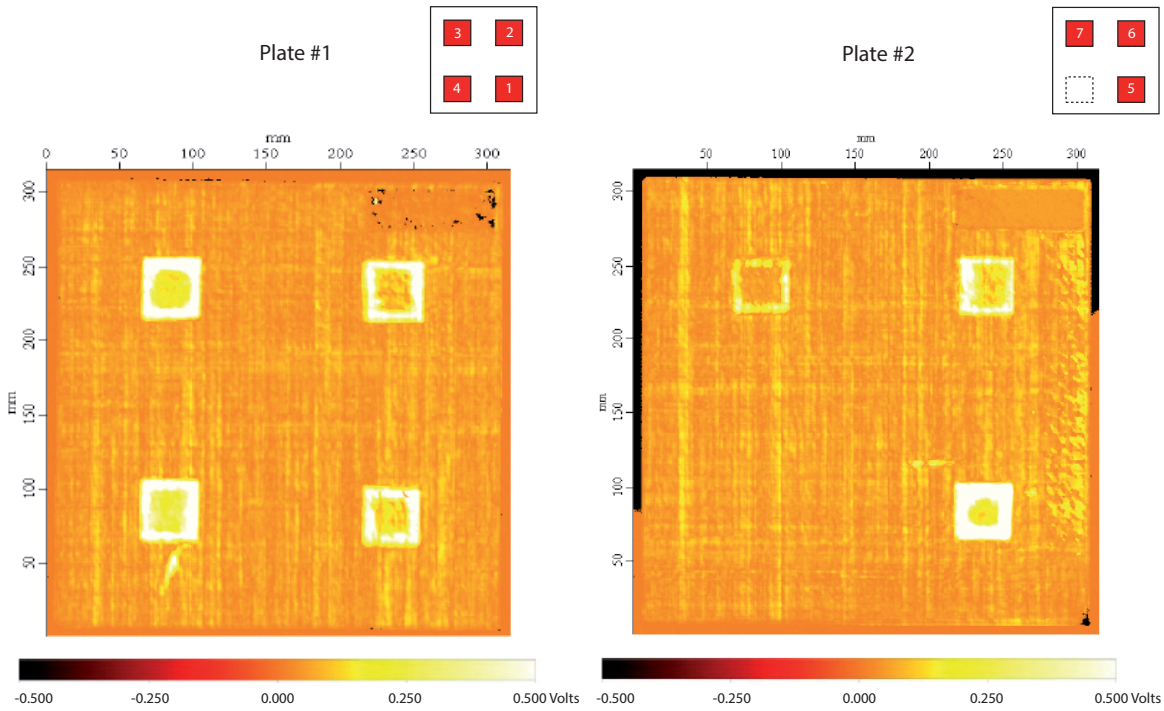

Figure 7.10: MA images of the two composite specimen: while a varying degrees of de-bonding is clearly visible in the centers, the signal intensity is stronger at the edges of the inserts.

give a qualitative indication of the degree of delamination. Higher amplitude indicates a greater degree of discontinuity.

ToF images (Fig. 7.9) show that Teflon inserts of nominally correct size and spatial location are clearly visible in all plates: relative depth of inserts as determined from ToF images indicates equidistant depth spacing between successive inserts in the plates. To compare depths in the two different plates, the difference between the backwall ToF and the insert ToF are used to normalize results. Under this paradigm, a shorter ToF indicates that the feature is deeper in the structure, i.e., closer to the backwall/bottom of the stack. In plate 1, the normalized ToF measurements are 0.3 μs, 0.5 μs, 0.7 μs and 0.9 μs for inserts 1, 2, 3, and 4, respectively. The values of 1.1 μs, 1.3 μs, 1.5 μs and 1.7 μs are found for inserts 5 to 7 in plate numbers plus the undamaged case. Results are reported in Table 7.6.

MA images (Fig. 7.10) show that the degree of de-bonding introduced in the laminates via the Teflon plies is not homogenous over the insertion areas. A stronger signal intensity at the edges of the inserts is noticeable: the insert centers, however, show higher signal intensity than the background. This indicates that, even if a major degree of debonding at the edges of the inserts is present, a varying degrees of de-bonding is clearly visible in the centers. An additional linear delamination defect measuring 1.49 cm in length is noted on the lower left of plate 1. A similar but smaller indication is observable in the lower right quadrant of plate

Damage case	ToF	Damage case	ToF
Plate ♯ 1		Plate ♯ 2	
I	0.3 μs	V	1.1 μs
II	0.5 μs	VI	1.3 μs
III	0.7 μs	VII	1.5 μs
IV	0.9 μs	No Insert	1.7 μs

Table 7.6: The ToF estimated with an ultrasonic scan of the different damage cases in the two composite specimens.

2, above and to the left of the Teflon insert.

A further consideration is that the ultrasonic scan of the composite specimens confirmed the fact that the use of teflon inserts constitutes an effective method for introducing debonding regions within a laminated structure, both in terms damage intensity (MA images) and location in the plate through-the-thickness direction (ToF images).

7.2.2 The testing protocol

The experimental tests carried out on the composite specimens follow a suitable testing protocol aiming at ensuring the necessary statistical consistency to the obtained results. A set of ten different voltage acquisitions are performed for each actuator-sensor pair when

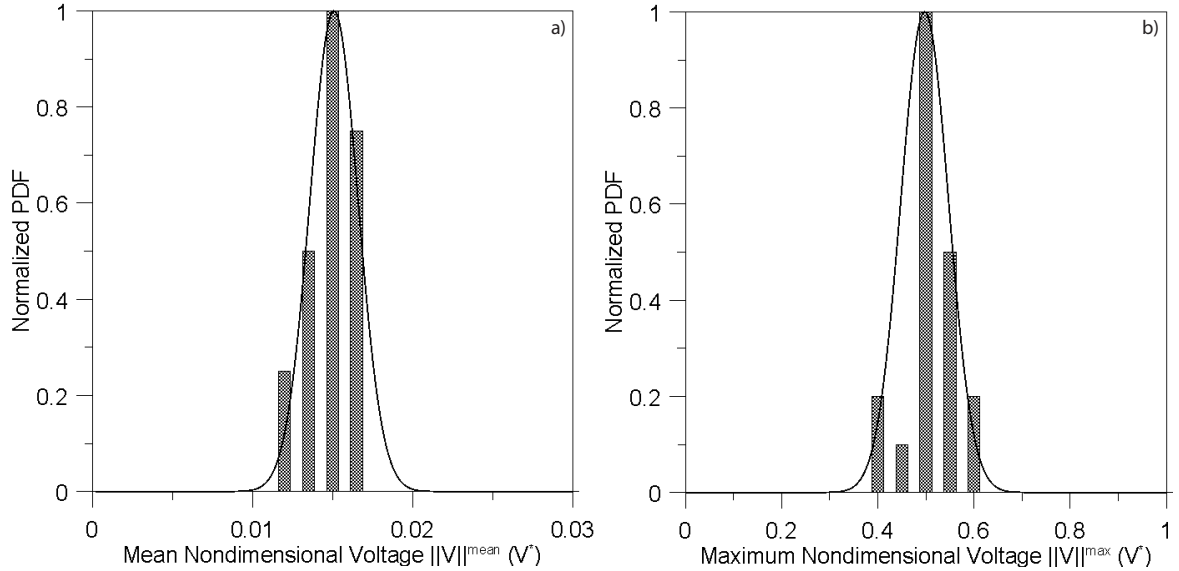

Figure 7.11: The ten nondimensional values of $\|V\|_i^{mean}$ (a) and $\|V\|_i^{max}$ (b) estimated for a set of acquisitions of the voltage output for the test on the composite specimens: the normal PDF associated to a normal distribution of the said quantities are shown in solid line.

the proposed SHM routine is implemented, for a total of 160 measures. In particular, the maximum and the mean absolute value $\|V\|$ are estimated for each acquisition, allowing to associate a standard deviation of such quantities to each acquisition set as

$$\sigma_{\|V\|^{max}} = \sqrt{\frac{\sum_{i=1}^{N}(\|V\|_i^{max} - \|\bar{V}\|^{max})}{N}} \tag{7.6}$$

$$\sigma_{\|V\|^{mean}} = \sqrt{\frac{\sum_{i=1}^{N}(\|V\|_i^{mean} - \|\bar{V}\|^{mean})}{N}} \tag{7.7}$$

where N=10, and $\|\bar{V}\|^{max,mean}$ represent the average values of the estimated maximum and mean values $\|V\|_i^{max,mean}$ associated to each one of the 10 acquisitions constituting a set of measures. Each set is repeated until the conditions

$$\frac{\sigma_{\|V\|^{max,mean}}}{\|\bar{V}\|^{max,mean}} < 10\% \tag{7.8}$$

are met, ensuring the statistical consistency of the acquired data: once a set of ten measures is obtained for a damage case, the average signal of the acquisitions is estimated and

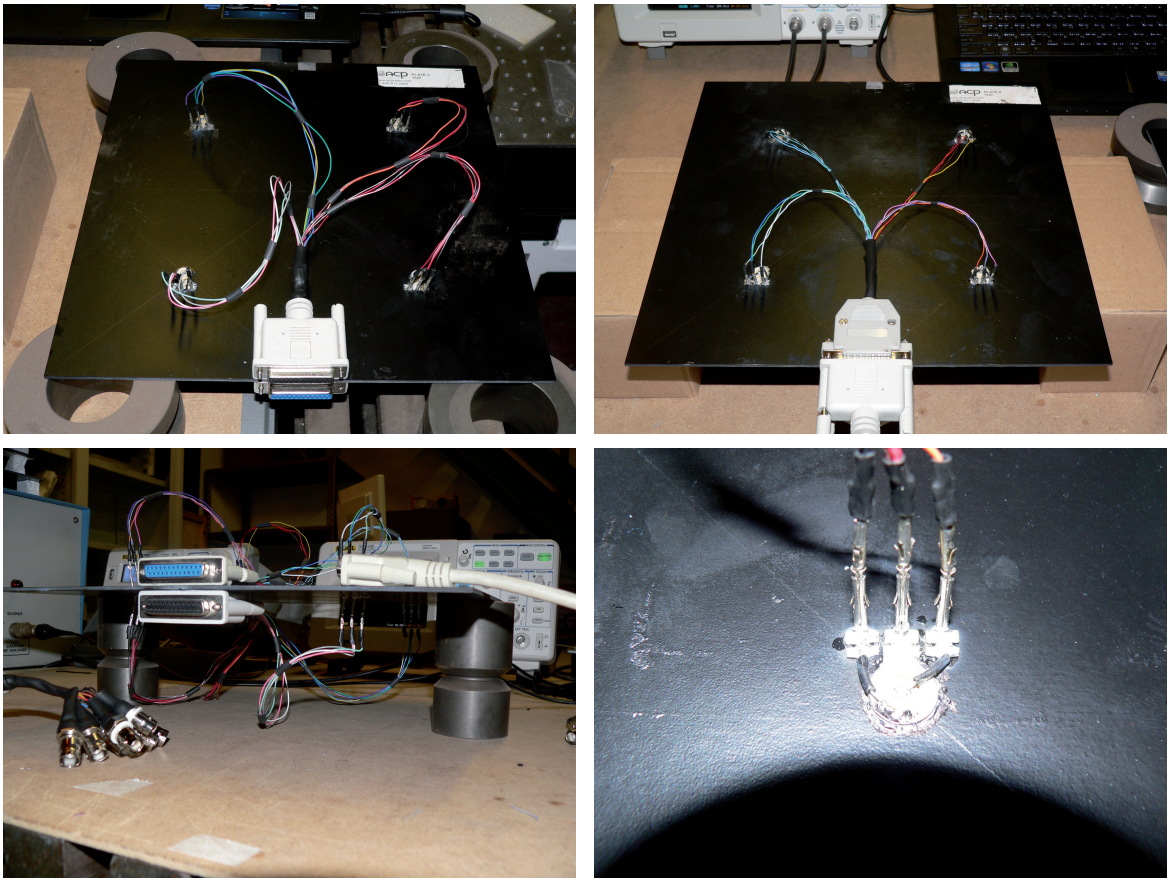

Figure 7.12: The instrumented composite specimens with the SHM system.

considered as the reference output voltage for the specific damage case. The ten nondimensional values of $\|V\|_i^{max}$ and $\|V\|_i^{mean}$ estimated for a particular set are shown in Fig. 7.11. Here the normalized PDFs associated to a normal distribution characterized by $\|\bar{V}\|^{max,mean}$ as mean values and standard deviations satisfying Eqs. (7.6) and (7.7) are reported in solid black line. As shown, all the estimated data is gathered in the areas defined by the PDFs.

7.2.3 Results and discussion

The time histories of the voltage acquired for the two composite specimens (Fig. 7.12) are shown in Figs. 7.13 and 7.14: the output signals obtained using the Top and the Bottom configurations are reported, respectively. As done for the aluminum specimens or in the numerical tests, the propagation velocity of the various wave structures appearing in the voltage time histories is estimated to enable their identification. From a theoretical point of view, the velocities are [32]

$$c_{P_3} = \sqrt{\frac{2\boldsymbol{\lambda}_3 + \boldsymbol{\mu}_3}{\rho}} = 2715.8 \quad \text{m/s} \tag{7.9}$$

$$c_{S_3} = \sqrt{\frac{\boldsymbol{\mu}_3}{\rho}} = 1449.1 \quad \text{m/s} \tag{7.10}$$

$$c_{R_1} = \frac{0.862 + 1.14\nu_{13}}{1 + \nu_{13}} c_{S_1} = 5433.7 \quad \text{m/s} \tag{7.11}$$

where the 3 and 1 subscripts indicate the direction normal to the plate surface and the direction collinear to the orientation of the carbon fibers of the laminate first layer, respectively. To estimate the velocities, the data reported in Table 7.5 are adopted. The values of the propagation speeds obtained analyzing the experimental data are shown in Fig. 7.15: as for the numerical tests, good accordance with the theory is obtained. Differently from the previous cases, however, an underestimation of all propagation speeds is here shown.

Besides the estimation of the propagation velocities, the analysis of time intervals between the different peaks appearing in the voltage time histories confirms the nature of the waves structures as Rayleigh, primary or secondary waves. In this case, a lower number of multiple reflection and mode conversion phenomena characterizes the system response if compared to the numerical counterparts described in Chapter 6, revealing that a higher dissipation takes place in the propagation domain.

The analysis of the voltage acquired in Figs. 7.13 and 7.14 shows again that two different phenomenologies characterize the response in terms of wave propagation. The experimental data show that it is possible to distinguish a guided-wave-like behavior defined by the presence of a complex wave structure which emerges in the voltage time histories associated to the damage cases I and II. As noticed in in the numerical simulation, no peaks denoting the arrival of P- and S-waves is observable in the acquired voltage. Damage cases IV

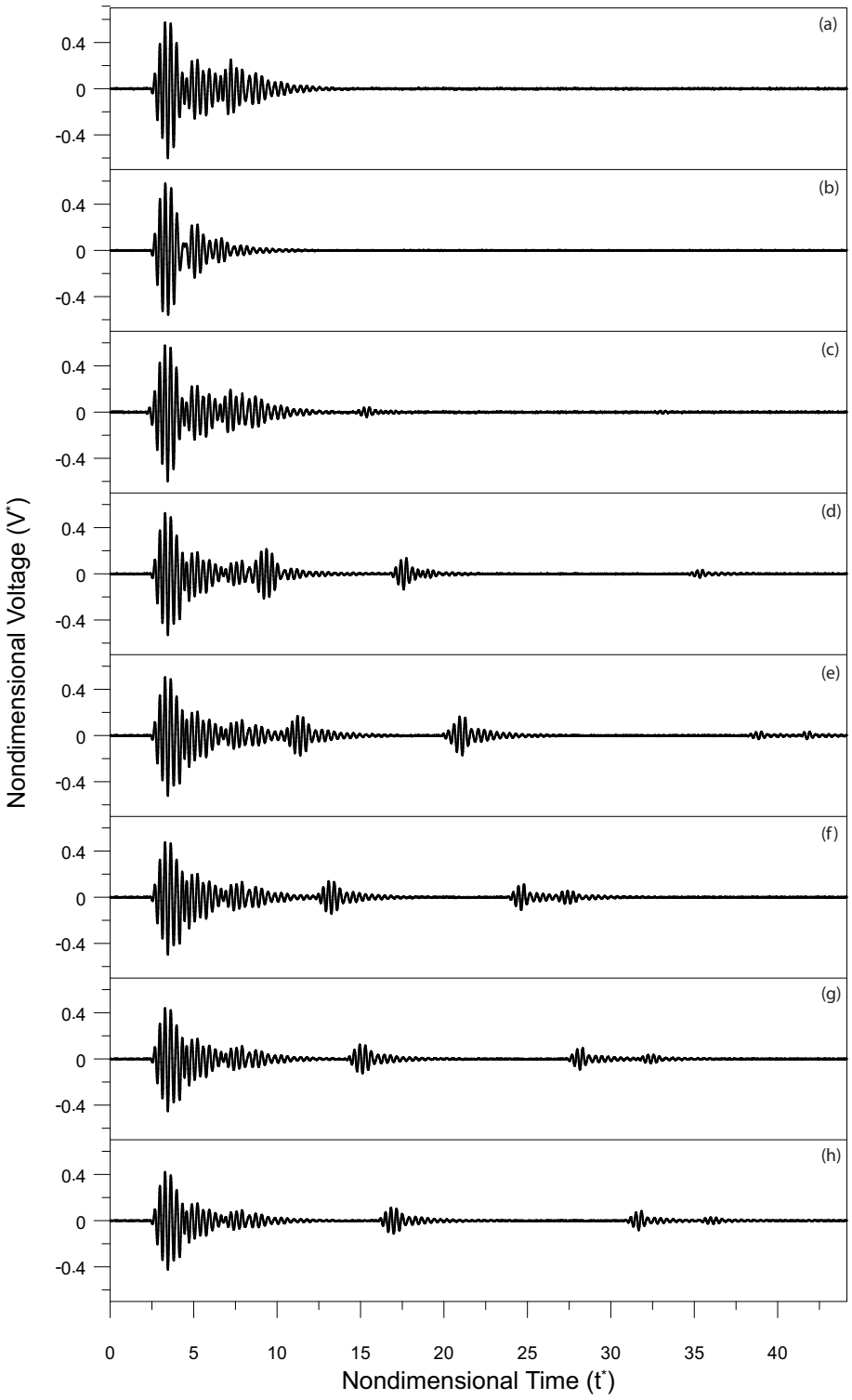

Figure 7.13: The voltage acquired by the sensing system in the Top configuration for different damage scenarios: the delamination is located in position from 1 to 7 (figures from (a) to (g)). The non-damaged case is also shown (h).

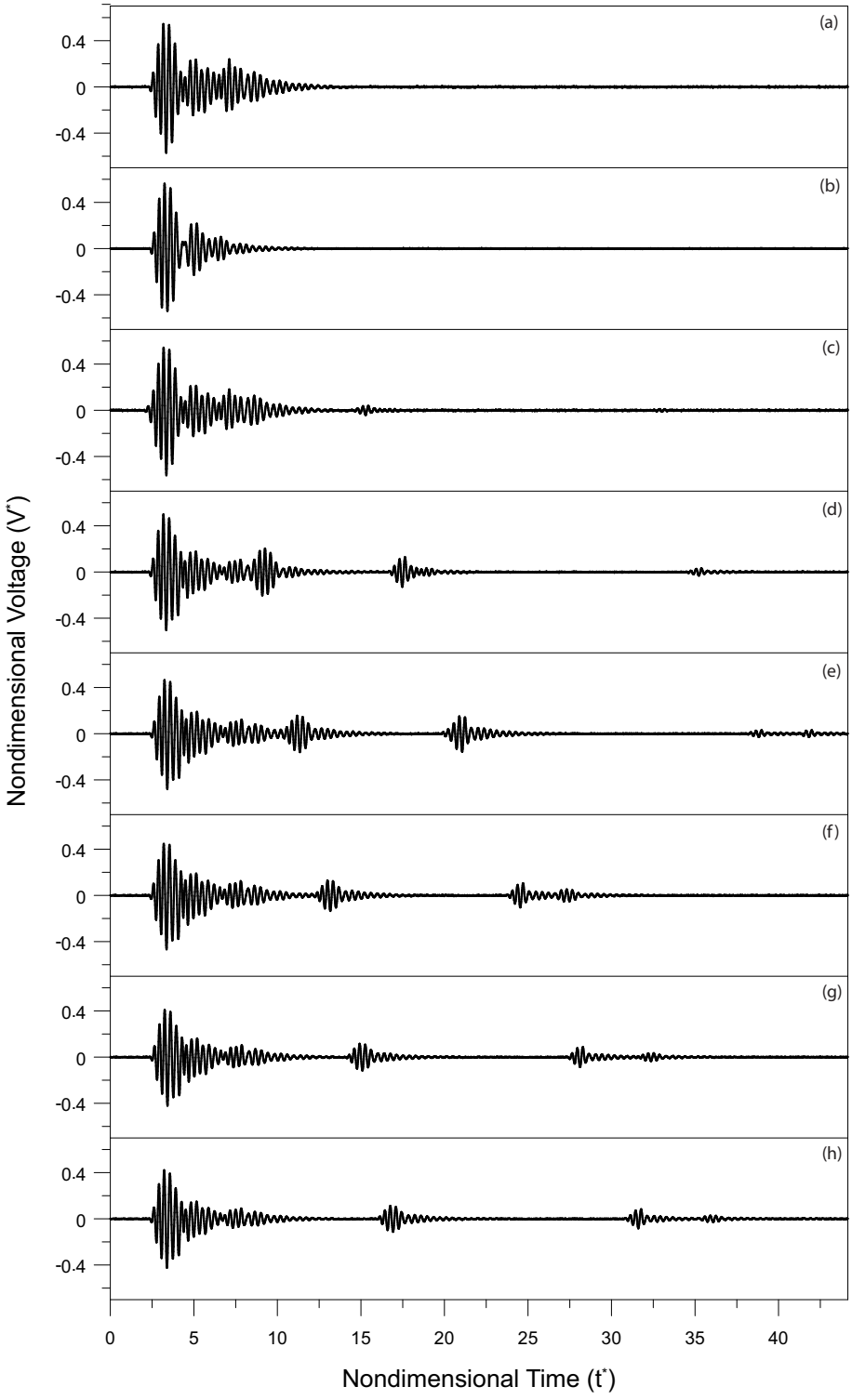

Figure 7.14: The voltage acquired by the sensing system in the Bottom configuration for different damage scenarios: the delamination is located in position from 1 to 7 (figures from (a) to (g)). The non-damaged case is also shown (h).

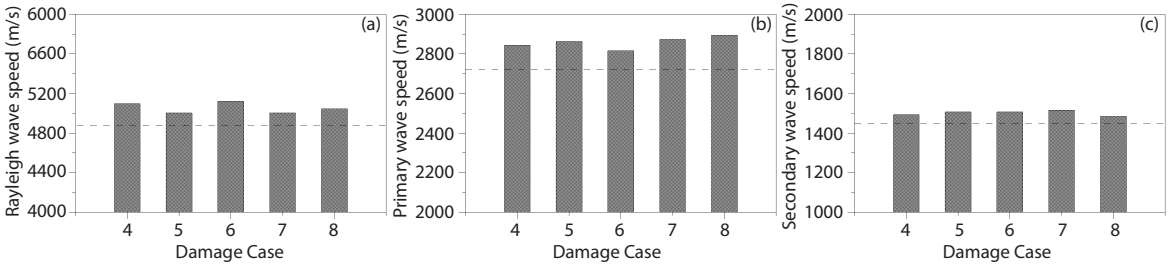

Figure 7.15: The theoretically (dot line) and experimentally (columns) estimated values for the Rayleigh c_{R_1} (a), Primary c_{P_3} (b) and Secondary c_{S_3} (c) wave speed for different damage scenarios. The data gathered using the Top configuration of the PZT transducers was used.

to VII (plus the undamaged case), instead, feature the appearance of voltage peaks which represent the reflection of primary and secondary waves at the upper/lower surface of the plate, as previously ascertained: a transition between the two behaviors is again found for damage case III. The estimation of the signal power content gathered in the -3dB bandwidth about the excitation frequency (8 MHz) with respect to the same quantity estimated for the input signal reveals that also in this case two different regimes are present (Fig. 7.17: when a surface delamination is present (namely, cases I, II and III), only the 10% percent of such power is distributed in the mentioned frequency bandwidth, implying the presence of a strong modulation of the power content of the excitation signal in the frequency domain due

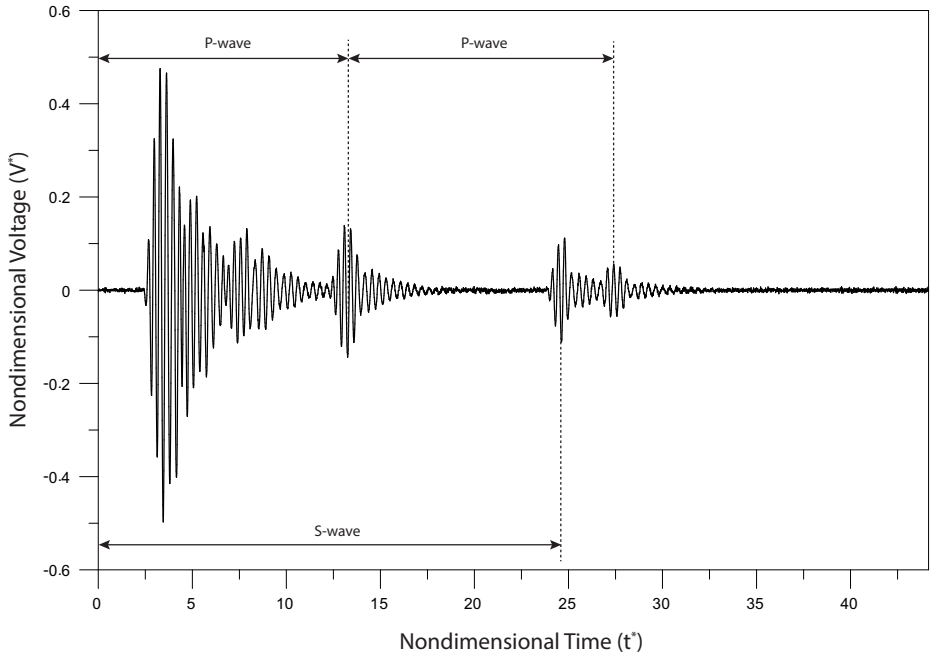

Figure 7.16: The time history of the voltage acquired by the PZT sensor for the damage case VI in the Top configuration.

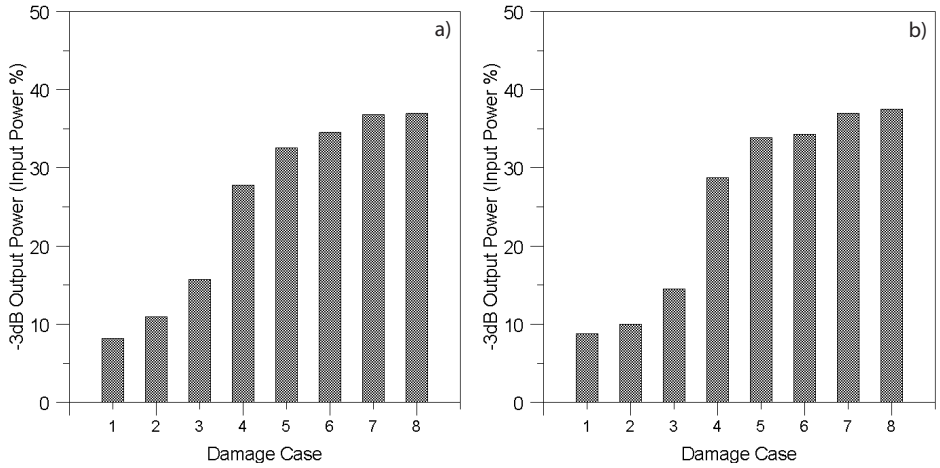

Figure 7.17: The ratio between the power content of the output and input signals in the -3dB bandwidth about 8MHz (%) estimated using the Top (a) and Bottom (b) configurations of the PZT transducers.

to interference effects, as discussed in Section 6.1.5. When the damage is located deeper in the specimen or if it is not present at all (cases IV to VIII), the percent of the signal power exhibited in the -3dB bandwidth about the 8MHz frequency rises up to the average value of 35%, as minor effects are due to the ultrasonic interference phenomena and P- and S-waves appear clearly in the voltage time histories.

To ascertain the presence of a deep delamination, a further step needs to be done: as shown in Fig. 7.18, the estimation of the ToF index is performed. Once more the analysis of such index, giving a quantitative measure of the time lag existing between the arrival of primary and secondary waves at the sensor location, provides a robust information about the presence and position of the delamination in the thickness direction.

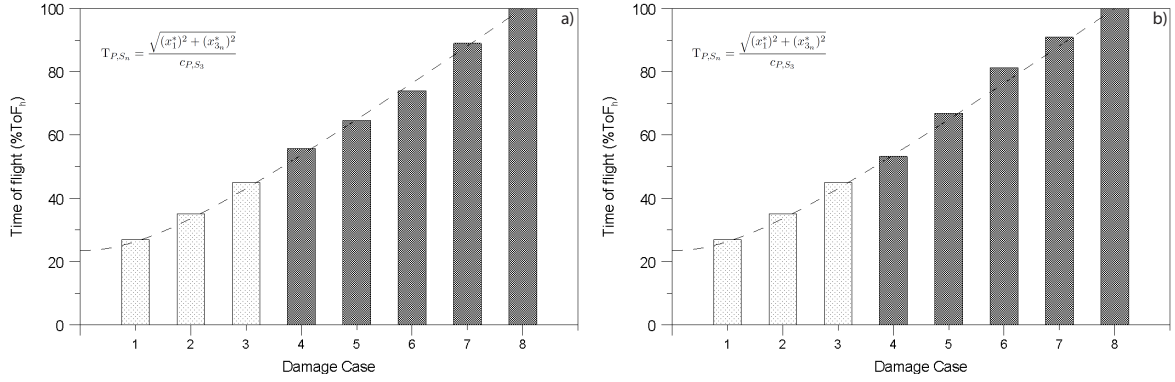

Figure 7.18: The ToF$_n$ index estimated for different damage scenarios using the Top (a) and Bottom (b) configurations of the PZT transducers. The dotted line represents the theoretical variations of the ToF$_n$ (see Section 6.1.4).

Chapter 8

Conclusions

The objective of this thesis was to develop an innovative SHM technique that exploits PZT-induced waves in composite laminates to detect the presence of delaminations. The SHM technique here proposed is intended to set the initial stage of a broader approach to structural health monitoring aimed at damage detection in composite plate-like structures based on the exploitation of the damage-induced lag in the times of arrival of primary and secondary elastic waves traveling in the plate thickness direction as the key mechanism for enhanced detection capabilities.

The initial part of the work was based on the analysis of the theoretical problem addressing the generation and propagation of elastodynamic fields in plate-like structures, with piezoelectric transducers used as excitation sources. With the aim of defining the mathematical background needed to analyze the problem at hand, the point-source synthesis of the pressure and velocity fields were first discussed in the acoustic case, allowing to revisit the concepts of Green functions and far-field approximation in the solution of Helmholtz equations. The next step was represented by the analysis of point-wise force density source-generated elastodynamic fields in full space: here, the increase of the problem rank with respect to the acoustic case has led to the definition of Green tensors of second, third and fourth order, allowing to describe the solution of the elastodynamic problem in terms of radiation characteristics, composed of primary (P) and secondary (S) waves emanating from the source. Exploiting the linearity of the problem, the previously obtained mathematical tools where then used to obtain a synthesis of the elastodynamic field generated by a finite-surface force density source in the underlying half-space: in particular, the case of a synchronous strip-like aperture characterized by a normal force density distribution and representing the simplest model of a piezoelectric actuator was addressed. In such procedure, an integral representation of the solution of the Rayleigh-Sommerfeld type was used adopting a spectral plane wave decomposition of the second-rank Green tensor in half-space. As a result, the

radiation characteristics defining the elastodynamic field generated by the PZT-like source were finally obtained: here the propagation of P- and S-waves was described, and the presence of mode-conversion phenomena occurring at the domain boundary together with the onset of Rayleigh waves was analyzed.

The detailed analysis of the physics involved in the generation of elastic waves through the use of piezoelectric transducers has enabled the definition of an innovative SHM procedure elaborated in the subsequent phase of the work. The time lag between the times of arrival of PZT-generated P and S waves to the sensor location was adopted as means to detect the presence of delaminations in composite laminated plate-like structures. Primary and secondary waves traveling downward in the plate thickness direction from its upper surface (where the PZT actuator is located) are reflected either by the plate lower surface, or, when damage exists, by the delamination located in between the composite laminae. Affecting the traveling path of P and S waves, the presence of the delamination was considered to vary the time of arrival of the mentioned waves to the upper surface, where an additional piezoelectric transducer acting as sensor is placed, implementing a pulse-echo configuration of the proposed SHM routine. In particular, due to the different propagation speeds of primary and secondary waves, the percent variations in the time lag existing between their arrivals at the sensor location was identified as the key quantity of the damage detection mechanism. To practically implement the described SHM approach, an innovative configuration of the actuating-sensing system was designed, with a piezoelectric disk surrounded by a PZT ring acting as actuator and sensor, respectively. Moreover, 8 MHz 4.5 cycles tone-burst signals with a 15 Volts amplitude were adopted as excitation signal in the delamination detection procedure. The frequency content of the signal, in particular, was chosen as ideal compromise capable of satisfying the constraints imposed on the input signal wavelength by the reduced value of the characteristic size of the damage to be identified (namely, the delamination thickness) and the resonance condition of the actuator, which guarantees a magnification of the actuating skills delivered by the piezoelectric disk.

The subsequent implementation of two- and three-dimensional numerical models using the COMSOL Multiphysics® software allowed to reach a better understanding of the phenomena associated to the interaction of primary and secondary waves with the delamination inserted in the system and simulated as a teflon ply located between the layers of the structure. To obtain such detailed information, the linear governing equations of an eight-layer carbon fiber composite plate were implemented in strong form, together with the constitutive laws of the composite laminates and the constitutive equations of the piezoelectricity characterizing the behavior of the actuator-sensor pair. The possibility of directly prescribing and receiving the input and output signals of the system, enabled a careful description of the

electromechanical coupling which characterizes the behavior of the piezoelectric transducers.

Results of the numerical analyses have shown a precise correlation between the delamination presence and position, and the (percent) values of the estimated ToF of P and S waves, i.e., the above discussed time lag. In particular, it was ascertained that when a delamination is present close to the surface area of the plate (namely, above the third layer starting the count of the laminae from the surface of the plate where the PZT transducers are mounted on), no peaks associable to the arrival of P and S waves are clearly visible in the time histories of the acquired output voltage. Complex wave structures, where only the Rayleigh waves can be identified, were obtained when the mentioned damage cases are investigated. A subsequent analysis of the PSD of the acquired output signals revealed that a substantial modulation of the power content of the analyzed output signals takes place when a surface delamination is considered: only about 10% of the power of the input signal contained in a -3dB bandwidth about the 8 MHz frequency is still present in the same bandwidth when the output signals associated to surface delaminations were considered. A value of 40% was found for the other damage cases (plus the undamaged case). Such modulation in the frequency domain of the power content of the output signal is due to the ultrasonic interference effects which are manifested as a consequence of the superimposition of primary and secondary waves being reflected at the plate surfaces: these phenomena were found to be particularly significant when the distance between the actuator and the delamination surface is small if compared to the distance existing between the actuator and the sensor edges. In fact, the ratio between such quantities was found to regulate a transition between a guided wave-like behavior of acquired ultrasonic waves and a propagation of primary and secondary waves in a half space-like domain. In this sense, a two-phase SHM procedure was formulated: (i) first, the percent power content of the output signal in the -3dB bandwidth about the 8 MHz frequency is estimated, so as to ascertain the presence of a surface damage; (ii) then, the ToF of P and S waves is calculated, to detect both the presence and location of deep delaminations in the through-the-thickness direction of the plate. Additional numerical tests have shown that a delamination featuring a diameter which is twice the diameter of the PZT actuator constitutes the minimum extent of an observable damage, while no delamination can be detected when it is not located underneath the actuator-sensor pair. Finally, the analysis of the numerical results obtained with the 3D simulations have shown that the effects associated to the anisotropy of the analyzed propagation domain can limit the effectiveness of the proposed SHM routine if the acquisition location is not chosen appropriately. The different wave speeds of the several components appearing in the acquired voltage time histories, in fact, can cause a superposition of such components making the interpretation of the signal very hard to accomplish. In the analyzed case, in particular, an acquisition point

over the piezoelectric ring-like sensor which is in line with the orientation of the carbon fibers of the plate first lamina was chosen.

The experimental campaign subsequent to the numerical tests was characterized by the investigation of both isotropic and composite specimens. In the first case, two aluminum specimens were considered: an epoxy resin was used to bond together the surfaces of two pair of plates, apart from a 1"×1" region where no resin was applied, thus creating a no-bonding zone which simulates the presence of delaminations. The two specimen were then put in a mechanical press to ensure an accurate adhesion of the plates. Results indicated that a phenomenology similar to that observed in the numerical results is present, both in terms of the estimated ToF (here only one damaged case was investigated, with the damage located in the specimen midplane) with a reduction of about 50% of its value if compared to the undamaged case, and in terms of the estimated values of Rayleigh, primary and secondary wave speeds, respectively. In the second phase of the experimental tests, two carbon fiber composite plates with a $(0^o/45^o/90^o/135^o)_s$ stacking sequence were analyzed: 1"×1" teflon plies were inserted, during the manufacturing process, between the plate laminae, at the center of each one of the four quadrants defined on the plates, for a total number of seven damage scenarios plus an undamaged case. To enhance the statistical properties of the tests, each damage case was analyzed twice: a PZT actuator-sensor pair was mounted on the top and bottom surfaces of the plates, at the center of each quadrants, for a total of 16 PZT couples in the two specimens. Ten acquisitions for every actuator-sensor pair were carried out, and repeated until the desired consistency was obtained: the average of the collected signals was thus considered as representative of the analyzed damage scenario. An ultrasonic analysis of the realized specimens has finally been carried out using a AET-6 large-axis immersion scanner, to perform a traditional ToF and a maximum amplitude (MA) imaging of the plates, so as to validate the technique adopted to simulate the presence of delaminations in the system.

The obtained results have shown that a fine agreement with the numerical simulations is obtained. As a matter of fact, the experimental tests prove the existence of a dual regime in the system response associated to the delamination location. When a surface delamination is present (placed between layers 1-2, 2-3 and 3-4 of the plates), less than 15% of the power of the input signal contained in the -3dB bandwidth about the 8 MHz frequency was found to be present in the same bandwidth for the output signals, while an average value of 35% was found for the other cases. An increasing monotonic pattern was observed to be followed by the estimated ToF values when delaminations located deeper in the plate thickness were considered, the limit case being represented by the undamaged case.

Different aspects of the SHM approach presented in this work need to be addressed

in future research before its implementation in real-world applications can be considered as a feasible option. The implementation of the proposed damage detection procedure in consonance with the realization of a large network of transducers proposes technical as well as methodological challenges that must be analyzed in detail. Moreover, the behavior of the discussed SHM procedure in operational conditions needs to be verified. From a theoretical point of view, a detailed quantitative analysis of the effects of the ultrasonic interference phenomena (i.e., those regulating the transition from the observed guided-wave-like response of the structural system to a regime in which the propagation of P and S waves characteristic of half spaces takes place), needs to be carried out. The proposed local approach making use of the distinct features of primary and secondary waves constitutes an original contribution to the SHM literature and a new perspective in the field of ultrasonic damage detection procedures.

Appendix A

Elastic Waves in Wave-Guides

A.1 The Rayleigh-Lamb equations

For time-harmonic wave motion in an elastic layer the equation relating frequency or phase velocity to the wavenumber can be derived on the basis of the principle of constructive interference [**?**], or employing expressions for the field variables representing a standing wave in the direction normal to the plate surface and a propagating wave in the in-plane directions, as done in most treatments. The expressions are then substituted into the boundary conditions to derive the frequency equation. This more straightforward approach will be followed here.

We consider the equations of motion

$$\mu\nabla^2\boldsymbol{u} + (\lambda+\mu)\nabla\nabla\cdot\boldsymbol{u} = \rho\ddot{\boldsymbol{u}} \tag{A.1}$$

where $\boldsymbol{u}$ denotes the displacement vector, ρ is the density of the propagation media (assumed homogeneous and isotropic) and λ and μ are the Lamè constants. We can make use of the Helmholtz decomposition [32] to write the displacement field as

$$\boldsymbol{u} = \nabla\varphi + \nabla\wedge\boldsymbol{\psi} \tag{A.2}$$

where the scalar and the vectorial potentials ∇ and $\boldsymbol{\psi}$ are introduced, respectively. Equation (A.1) can be rewritten as

$$\mu\nabla^2\left[\nabla\varphi + \nabla\wedge\boldsymbol{\psi}\right] + (\lambda+\mu)\nabla\nabla\cdot\left[\nabla\varphi + \nabla\wedge\boldsymbol{\psi}\right] = \rho\frac{\partial^2}{\partial t^2}\left[\nabla\varphi + \nabla\wedge\boldsymbol{\psi}\right] \tag{A.3}$$

which, after some rearrangements, reads

$$\nabla\left[(\lambda+2\mu)\nabla^2\varphi - \rho\ddot{\varphi}\right] + \nabla\wedge\left[\mu\nabla^2\boldsymbol{\psi} - \rho\ddot{\boldsymbol{\psi}}\right] = 0 \tag{A.4}$$

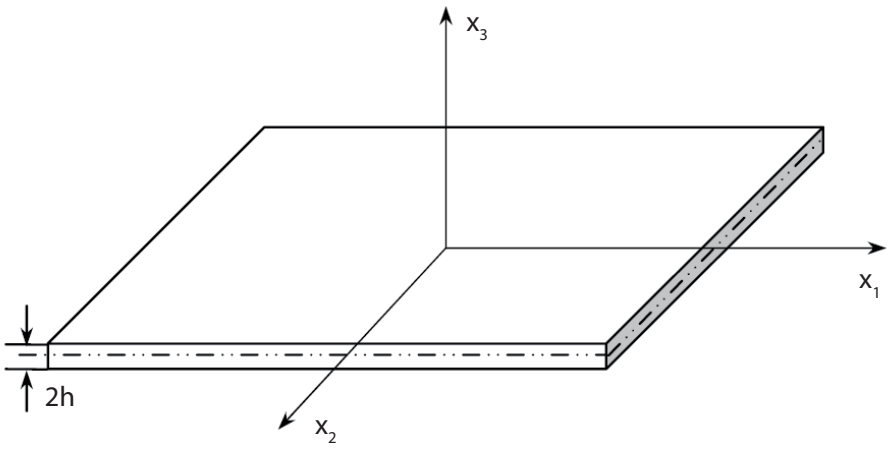

Figure A.1: A thin homogeneous and isotropic plate of 2h in thickness.

It is apparent that the above equation is satisfied only if

$$\nabla^2\varphi = \frac{1}{c_P^2}\ddot{\varphi} \tag{A.5}$$

$$\nabla^2\boldsymbol{\psi} = \frac{1}{c_S^2}\ddot{\boldsymbol{\psi}} \tag{A.6}$$

where c_P and c_S represent the primary and secondary wave speed, reading

$$c_P = \sqrt{\frac{\lambda+2\mu}{\rho}} \tag{A.7}$$

$$c_S = \sqrt{\frac{\mu}{\rho}} \tag{A.8}$$

The solution of equations (A.5) and (A.7) is composed of three different wave types: a pressure wave (PV), for which the polarization and propagation directions coincide, and two shear waves for which the polarization direction is orthogonal to the propagation direction [32, 91]. In particular, a displacement direction normal to the vertical plane Π containing the propagation direction denotes horizontal shear waves (SH), while a polarization direction orthogonal to the propagation direction but laying in the vertical plane Π is characteristic of shear vertical waves (SV) (see Fig. A.1). Due to the physical laws regulating the wave reflections and the mode conversion phenomena which occur at the boundaries of the propagation domain, it can be demonstrated that SH waves are decoupled from SV and P waves: their behavior can thus be analyzed separately from P and SV.

Due to these considerations, a plane strain assumption can be made to simplify the study of the propagation of P and SV waves. We thus impose that

$$u_2 \equiv 0 \tag{A.9}$$

$$\frac{\partial}{\partial x_2} \equiv 0 \tag{A.10}$$

and so, consequently, we have

$$u_1 = \frac{\partial\varphi}{\partial x_1} + \frac{\partial\psi}{\partial x_3} \tag{A.11}$$

$$u_3 = \frac{\partial\varphi}{\partial x_3} - \frac{\partial\psi}{\partial x_1} \tag{A.12}$$

The relevant components of the stress tensor follow from Hooke's law as

$$\tau_{31} = \mu\left(\frac{\partial u_3}{\partial x_1} + \frac{\partial u_1}{\partial x_3}\right) = \mu\left(2\frac{\partial^2\varphi}{\partial x_1\partial x_3} - \frac{\partial^2\varphi}{\partial x_1} + \frac{\partial^2\psi}{\partial x_3}\right) \tag{A.13}$$

$$\tau_{33} = \lambda\left(\frac{\partial u_1}{\partial x_1} + \frac{\partial u_3}{\partial x_3}\right) + 2\mu\frac{\partial u_3}{\partial x_3} = \lambda\left(\frac{\partial^2\varphi}{\partial x_1} + \frac{\partial^2\varphi}{\partial x_3}\right) + 2\mu\left(\frac{\partial^2\varphi}{\partial x_3} - \frac{\partial^2\psi}{\partial x_1\partial x_3}\right) \tag{A.14}$$

To investigate wave motion in the elastic layer, we consider solutions of of the form

$$\varphi = \Phi(x_3)\exp\left[i(kx_1 - \omega t)\right] \tag{A.15}$$

$$\psi = \Psi(x_3)\exp\left[i(kx_1 - \omega t)\right] \tag{A.16}$$

representing standing waves in the x_3-direction propagating in the x_1-direction. Substituting Eqs. (A.15) and (A.16) in Eqs. (A.5) and (A.7) we have

$$\Phi(x_3) = A_1\sin(px_3) + A_2\cos(px_3) \tag{A.17}$$

$$\Psi(x_3) = B_1\sin(qx_3) + B_2\cos(qx_3) \tag{A.18}$$

where $p^2 = \frac{\omega^2}{c_P^2} - k^2$, $q^2 = \frac{\omega^2}{c_S^2} - k^2$ and $k = \frac{2\pi}{\lambda_{wave}}$. In the expressions for the displacement and the stress components, which are obtained from Eqs. (A.11)-(A.14), the term $\exp\left[i(kx_1 - \omega t)\right]$ appears as a multiplier. Since the exponential appears in all of the expressions it does not play a further role in the determination of the frequency equation and it is therefore omitted in the sequel. Thus we can write

$$u_1 = ik\Phi + \frac{D\Psi}{Dx_3} \tag{A.19}$$

$$u_3 = \frac{D\Phi}{Dx_3} - ik\Psi \tag{A.20}$$

and

$$\tau_{31} = \mu\left(2ik\frac{D\Phi}{Dx_3} + k^2\Psi + \frac{d^2\Psi}{dx_3{}^2}\right) \tag{A.21}$$

$$\tau_{33} = \lambda\left(-k^2\Phi + \frac{d^2\Phi}{dx_3{}^2}\right) + 2\mu\left(\frac{d^2\Phi}{dx_3{}^2} - ik\frac{D\Psi}{Dx_3}\right) \tag{A.22}$$

The inspection of Eqs. (A.19)-(A.22) shows that the displacement components can be written in terms of elementary functions. For the displacement in the x_1-direction the motion is symmetric (antisymmetric) with regard to $x_3 = 0$, if u_1 contains cosines (sines). The displacement in the x_3-direction is symmetric (antisymmetric) if u_3 contains sines (cosines).

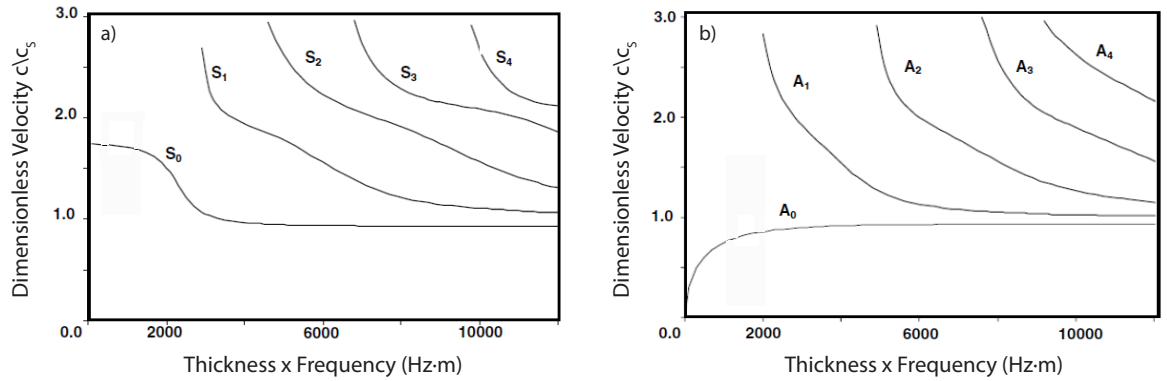

Figure A.2: Dispersion curves of symmetric (a) and antisymmetric (b) modes in an aluminium plate (c_S =3170 m/s) [135].

The modes of wave propagation in the elastic layer may thus be split up into two systems of symmetric and antisymmetric modes, respectively:

Symmetric modes:

$$\begin{aligned}
\Phi &= A_2 \cos(px_3) \\
\Psi &= B_1 \sin(qx_3) \\
u_1 &= ikA_2 \cos(px_3) + qB_1 \cos(qx_3) \\
u_3 &= -pA_2 \sin(px_3) - ikB_1 \sin(qx_3) \\
\tau_{31} &= \mu[-2ikpA_2 \sin(px_3) + (k^2 - q^2)B_1 \sin(qx_3)] \\
\tau_{33} &= -\lambda(k^2 + p^2)A_2 \cos(px_3) - 2\mu[p^2 A_2 \cos(px_3) + ikqB_1 \cos(qx_3)]
\end{aligned} \tag{A.23}$$

Antisymmetric modes:

$$\begin{aligned}
\Phi &= A_1 \sin(px_3) \\
\Psi &= B_2 \cos(qx_3) \\
u_1 &= ikA_1 \sin(px_3) - qB_2 \sin(qx_3) \\
u_3 &= pA_1 \cos(px_3) - ikB_2 \cos(qx_3) \\
\tau_{31} &= \mu[2ikpA_1 \cos(px_3) + (k^2 - q^2)B_2 \cos(qx_3)] \\
\tau_{33} &= -\lambda(k^2 + p^2)A_1 \sin(px_3) - 2\mu[p^2 A_1 \sin(px_3) - ikqB_2 \sin(qx_3)]
\end{aligned} \tag{A.24}$$

The frequency relation, i.e. the expression relating ω to the wave number k is now obtained from the boundary conditions. If the boundaries are free, we have at $x_3 = \pm h$:

$$\tau_{31} = \tau_{33} = 0 \tag{A.25}$$

For the symmetric modes the boundary conditions yield a system of two homogeneous equations for the constants A_2 and B_1. Similarly, for the antisymmetric modes two homogeneous

equations for the constants A_1 and B_2 are obtained. Since the systems are homogeneous, the determinant of the coefficients must vanish, which yields the frequency equation. Thus, for the symmetric modes we find

$$\frac{(k^2-q^2)\sin(qh)}{2ikp\sin(ph)} = -\frac{2\mu ikq\cos(qh)}{(\lambda k^2+\lambda p^2+2\mu p^2)\cos(ph)} \tag{A.26}$$

This equation can be rewritten as

$$\frac{\tan(qh)}{\tan(ph)} = -\frac{4k^2pq}{(q^2-k^2)^2} \tag{A.27}$$

For the antisymmetric modes the boundary conditions yields

$$-\frac{(k^2-q^2)\cos(qh)}{2ikp\cos(ph)} = \frac{2\mu ikq\sin(qh)}{(\lambda k^2+\lambda p^2+2\mu p^2)\sin(ph)} \tag{A.28}$$

or

$$\frac{\tan(qh)}{\tan(ph)} = -\frac{(q^2-k^2)^2}{4k^2pq} \tag{A.29}$$

These equations (also called dispersion equations) show the dependency of the wave speed on the thickness-frequency product, evidencing the dispersive nature of Rayleigh-Lamb waves.

A.2 The Rayleigh surface waves

The possibility of a wave traveling along the free surface of an elastic half-space such that the disturbance is largely confined to the neighborhood of the boundary was considered by Rayleigh [95]

The criterion for surface waves or Rayleigh waves is that the displacement decays exponentially with distance from the free surface. Here we investigate the existence of Rayleigh

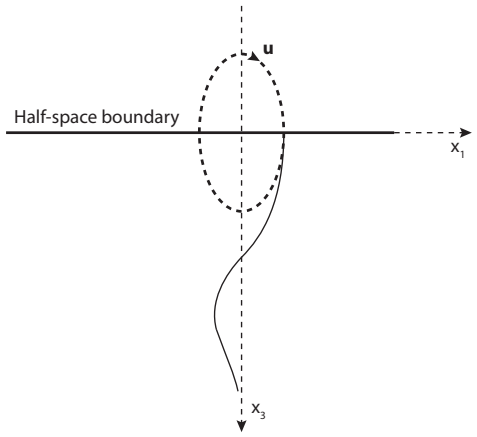

Figure A.3: Polarization of Rayleigh waves [32].

waves for the two-dimensional case of plane waves propagating in the x_1-direction (see figure 5.11). We consider displacement components of the form,

$$\begin{aligned} u_1 &= Ae^{-kx_3}\exp[ik(x_1 - ct)] \\ u_2 &= 0 \\ u_3 &= Be^{-kx_3}\exp[ik(x_1 - ct)] \end{aligned} \tag{A.30}$$

The real part of b is supposed to be positive, so that the displacements decrease with increasing x_3 and tend to zero as x_3 increases beyond bounds. Substitution of Eq. (A.30) into the displacement equations of motion yields two homogeneous equations for the constants A and B. A nontrivial solution of this system of equations exists if the determinant of the coefficients vanishes, which leads to the equation

$$[c_P^2 b^2 - (c_P^2 - c^2)k^2][c_S^2 b^2 - (c_S^2 - c^2)k^2] = 0 \tag{A.31}$$

whose roots are

$$b_1 = k\left(1 - \frac{c^2}{c_P^2}\right)^{\frac{1}{2}} \tag{A.32}$$

$$b_2 = k\left(1 - \frac{c^2}{c_S^2}\right)^{\frac{1}{2}} \tag{A.33}$$

It is noted that b_1 and b_2 are real and positive if $c < c_S < c_P$ and if positive roots are taken.

The ratios (B/A) corresponding to b_1 and b_2 can now be computed as

$$\left(\frac{B}{A}\right)_1 = -\frac{b_1}{ik} \tag{A.34}$$

$$\left(\frac{B}{A}\right)_2 = \frac{ik}{b_2} \tag{A.35}$$

Returning to Eq. (A.30), a general solution of the displacement equations of motion may thus be written in the form

$$u_1 = \left[A_1 e^{-b_1 x_3} + A_2 e^{-b_2 x_3}\right]\exp[ik(x_1 - ct)] \tag{A.36}$$

$$u_3 = \left[-\frac{b_1}{ik}A_1 e^{-b_1 x_3} + \frac{ik}{b_2}A_2 e^{-b_2 x_3}\right]\exp[ik(x_1 - ct)] \tag{A.37}$$

The constants A_1 and A_2 and the phase velocity c have to be chosen such that the stresses τ_{33} and τ_{31} vanish at $x_3 = 0$. By substituting Eqs. (A.36) and (A.37) into the expressions for τ_{33} and τ_{31} at $x_3 = 0$, we obtain after some manipulation

$$2b_1 A_1 + \left(2 - \frac{c^2}{c_S^2}\right)k^2 \frac{A_2}{b_2} = 0 \tag{A.38}$$

$$\left(2 - \frac{c^2}{c_S^2}\right)A_1 + 2b_2 \frac{A_2}{b_2} = 0 \tag{A.39}$$

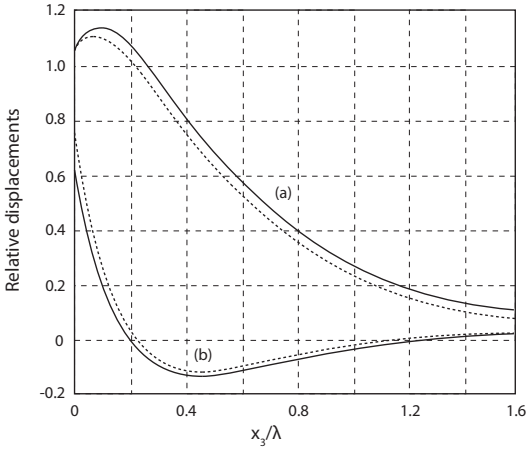

Figure A.4: Displacement amplitudes $u_3/u_{3_{x_3=0}}$ (a) and $u_1/u_{3_{x_3=0}}$ (b) for $\nu = 0.25$ (dashed line) and $\nu = 0.34$ (solid line).

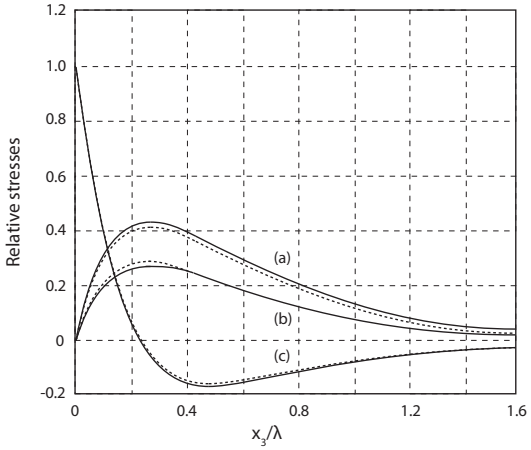

Figure A.5: Stresses amplitudes $\tau_{13}/\tau_{11_{x_3=0}}$ (a), $\tau_{33}/\tau_{11_{x_3=0}}$ (b) and $\tau_{11}/\tau_{11_{x_3=0}}$ (c) for $\nu = 0.25$ (dashed line) and $\nu = 0.34$ (solid line).

For a nontrivial solution the determinant of the coefficients of A_1, A_2 must vanish, which yields the following well-known equation for the phase velocity of Rayleigh waves:

$$\left(2 - \frac{c^2}{c_T^2}\right)^2 - 4\left(1 - \frac{c^2}{c_L^2}\right)^{1/2}\left(1 - \frac{c^2}{c_T^2}\right)^{1/2} = 0 \tag{A.40}$$

It is noted that the wavenumber does not enter in the above equation, and surface waves at a free surface of an elastic half-space are thus nondispersive.

Denoting the phase velocity of Rayleigh waves by c_R, Eq. (A.40) can be considered as an equation for c_R/c_S, with Poisson's ratio ($0 \leq \nu \leq 0.5$) as independent parameter. A good approximation of c_R can be written as

$$c_R = \frac{0.862 + 1.14\nu}{1 + \nu} c_S \tag{A.41}$$

For two values of Poisson's ratio, figure Fig. A.4 shows the variations of the displacements with depth. The displacements are referred to the normal displacement u_3 at the surface, and they are plotted versus the ratio of x_3 and the wavelength. The variations of the stresses with depth are shown in Fig. A.5, where the stresses are referred to τ_{11} at $x_3 = 0$.

The figures show the localization of the wave motion in a thin layer near the surface, of a thickness which is about twice the wavelength of the surface waves. Since the displacement components u_1 and u_3 are 90^o out of phase, the trajectories of the particles are ellipses. For the coordinate axes of Fig. A.3 the motion is clockwise at the free surface. At a depth of $x_3 \sim 0.2\lambda$ the direction of rotation reverses, since u_1 changes sign. The semimajor axes of the ellipses are normal to the free surface; the semiminor axes are parallel to the free surface. At the free surface the normal displacement is about 1.5 times the tangential displacement.

Appendix B

The Differential Evolutionary Algorithm-Based Optimization Code

B.1 Numerical interface with the COMSOL®software

```
function [V_out] = Run_Comsol(dt,t_end,dx,mesh_level,name_rs,name_ls,x_c,d_c,h_c,fem)


fem = rmfield(fem, 'mesh'); %removes the specified field from the structure array s.

% Ricerca Sensore e Variazione Lunghezza

for n=1:length(fem.draw.s.name)
    str=cell2mat(fem.draw.s.name(n));

    if strcmp(str,name_rs)==1
       sens_r=n;
    end

    if strcmp(str,name_ls)==1
       sens_l=n;
    end

end

y_c=h_c/2;
fem.draw.s.objs{1,sens_r}=rect2(d_c,h_c,'base','center','pos',{x_c,y_c},'rot','0');
```

```
23 fem.draw.s.objs{1,sens_l}=rect2(d_c,h_c,'base','center','pos',{-x_c,y_c},'rot','0');
24
25 fem.geom=geomcsg(fem);
26
27 if length(fem.draw.s.name) >= 40
28 % Initialize mesh
29 fem.mesh=meshinit(fem, ...
30                   'hauto',mesh_level);
31
32 % Refine mesh
33 fem.mesh=meshrefine(fem, ...
34                     'mcase',0, ...
35                     'rmethod','regular');
36
37 % % Refine mesh
38 % fem.mesh=meshrefine(fem, ...
39 %                       'mcase',0, ...
40 %                       'rmethod','regular', ...
41 %                       'subdomain',[9,10,11,12,13,14,15,16,17,18,19,20,21,22,23,24,
42 %                                                          25,26,27,28,29,30,31,40]);
43
44 else
45
46 % Initialize mesh
47 fem.mesh=meshinit(fem, ...
48                   'hauto',mesh_level);
49
50 % Refine mesh
51 fem.mesh=meshrefine(fem, ...
52                     'mcase',0, ...
53                     'rmethod','regular', ...
54                     'subdomain',[9,10,11,12,13,14,15,16,17,18,19,20,21,22,23,24,25,
55                                                                          26,27]);
56
57 % % Refine mesh
58 % fem.mesh=meshrefine(fem, ...
59 %                       'mcase',0, ...
60 %                       'rmethod','regular', ...
61 %                       'subdomain',[9,10,11,12,13,14,15,16,17,18,19,20,21,22,23,24,
62 %                                                                  25,26,27]);
63
64 end
65
66 % if length(fem.draw.s.name) >= 40
67 % % Initialize mesh
```

```
% fem.mesh=meshinit(fem, ...
%                    'hmax',dx, ...
%                    'point',[], ...
%                    'edge',[], ...
%                    'subdomain',[9,10,11,12,13,14,15,16,17,18,19,20,21,22,23,24,25,
%                                                                 26,27,28,29,30,31,40]);
%
% % Initialize mesh
% fem.mesh=meshinit(fem, ...
%                    'hauto',mesh_level, ...
%                    'point',[], ...
%                    'edge',[], ...
%                    'subdomain',[1,2,3,4,5,6,7,8,32,33,34,35,36,37,38,39], ...
%                    'meshstart',fem.mesh);
% else
%
% % Initialize mesh
% fem.mesh=meshinit(fem, ...
%                    'hmax',dx, ...
%                    'point',[], ...
%                    'edge',[], ...
%                    'subdomain',[9,10,11,12,13,14,15,16,17,18,19,20,21,22,23,24,25,
%                                                                       26,27]);
%
% % Initialize mesh
% fem.mesh=meshinit(fem, ...
%                    'hauto',mesh_level, ...
%                    'point',[], ...
%                    'edge',[], ...
%                    'subdomain',[1,2,3,4,5,6,7,8,28,29,30,31,32,33,34,35], ...
%                    'meshstart',fem.mesh);
% end

% ODE Settings
clear ode
clear units;
units.basesystem = 'SI';
ode.units = units;
fem.ode=ode;

% Multiphysics
fem=multiphysics(fem);

% Extend mesh
fem.xmesh=meshextend(fem);
```

```
113
114 % Solve problem
115 fem.sol=femtime(fem, ...
116                 'solfile','on', ...
117                 'solcomp',{'V','u1','u3'}, ...
118                 'outcomp',{'V','u1','u3'}, ...
119                 'blocksize','auto', ...
120                 'plotinterp',{'u1','u3','V','V'}, ...
121                 'plotinterppar',{{'recover','off','phase',0,'geomnum',1,
122                                     'probecoord',[0.25 -0.096]}, ...
123                                 {'recover','off','phase',0,'geomnum',1,
124                                     'probecoord',[0 -0.092999]}, ...
125                                 {'recover','off','phase',0,'geomnum',1,
126                                       'probecoord',[0 0.01492]}, ...
127                                 {'recover','off','phase',0,'geomnum',1,
128                                         'probecoord',[0.35 0.01492]}}, ...
129                 'tlist',[colon(0,dt,t_end)], ...
130                 'tout','tlist', ...
131                 'tsteps','strict', ...
132                 'atol',{'0.001'});
133
134 V_out=postinterp(fem,'V',[x_c; h_c],'solnum','all');
135
136 end
```

B.2 The optimizer

```
1  function [Output,names,num_cases]=Optimizer(N,M,K,H,threshold,pop_0,models,dt,t_end,
2                                               dx,mesh_level,x_max,x_min,d_max,d_min,
3                                               x_lim_l,x_lim_r)
4
5  names=fieldnames(models);
6  num_cases=max(size(names));
7
8  Out_pop=zeros(M,2,N);
9
10 h = waitbar(0,'Please wait...');
11
12 for n=1:N
13
14
15     if n==1;
16        pop=pop_0;
```

```
17      end
18
19      for i=1:M
20
21
22          waitbar(0.1*(i/M)+(n-1)/N)
23
24          fprintf('Generation: %1.0f, Individual %1.0f\n',n,i)
25
26          V_target=pop(i,:);
27
28          select=0;
29          tries=0;
30
31          while not(select)
32
33                num=randperm(M);
34                k=0;
35                if num(k+1)~=3;
36                   V1=pop(num(k+1),:);
37                else
38                   k=1;
39                   V1=pop(num(k+1),:);
40                end
41                if num(k+2)~=3;
42                   V2=pop(num(k+2),:);
43                else
44                   k=1;
45                   V2=pop(num(k+2),:);
46                end
47                if num(k+3)~=3;
48                   V3=pop(num(k+3),:);
49                else
50                   k=1;
51                   V3=pop(num(k+3),:);
52                end
53
54                V23=V2-V3;
55                V4=V1+K*V23;
56
57                if V4(1) > d_max
58                   V4(1)= d_max;
59                elseif  V4(1) < d_min
60                        V4(1) = d_min;
61                end
```

```
62
63              if V4(2) > x_max
64                 V4(2)= x_max;
65              elseif  V4(2) < x_min
66                      V4(2) = x_min;
67              end
68
69              if V4(2)+V4(1)/2 > x_lim_r
70                 V4(2)= x_lim_r-V4(1)/2;
71              elseif V4(2)-V4(1)/2 < x_lim_l
72                 V4(2)= x_lim_l+V4(1)/2;
73              end
74
75              toss1=rand(1);
76              toss2=rand(1);
77
78              if toss1 > H
79                 V_trial(1) = V_target(1);
80              else
81                 V_trial(1) = V4(1);
82              end
83
84              if toss2 > H
85                 V_trial(2) = V_target(2);
86              else
87                 V_trial(2) = V4(2);
88              end
89
90              if V_trial(1) == V_target(1) && V_trial(1) == V_target(1)
91                 select=0;
92                 tries=tries+1;
93                 if tries==5;
94                    select=1;
95                 end
96              else
97                 select=1;
98              end
99
100             if V_trial(2)+V_trial(1)/2 > x_lim_r
101                V_trial(2)= x_lim_r-V_trial(1)/2;
102             elseif V_trial(2)-V_trial(1)/2 < x_lim_l
103                V_trial(2)= x_lim_l+V_trial(1)/2;
104             end
105
106         end
```

```
107
108         done = 0;
109
110         if i ~= 1 && n ~= 1
111            r = max(size(Out));
112            l=0;
113            for k=1:r
114                if V_target(1) == Out(k,1) && V_target(2) == Out(k,2) && l==0
115                   I_target = Out_I(:,k);
116                   Ir_target = Out_Ir(:,k);
117                   V_out_target = Out_V(:,:,k);
118                   done=1;
119                   l=1;
120                   fprintf('V_target Aleardy Computed - Width:
121               end
122            end
123         end
124
125         switch done
126
127         case 0
128
129         fprintf('Width: %6.4f, Diameter %6.4f\n',V_target(1),V_target(2))
130
131              for k=1:num_cases
132
133                  fprintf('V_target, caso %1.0f\n',k)
134                  fem=getfield(models,names{k,1});
135                 [V_out] = Run_Comsol(dt,t_end,dx,mesh_level,'R7','R6',V_target(2),
136                                                          V_target(1),1.492e-2,fem);
137                  V_out_target(:,k) = V_out;
138                  V_max_target(k) = max(V_out);
139
140              end
141
142              for k=1:num_cases-1
143                  I_target(k)=abs(V_max_target(k)-V_max_target(length(V_max_target)))
144                  ./V_max_target(length(V_max_target));
145                  Ir_target(k)=I_target(k);
146                  if I_target(k)>1
147                     I_target(k)=1;
148                  end
149              end
150         end
151
```

```
152         done = 0;
153
154         if i ~= 1 && n ~= 1
155            r = max(size(Out));
156            l=0;
157            for k=1:r
158                if V_trial(1) == Out(k,1) && V_trial(2) == Out(k,2) && l==0;
159                   I_trial = Out_I(:,k);
160                   Ir_trial = Out_Ir(:,k);
161                   V_out_trial = Out_V(:,:,k);
162                   done=1;
163                   l=1;
164                   fprintf('V_trial Aleardy Computed - Width:
165               end
166            end
167         end
168
169         switch done
170
171         case 0
172
173         fprintf('Width: %6.4f, Diameter %6.4f\n',V_trial(1),V_trial(2))
174
175              for k=1:num_cases
176
177                  fprintf('V_trial, caso %1.0f\n',k)
178                  fem=getfield(models,names{k,1});
179                  [V_out] = Run_Comsol(dt,t_end,dx,mesh_level,'R7','R6',V_trial(2),
180                                                              V_trial(1),1.492e-2,fem);
181                  V_out_trial(:,k) = V_out;
182                  V_max_trial(k) = max(V_out);
183
184              end
185
186              for k=1:num_cases-1
187
188                  I_trial(k)=abs(V_max_trial(k)-V_max_trial(length(V_max_trial)))
189                  ./V_max_trial(length(V_max_trial));
190                  Ir_trial(k)=I_trial(k);
191                  if I_trial(k)>1
192                     I_trial(k)=1;
193                  end
194              end
195         end
196
```

```
197
198
199         j=2*i-1+2*(n-1)*M;
200
201         Out(j,:) = V_target;
202         Out(j+1,:) = V_trial;
203         Out_I(:,j) = I_target;
204         Out_I(:,j+1) = I_trial;
205         Out_Ir(:,j) = Ir_target;
206         Out_Ir(:,j+1) = Ir_trial;
207         Out_V(:,:,j) = V_out_target;
208         Out_V(:,:,j+1) = V_out_trial;
209
210         n_obs_target = 0;
211         n_obs_trial = 0;
212
213         for k = 1:num_cases-1
214             if I_target(k) >= treshold
215                n_obs_target = n_obs_target+1;
216             end
217
218             if I_trial(k) >= treshold
219                n_obs_trial = n_obs_trial+1;
220             end
221         end
222
223         m_target=mean(Ir_target);
224         m_trial=mean(Ir_trial);
225
226         if n_obs_target > n_obs_trial && m_target > m_trial
227            pop(i,:) = V_target;
228         elseif n_obs_target == n_obs_trial && m_target >= m_trial
229            pop(i,:) = V_target;
230         elseif n_obs_target < n_obs_trial && m_target < m_trial
231            pop(i,:) = V_trial;
232         elseif n_obs_target == n_obs_trial && m_target <= m_trial
233            pop(i,:) = V_trial;
234         end
235
236     end
237
238     Out_pop(:,:,n)=pop;
239     nome=['Generation_', num2str(n)];
240     save(nome,'pop');
241 end
```

```
242
243 close(h)
244
245 Output = struct('Vectors', Out, 'Indeces_I', Out_Ir, 'Voltages', Out_V,
246                  'Populations',Out_pop);
247
248 end
```

Bibliography

[1] K. Worden, C.R. Farrar, G. Manson, G. Park, "The fundamental axioms of structural health monitoring ", *Proceedings of the Royal Society A: Mathematical, Physical and Engineering Sciences*, Vol. 463, pp. 1639-1664 (2007).

[2] P. Moyo, J.M.W. Brownjohn, "Detection of anomalous structural behaviour using wavelet analysis ", *Mechanical Systems and Signal Processing*, Vol. 16, pp. 429Ű445 (2002).

[3] C.R. Farrar, N.A.J. Lieven, M.T. Bement, "An introduction to damage prognosis", *Damage Prognosis: for Aerospace, Civil and Mechanical Systems*, *John Wiley & Sons*, Chichester (2005).

[4] D. Rees, W.K. Chiu, R. Jones, "A Numerical Study of Crack Monitoring in Patched Structures Using a Piezo Sensor", *Smart Materials and Structures* Vol.1, pp. 202Ű205 (1992).

[5] C. Marantidis, C. B. Van Way, J.N. Kudva, "Acoustic emission Sensing in an On-board Smart Structural Health Monitoring System for Military Aircraft", *Proceedings of the SPIE Conference on Smart Structures and Integrated Systems*, pp. 258Ű264 (1994).

[6] L. Kollar, R.J. Steenkiste, "Calculation of the Stresses and Strains in Embedded Fiber Optic Sensors", *Composite Materials*, Vol. 32, pp. 1647Ű1679 (1998).

[7] J.N. Schoess, J.D. Zook, "Test Results of Resonant Integrated Microbeam Sensor (RIMS) for Acoustic Emission Monitoring", *Proceedings of the SPIE Conference on Smart Electronics and MEMS*, pp. 326Ű332 (1998).

[8] C. Hautamaki, S. Zurn, S.C. Mantell, D.L. Polla, "Experimental Evaluation of MEMS Strain Sensors Embedded in Composites", *Microelectromechanical Systems*, Vol. 8, pp. 272Ű279 (1999).

[9] R.E. Seydel, F.K. Chang, "Implementation of a Real-time Impact Identification Technique for Stiffened Composite Panels", *Proceedings of the 2nd International Workshop on Structural Health Monitoring*, Stanford University, CA, pp. 225Ű233 (1999).

[10] W.K. Chiu, S.C. Galea, L.L. Koss, N. Rajic, "Damage Detection in Bonded Repairs Using Piezoceramics ", *Smart Materials and Structures*, Vol. 9, pp. 466Ű475 (2000).

[11] D. Montalvao, N.M.M. Maia, A.M.R. Ribeiro, "A review of vibration-based structural health monitoring with special emphasis on composite materials", *The Shock and Vibration Digest*, Vol. 38, pp. 295Ű324 (2006).

[12] J.D. Achenbach, "Quantitative nondestructive evaluation", *Solids and Structures*, Vol. 37, pp. 13Ű27 (2000).

[13] F.K. Chang, "Introduction to health monitoring: context, problems, solutions", *Presentation at the 1st European Pre-workshop on Structural Health Monitoring*, Paris, France, July 9th (2002).

[14] V. Giurgiutiu, C.A. Rogers, "Recent advancements in the Electro-Mechanical (E/M) impedance method for structural health monitoring and NDE", *Proceedings of the SPIE*, pp. 536Ű547 (1998).

[15] O.S. Salawu, "Detection of structural damage through changes in frequency: a review", *Engineering Structures*, vol. 19, pp. 718Ű723 (1997).

[16] Y. Zou, L. Tong, G.P. Steven, "Vibration-based model-dependent damage (delamination) identification and health monitoring for composite structures - a review", *Sound and Vibration*, Vol 230, pp. 357Ű378 (2000).

[17] C.R. Farrar, S.W. Doebling, D.A. Nix, "Vibration-based structural damage identification ", *Philosophical Transactions of the Royal Society, A: Mathematical, Physical and Engineering Sciences*, Vol. 359, pp. 131Ű149 (2001).

[18] N. Tandon, A. Choudhury, "A review of vibration and acoustic measurement methods for the detection of defects in rolling element bearings", *Tribology International*, Vol. 32, pp. 469Ű480 (1999).

[19] S.W. Doebling, C.R. Farrar, M.B. Prime, D.W. Shevitz, "Damage Identification and Health Monitoring of Structural and Mechanical Systems from Changes in Their Vibration Characteristics: A Literature Review", *Los Alamos National Laboratory Report*, LA-13070-MS (1996).

[20] J.Y. Shen, J.L. Sharpe, "An overview of vibration-based nondestructive evaluation techniques", *Proceedings of the SPIE*, pp. 117Ű128 (1998).

[21] G. Park, H. Sohn, C.R. Farrar, D.J. Inman "Overview of Piezoelectric Impedance-based Health Monitoring and Path Forward", *The Shock and Vibration Digest*, Vol. 35, pp. 451-463 (2003).

[22] N. Kong, D.S Ha, A. Erturk, D.J. Inman, "Resistive Impedance Matching Circuit for Piezoelectric Energy Harvesting", *Intelligent Material Systems and Structures*, Vol. 21, pp. 1293-1302 (2010).

[23] V.G.M. Annamdas and M.A. Radhika "Electromechanical impedance of piezoelectric transducers for monitoring metallic and non-metallic structures: A review of wired, wireless and energy-harvesting methods", *Intelligent Material Systems and Structures*, Vol. 24, pp. 1021Ű1042 (2013).

[24] J. Sirohi, I. Chopra, "Fundamental Understanding of Piezoelectric Strain Sensors", *Intelligent Material Systems and Structures*, Vol. 11, pp. 246-257 (2000).

[25] G. Park2, H.H. Cudney, D.J. Inman "Impedance-based Health Monitoring of Civil Structural Components", *ASCE Journal of Infrastructure Systems*, Vol.6, pp. 153-160 (2000).

[26] M. Ohtsu, "Acoustic emission characteristics in concrete and diagnostic applications", *Acoustic Emission*, Vol.6, pp. 99-108 (1987).

[27] M. Ohtsu, Y. Tomoda, "Phenomenological model of corrosion process in reinforced concrete identified by acoustic emission", *ACI Materials*, Vol.105, pp. 194-199 (2008).

[28] M. Fregonese, H. Idrissi, H. Mazille, L. Renaud, Y. Cètre, "Monitoring pitting corrosion of 304L and 316L austenitic stainless steels by acoustic emission: influence of the pit morphology", *Proceedings European Corrosion Congress*, Aachen, Germany, (1999).

[29] L. Golaski, P. Gebski, K. Ono, "Diagnostics of reinforced concrete bridges by acoustic emission ", *Acoustic Emission*, Vol. 20, pp. 83-98 (2002).

[30] J.D.N. Cheeke, "Fundamentals and Applications of Ultrasonic Waves", *CRC Press*, Boca Raton (2002).

[31] J.L. Rose, "Ultrasonic Waves in Solid Media", *Cambridge University Press*, New York (1999).

[32] J.D. Achenbach, "Wave propagation in elastic solids ", *North-Holland*, Amsterdam (1973).

[33] C.S. Wang, F.K. Chang, "Built-in diagnostics for impact damage identification of composite structures ", *Proceedings of the 2nd International Workshop on Structural Health Monitoring*, Stanford, CA, USA, September 8-10, pp. 612Ű621 (1999).

[34] B. Tang, E.G. Henneke, "Lamb-wave monitoring of axial stiffness reduction of laminated composite plates", *Materials Evaluation*, Vol. 47, pp. 928Ű934 (1991).

[35] K.S. Tan, N. Guo, B.S Wong, C.G. Tui, "Experimental evaluation of delaminations in composite plates by the use of Lamb waves", *Composites Science and Technology*, Vol. 53, pp. 77Ű84 (1995).

[36] D.N. Alleyne, P. Cawley, "The interaction of Lamb waves with defects", *IEEE Transactions on Ultrasonics, Ferroelectrics and Frequency Control*, Vol. 39, pp. 381Ű397 (1992).

[37] N. Guo, P., Cawley, "Lamb waves for the NDE of composite laminates. ", *Review of Progress in Quantitative Nondestructive Evaluation*, Vol. 11, pp. 1443Ű1450 (1992).

[38] P. Cawley, D.N. Alleyne, "The use of Lamb waves for the long range inspection of large structures", *Ultrasonics*, Vol. 34, pp. 287Ű290 (1996).

[39] D.N. Alleyne, P. Cawley, "Optimisation of Lamb wave inspection techniques", *NDT&E International*, Vol. 25, pp. 11Ű22 (1992).

[40] Y.S. Roh, F.K. Chang, "Effect of impact damage on Lamb wave propagation in laminated composites ", *Proceedings of the ASME International Mechanical Engineering Congress and Exposition (Dynamic Responses and Behavior of Composites)*, San Francisco, CA, USA, November 12-17, pp. 127Ű138 (1995).

[41] Z. Su, L. Ye, Y. Lu, "Guided Lamb waves for identification of damage in composite structures: a review", *Sound and Vibration*, Vol. 295, pp. 753Ű780 (2006).

[42] A. Raghavan, C.E.S. Cesnik, "Review of guided-wave structural health monitoring", *The Shock and Vibration Digest*, Vol. 39, pp. 91Ű114 (2007).

[43] J.L. Rose, "A baseline and vision of ultrasonic guided wave inspection potential", *Pressure Vessel Technology*, Vol. 124, pp. 273Ű282 (2002).

[44] D.E. Chimenti, "Guided waves in plates and their use in materials characterization ", *Applied Mechanics Review*, Vol. 50, pp. 247Ű284 (1997).

[45] J.L. Rose, "Guided wave nuances for ultrasonic nondestructive evaluation", *IEEE Transactions on Ultrasonics, Ferroelectrics and Frequency Control*, Vol. 47, pp. 575Ű583 (2000).

[46] B.C. Lee, K.J. Staszewski, "Modelling of Lamb waves for damage detection in metallic structures: part I - wave propagation", *Smart Materials and Structures*, Vol 12, pp. 804Ű814 (2003).

[47] K. Harri, P. Guillaume, S. Vanlanduit "On-line damage detection on a wing panel using transmission of multisine ultrasonic waves ", *NDT&E International*, Vol. 41, pp. 312-317 (2008).

[48] M. Lemistre, D. Balageas, "Structural health monitoring system based on diffracted Lamb wave analysis by multiresolution processing ", *Smart Materials and Structures*, Vol. 10, pp. 504-511 (2001).

[49] S.H.D. Valdes, C. Soutis, "A structural health monitoring system for laminated composites ", *Proceedings of the 3rd International Workshop on Structural Health Monitoring*, Stanford, CA, USA, September 12-14, pp. 1476-1485 (2001).

[50] S.S. Kessler, S.M. Spearing, C. Soutis, "Damage detection in composite materials using Lamb wave methods ", *Smart Materials and Structures*, Vol. 11, pp. 269-278 (2002).

[51] P.T. Coverley, W. Staszewski, "Impact damage location in composite structures using optimized sensor triangulation procedure", *Smart Materials and Structures*, Vol. 12, pp. 795Ű803 (2003).

[52] J.E. Michaels, "Detection, localization and characterization of damage in plates with an in situ array of spatially distributed ultrasonic sensors", *Smart Materials and Structures*, Vol. 17, pp. 1501-1516 (2008).

[53] J.E. Michaels, T.E., Michaels, "Guided wave signal processing and image fusion for in situ damage localization in plates", *Wave Motion*, Vol. 44, pp. 482Ű492 (2007).

[54] P.S. Tua, S.T. Quek, Q. Wang, "Detection of cracks in cylindrical pipes and plates using piezo-actuated Lamb waves", *Smart Materials and Structures*, Vol. 14, pp. 1325Ű1342 (2005).

[55] H.G. Chen, Y.J. Yan, W.H. Chen, J.S Jiang, L. Yu, Z.Y. Wu, "Early damage detection in composite wingbox structures using Hilbert-Huang transform and genetic algorithm", *Structural Health Monitoring: An International Journal*, Vol. 6, pp. 281Ű297 (2007).

[56] G. Konstantinidis, B.W. Drinkwater, P.D. Wilcox, "The temperature stability of guided wave structural health monitoring systems", *Smart Materials and Structures*, Vol. 15, pp. 967Ű976 (2006).

[57] W.J. Staszewski, C. Biemans, C. Boller, G.R. Tomlinson, "Crack propagation monitoring in metallic structures using piezoceramic sensors", *Proceedings of the International Conference on Smart Materials, Structures and Systems*, Bangalore, India, July 7-10, pp. 532Ű541 (1999).

[58] D.C. Betz, W.J. Staszewski, G. Thursby, B. Culshaw, "Structural damage identification using multifunctional Bragg grating sensors: II. damage detection results and analysis", *Smart Materials and Structures*, Vol. 15, pp. 1313Ű1322 (2006).

[59] W.J. Staszewski, K. Worden, "Signal processing for damage detection", *Health Monitoring of Aerospace Structures: Smart Sensor Technologies and Signal Processing*, *John Wiley & Sons*, Chichester, pp. 163Ű206 (2004).

[60] X. Zhao, H. Gao, G. Zhang, B. Ayhan, F. Yan, C. Kwan, J.L. Rose, "Active health monitoring of an aircraft wing with embedded piezoelectric sensor/actuator network: I. defect detection, localization and growth monitoring", *Smart Materials and Structures*, Vol. 16, pp. 1208Ű1217 (2007).

[61] S. Hurlebaus, M. Niethammer, L.J. Jacobs, C. Valle, "Automated methodology to locate notches with Lamb waves", *Acoustics Research Letters Online*, Vol. 4, pp. 97Ű102 (2001).

[62] D. Posenato, F. Lanata, D. Inaudi, I.F.C. Smith, "Model-free data interpretation for continuous monitoring of complex structures", *Advanced Engineering Informatics*, Vol. 22, pp. 135Ű144 (2008).

[63] R.K. Ing, M. Fink, "Time-reversed Lamb waves", *IEEE Transactions on Ultrasonics, Ferroelectrics and Frequency Control*, Vol. 45, pp. 1032Ű1043 (1998).

[64] B. Boashash, "Time-Frequency Signal Analysis, Methods and Applications", *Longman Cheshire Press*, Melbourne (1992).

[65] D. Alleyne, P. Cawley, "A 2-dimensional Fourier transform method for the quantitative measurement of Lamb modes", *Proceedings of the Review of Progress in Quantitative Nondestructive Evaluation*, Vol. 10, pp. 201Ű208. Plenum Press, New York (1991).

[66] W. Gao, C. Glorieux, J. Thoen, "Laser ultrasonic study of Lamb waves: determination of the thickness and velocities of a thin plate", *International Journal of Engineering Science*, Vol. 41, pp. 219Ű228 (2003). 29

[67] Y.L. Koh, W.K. Chiu, N. Rajic, "Integrity assessment of composite repair patch using propagating Lamb waves", *Composite Structures*, Vol. 58, pp. 363Ű371 (2002).

[68] Y.L. Koh, W.K. Chiu, N. Rajic, "Effects of local stiffness changes and delamination on Lamb wave transmission using surface-mounted piezoelectric transducers", *Composite Structures*, Vol. 57, pp. 437Ű443 (2002).

[69] K. Heller, L.J. Jacobs, J. Qu, "Characterization of adhesive bond properties using Lamb waves", *NDT&E International*, Vol. 33, pp. 555Ű563 (2000).

[70] F. EI Youbi, S. Grondel, J. Assaad, "Signal processing for damage detection using two different array transducers", *Ultrasonics*, Vol. 42, pp. 803Ű806 (2004).

[71] M. Rguiti, S. Grondel, F. EI Youbi, C. Courtois, M. Lippert, A. Leriche, "Optimized piezoelectric sensor for a specific application: detection of Lamb waves", *Sensors and Actuators*, Vol. A126, pp. 362Ű368 (2006).

[72] C.K.W. Wong, W.K. Chiu, N. Rajic, S.C. Galea, "Can stress waves be used for monitoring sub-surface defects in repaired structures? ", *Composite Structures*, Vol. 76, pp. 199Ű208 (2006).

[73] J.B. Ihn, F.K. Chang, "Detection and monitoring of hidden fatigue crack growth using a built-in piezoelectric sensor/actuator network: I. diagnostics", *Smart Materials and Structures*, Vol. 13, pp. 609Ű620 (2004).

[74] J.B. Ihn, F.K. Chang, "Detection and monitoring of hidden fatigue crack growth using a built-in piezoelectric sensor/actuator network: II. validation using riveted joints and repair patches", *Smart Materials and Structures*, Vol. 13, pp. 621Ű630 (2004).

[75] Y.Y. Kim, E.H. Kim, "Effectiveness of the continuous wavelet transform in the analysis of some dispersive elastic waves", *Acoustical Society of America*, Vol. 110, pp. 1Ű9 (2001).

[76] D.U. Sung, J.H. Oh, C.G. Kim, C.S. Hong, "Impact monitoring techniques for smart composite laminates", *Proceedings of the 2nd Asian-Australasian Conference on Composite Materials (ACCM-2)*, Korea, August 18-20, pp. 1123Ű1128 (2000).

[77] F.K. Chang, F.C. Markmiller, J.B. Ihn, K.Y. Cheng, "A potential link from damage diagnostics to health prognostics of composites through built-in sensors", *Vibration and Acoustics*, Vol. 129, pp. 718Ű729 (2007).

[78] I. Daubechies, "The wavelet transform, time-frequency localization and signal analysis", *IEEE Transactions on Information Theory*, Vol. 36, pp. 961Ű1005 (1990).

[79] D.E. Newland, "Wavelet analysis of vibration, part I: theory", *Vibration and Acoustics*, Vol. 116, pp. 409Ű416 (1994).

[80] D.E. Newland, "Wavelet analysis of vibration, part II: wavelet maps", *Vibration and Acoustics*, Vol. 116, pp. 417Ű425 (1994).

[81] C.A. Paget, S. Grondel, K. Levin, C. Delebarre, "Damage assessment in composites by Lamb waves and wavelet coefficients", *Smart Materials and Structures*, Vol. 12, pp. 393Ű402 (2003).

[82] P.M. Morse, K.U. Ingard, "Theoretical Acoustics ", *McGraw-Hill*, New York (1968).

[83] A.T. De Hoop, "Handbook of radiadtion and scattering of waves ", *Academic Press*, London (1995).

[84] K.J. Langeberg, R. Marklein, K. Mayer, "Ultrasonic Nondestructive Test of Materials - Theoretical Foundations ", *CRC Press*, New York (2012).

[85] K.J. Langeberg, "Theorie elektromagnetischer Wellen ", *Vorlesungsmanuskript Universitat Kassel*, Kassel (2005).

[86] J.A. DeSanto, "Scalar Wave Theory ", *Springer-Verlag*, Berlin (1992).

[87] M. Abramowitz, I.A. Stegun, "Handbook of mathematical functions ", *Dover Publications*, New York (1965).

[88] G. Doetsch, "Funktionaltrasformationen ", *Springer-Verlag*, Berlin (1967).

[89] E. Martensen, "Potentialtheorie ", *B.G. Teubner*, Stuttgart (1968).

[90] D. Colton, R. Krees, "Integral equation methods in scattering theory ", *Jhon Wiley & Sons*, New York (1983).

[91] B.A. Auld, "Acoustic fields and waves in solids, Vol. I and Vol. II ", *Jhon Wiley & Sons*, New York (1973).

[92] G.F. Miller, H.Pursey, "The field and radiation impedance of mechanical radiators on the free surface of a semi-infinite isotropic solid ", *Proceedings of the Royal Society*, Vol. 223, pp. 521-541 (1954).

[93] A.H. Harker, "Elastic waves in solids ", *Adam Hilger*, Bristol (1988).

[94] R. Marklein, "The Finite Integration Technique as a general tool to compute acoustic, electromagnetic, elastodynamic and coupled wave fields ", *Review of Radio science 1999-2002*, IEEE Press, Piscataway (2002).

[95] L. Rayleigh, "On waves propagated along the plane surface of an elastic solid ", *Proc. Lond. Math. Soc.*, Vol. 17, pp. 4-11 (1885).

[96] T. Ikeda, "Fundamentals of Piezoelectricity ", *Oxford University Press*, Oxford (1990).

[97] W.G. Cady, "An Introduction to the Theory and Application of Electromechanical Phenomena in Crystals ", *McGraw-Hill*, London (1946).

[98] H. Sohn, C.R. Farrar, F.M. Hemez, D.D. Shunk, D.W. Stinemates, B.R. Nadler, J.J. Czarnecki, "A Review of Structural Health Monitoring Literature: 1996-2001 ", *Los Alamos National Laboratory Report*, LA-13976-MS, (2004).

[99] Z. Su, L. Ye, "Identification of Damage Using Lamb Waves ", *Springer-Verlag*, Berlin (2009).

[100] K. Diamanti, C. Soutis, J.M. Hodgkinson, "Lamb waves for the non-destructive inspection of monolithic and sandwich composite beams", *Composites Part A*, Vol. 36, pp. 189-195 (2005)

[101] W.M. Ostachowicz, "Damage detection of structures using spectral finite element method ", *Computers and Structures*, Vol. 86, pp. 454-462 (2008).

[102] H. Sohn, D. Dutta, J.Y. Yang, H.J. Park, M. DeSimio, S. Olson, E. Swenson, "Delamination detection in composites through guided wave field image processing", *Computer Science and Technology*, Vol. 71, pp. 1250-1256 (2011).

[103] P. Vachon, V. Brailovski, P. Terriault, "Prediction of the propagation of impact-induced delamination in carbon/epoxy laminates ", *Composite Structure*, Vol. 95, pp. 227-235 (2013).

[104] P. Vachon, V. Brailovski, P. Terriault, "Impact-induced damage and damage propagation under flexural load in TiNi and Kevlar-stitched carbon/epoxy laminates ", *Composite Structure*, Vol. 100, pp. 424-435 (2013).

[105] Y. Zou, L. Tong, G.P. Steven, "Vibration-based model-dependent damage (delamination) identification and health monitoring for composite structures Ů a review ", *Sound and Vibration*, Vol. 230, pp. 357-378 (2000).

[106] C.T. Sun, C.J. Jib, "Quasi-static modeling of delamination crack propagation in laminates subjected to low velocity impact ", *Science and Technology*, Vol. 54, pp. 185-191 (1995).

[107] S. Takeda, S. Minakuchi, Y. Okabe, N. Takeda, "Delamination monitoring of laminated composites subjected to low-velocity impact using small-diameter FBG sensors ", *Composites Part A*, Vol. 36, pp. 903-908 (2005).

[108] R. Olsson, M.V. Donadon, B.G. Falzon, "Delamination threshold load for dynamic impact on plates ", *Solids and Structures*, Vol. 43, pp. 3124-3141 (2006).

[109] R. Olsson, "Analytical model for delamination growth during small mass impact on plates ", *Solids and Structures*, Vol. 47, pp. 2884-2892 (2010).

[110] N. Toyama, J. Takatsubo, "Lamb wave method for quick inspection of impact-induced delamination in composite laminates ", *Composites Science and Technology*, Vol. 64, pp. 1293-1300 (2004).

[111] S.C. Wooh, C. Wei, "A high-fidelity ultrasonic pulse-echo scheme for detecting delaminations in composite laminates ", *Composites Part B*, Vol. 30, pp. 433-441 (1999).

[112] R.A. Esmaeel, F. Taheri, "Delamination detection in laminated composite beams using the empirical mode decomposition energy damage index ", *Composites Structures*, Vol. 94, pp. 1515-1523 (2012).

[113] A.R. Oskouei, A. Zucchelli, M. Ahmadi, G. Minak, "An integrated approach based on acoustic emission and mechanical information to evaluate the delamination fracture toughness at mode I in composite laminate ", *Materials and Design*, Vol. 32, pp. 1444-1455 (2011).

[114] I. Amenabar, A. Mendikute, A. Lopez-Arraiza, M. Lizaranzu, J. Aurrekoetxea, "Comparison and analysis of non-destructive testing techniques suitable for delamination inspection in wind turbine blades ", *Composites Part B*, Vol. 42, pp. 1298-1305 (2011).

[115] C. Ramadas , K. Balasubramaniam, M. Joshi, C.V. Krishnamurthy, "Characterisation of rectangular type delaminations in composite laminates through B- and D-scan images generated using Lamb waves ", *NDT&E International*, Vol. 44, pp. 281-289 (2011).

[116] P.H. Johnston, C.D. Appleget, M.T. Odarczenko "Characterization of delaminations and transverse matrix cracks in composite laminates using multiple-angle ultrasonic inspection ", *AIP Conf. Proc.* Denver, CO, USA, July 15-20, pp. 1011-1018 (2012).

[117] N. Guoa, P. Cawley "The interaction of Lamb waves with delaminations in composite laminates ", *Acoustical Society of America* Vol. 93, pp. 2240-2246 (1993).

[118] W.J. Percival, E.A. Birt, "A study of Lamb wave propagation in carbon-fibre composites", *Insight*, Vol. 39, pp. 728-735 (1997).

[119] O. Diligent, M.J.S. Lowe, "Reflection of the S_0 Lamb mode from a flat bottom circular hole", *Journal of the Acoustical Society of America*, Vol. 118, pp. 2869-2879 (2005).

[120] M.J.S. Lowe , O. Diligent, "Low-frequency reflection characteristics of the S_0 Lamb wave from a rectangular notch in a plate", *Journal of the Acoustical Society of America*, Vol. 111, pp. 64-74 (2002).

[121] J. Kim, B. Ko, J.K. Lee, C.C. Cheong, "Finite element modeling of a piezoelectric smart structure for the cabin noise problem", *Smart Materials and Structures*, Vol. 8, pp. 380-389 (1999).

[122] N. Huang, L. Ye, Z. Su, "Parameterised modelling technique and its application to artificial neural network-based structural health monitoring", *Proceedings of the 4th Asian-Australasian Conference on Composite Materials*, Sydney, Australia, July 6-9, pp. 999-1004 (2004).

[123] E.B. Flynn.D. Todd, "Optimal Placement of Piezoelectric Actuators and Sensors for Detecting Damage in Plate Structures", *Smart Materials and Structures*, Vol. 21, pp. 265-274 (2010).

[124] C.C. Olson, M.D. Todd, K. Worden, C. Farrar, "Improving excitations for active sensing in structural health monitoring via evolutionary algorithms ", *Vibration and Acoustics*, Vol. 129, pp. 784-802 (2007).

[125] R. Storn, K. price, "Differential Evolution - A Simple and Efficient Heuristic for Global Optimization over Continuous Spaces ", *Global Optimization*, Vol. 11, pp. 341-359 (1997).

[126] M.E. Pedersen, "Good parameters for differential evolution ", *Hvass Laboratories*, Technical Report no. HL1002 (2010).

[127] K. Worden, A.P. Burrows, "Optimal sensor placement for fault detection ", *Engineering Structures*, Vol. 23, pp. 885-901 (2010).

[128] J. Vesterstrom, R. Thomsen, "A comparative study of differential evolution, particle swarm optimization, and evolutionary algorithms on numerical benchmark problems", *Congress on Evolutionary Computation*, Vol.2, pp. 1980-1987 (2004).

[129] Y.J. Wang, J.S. Zhang, "Global optimization by an improved differential evolutionary algorithm ", *Applied Mathematics and Computation*, Vol. 188, pp. 669-680 (2007).

[130] S.W. Doebling, C.R. Farrar, M.B. Prime, "Summary review of vibration-based damage identification methods, ", *The Shock and Vibration Digest*, Vol. 30, pp.91-105 (1998).

[131] B. Peeters, J. Maeck, G. DeRoeck, "Vibration-based damage detection in civil engineering: excitation sources and temperature effects ", *Smart Materials and Structures*, Vol. 10, pp. 518-527 (2010).

[132] M.T. Bement, T.R. Bewley, "Excitation design for damage detection using iterative adjoint-based optimization Ů Part 1: Method development ", *Mechanical Systems and Signal Processing*, Vol. 23, pp. 783-793 (2009).

[133] R.J. Alonso, M. Noori, S. Saadat, A. Masuda, Z. Hou, "Effects of excitation frequency on detection accuracy of orthogonal wavelet decomposition for structural health monitoring ", *Earthquake Engineering and Engineering Vibration*, Vol. 3, pp. 101-106 (2004).

[134] J.M. Nichols, M.D. Todd, M. Seaver, L. Virgin, "Use of chaotic excitation and attractor property analysis in structural health monitoring", *Physical Review E, Statistical Physics, Plasmas, Fluids, and Related Interdisciplinary Topics*, Vol. 67, pp. (016209)1-8 (2003).

[135] V. Giurgiutiu, "Tuned lamb wave excitation and detection with piezoelectric wafer active sensors for structural health monitoring ", *Intelligent Material Systems and Structures*, Vol. 16, pp. 291-305 (2005).

[136] J.S. Bendat, A.G. Piersol, "Engineering applications of correlation and spectral analysis ", *Jhon Wiley & Sons*, New York (1993).

[137] PI Ceramic "Data Piezoceramic Materials (PZT) and Temperature Coefficients ", *www.piceramic.com* (2013).

[138] S. Sherrit, S.P. Leary, B.P. Dolgin, Y. Bar-Cohen, R.D. Tasker "Analysis of the impedance resonance of piezoelectric stacks ", *Proceedings of the 2000 IEEE Ultrasonics Symposium*, San Juan, Puerto Rico, October 22-25 (2000).

[139] Y.H. Kim, D.H. Kim, J.H. Han, C.G. Kim, "Damage assessment in layered composites using spectral analysis and Lamb wave", *Composites: Part B*, Vol. 38, pp. 800-809 (2007).

[140] V. Giurgiutiu, A. Cuc, "Embedded non-destructive evaluation for structural health monitoring, damage detection, and failure prevention ", *The Shock and Vibration Digest*, Vol. 37, pp. 83-105 (2005).